



UNIVERSITY OF ZAGREB

FACULTY OF GEODESY

MATEJ VARGA

**The Application of Crustal Models in
Regional Modelling of the Earth's Gravity
Field**

DOCTORAL THESIS

Zagreb, 2018



UNIVERSITY OF ZAGREB

FACULTY OF GEODESY

MATEJ VARGA

**The Application of Crustal Models in
Regional Modelling of the Earth's Gravity
Field**

DOCTORAL THESIS

Supervisors:

Professor Tomislav Bašić, PhD
Professor Dimitrios Tsoulis, PhD

Zagreb, 2018



SVEUČILIŠTE U ZAGREBU
GEODETSKI FAKULTET

MATEJ VARGA

**Primjena modela kore pri regionalnom
modeliranju Zemljinog polja sile teže**

DOKTORSKI RAD

Mentori:

Prof. dr. sc. Tomislav Bašić
Prof. dr. sc. Dimitrios Tsoulis

Zagreb, 2018

Declaration of authorship

I, *Matej Varga*, hereby declare that this doctoral thesis, titled *The Application of Crustal Models in Regional Modelling of the Earth's Gravity Field*, is entirely my own work. It is submitted in fulfillment of the requirement for the degree of *Doctor of Science* at the University of Zagreb. To the best of my knowledge, I always referenced publications, data and software created and published by other authors.

Signed: *Matej Varga*

Date: January 22, 2018

Thesis information

I. Author

Name and Surname Matej Varga
Date of birth March 18th, 1989
Place of birth Zagreb, Croatia

II. Supervisors

1. Prof. Tomislav Bašić, PhD
University of Zagreb, Faculty of Geodesy
Kačićeva 26 10000 Zagreb, Croatia
tomislav.basic@geof.hr
2. Prof. Dimitrios Tsoulis, PhD
Aristotle University of Thessaloniki, School of Rural and Surveying Engineering
Univ Box 440, 54124 Thessaloniki, Greece
tsoulis@auth.gr

III. Study programme

University University of Zagreb
Faculty Faculty of Geodesy
Study programme Postgraduate doctoral study of geodesy and
 geoinformatics
Scientific area Technical Sciences
Scientific field Geodesy
Scientific branch Marine, satellite and physical geodesy

IV. Institution

University of Zagreb
Faculty of Geodesy
Kačićeva 26, 10000 Zagreb
Croatia
Tel: + 385 (1) 4639 222
Fax: + 385 (1) 4828 081
e-mail: pisarnica@geof.hr
WGS84: $\varphi = 45^{\circ}48'31.7''$, $\lambda = 15^{\circ}57'49.0''$
HTRS96/TM: $E = 458\,300$ m, $N = 5\,074\,470$ m

V. Timeline and commission

Enrollment in the study programme	October 1 st , 2012
Student ID number	PD-511
Defense of the theme	July 8 th , 2015
Faculty Council report	July 16 th , 2015
Theme approved by the University council	October 13 rd , 2015
Supervisors report on the Faculty Council	November 29 th , 2017
Evaluation committee	Prof. Mario Brkić, PhD ^a Assis.-Prof. Milan Rezo, PhD ^b Prof. Bojan Stopar, PhD ^c
Thesis evaluation report on the Faculty Council	December 21 st , 2017
Defense committee	Prof. Mario Brkić PhD Assis.-Prof. Milan Rezo, PhD Prof. Bojan Stopar, PhD
Defense	January 23 rd , 2018
Thesis ID number	92

^aFaculty of Geodesy, *University of Zagreb*, Zagreb, Croatia

^bFaculty of Geotechnical Engineering, *University of Zagreb*, Zagreb, Croatia

^cFaculty of Civil and Geodetic Engineering, *University of Ljubljana*, Ljubljana, Slovenia

VI. Thesis in numbers

Doctoral thesis has 240 pages, 2 parts, 11 chapters, 110 figures, 63 tables and 442 cited references.

VII. Citation

Varga, M. (2018). *The Application of Crustal Models in Regional Modelling of the Earth's Gravity Field*, PhD thesis, Faculty of Geodesy, University of Zagreb.

VIII. Digital version

Available on the permanent link:
to be uploaded

Acknowledgments

“Although my senses were searching the desert fatiguelessly, discovering nothing although finding a lot, my soul was illuminated by a thousand suns, but could never ever touch the perfection of a single atom.”

Ibn Sina 981-1037 AD

First, I wish to thank my supervisor and *boss* Prof. Tomislav Bašić for leading me in my development as a scientist and teacher. I admire his knowledge and wisdom about geodesy and life in general. He supported and advised me without hesitation and solved many doubts that have arisen along the way. It is my privilege to be his associate.

I am happy to have a second supervisor Prof. Dimitrios Tsoulis who supported me from the beginning. His valuable advices and comments contributed to the improvement of this thesis.

There is a man who taught me how to be a scientist, how to analyse and solve problems. Above all, his presence and work persistently reminds me of the two characteristics of all great men: sincerity and modesty. Dear Prof. Mario Brkić, thank you.

My grateful thanks to the close colleagues Marijan, Olga, Marko and Marija. From them, I have learned a lot about cooperation and team-work. Special thanks to Marijan; for all our funny&supportive talks, discussions, and great time we've spent together in our office. I am thankful to the numerous other colleagues at the Faculty who helped and supported me all these years.

Many thanks to Dr.-Ing. Heiner Denker and Prof. Dr.-Ing. Jürgen Müller from the Institut für Erdmessung (IfE), Leibniz Universität Hannover (LUH) for their hospitality during the crucial stages of my PhD research.

The authors of the software routines that were used as a starting point for my research are greatly acknowledged. Especially, Carl Christian Tscherning (1942-2014), René Forsberg, Mario Brkić, Ramazan Alpay Abbak and Jianliang Huang. They kindly shared their work allowing me and all other academics to continue researching and contributing in development of this scientific branch.

Big thanks to my friends Ivan, Matej, Ivo, Luka, Jakov, Nikola and Darko for making my life happier and enjoyable.

To my mother Anka, father Jakob and sister Katarina. Words can never describe how happy and grateful I am to have you.

Finally, special thanks to my beautiful wife Tomislava. My inexhaustible source of happiness and motivation. A cornerstone of our (still) small family. With you, every day of my life is a gift.



In Zagreb, January 2018

Dedication

I dedicate this work to my grandmother Kata and grandfather Ivan who did not live enough to see it finished.

May their souls rest in eternal peace.

Abstract

One of the ultimate goals in geodesy, a 1 cm geoid model, is still unreachable for most of the areas worldwide. Several theoretical, methodological, numerical and data problems will have to be resolved in order to achieve it. The main motivation of this research is in making methodological and empirical contribution towards resolving some of the open problems in the regional gravity field and geoid modeling.

Topographic and density effects which affect short and very-short wavelengths of the gravity field have been traditionally modelled using the constant parameters of the Earth's crust. As such parameters are only an approximation, this has been a limitation in more accurate filtering and reduction of the gravity data. Therefore, a methodology was developed which allows inclusion of surface and three dimensional crustal models in all steps of geoid determination. Prior to this, surface crustal density models were developed based on the inversion methods according to Pratt-Hayford, Airy-Heiskanen, and Parasnis-Nettleton. Additionally, three-dimensional crustal models EPcrust and CRUST1.0 were included in the computations. As a result of including crustal density models, the accuracy of developed gravimetric geoid models was improved from 1 to 3 cm.

The second major focus of research was related to the problem of the diversity of possible geoid computation methods and dozens of ways to perform reduction of the gravity field. The comparison of two widely used geoid modelling approaches was performed: Royal Institute of Technology (KTH) and Remove-Compute-Restore (RCR). Furthermore, *compute* step in RCR approach may be performed using several spectral and spatial methods. Therefore, different geoid computation methods were compared, including analytic Stokes integration using different deterministic modifications of the Stokes' kernels, planar and spherical Fast Fourier Technique (FFT), flat-Earth and 3D least squares collocation (LSC). KTH approach, being a relatively straightforward geoid modelling approach compared to the RCR, was used for the analysis of the influence of all input models and parameters on the accuracy computed geoid models. From the large number of computed geoid solutions, two final gravimetric and hybrid geoid models for Croatia were selected HRG2018-RCR and HRG2018-KTH having standard deviation of $\pm 3.0\text{ cm}$ and $\pm 3.5\text{ cm}$. The accuracy of geoid models was validated on GNSS/levelling points with seven parametric models using a unique *cross-validation* fitting methodology. Few other aspects of regional gravity field modeling were researched: i) investigation of the influence of input models and parameters in obtaining residual gravity field used in the RCR approach, ii) validation of the accuracy of global geopotential models, and iii) validation of gridding methods for several types of gravity anomalies.

Keywords: gravimetric geoid, GNSS/levelling, crustal models, topographic reduction, remove-compute-restore (RCR), least squares modification of Stokes' formula with additive corrections (KTH)

Sažetak

Jedan od glavnih ciljeva geodezije, 1 cm model geoida, još je uvijek nemoguće izračunati u mnogim područjima diljem svijeta. Za postizanje toga moraju se riješiti mnogi teoretski, metodološki, numerički i podatkovni problemi u postupku modeliranja polja ubrzanja sile teže. Glavna motivacija ovog istraživanja je rješavanje nekih od otvorenih problema regionalnog modeliranja sile teže i geoida.

Modeliranje topografskih efekata, koji utječu na kratke i ultra-kratke valne duljine polja sile tež, uobičajeno se radi korištenjem konstantnih vrijednosti parametara Zemljine kore. To predstavlja ograničenje u pogledu točnosti redukcije mjerenja ubrzanja sile teže. Stoga je razvijena i primijenjena metodologija koja omogućava korištenje dvodimenzionalnih (2D) i trodimenzionalnih (3D) modela kore. Prethodno su izrađeni modeli površinskih gustoća kore korištenjem inverznih metoda Parasnis-Nettletona, Airy-Heiskanena i Pratt-Hayforda. U računanjima i analizama su korišteni i dostupni trodimenzionalni globalni modeli kore EPCrust i CRUST1.0. Rezultati upućuju na značajan utjecaj parametara i modela kore na točnost izračunatih modela geoida.

Drugi fokus istraživanja odnosi se na postojeće različitosti u pristupima i metodama pri redukciji gravimetrijskih podataka i računanju geoida. U tom kontekstu, napravljena je usporedba dva najkorištenija pristupa računanja modela geoida - remove-compute-restore (RCR) i metode najmanjih kvadrata s adicijskim korekcijama (KTH). Korak *compute* u RCR pristupu može se napraviti brojnim spektralnim i prostornim metodama. Stoga su uspoređene različite metode računanja geoida, koje uključuju analitičko rješenje Stokesovog integrala (koristeći različite determinističke modifikacije Stokesovog integrala), ravninski i sferni FFT, 2D i 3D LSC.

KTH pristup, kao relativno direktan pristup u usporedbi s RCR pristupom, korišten je za analizu utjecaja svih ulaznih modela i parametara na izračunate modele geoida i njihovu točnost.

Točnost modela geoida procijenjena je usporedbom na raspoloživim GNSS/nivelmanskim točkama korištenjem sedam različitih parametarskih modela primjenom modificiranog postupka. Parametarski model s najmanjim standardnim odstupanjem korišten je za fitanje gravimetrijskog i dobivanje hibridnog modela geoida.

Iz svih izračunatih rješenja, izabrani su konačni gravimetrijski i hibridni modeli geoida za hrvatsko područje: HRG2018-RCR i HRG2018-KTH, sa standardnim odstupanjem $\pm 3.0\text{ cm}$ i $\pm 3.5\text{ cm}$.

Obrađeni su i drugi problemi kao što su: utjecaj ulaznih modela i parametara na dobivanje rezidualnog polja sile teže u RCR pristupu, točnost globalnih geopotencijalnih modela (GGM) i točnost metoda interpolacije anomalija ubrzanja sile teže.

Ključne riječi: gravimetrijski geoid, GNSS/niveliranje, modeli kore, topografske redukcije, remove-compute-restore (RCR) pristup, modifikacija Stokesa po najmanjim kvadratima s dodatnim korekcijama (KTH)

Table of Contents

Declaration of autorship	i
Thesis information	i
Acknowledgements	iii
Dedication	v
Abstract	vii
List of Acronyms	xv
List of Symbols	xvii
1 Introduction	1
1.1 Statement of the problem	2
1.2 Thesis objectives	2
1.3 Expected scientific contribution	3
1.4 Literature review	4
1.5 Chapter summary	9
I Theory	11
2 Fundamentals of gravitational field	13
2.1 Earth's gravity field	14
2.2 Normal Field	15
2.3 Disturbing field	17
2.3.1 Anomalous gravity field	17
2.3.2 Bruns formula, fundamental equation of physical geodesy and Boundary Value Problem	18
3 Topographic reductions	21
3.1 Free air reduction	22
3.2 Bouguer reduction	23
3.2.1 Complete Bouguer reduction	24
3.2.2 Terrain correction	24
3.2.3 2D and 3D rectangular prisms	27
3.2.4 Complete Bouguer anomaly	29
3.3 Isostasy	30
3.3.1 Pratt-Hayford topographic-isostatic model	30

3.3.2	Pratt-Hayford reduction	31
3.3.3	Airy-Heiskanen topographic-isostatic model	32
3.3.4	Airy-Heiskanen reduction	33
3.4	Residual Terrain Model	34
3.5	Review	35
4	Geoid Determination	37
4.1	Introduction	37
4.2	Stokes' theorem	39
4.2.1	Molodenskii's theory	41
4.3	Data for gravimetric geoid determination	42
4.4	Surface crustal density models	43
4.4.1	Pratt-Hayford	44
4.4.2	Airy-Heiskanen	44
4.4.3	Parasnis-Nettleton	45
4.5	Geoid determination approaches and methods	46
4.5.1	Types of geoid models	47
4.6	KTH approach	52
4.6.1	Approximate geoid undulation	53
4.6.2	Signal and error (noise) degree variances	54
4.6.3	Terrestrial data error degree variances	54
4.6.4	Least-squares modification parameters	55
4.6.5	Additive Corrections	56
4.6.5.1	Topographic correction	56
4.6.5.2	Downward Continuation correction	56
4.6.5.3	Atmospheric Correction	57
4.6.5.4	Ellipsoidal correction	57
4.7	Remove-compute-restore approach	58
4.7.1	'Pure RTM' variation	58
4.7.2	Global geopotential models	59
4.7.3	Compute	63
4.7.4	Least Squares Collocation	63
4.7.4.1	Planar logarithmic covariance model	66
4.7.5	Stokes integration	67
4.7.5.1	Original 'analytic' Stokes kernel	67
4.7.5.2	Kernel modifications	68
4.7.6	Spectral methods	72
4.7.6.1	Planar FFT	72
4.7.6.2	Spherical FFT	73
4.7.6.3	Spherical multi-band FFT	73
4.7.6.4	Spherical 1D FFT	74
4.7.7	Restore	74

4.8	Accuracy validation and fitting of geoid models	75
4.8.1	Relative geoid accuracy validation	78
4.9	Gridding and interpolation	79
II	Research	81
5	Data, study area, and software	83
5.1	Terrestrial and marine gravity anomalies	83
5.2	Validation of gridding methods using different types of gravity anomaly	91
5.3	GNSS/levelling dataset	95
5.4	Global geopotential models	95
5.4.1	Global geopotential models validation	98
5.4.1.1	Validation on GNSS/levelling points	99
5.4.1.2	Validation on gravity points	103
5.4.1.3	Validation with varying maximal degree of expansion	104
5.4.1.4	Review	107
5.5	Digital elevation models	110
5.6	Crustal density models	112
5.6.1	Development of the crustal density models	115
5.7	Study area	118
5.8	Software	122
6	Residual gravity field modeling	125
6.1	Residual gravity anomalies as a function of different parameters or models	127
6.2	Residual gravity anomalies as a function of two different parameters	131
6.3	Review	134
7	KTH approach geoid	137
7.1	HRG2018-KTH: new gravimetric and hybrid geoid models	138
7.2	Additive corrections	141
7.3	Influence of input parameters and models on geoid solutions	143
8	RCR approach geoid	151
8.1	Solutions using different crustal density models	152
8.2	Solutions using different computation methods	154
8.2.1	'Classic' Stokes	154
8.2.2	Planar FFT	155
8.2.3	LSC with flat-Earth logarithmic covariances	157
8.2.4	Least Squares Collocation	157
8.2.5	Spherical multi-band FFT	158
8.2.6	Spherical 1D FFT	160
8.2.7	Validation of geoid models computed with RCR and KTH approaches	163
8.2.7.1	Differences between geoid models computed using different methods	163

8.3	HRG2018-RCR: new gravimetric and hybrid geoid models	166
8.3.1	Validation and fitting of geoid models using GNSS/levelling data	168
8.3.2	Relative geoid accuracy validation	173
8.4	Review	174
9	Conclusions and future research	177
	Future research	179
	Bibliography	183
Appendix A	Flowcharts of KTH and RCR geoid determination approaches	203
Appendix B	Gridded geoid undulation differences between KTH and RCR solutions	205
Appendix C	Models of topographic reductions and gravity anomalies	211
Appendix D	Developed software	217
Appendix E	Additional tables	223
	List of Figures	227
	List of Tables	232
	Curriculum Vitae	237

List of Acronyms

A-H Airy-Heiskanen topographic-isostatic model
BVP Boundary Value Problem
CFT continuous Fourier transform
CHAMP CHAllenging Minisatellite Payload
CROPOS CROatian POsitioning System
DEM digital elevation model
DFT discrete Fourier transform
DSM digital surface model
DTE direct topographical effect
DTM digital terrain model
DWC Downward Continuation
ECF empirical covariance function
EGG European Gravimetric Quasigeoid
ETRS89 European Terrestrial Reference System 1989
FEFG fundamental equation of physical geodesy
FFT Fast Fourier Technique
FSC Fast Spherical Collocation
GCM geoid computation method
GEOCOL spherical 3D LSC
GEOFOUR planar FFT
GGM Global Geopotential Model
GIS Geographic Information System
global DEM global digital elevation model
GMSE Global Mean Square Error
GNSS Global Navigation Satellite System
GOCE Gravity Field and Steady-State Ocean Circulation Explorer
GPCOL planar LSC
GRACE Gravity Recovery and Climate Experiment
Graflab GRAvity Field LABoratory
GRAVSOFT Gravity Prediction Software
GRS80 Geodetic Reference System 1980
GUI Graphical User Interface
Harmsynth Harmonic Synth

HRG2009	Croatian quasi-geoid 2009
HRS	Height Reference System
HTRS96	Croatian Terrestrial Reference System 1996
HVRS71	Croatian Height Reference System 1971.5
IAG	International Association of Geodesy
ICGEM	International Centre for Global Earth Models
IDW	Inverse Distance to a Power
IfE	Institut für Erdmessung
IGSN71	International Gravity Standardization Network 1971
IHRS	International Height Reference System
ISG	International Service for the Geoid
KTH	Royal Institute of Technology
LiDAR	Light Detection and Ranging
LSC	least squares collocation
LSMSA	Least Squares Modification of Stokes' formula with Additive corrections
LSMSSOFT	KTH Least-Squares Modification software
LUH	Leibniz Universität Hannover
LVD	local vertical datum
MSL	mean sea level
P-N	Parasnis-Nettleton's inversion method
RBFs	radial base functions
RCR	Remove-Compute-Restore
RMS	Root Mean Square
RMSE	Root Mean Square Error
RTK	Real Time Kinematic
RTM	Residual Terrain Modelling
SAR	Synthetic Apertur Radar
SFRJ	Socialist Federal Republic of Yugoslavia
SH	spherical harmonic
SI	International System of Units
SP1D	spherical 1D FFT
SPFOUR	spherical multi-band FFT
Stokes	analytic Stokes integration method
SVD	Singular Value Decomposition
TC	terrain correction
TIN	triangulated irregular network
UNB	Stokes-Helmert
WGS84	World Geodetic System 1984
WHS	World Height System

List of Symbols

R^2 coefficient of determination

φ, λ, h coordinates, ellipsoidal or geodetic latitude, longitude and height)

r, θ, λ coordinates, spherical polar coordinates (radial distance, colatitude, longitude)

x, y, z coordinates, local rectangular

ρ_c density of the crust

ρ_w density of the water

ρ_m density of the mantle

dc_n error degree variances

GM product of gravitational constant and mass of the body

Δg_{FA} gravity anomaly, free-air

Δg_{SB} gravity anomaly, simple Bouguer

Δg_{CB} gravity anomaly, complete Bouguer

Δg_{GGM} gravity anomaly, GGM; $\Delta g_{GGM} = \Delta g_{FA} - \Delta g_{GGM}$

$\Delta g_{FA-GGM-RTM}$ gravity anomaly, residual gravity anomaly in RCR approach; $\Delta g_{FA-GGM-RTM} = \Delta g_{FA} - \Delta g_{GGM} - \Delta g_{RTM}$

Δg_{RTM} gravity anomaly, RTM; $\Delta g_{RTM} = \Delta g_{FA} - \Delta g_{RTM}$

N geoid undulation

ζ height anomaly

gra gravimetric geoid model

$\Delta N_{GNSS/lev.-geoid}$ geoid undulation difference between GNSS/levelling point and point from the geoid model

G Newtonian gravitational constant, $6.67408(31) \cdot 10^{-11} \text{ m}^3 \text{ kg}^{-1} \text{ s}^{-2}$

n, m degree and order of expansion of the GGM

h height, ellipsoidal (geodetic)

H height, orthometric

H^* height, normal

H' depth

hyb hybrid (fitted to LVD) geoid model

\tilde{N} KTH approach, approximate geoid height

δN_{atm} KTH, atmospheric effect (correction) on N

δN_{top}^{comb} KTH, combined topographic effect (correction) on N

δN_{DWC} KTH, DWC effect (correction) on N

δN_{ell} KTH, ellipsoidal effect (correction) on N

-
- ψ Stokes integral as a function of the ψ
 $N_{GNSS/lev.}$ geoid undulation obtained by GNSS/levelling
 N_{geoid} geoid undulation obtained by interpolation gravimetric geoid
 a, b, J_2, e parameters of the ellipsoid; semi-major axis, semi-minor axis, dynamical flattening
(second-degree zonal harmonic coefficient), eccentricity of the ellipsoid
 Q point on the ellipsoid
 S point on the Earth's topography surface
 P point on the geoid
 δg_B reduction, Bouguer
 δg_{FA} reduction, free-air
 δg_{RTM} reduction, RTM
 R mean radius of the Earth, 6371 km
 ψ spherical distance between computation and integration point
 δg_{TC} reduction, terrain correction
 T disturbing potential
 V_s velocity, shear wave
 V_p velocity, pressure wave
 V gravitational potential
 W gravity potential of the real Earth (sum of the gravitational and centrifugal potential)

Chapter 1

Introduction

“If I have seen further than others, it is by standing upon the shoulders of giants.”

Sir Isaac Newton, 1643-1727

Earth’s gravity field has been a subject of exploration and research since the end of the 16th century. Its importance manifests in many tasks in geosciences, including geodesy and geophysics. Today, modeling of the Earth’s gravity field is still one of the main scientific interests in geosciences.

Gravimetry (Latin: *gravis*, heavy, Greek: *μετρεω*, measure), measurements of the gravity field, have been continuously performed using absolute and relative gravimeters since 1940s, and have increased substantially both in terms of an accuracy and spatial coverage. Today, gravity is measured with accuracy of around 1 μ Gal using absolute gravimeters, and 2-10 μ Gal using relative gravimeters. A significant increase in the quantity of the globally available data has started from 2000 after the start of satellite gravity missions CHALLENGING Minisatellite Payload (CHAMP), Gravity Recovery and Climate Experiment (GRACE) and Gravity Field and Steady-State Ocean Circulation Explorer (GOCE). Since satellite gravimetry measure gravity field globally (up to approximately 100 km), data from other measurement instruments have to be used for filling spectral and spatial gaps, such as airborne and shipborne gravimetric data.

Apart from the standard gravimetric data, other sources of information such as crustal data and models have the potential for inclusion into the gravity field modelling. Crustal models may be created from several types of geodetic, geophysical, geological, and seismological data using geophysical inversion methods and procedures. Such data provide more information about the internal structure of the Earth. For a long time global and regional crustal structure of the Earth was mostly unknown due to a lack of the appropriate geophysical and geological data. For comparison purposes, digital elevation models, as models of the Earth’s external topography, are published in resolutions of 1'' or 3'' since 2000, while the most recent and detailed global crustal model was published in 2015 and has resolution of 1°. This means crustal models, describing situation below Earth’s topographic surface, give almost 3600 times less details. From these reasons, Earth’s complex and layered crustal structure was usually approximated and described with only few globally estimated parameters. For example, constant value of 2670 kgm⁻³ has

been almost exclusively used as the best approximated global mean crustal density value (Hinze 2003). The situation has changed in the last two decades, as there have been numerous attempts to acquire data about the Earth's internal structure, as well as to develop and improve crustal models. Available crustal models have opened up a possibility of applying them in gravity field modelling, instead of using only approximate global values.

On the other hand, mathematical and computational methods for modelling of the gravity field have been developed and improved throughout the years, along with increasing collection and availability of the gravity and crustal data on all spatial scales. Methods for geoid determination have been theoretically founded, with less simplifications and approximations. Error sources which affected geoid solutions and had to be neglected in the past are currently successfully removed, modeled and filtered in the modeling process.

As a consequence, geoid computation process has diverged in a number of different ways. Currently few geoid determination approaches are used, whereas each approach has again diverged in several methods. For example, only gravity anomaly data may be used in analytic Stokes method, while in Least Squares Collocation method both gravity anomalies and gravity gradients data can be used. From the theoretical standpoint, if methods are mathematically well-defined, they shall all give the same or almost similar result. From the practical point of view, this is almost never the case. This leads to some kind of paradoxical situation where the *true* geoid surface can possibly be only one (specific value of the real potential W_0), but the geoid model, as its best approximation, can be computed in almost infinite number of different ways. In fact, there are no two researchers that will derive exactly the same geoid model. This was shown in multiple cases where different groups of scientists came out with differences between geoid solutions of more than 5 or 10 cm. See, for instance, development of the NKG2015 (Ågren et al. 2015) or GEOMED2 (Barzaghi et al. 2017) geoid models.

1.1 Statement of the problem

One of the main tasks of geodesist's is determination of the geopotential surface- geoid. From the beginning of the 21st century, the ultimate goal has been determination of the geoid model with 1 cm accuracy. However, this is possible only with the optimal usage of all available data and methods. One of the current limitations towards achieving a geoid model with wanted accuracy is in using constant crustal parameters in gravity field modelling. Errors in modelling are included because in local and regional areas crustal structure is significantly different to be satisfactorily approximated with such simplification. Although examples in the world exist where crustal models were used in computations, there are methodological unknowns on how to derive and implement crustal models, as well as insufficient empirical research on different study areas worldwide.

1.2 Thesis objectives

The main objectives of the thesis are:

- Development of methodology for including two (2D) and three dimensional (3D) crustal density models in all steps of regional gravity field modelling and geoid determination.
- Development of the lateral (2D) crustal density models for the study area.
- Assessment of the influence of crustal density models on the accuracy of geoid models by using:
 - different constant crustal density values (1D),
 - developed surface (2D or lateral) crustal density models,
 - existing 3D crustal models (EPcrust and CRUST1.0).
- Determination of updated and improved gravimetric and hybrid geoid models for the Republic of Croatia.
- Comparison of the most often used geoid determination approaches: Remove-Compute-Restore (RCR) and Royal Institute of Technology (KTH).
- Comparison of spatial and spectral geoid computation methods.
- Assessment of the influence of all input parameters and models on the accuracy of geoid models.

All computations are performed over the study area which covers the territory of the Republic of Croatia and its close surrounding.

1.3 Expected scientific contribution

Expected scientific contributions of the thesis are:

- Lateral (2D) crustal density models developed using Pratt-Hayford's, Airy-Heiskanen's, and Parasnis-Nettleton's inversion methods for the study area.
- Estimation of the optimal constant crustal density value over the study area.
- New gravimetric and hybrid geoid models for the Republic of Croatia computed using the most recent geopotential, elevation and crustal models.
- Maps of terrain correction, Faye, simple Bouguer, complete Bouguer, and topographic-isostatic gravity anomalies over the study area.
- Closer insights into the importance of various input parameters and models (crustal, geopotential and elevation) on reduced gravity anomalies and computed geoid undulations.
- Statistical and visual results related to the comparison and validation of the RCR and KTH geoid modelling approaches.
- Results of comparisons and validations of geoid models computed using several spatial and spectral geoid computation methods: analytic Stokes' integration with different kernel modifications, spectral methods (planar, spherical, spherical multi-band FFT), least squares collocation (planar and 3D).
- Results of the accuracy validation of the most recently published global geopotential models from the GOCE and GRACE satellite gravity missions using the independent gravity and GNSS/levelling data.
- Results of the investigations of the interpolation (gridding) methods for several types of gravity anomalies. Eleven interpolation methods with different input parameters are used including: Inverse Distance to a Power (IDW), Kriging, Minimum Curvature, Modified Shepard's, Natural Neighbour, Nearest Neighbour, Polynomial Regression, radial base

functions (RBFs), triangulated irregular network (TIN), Moving Average, Local Polynomial. Types of gravity anomalies included in the investigations are: free-air, simple Bouguer, complete Bouguer, residual (FA-GGM-RTM) gravity anomalies.

- Known accuracy of the gravimetric and hybrid geoid models using different fitting parametric models: bias, linear, 2nd and 3rd polynomials, 4, 5, and 7 parameters.
- Developed scripts for calculation of topographic and topographic-isostatic effects on gravity field quantities with possibility for using global and regional 2D and 3D crustal models.
- Developed scripts for gravity field modelling and geoid determination allowing automated and seamless determination of geoid models starting from the input parameters and models without necessity for a manual work.

1.4 Brief literature review

A brief literature review is given in this section with reference to the publications which are relevant for this thesis either from a theoretical or practical aspect. The section is divided in a few topic-related subsections in order to improve comprehension. Additional references are also provided throughout the part I: Theory.

Crustal density models in regional geoid determination

Several investigations have been conducted in the past related to the usage of the Earth's crustal data and models in regional gravity field modelling and geoid determination. [Martinec \(1993\)](#) shows theoretically that small density variations can have an effect on the gravity reduction and then on geoid undulations of more than 1 decimeter in mountainous areas. He investigated density effects of lateral (horizontal) anomalies and approximated topography with mass columns. [Tziavos et al. \(1996\)](#) studied the effect of surface density variation in modelling of terrain effects. [Kühtreiber \(1998b\)](#) evaluated contributions of a density variation using RCR approach for geoid model in the central part of Austria. He found that small changes in density can change gravimetric geoid by more than 10 cm. [Pagiatakis and Armenakis \(1999\)](#) used Geographic Information System (GIS) to create surface crustal density model from geological maps for the Canadian territory. [Pagiatakis et al. \(1999\)](#) and [Esan \(2000\)](#) found that the effect of surface densities have almost 3 mGal effect on terrain corrections and 1 decimeter on geoid undulations. According to [Omang \(2000\)](#), the use of density informations in the geoid determination did alter the geoid by as much as 20-30 cm, but the improvement in hybrid geoid models were not conclusive. [Huang et al. \(2001\)](#) and [Huang \(2002\)](#) implemented [Martinec \(1993\)](#) theoretical research and studied lateral variation of topographical density on gravity and geoid in western Canada, and found that the effect on the geoid ranges from -7.0 to 2.8 cm. [Kuhn \(2000\)](#), [Kuhn \(2001\)](#), and [Kuhn \(2003\)](#) used Pratt-Hayford (P-H), Airy-Heiskanen (A-H) and Vening-Meinesz (V-M) topographic-isostatic models and geological information to compute geoid in Germany. He found out that the effect may reach 1 decimeter. [Tziavos and Featherstone \(2001\)](#) improved geoid solutions by 1-2 cm when using density models in Australia. [Sjöberg \(2004b\)](#) computed the total effect on the geoid due to the lateral density anomaly which can be more than 2 cm for elevations higher than 1000 m and in extreme cases may reach more than few decimeters.

Kiamehr (2006a) and Kiamehr (2006b) studied lateral density effects on geoid by creating a density variation model using Pratt-Hayford model and found differences of more than 2 dm compared to constant crustal density values. Herceg et al. (2015) investigated how uncertainties in seismic and density structure of the crust propagate to uncertainties in the mantle and gravity anomalies. In his work he used satellite gravity data from GOCE mission and global crustal models CRUST 5.1, CRUST 2.0 and CRUST 1.0.

Tsoulis (2013) gave an overview on the geodetic uses of global digital crustal models for retrieval of very-high frequencies of the measured gravity field. He concluded that crustal data and models should be implemented whenever possible both for global and regional gravity field modelling, but this is still not routinely done due to the low resolution and unknown quality of available data.

Modelling of topographic effects

One of the central issues in geoid determination is modelling of topographic gravity potential effects. Throughout years, many methods and algorithms have been published for calculation of the effects in spatial and spectral domains. The main difference between methods is the way they define, approximate and formulate a *unit* or a *body* for which topographic attraction or potential is calculated. Possible *bodies* used as approximations of real topographic masses in the spatial domain are:

- prisms (Everest 1830, Nagy 1966a, Nagy 1966b, Hjelt 1974, Ketelaar 1976, Forsberg 1984, Ketelaar 1987, Werner and Scheeres 1996, Tsoulis 1998, Tsoulis 1999, Nagy et al. 2000, Smith 2000, Smith et al. 2001, Tsoulis 2001, Heck and Seitz 2007, Tsoulis et al. 2009),
- line-masses (Tsoulis 1999, Wild-Pfeiffer 2008),
- point-masses (Tsoulis 1999, Heck and Seitz 2007, Wild-Pfeiffer 2008, Reguzzoni et al. 2013),
- layer-masses (Tsoulis 1999, Tsoulis et al. 2003, Wild-Pfeiffer 2008),
- Gauss-Legendre quadrature (Hwang et al. 2003, Asgharzadeh et al. 2007, Roussel et al. 2015, Uieda et al. 2016),
- polyhedral bodies (Coggon 1976, Pohánka 1988, Tsoulis et al. 2003, Tsoulis 2012, D'Urso 2013, D'Urso 2014, Werner 2017),
- tesseroids (Ku 1977, Heck and Seitz 2007, Wild-Pfeiffer 2008, Tsoulis et al. 2009, Li et al. 2011, Grombein et al. 2013, Hirt and Kuhn 2014, Uieda et al. 2016),
- tetrahedra (Casenave et al. 2016),
- prisms and tesseroids combination (Tsoulis et al. 2009, Shen and Han 2013),
- prisms and polyhedrons combination (Chai and Hinze 1988, Garcia-Abdeslem 2005, D'Urso 2015).

Some of the available routines for calculation of topographic effects include: TC (Forsberg 1984, Tscherning 1994), Terrain (Ma and Watts 1994), INTLOG5A (Smith 2000), TcLight (Biagi and Sanso 2001), TCQ (Hwang et al. 2003), FA2BOUG (Fullea et al. 2008), GTeC (Cella 2015), GTE (Sampietro et al. 2016, Capponi et al. 2018), and Tesseroids (Uieda et al. 2010, Uieda et al. 2016).

Topographic effects using surface and 3D crustal densities

One of the main focuses of research in this thesis is integration of surface (2D) and 3D crustal density models in gravity field modelling and geoid determination. Source code called *TC* is used as a starting routine, which was developed by prof. René Forsberg, PhD in 1984 (Forsberg 1984). Since then the code was updated several times, and the latest update was done in September 2009. The code is written in Fortran programming language and still has widespread usage in physical geodesy worldwide, especially in geoid determination using RCR approach (see also GRAVSOFTE package, Tscherning 1994, Forsberg and Tscherning 2008). The software has possibilities for computation of terrain, topographic-isostatic and RTM correction for different gravity field functionals, such as gravity anomalies and geoid undulation. Analytic numerical integration of the effects of topographic masses is performed by division of topography on rectangular prisms. The effect of topography for wanted gravity field functionals in some computation point is obtained by summation of the prisms within the selected radius of integration. For increasing of the calculation efficiency, integration area is divided in two zones. Standard input data are fine, coarse and reference digital elevation models. Forberg's original version of *TC* uses constant crustal density for all topographic masses. In 1994, original *TC* code was modified by Mario Brkić (Brkić 1994a, Brkić and Bašić 2001). Prisms with constant densities were divided in vertical z direction. What was before one prism with constant density, became several prisms where each prism has its own density. Vertical limits of prisms were defined by layers from the models of crustal thickness. In Brkić (1994a) study topographic masses are divided on three layers in vertical direction defined by crustal thickness (depths): 1) sediment 2) crustal thickness, and 3) Moho. Each thickness layer has corresponding density layer, therefore there were three density layers for sediments, crustal thickness and Moho. Brkić's solution enables integration of including additional available layers or even complete 3D seven-layered crustal models, such as CRUST1.0, in computation of topographic effects.

RCR vs KTH approach

Theoretical research on the differences between most frequently used geoid determination approaches, RCR and KTH, is given in Klu (2015) and Sjöberg and Bagherbandi (2017a). Only few empirical studies have been published where these two approaches are compared on the same test-area and using identical input data. Ågren et al. (2009) compared geoid models over Sweden and reported Root Mean Square (RMS) 2.2 cm for KTH and 4.0 cm for RCR after 1-parameter fitting. Abbak et al. (2012) compared RCR and KTH over mountainous area in central Turkey and found that the accuracy of geoid computed with KTH is around 3 cm, which is slightly better than geoid computed using RCR approach. Yildiz et al. (2012) computed geoid models for the Auvergne area in France. Geoid computed using KTH approach had accuracy of 2.4 cm, and 2.9 cm for geoid computed using RCR approach.

Geoid models around the world

Large number of geoid models have been published since first attempts somewhere in 1950^s. They were mainly developed for two purposes. First, for scientific purposes as a part of research

and development of various geoid computational methodologies and methods. Second, for practical usage in transformation from ellipsoidal to orthometric heights in national height reference system. As part of the International Association of Geodesy (IAG) service, International Service for the Geoid (ISG) is running a geoid repository where large number of geoid models from different countries over all continents are collected and stored (see, [Reguzzoni et al. 2017](#)). The web-link of repository is [IAG \(2017\)](#). A list of the geoid models developed for different parts of the world along with corresponding references is given in table 1.1.

Regional gravity field modelling in the Republic of Croatia

Gravity field modelling and especially geoid determination in Croatia has a long tradition lasting more than three decades. [Čolić et al. \(1992\)](#) created the first digital surface density model for the test area "Slovenia and surrounding part of Croatia" for the regional uses in physical geodesy. [Brkić \(1994b\)](#) investigated inclusion of the Earth's crustal layers, including models of the surface density distribution and base sediments' depths, in reduction of the topographic effects from gravity-field field measurements. [Petrović and Čolić \(1994\)](#) estimated density contrast at the Mohorovičić discontinuity from the correlation with the geoid. [Čolić et al. \(1996\)](#) used several kinds of geodetic, gravimetric, and geophysical data in gravity field modelling for calculation of topographic and topographic-isostatic effects. [Švehla \(1998\)](#) and [Čolić et al. \(1999\)](#) calculated an astro-geodetic geoid model for the city of Zagreb and Croatia. [Bašić et al. \(2000\)](#) described establishment of new geoidal points in the Republic of Croatia. [Hećimović \(2000\)](#) modeled and compared gravimetric, GPS/levelling, gravimetric and astro-geodetic geoid models in Germany and Croatia. [Brkić \(2001b\)](#) implemented three layer Earth's crust approximation in topographic reductions. The research continued in [Brkić and Bašić \(1997\)](#), [Brkić and Bašić \(2000\)](#), [Brkić \(2001a\)](#), [Brkić and Bašić \(2001\)](#) where terrain correction is computed in spatial and spectral domain. [Hećimović and Bašić \(2002\)](#) evaluated different Global Geopotential Model (GGM) over Croatian territory. [Hećimović \(2005\)](#) compared European Vertical Reference Network solution UELN95/98 with CHAMP and GRACE global gravity models. [Hećimović \(2000\)](#) modeled terrain effects of gravity field functionals using different DEMs and DEMs resolutions in Croatia. In [Pavasović \(2007\)](#), [Pavasović et al. \(2008\)](#), and [Pavasović \(2008\)](#) GRACE monthly solutions are compared on 138 GNSS/levelling points across Croatia. [Liker et al. \(2010\)](#) performed quality control of the national geoid model HRG2000, and different CHAMP and GRACE GGMs using 65 control GNSS/levelling points. [Varga \(2012a\)](#) and [Varga \(2012b\)](#) created a model of Airy-Heiskanen topographic-isostatic anomalies for Croatian territory. He tested different values of reference densities and compensation depths. [Varga et al. \(2012\)](#) reviewed regional geoid models in the world at that period. [Grgić et al. \(2014\)](#) investigated application of HRG2009 geoid model in tunnel construction. [Rezo et al. \(2014\)](#) analysed influence of Earth's topographic masses on deflections of vertical. [Repanić et al. \(2015\)](#) determined vertical gravity gradient for Croatian area. [Bjelotomić et al. \(2015\)](#) investigated possibilities of the refinement of the geoid model on Croatian islands with sparse terrestrial gravity data. [Grgić et al. \(2015\)](#) reviewed height systems in some European countries. [Dragčević et al. \(2016\)](#) validated HRG2000 and HRG2009 geoid solutions over the area of City of Zagreb on the newly established network of GNSS/levelling points. They found standard deviation of HRG2000 is 3.7 cm, and HRG2009 2.4 cm. In [Varga et al. \(2016\)](#) initial considerations of the modernization of the Croatian Height Reference

Table 1.1: A list of geoid models and corresponding references worldwide

Country, continent	Reference
Africa	Obenson 1974, Merry et al. 2005, Gachari 1998
Algeria	Benahmed Daho and Kahlouche 2000, Daho et al. 2006
Antarctica	Scheinert et al. 2008, Schwabe et al. 2012
Argentina	Tocho et al. 2007, GAR (Corchete and Pacino 2007), GEOIDEAR16 (Piñón et al. 2017)
Australia	AUSGeoid98 (Featherstone et al. 2001), AUSGeoid09 (Featherstone et al. 2011), AGQG2017 (Featherstone et al. 2018)
Austria	AGG97 (Kühtreiber 1998a), Kühtreiber 2002
Bolivia	BOLGEO (Corchete et al. 2006)
Brasil	MAPGEO2015 (de Matos et al. 2016)
Cameroon	CGM05 (Kamguia et al. 2007)
Canada	CGG1993 (Sideris and She 1995), CGG2000 (Véronneau and Huang 2002, Véronneau et al. 2006), CGG2010, CGG2013 (Huang and Véronneau 2013)
Caribbean Sea	Smith and Small 1999
Croatia	HRG2009 (Bašić and Bjelotomić 2014), HRG2015 (Bjelotomić 2015)
Czech Republic	CR2000 (Kostelecký et al. 2004), CR2005 (Kostelecký et al. 2004)
Egypt	EGY-HGM2016 (El-Ashqer et al. 2017), Abd-Elmotaal 2017
Ethiopia	Hunegnaw 2001
Europe	EGG1 (Torge et al. 1983), Denker and Torge 1992, EGG97 (Denker et al. 1997), EGG98 (Denker and Torge 1998), EGG07 (Denker et al. 2009), EGG2015 (Denker 2015)
France	QGF96, RAF96, GGF97, QGF98, RAF98, RAF09, Ismail and Jamet 2015, Ismail 2016
Germany	GCG2005 (Liebsch et al. 2006)
Ghana	Klu 2015, GGG2017 (Yakubu et al. 2017)
Great Britain	OSGM02 (Iliffe et al. 2003), OSGM05 (Ziebart et al. 2008)
Greece	Daras 2008
Hong-Kong	HKGEIOD-2016 (Guo et al. 2017)
Hungary	HGTUB98 (Toth et al. 2000), HGTUB2007 (Tóth 2009)
Iberia	IGG2005 (Corchete et al. 2005)
Indonesia	Kasenda 2009
Iran	Kiamehr 2006a, Abdollahzadeh and Alamdari 2011
Italy	ITALGEO99 (Barzaghi et al. 2002), ITALGEO05 (Barzaghi et al. 2007), ITG2009 (Corchete 2010)
Japan	GSIGEO2000 (Kuroishi et al. 2002), JGEOID2004 (Kuroishi and Keller 2005), JGEOID2008 (Kuroishi 2009), Odera et al. 2012
Kazakhstan	Inerbayeva 2010
Korea	Yun 1999
Malaysia	Vella 2003
Mediterranean Sea	Brovelli and Sansó 1993, Barzaghi et al. 2017
Moldova	Danila 2012
Morocco	Corchete et al. 2007
Mozambique	Fan 2002
New Zealand	Amos 2007, NZGeoid09 (Claessens et al. 2011), NZGM2010 (Abdalla and Tenzer 2011)
Nordic- Baltic Region	Tscherning 1982, Forsberg et al. 1997, Omang and Forsberg 2002, Ellmann 2004, NKG2015 (Ågren et al. 2016)
Norway	Gerlach and Ophaug 2017
Oman	Lasagna 2017
Pakistan	Sadiq et al. 2010
Philippines	PGM2016 (Gatchalian, Forsberg, and Olesen Gatchalian et al.)
Poland	Łyszkowicz 2010, Kuczynska-Siehiem et al. 2016
Saudi Arabia	Abdalla and Mogren 2015
Slovenia	SLOAMG2000 (Kuhar et al. 2011)
South America	Blitzkow et al. 2016
South America	de Matos et al. 2014, GEOID2015 (Blitzkow et al. 2016)
Sudan	KTH-SDG08 (Abdalla and Fairhead 2011, Abdalla 2009), SUD-GM2014 (Godah and Krynski 2015)
Sweden	Nahavandchi 1998, KTH08 (Ågren et al. 2009)
Switzerland	Marti 1997, CHGEO2004 (Marti 2004, Marti 2007)
Tanzania	Olliver 2007, TZG08 (Ulotu 2009)
Tierra Del Fuego	Gomez et al. 2014
Turkey	TG-91 (Ayhan 1993), THG-09 (Kiliçoğlu et al. 2011)
Uganda	Sjöberg et al. 2015, Ssendendo 2015
USA	GEOID90 (Milbert 1991), GEOID96 (Smith and Milbert 1999), GEOID99 (Smith and Roman 2001), USGG2009 (Wang et al. 2012)
Zambia	Nsombo 1998

Table 1.2: Information and validation of previous geoid model solutions over Croatia

Stats and info	HRG2000		HRG2009		HRG2015
	Grgić et al. 2010	Bašić and Bjelotomić 2014	Bašić and Bjelotomić 2014	Bašić and Bjelotomić 2014	Bjelotomić 2015
min [cm]	-38	-27.5	-7.1	-7.8	-11.8
max [cm]	42	24.2	6.9	5.8	15.8
mean [cm]	1	-2.4	-0.04	-1.2	0.4
st. dev. [cm]	10.9	11.4	2.7	3.5	4.7
comp. method	RCR/LSC		RCR/LSC		KTH
no. gravity points	7500		~ 29300		~ 28000
no. GNSS/lev.	495	59	495	59	59

System by implementation of the gravimetric geoid-based vertical datum were considered.

Geoid determination

Since 1990s, several geoid model solutions have been determined for the territory of Croatia. After preliminary research by Čolić et al. (1992) and Čolić et al. (1993) for Slovenia and part of Croatia, the first gravimetric geoid since Croatian independence was developed by Bašić and Čolić (1993). Afterwards, following models were published: HRG98 and HRG98a (Bašić et al. 1999, Bašić and Brkić 1999a, Bašić and Brkić 1999b), HRG2000 (Bašić 2000, Bašić and Hećimović 2006), HRG2009 (Bašić and Bjelotomić 2014), HRG2015 (Bjelotomić 2015). Results of validation of the three latest geoid solutions HRG2000, HRG2009, and HRG2015 are given in table 1.2. HRG2000 was the first official geoid solution with an accuracy of around 11 cm.

The currently official model used for transformation of ellipsoidal to normal-orthometric heights is Croatian quasi-geoid 2009 (HRG2009). Its development in 2009 brought a huge improvement in accuracy compared to the past geoid models with an external accuracy of -1.2 ± 3.5 cm. It was computed from around 30 thousand free-air gravity anomalies by RCR approach using LSC method. EGM2008 and SRTM3 were used as input data. Taking into account not large number and somewhere questionable reliability of the data as well as complex topography and non-rectangular shape of Croatia with high and rough mountains and unsurveyed sea areas, HRG2009 is still a state-of-the-art geoid model. Without significant efforts in creating a more detailed gravity database, accuracy at the 1-2 cm level, which is a geodetic goal nowadays, is probably not possible.

The latest geoid solution HRG2015 is a first geoid model computed using the KTH approach. It's accuracy is 0.4 ± 4.7 cm.

1.5 Chapter summary

In chapter 1 Introduction is given on the subjects of research. Motivation, problems, objectives and expected scientific contribution of the research is described.

The thesis is divided in two parts; first part, where theoretical foundations are briefly explained using existing references, and second part, author's research, contribution with numerical investigations, results and discussion. The first part is divided in three chapters: gravity field (chapter 2), topographic reductions in gravity field modelling (chapter 3) and geoid determination (chapter 4).

In chapter 2 the basics of gravity field and physical geodesy are described. In chapter 3 topographic effects in gravity field modelling are explained in more detail. Equations are given for different types of gravity reductions and anomalies starting from free-air, then simple and complete Bouguer, Airy-Heiskanen and Pratt-Hayford, and RTM anomalies. Their properties are described from the perspective of their usefulness for different geodetic and geophysical applications. Mathematical apparatus is given for calculation of terrain effects using surface (2D) and 3D crustal models. In chapter 4 solution of the boundary value problem is in focus. RCR and KTH approaches and different spatial and spectral methods of geoid determination are described. Stokes' kernel modifications are given. The process of gravimetric and global geopotential models validation and fitting is presented.

After providing theoretical foundations, part II starts with chapter 5 referring to the input data: gravity anomalies, GNSS/levelling data, global geopotential models, digital elevation models and crustal models. Study area is visualized on which computations are performed, as well as the spatial borders (extent) of the used models. In chapter 5.4.1 different satellite and combined global geopotential models are validated using available GNSS/levelling and gravity points. The most appropriate GGM is found over Croatian territory. Remove step of RCR approach is studied in chapter 6, where residual gravity field modelling is performed with all combinations of input parameters and models. In final two chapters 7 and 8, RCR and KTH geoid computation approaches are compared and analysed in order to derive the best possible geoid model for the study area, as well as to study effects of crustal models in each step of geoid determination.

Part I
Theory

Chapter 2

Fundamentals of gravitational field

“Almost every geodetic measurement depends in a fundamental way on the Earth’s gravity field.”

W. A. Heiskanen, H. Moritz, Physical geodesy, 1967

Theoretical foundations related to the gravity field are briefly presented in this chapter. Basic definitions of real, normal and disturbing gravity field, as well as other related functionals, such as gravity anomalies, are described.

All quantities are expressed in spherical or rectangular coordinate systems which is illustrated in figure 2.1. Spherical coordinates are geocentric latitude φ , geocentric longitude λ and radius from the center of the Earth r , whereas rectangular coordinates are x , y and z which are also known as Cartesian coordinates. Conversion between rectangular and spherical coordinates is performed using expressions:

$$x = r \cos \varphi \cos \lambda, y = r \cos \varphi \sin \lambda, z = r \sin \varphi. \quad (2.1)$$

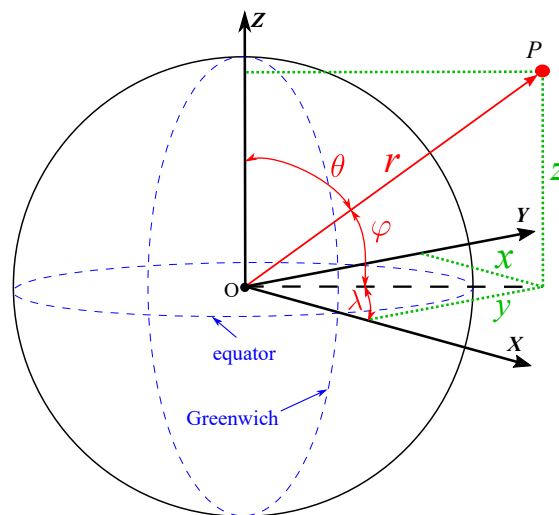


Figure 2.1: Definition of spherical and rectangular coordinate systems (after Hofmann-Wellenhof and Moritz 2005)

2.1 Earth's gravity field

Gravity force is the force of attraction on some point with mass m_1 due to: 1) gravitational force: the gravitational attraction of the body with mass m_2 , and 2) centrifugal force: caused by the rotation of the mass. According to *the law of gravitational attraction*, formulated by an English scientist Isaac Newton (1643-1727), gravitational force between two masses is:

$$F = G \frac{m_1 m_2}{l^2}. \quad (2.2)$$

The law is valid for all bodies in the universe, and the force is directly proportional to the product of masses and inversely proportional to the square of the distance between them. Each mass in the gravitational field has gravity potential W , which consists from gravitational potential V and centrifugal potential Φ (Hofmann-Wellenhof and Moritz 2005, eq. 2-7, p. 43):

$$W = W(x, y, z) = V + \Phi. \quad (2.3)$$

Gravitational potential V is a potential energy an object has in a gravitational field:

$$V = G \iiint_v \frac{dm}{l}, \quad (2.4)$$

while centrifugal potential Φ is a potential energy an object has because of the gravitational acceleration:

$$\Phi = \frac{1}{2} \omega^2 (x^2 + y^2), \quad (2.5)$$

where: v is Earth's volume, dm is mass element, x, y, z are Earth-fixed rectangular coordinates, l is the distance between masses, ρ is mass density, G is the Newtonian gravitational constant, ω is the angular velocity of the Earth's rotation. Gravity potential varies with time, but here it will be assumed to be fixed at some time epoch.

Gravity vector \mathbf{g} is gradient of the gravity potential W (Hofmann-Wellenhof and Moritz 2005, eq. 2-10, p. 44):

$$\mathbf{g} = \nabla W = -g \begin{pmatrix} \cos \Phi \cos \Lambda \\ \cos \Phi \sin \Lambda \\ \sin \Phi \end{pmatrix} = \begin{pmatrix} W_x \\ W_y \\ W_z \end{pmatrix} \equiv \left[\frac{\partial W}{\partial x}, \frac{\partial W}{\partial y}, \frac{\partial W}{\partial z} \right], \quad (2.6)$$

where Φ and Λ are astronomical latitude and longitude, W_x , W_y , and W_z are partial derivatives of W . Direction of gravity vector, conventionally taken as positive towards the center of the Earth, defines the curve- Earth's plumb line or vertical. The magnitude of gravity vector \mathbf{g} is *gravity acceleration* (sometimes referred as only *acceleration* or *gravity*) measured by absolute and relative gravimeters.

Second-order derivatives of gravity potential W are gravity gradients, which form the Eötvös tensor:

$$W_{rr} = \nabla(\nabla W) = \nabla g = \begin{bmatrix} W_{xx} & W_{xy} & W_{xz} \\ W_{yx} & W_{yy} & W_{yz} \\ W_{zx} & W_{zy} & W_{zz} \end{bmatrix}. \quad (2.7)$$

International System of Units (SI) unit for gravity acceleration is $[\text{ms}^{-2}]$, though miligal is commonly used in most applications and publications, where:

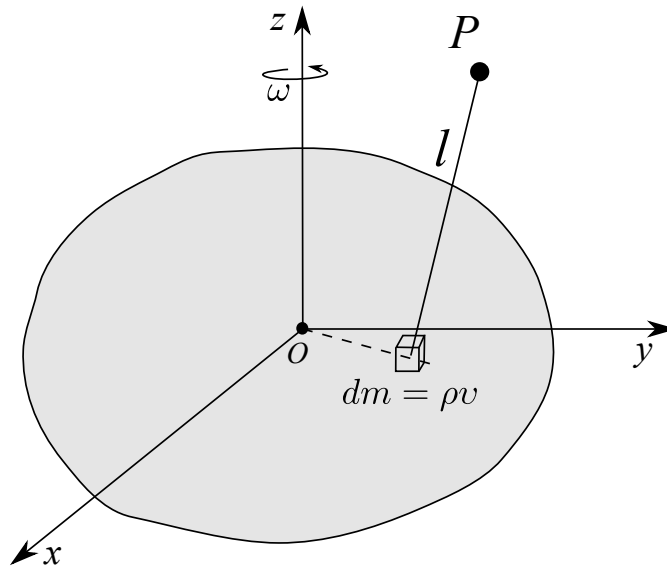


Figure 2.2: The gravitational potential (after Hofmann-Wellenhof and Moritz 2005)

$$1 \text{ mGal} = 10^{-3} \text{ Gal} = 10^{-5} \text{ ms}^{-2} = 10^{-3} \text{ cms}^{-2}.$$

Unit for gravitational potential is $[\text{m}^2\text{s}^{-2}]$, and for gravity gradients 10^{-9} s^{-2} or Eötvös [E].

2.2 Normal Field

In the most simple approximation Earth is a rotating sphere, and in the second approximation it is an equipotential (level) rotational ellipsoid. The theory of equipotential ellipsoid was firstly explained by P. Pizzetti (Pizzetti 1894) and C. Somiglianna (Somigliana 1929). Level ellipsoid is defined as a mathematical approximation (or model) of the real gravity potential W which generates normal potential U (Hofmann-Wellenhof and Moritz 2005):

$$U = \Psi + \Phi, \quad (2.8)$$

where Ψ is the gravitational potential of the ellipsoid and Φ the centrifugal potential. Normal gravity vector γ is defined as gradient of the potential U (Hofmann-Wellenhof and Moritz 2005, eq. 2-10, p. 44):

$$\gamma = \nabla U = -\gamma_0 \begin{pmatrix} \cos \varphi \cos \lambda \\ \cos \varphi \sin \lambda \\ \sin \varphi \end{pmatrix} = \begin{pmatrix} U_x \\ U_y \\ U_z \end{pmatrix} \equiv \left[\frac{\partial U}{\partial x}, \frac{\partial U}{\partial y}, \frac{\partial U}{\partial z} \right], \quad (2.9)$$

where γ_0 is magnitude of normal gravity, φ and λ are geodetic latitude and longitude, U_x , U_y , and U_z are partial derivatives of U .

Conventionally, equipotential ellipsoid is completely described with four basic constants which define geometric and physical properties of the *normal Earth*. Ellipsoids Geodetic Reference System 1980 (GRS80) and World Geodetic System 1984 (WGS84) are mostly used in

Table 2.1: Defining constants of GRS80 ellipsoid

Symbol	Parameter	Value
a	semi-major axis	6378137 m
GM	geocentric gravitational constant	$3.986005 \cdot 10^{14} \text{m}^3 \text{s}^{-2}$
J_2	dynamic form factor	0.001 082 63
ω	angular velocity of the Earth's rotation	$7.2921159 \cdot 10^{-5} \text{s}^{-1}$

geodesy (Moritz 1980 and Moritz 2000). Defining constants of the GRS80 ellipsoid are given in table 2.1.

Equipotential ellipsoid has following properties: a) it has the same angular velocity ω and mass as the actual Earth, 2) its potential U_0 on the ellipsoid surface is equal to the potential W_0 on the geoid, and 3) its center is in the centre of the masses of the Earth (Li and Götze 2001).

Normal gravity

The magnitude of normal gravity γ_0 on the surface of level ellipsoid (point Q on the figure 2.3) is calculated from the Somigliana-Pizzetti closed-form equation (Somigliana 1929):

$$\gamma_0 = \gamma_Q = \frac{\gamma_e(1 + k\sin^2\phi)}{(1 - e^2\sin^2\phi)^{\frac{1}{2}}} = \frac{\gamma_e\cos^2\phi + (1 - f)\gamma_p\sin^2\phi}{\sqrt{\cos^2\phi + (1 - f^2)\sin^2\phi}}, \quad (2.10)$$

where ϕ is geocentric latitude of the point, γ_e is normal gravity on the equator, γ_p normal gravity on the poles, a and b are the semi-major and semi-minor axes of the level ellipsoid, e first numerical eccentricity of the ellipsoid, and k is a normal gravity constant obtained from $k = \frac{b\gamma_p}{a\gamma_e} - 1$.

Normal gravity at the height above the level ellipsoid γ_h is obtained as:

$$\gamma_h = \gamma_0 + \frac{\partial\gamma}{\partial h}h + \frac{1}{2}\frac{\partial^2\gamma}{\partial h^2}h^2, \quad (2.11)$$

which means normal gravity is first computed on the surface of level ellipsoid ($h = 0$), but is then upward continued on the height h , neglecting all masses. Term $\frac{\partial\gamma}{\partial h}h$ is sometimes referred as free-air reduction.

The 2.11 equation may be converted into more simpler and exact form:

$$\gamma_h = \gamma_0 \left[1 - \frac{2}{a} (1 + f + m - 2f\cos^2\theta)h + \frac{3}{a^2}h^2 \right], \quad (2.12)$$

where $\theta = 90^\circ - \phi$, f is the geometrical flattening, $m = \frac{\omega^2 a^2 b}{GM}$ is the ratio of centrifugal and gravity acceleration at the equator.

Both equations 2.11 and 2.12 may be applied if normal gravity is needed at the topographic surface (γ_H or γ_{H^*}), for example in free-air reduction. In these cases, ellipsoidal height h is replaced with orthometric height H or normal orthometric height H^* .

2.3 Disturbing field

Disturbing (anomalous) potential T is defined as the difference between gravity potential of the Earth W and normal gravity potential of the level ellipsoid U :

$$T = W - U, \quad (2.13)$$

where normal gravity potential U accounts for approximately 99.99995 % of the gravity potential W .

Disturbing potential T is a function has to be valid for two conditions in a mass-free space: Laplace's and Poisson's equations. Laplace's equation is valid outside of the topographic and atmospheric masses (Hofmann-Wellenhof and Moritz 2005, p. 95, eq. 2-253):

$$\Delta T = \frac{\partial^2 T}{\partial^2 x} + \frac{\partial^2 T}{\partial^2 y} + \frac{\partial^2 T}{\partial^2 z} = 0, \quad (2.14)$$

whereas Poisson's equation is valid inside topographic masses (Hofmann-Wellenhof and Moritz 2005, p. 44, eq. 2-9):

$$\Delta T = -4\pi G\rho. \quad (2.15)$$

From the disturbing potential T various functionals may be computed and used by three types of methods: a) linear approximation methods, b) integral formula methods, and c) frequency domain or spectral methods (Tscherning et al. 1990). In linear approximation method, all anomalous quantities are spatial derivatives (functionals) or functions of the T in the latitude, longitude or radial (vertical) direction (see table 2.2). Functionals have smaller values and are suitable for modelling and computation (Vaníček and Krakiwsky 2015).

Table 2.2: Functionals of disturbing potential T in spherical approximation (e.g. Denker 1988)

Functional of T	Equation	Unit
disturbing potential	$T = W - U$	$[\text{m}^2\text{s}^{-2}]$
height anomaly	$\zeta = \frac{T}{\gamma}$	[m]
geoid undulation	$N = \frac{T - 2\pi G\rho H^2}{\gamma_0}$	[m]
gravity anomaly	$\Delta g = -\frac{\partial T}{\partial r} - \frac{2}{r}T$	[mGal]
gravity disturbance	$\delta g = -\frac{\partial T}{\partial r}$	[mGal]
meridional DOV	$\xi = -\frac{1}{r\gamma} \frac{\partial T}{\partial \varphi}$	["]
prime vertical DOV	$\eta = -\frac{1}{r\gamma \cos \varphi} \frac{\partial T}{\partial \lambda}$	["]

2.3.1 Anomalous gravity field

The differences between gravity measurements on topographic surface originate from the mass surplus and deficits, as well as from the density anomalies in the Earth's lithosphere. Usually,

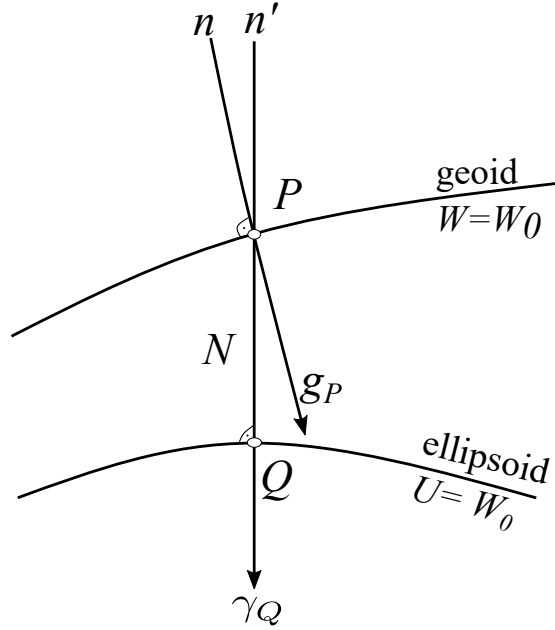


Figure 2.3: Geoid and ellipsoid (after Hofmann-Wellenhof and Moritz 2005)

in order to make measurements interpretable and meaningful, modelling and calculations are performed in the anomalous gravity field. Anomalous gravity field is obtained when normal gravity field is subtracted from the real gravity field. Gravity anomaly Δg is one of the most important quantities of the anomalous (disturbing) field. In the broadest sense, it is defined as the difference between *actual* (measured or observed) and *normal* (theoretical) gravity. If g_P is a gravity value of the point on the geoid, and γ_Q normal gravity of the point on the level ellipsoid, then (Hofmann-Wellenhof and Moritz 2005):

$$\Delta g_P = g_P - \gamma_Q = \left[-\frac{\partial T}{\partial r} + \frac{T}{\gamma} \frac{\partial \gamma}{\partial r} \right] \Big|_P, \quad (2.16)$$

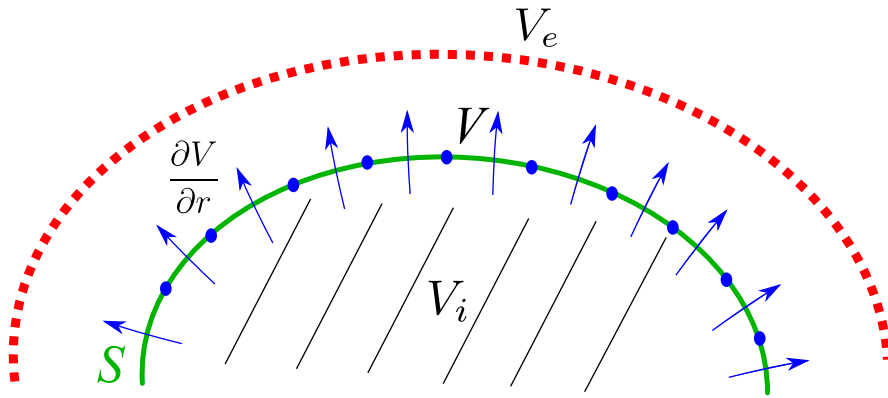
where r is the radial distance between point P and the Earth's center of mass. The above equation is illustrated on figure 2.3.

2.3.2 Bruns formula, fundamental equation of physical geodesy and Boundary Value Problem

Three boundary value problems are important from geodetic perspective and are defined as follows (Heiskanen and Moritz 1967):

1st or Dirichlet's BVP. The potential in the interior V_i and exterior V_e of the boundary surface may be computed from the values of the function V given at the surface S .

2nd or Neumann's BVP. The potential in the interior V_i and exterior V_e of the boundary surface may be computed from the values of the first normal derivatives of the function $\frac{\partial V}{\partial r}$ given at the surface S .

Figure 2.4: 3rd Boundary Value Problem (after Hofmann-Wellenhof and Moritz 2005)

3rd BVP. The potential in the interior V_i and exterior V_e of the boundary surface may be computed from the values of the function V and first normal derivatives of the function $\frac{\partial V}{\partial r}$. See figure 2.4.

Three boundaries may be selected for the solution of the BVP:

Topographic surface when quasi-geoid model is obtained as a solution. According to [Molodenskii \(1962\)](#) no gravity reduction is needed, as all topographic masses are inside the boundary surface. However, the Earth's surface is very rough so solution might not exist in more complex terrains.

Geoid when topographic masses have to be reduced inside the boundary surface. Also known as the classical solution of the Boundary Value Problem (BVP) ([Heiskanen and Moritz 1967](#)).

Reference ellipsoid as a modern alternative where measurements used for obtaining solution are given on the level ellipsoid.

Traditionally, BVP has been the problem of determining geoid from geodetic measurements such as gravity and potential difference ([Moritz 1989](#)). Both N and T are unknowns, but it is enough to know one quantity to compute another. Equations 2.17 and 2.18 relate observation (measured) quantities (Δg) with the unknown disturbing potential T through the differential operator $\frac{2}{R}T + \frac{\partial}{\partial r}$. This is known as the 3rd BVP. The solution of T in the exterior space exist, only if partial derivatives $\frac{\partial V}{\partial r}$ are known everywhere on the Earth's surface. Relationship between disturbing potential T , anomalous gravity anomaly Δg_P and geoid undulation N follows from the Bruns' equation ([Hofmann-Wellenhof and Moritz 2005](#), p. 93, eq. 2-237):

$$N = \frac{T}{\gamma} \quad (2.17)$$

and fundamental equation of physical geodesy (FEPG):

$$\frac{\partial T}{\partial h} - \frac{1}{\gamma} \frac{\partial \gamma}{\partial h} T + \Delta g = 0. \quad (2.18)$$

Geoid surface may be computed using Bruns' equation only if FEPG (eq. 2.18) has solution.

Chapter 3

Topographic reductions

“Since the Earth’s actual surface is not strictly a surface of equilibrium, on account of the elevation of the continents and islands above the sea level, it is necessary to consider in the first instance in what manner observations would have to be reduced in order to render the preceding theory applicable.”

George Gabriel Stokes, 1819-1903

Raw measurements of the gravity field are not suitable for interpretation and analysis. Various external effects are included in the measured gravity signal, which all have to be removed and filtered before usage in particular application. In geophysical applications gravity measurements are reduced and modeled, and as such, they are used for investigations of the Earth’s internal structure. Hereby, it is crucial that reduced gravity field has physical meaning and interpretation. On the other hand, geodesist’s primarily reduce gravity measurements to solve BVP and determine boundary surface. The solution of the classical BVP require that data refer to the boundary surface and that no masses exists outside of the boundary surface. Therefore, all gravity reductions in its principle shall: 1) move gravity station from the Earth’s surface to the boundary surface, and 2) reduce all atmospheric and topographic masses between topographical surface of the Earth were measurement are performed and boundary surface. For step 2) it is crucial to have knowledge about the crustal structure down to the boundary surface. Thus, if geoid is selected as boundary surface, the gravity measurements from the topographic surface (such as gravity anomalies Δg) have to be reduced down to the geoid P , as visualized in fig. 3.1. Because of the mostly unknown internal structure of the Earth this is one of the most complex and non-unique steps in gravity field modelling.

It should be noted that the equations given here refer to the reduction of the gravity anomalies Δg as they are mostly available and used data type for gravity field modelling and geoid determination. However, additional equations are available in references which may be applied for topographic reduction of other types of data and functionals of the gravity field, such as deflections of vertical (ξ , η) or gravity gradients (T_{zz}). Another note is related to the two symbols which are used throughout the text that follows; δ is used for *reduction*, and Δ for *anomaly*.

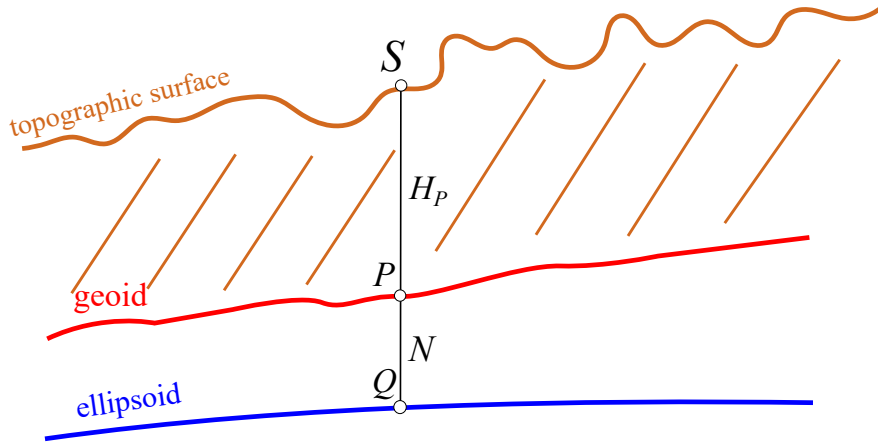


Figure 3.1: Reduction of gravity from Earth's topography surface S down to the geoid P

In geodesy and geophysics many methods are available for topographic reductions of the gravity field functionals: Free-Air, Bouguer, 1st and 2nd Helmert's condensation, Molodenskii, Airy-Heiskanen, Pratt-Hayford, Vening-Meinesz, inversion of Rudzki, and Residual Terrain Modelling (RTM). A chosen topographic reduction would ideally produce small and smooth gravity field anomalies (Δg) with geophysical meaning and with small indirect effect (Heiskanen and Moritz 1967). From the theoretical standpoint, all topographic reduction schemes should result in the same geoid model. However, this is not the case. Therefore, only Helmert's (second) condensation method, Molodenskii's method and RTM method are used for geoid modelling. Isostatic reduction schemes have large indirect effects on geoid undulations, and find only indirect application in geoid modelling, for example for derivation of crustal density models by inversion procedures or interpolation of anomalies (Sneeuw 2006).

3.1 Free air reduction

Given the gravity value at the surface of the Earth g (or more precise g_S), gravity value at the geoid P is obtained by analytic continuation with the free-air reduction. The gravity at point S is downward continued along the real plumb line down to the point P on the geoid. All topographic masses between point on the Earth's topographic surface S and corresponding point on the geoid P are neglected, and reduction is performed as in the mass-free space. Free-air gravity value is obtained as (Heiskanen and Moritz 1967):

$$g_{FA} = g + \delta g_{FA} = g + \left(-\frac{\partial g}{\partial H} H_P \right), \quad (3.1)$$

where H_P is orthometric height of the point P measured from the geoid up to the topographic surface, $\delta g_{FA} = -\frac{\partial g}{\partial H} H_P$ is free-air reduction or vertical gradient of the real Earth's gravity which depends on the location and real gravity field. Exact value of the real vertical gravity

gradient is obtained as:

$$\frac{\partial g}{\partial H} = -2gJ + 4\pi G\rho - 2\omega^2 \quad (3.2)$$

where J is the mean curvature of a level surface computed as $-\frac{W_{xx}+W_{yy}}{2g}$, and ρ stands for the density of the masses between topographic surface and geoid. Real vertical gravity gradient using equation 3.2 is usually not computed due to unknown density of topographic masses. It is approximated with a normal gravity gradient (Heiskanen and Moritz 1967, Tziavos et al. 2010):

$$\frac{\partial g}{\partial H} \approx \frac{\partial \gamma}{\partial H}, \quad (3.3)$$

where normal vertical gravity gradient is :

$$\frac{\partial \gamma}{\partial H} \approx -0.3086 \text{ [mgal/m]}. \quad (3.4)$$

Classical vs Molodenskii free-air gravity anomaly

Two theoretical definitions of free-air anomalies exist: *classical* and *Molodenskii*, which are defined by following expressions (e.g. Heiskanen and Moritz 1967, Barthelmes 2009):

$$\begin{aligned} \text{classical: } \Delta g_{FA} &= g - \gamma^H = g + \delta g_{FA}^H - \gamma_0, \\ \text{Molodenskii: } \Delta g_{FA} &= g - \gamma^{H*} = g + \delta g_{FA}^{H*} - \gamma_0, \end{aligned} \quad (3.5)$$

where γ^H is normal gravity computed at orthometric height H_P measured from geoid, and γ^{H*} is normal gravity at normal-orthometric height measured from telluroid. Telluroid is an imaginary surface approximating gravimetric geoid, defined by height anomalies ζ measured from the Earth's topography surface into topographic masses (see, e.g. Hirvonen 1961). Both γ^H and γ^{H*} are computed using equations 2.12 from section 2.2.

The distinction between classical and Molodenskii free-air anomaly is mainly a conceptual, while for practical purposes they can be considered identical (Heiskanen and Moritz 1967, p. 310).

3.2 Bouguer reduction

In Bouguer reduction, gravitational effect of topographic masses between Earth's topographic surface and geoid is modelled through the infinite plate of thickness H_P known as Bouguer plate (figure3.2). Gravity attraction of a Bouguer plate is computed from (Hofmann-Wellenhof and Moritz 2005, p. 135):

$$\delta g_B = 2\pi G\rho H_P, \quad (3.6)$$

where ρ is density, Bouguer gradient equals $-\frac{\partial g}{\partial h} = -2\pi G\rho$ expressed in $\frac{\text{mGal}}{\text{m}}$. Equation 3.6 is also known as direct topographical effect (DTE), or attraction change effect (Wichiencharoen 1982, Vaníček et al. 1995).

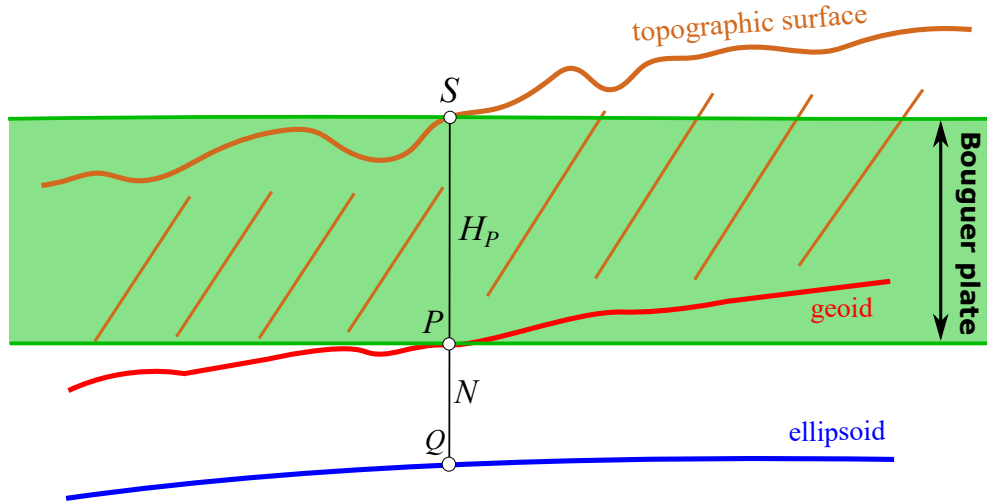


Figure 3.2: Bouguer plate: modelling the topography point-wise by an infinite plate of thickness H_P .

Usually when globally estimated value for crustal density is used $\rho = 2670 \text{ kgm}^{-3}$, equation 3.6 becomes:

$$\delta g_B \approx 0.1119 H_P. \quad (3.7)$$

Bouguer reduced gravity g_B is obtained by removing the effect of Bouguer plate from the g and then moving the station on the geoid (Hofmann-Wellenhof and Moritz 2005):

$$g_{sB} = g + \delta g_{FA} - \delta g_B. \quad (3.8)$$

Simple Bouguer gravity anomaly is:

$$\Delta g_{sB} = g_{sB} - \gamma_0. \quad (3.9)$$

3.2.1 Complete Bouguer reduction

Approximation of the topographic masses with the Bouguer plate is a simplified approximation of reality in the areas of complex and mountainous topography. The Bouguer plate does not remove all the attractive effect of the topographic masses as surplus or deficient masses are present around the point S . Excess' and deficits of masses are shown on figure 3.3. Masses are represented with blue colored rectangular prisms. Therefore, the effect of topographic masses is remedied by taking into account a terrain correction (TC). It is a key auxiliary quantity in gravity reductions containing the high frequency part of the gravity signal caused by the irregular part of the topography, which is not filtered by the Bouguer plate.

3.2.2 Terrain correction

Terrain correction smooths gravity for the variations in local topography by removing the effect of terrain variation relative to the height of the point gravity observation (figure 3.3). It is one

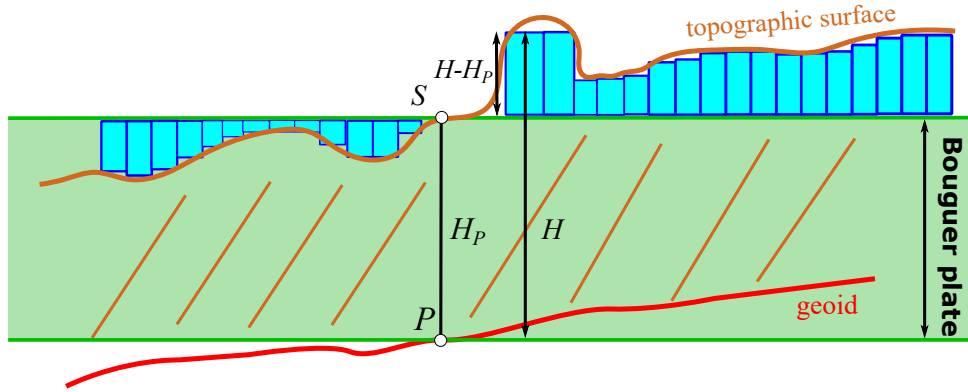


Figure 3.3: Terrain correction, illustrating residual gravitational effect caused by surplus and deficiencies of the topographic masses (after Hofmann-Wellenhof and Moritz 2005, p. 136).

order of magnitude smaller than Bouguer reduction in most areas, typically ranging from 1 to 5 mGal. However, in mountainous areas it can achieve values from 10 to 30 mGal.

According to Moritz (1968) terrain correction is equal to:

$$\delta g_{TC} = \frac{G\rho R^2}{2} \int_{\sigma} \frac{(H - H_P)^2}{l^3} d\sigma. \quad (3.10)$$

Analytic expression for the terrain correction is (Tziavos and Sideris 2013):

$$\delta g_{TC} = G \int \int \int_H^{H_P} \frac{\rho(x, y, z)(H_P - z)}{l^3} dx dy dz, \quad (3.11)$$

and is valid on the continent. Over the oceans, terrain correction is replaced by bathymetric correction (δg_{BC}) or density contrast effect given as (Tsoulis 1999, Tziavos and Sideris 2013, pp. 346, eq. 8.12):

$$\delta g_{BC} = G \int \int \int_{-H}^0 \frac{\Delta\rho(x, y, z)(H_P - z)}{l^3} dx dy dz, \quad (3.12)$$

where P is computation point, l is the distance between computation point and integration point $l = \sqrt{(x_P - x)^2 + (y_P - y)^2 + (H_P - z)^2}$, $\Delta\rho$ is the density contrast between the upper crust and water ($\approx 1670 \text{ kgm}^{-3}$).

Using equation 3.11 terrain correction in planar approximation becomes (Tziavos and Sideris 2013, pp. 344, eq. 8.8, Sideris 1995):

$$\begin{aligned} \delta g_{TC}(x_P, y_P) &= G \iint_{\sigma} \frac{-\rho(x, y)}{(l_0^2 + z^2)^{\frac{1}{2}}} \Big|_0^{\Delta H} dx dy = \\ &G \iint_{\sigma} \frac{\rho(x, y)}{l_0} \left[1 - \left[1 + \left(\frac{\Delta H}{l_0} \right)^2 \right]^{-\frac{1}{2}} \right] dx dy, \end{aligned} \quad (3.13)$$

where $\Delta H = H(x_P, y_P) - H(x, y)$ and $l_0^2 = (x_P - x)^2 + (y_P - y)^2$. Equation 3.13 after simplification becomes in planar approximation:

$$\delta g_{TC}(x_P, y_P) = \frac{1}{2} G \iint_{\sigma} \frac{\rho(x, y) [H(x_P, y_P) - H(x, y)]}{[(x_P - x)^2 + (y_P - y)^2]^{\frac{3}{2}}} dx dy. \quad (3.14)$$

Practical computation

Several computational methods for evaluation of the terrain correction integral (equation 3.11) exist, such as numerical integration, Fast Fourier transform or their combination. Topographic masses may be approximated by various geometrical bodies based on conventional numerical integration approaches, which evaluate the TC integral of equation 3.14 using a model of rectangular prisms with flat or inclined tops (Nagy 1966b). TC computation based on the closed analytic expressions is known to be time-consuming, but most accurate. Other methods for TC computation include a polynomial model or FFT, having the TC convolution integral expanded in the form of Taylor series (see, e.g. Schwarz et al. 1990).

Rectangular prisms

Since 1970s, closed analytical expressions for the gravity potential have been extensively used for computation of terrain effects in flat-Earth approximation (Nagy 1966b). One of the mostly used solutions is based on approximation of topographic masses around point of interest with rectangular prisms. The effect is computed and summed up for each prism $\sum \delta g_{TC}$ (Tziavos et al. 2010) inside computational area around the gravity point. Terrain correction may be computed for different gravity field functionals. For gravity anomalies, it is (Jung 1961, Forsberg 1984, Nagy et al. 2000):

$$\delta g_{TC} = G\rho \left\| \left\| x \ln(y+r) + y \ln(x+r) - z \arctan \frac{xy}{zr} \right\|_{x_1, y_1}^{x_2, y_2} \right\|_{z_1}^{z_2}, \quad (3.15)$$

and for geoid undulation:

$$\delta N_{TC} = G\rho \left\| \left\| xy \log(z+r) + xz \log(y+r) + yz \log(x+r) - \frac{x^2}{2} \arctan \frac{yz}{xr} - \frac{y^2}{2} \arctan \frac{xz}{yr} - \frac{z^2}{2} \arctan \frac{xy}{zr} \right\|_{x_1, y_1}^{x_2, y_2} \right\|_{z_1}^{z_2}, \quad (3.16)$$

where $r = \sqrt{(x_2 - x_1)^2 + (y_2 - y_1)^2 + (z_2 - z_1)^2}$, while geometry of the rectangular prisms is defined as in figure 3.4.

Terrain effects around computation point have largest values, which start to decrease with increasing distance. For this reason, integration of terrain effects is always performed only up to some radius r . Traditionally for terrain correction radius is $r \leq 200$ km. Terrain information, heights H , which define z component of the prisms, are taken from digital elevation model (DEM), which are nowadays available with the resolutions of up to 1'', and can for continental areas be quite large. Thus, computation of terrain effects requires high computational resources.

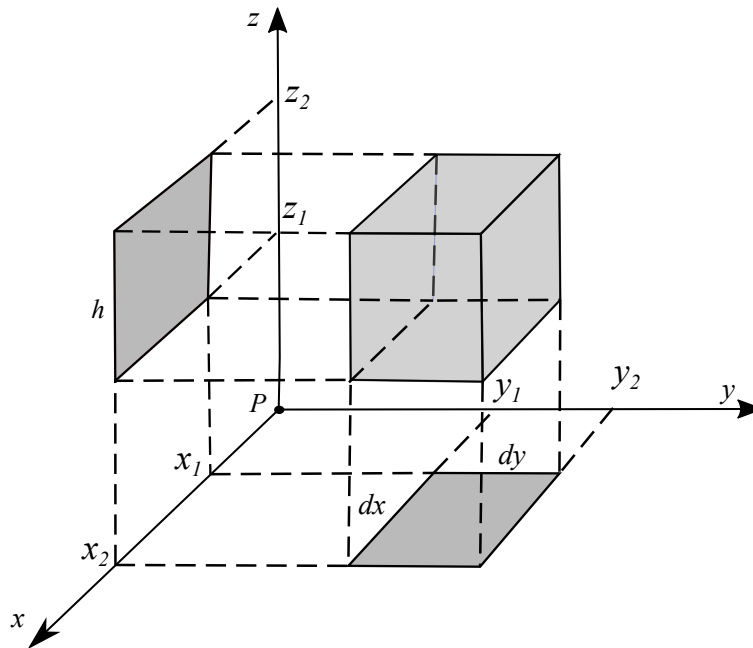


Figure 3.4: Rectangular prism (after Nagy 1966b).

Analytic equations from the above are accurate but time-consuming, because contributions of all prisms have to be calculated up to some radius around the computation point. This drawback has been resolved through several modifications:

- Integration area is split in two zones: *inner* and *outer* as in figure 3.5. DEMs of the finest (most-detailed) resolution are used in the inner zone, while coarser DEM are used for outer zone. Inner and outer zones are defined by parameters; inner radius r_1 and outer radius r_2 . Integration of the prisms in inner zone is performed up to some smaller radius, e.g. $5 < r_1 < 20$ km, while in outer zone up to maximal radius, e.g. $20 < r_2 < 200$ km.
- Spline densification of the vicinity around computation point with additional heights information, in case input DEM does not have high-resolution (less than few arc-seconds).
- Using approximative equations, such as MacMillan and mass plane, that are faster for computation.

More information along with detailed discussion may be found in Forsberg (1984) and Tziavos and Sideris (2013).

3.2.3 2D and 3D rectangular prisms

Rectangular prisms typically have uniform density value. Moreover, only one value ($\rho_c = 2670 \text{ kgm}^{-3}$) is used for the whole computation area as for most areas worldwide lateral density models do not exist (e.g. Hinze 2003). However equations allow to treat rectangular prisms as 3D bodies where each prism has its own density. It is possible to split prism in vertical direction in a number of prisms where each splitted prism has its own density. Then each splitted prism

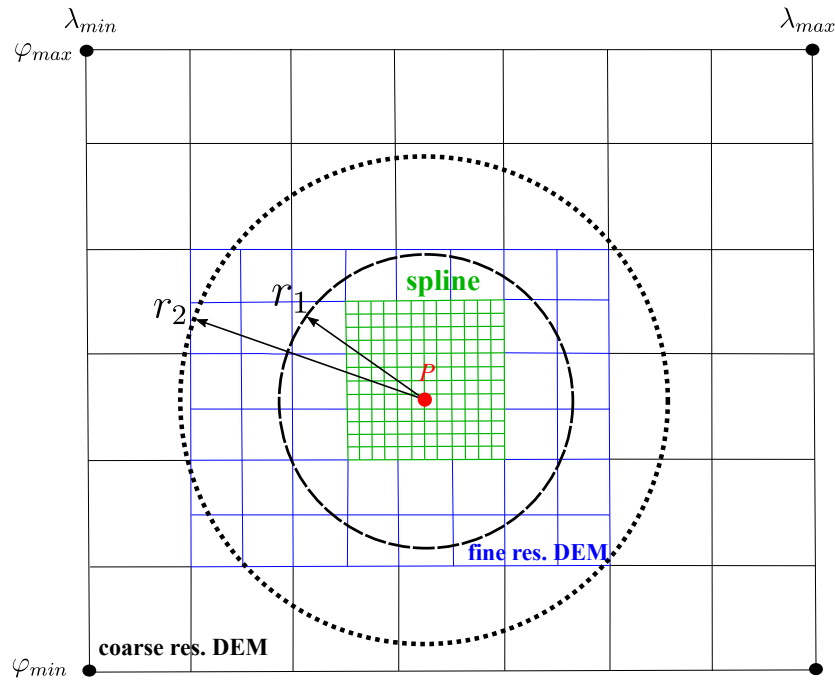


Figure 3.5: Computation of terrain effects using fine and coarse resolution DEMs up to radiuses r_1 and r_2 , with spline densification around computation point P .

gets its own density value ρ_c from available 3D crustal model.

In 2D case, density value may be appended to each rectangular prism in case for the whole computation area lateral (surface) density model exists. In 3D case, it is supposed that layered (horizon) crustal model has: 1) depths defining each layer or horizon, 2) densities for each layer. The example of such crustal model is CRUST1.0. Then each rectangular prism with coordinates x_1, x_2, y_1, y_2, z_1 and z_2 can be divided in additional prisms by modifying z_1 and z_2 limits. z_1 and z_2 limits are modified depending of the depth of layer from 3D crustal model. Therefore, what has previously been one rectangular prism, becomes several rectangular prisms depending of the number of layers (horizons) in the crustal model. For each reduction scheme few different cases may emerge, as z_1 and z_2 corners are changing depending of the reduction scheme. Detailed discussion of all possible cases are given in (Brkić, 1994b, pp. 29-40), where software routines were developed allowing inclusion of three crustal layers (horizons). These routines are modification of original Forsberg's TC program (Forsberg 1984). For the purpose of this thesis routines were furtherly modified allowing inclusion of up to eight layers, which now makes available 3D crustal models, such as EPcrust with three and CRUST1.0 with eight layers.

Representation of topography by rectangular prisms for constant density (1D), surface (2D) and 3D cases are shown in figure 3.6. Prisms geometry in x and y directions (length and width) is determined by resolution of the input DEM. All prisms have the same constant density values ρ_c in 1D case. In 2D case (subfigure *b*), each prism has its own crustal density value taken from

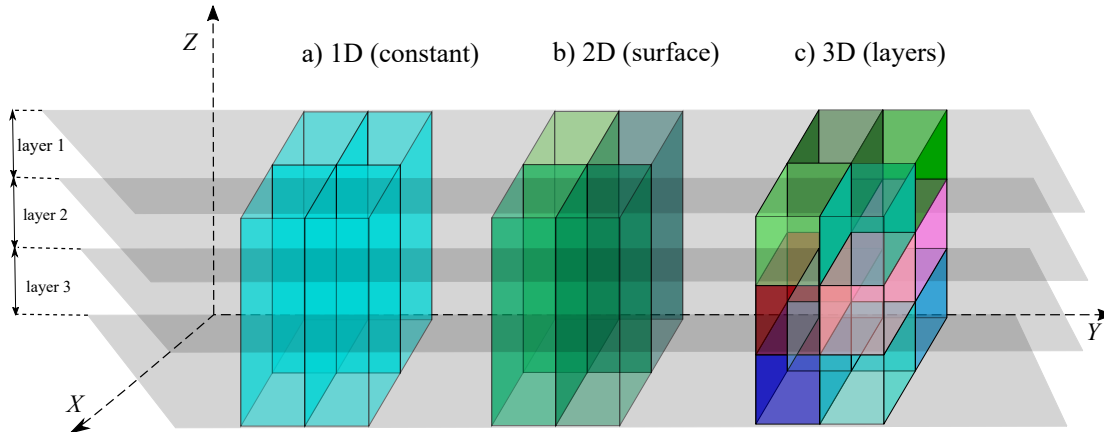


Figure 3.6: Rectangular prisms for three cases: a) constant crustal density ρ_c , b) surface (2D) crustal density model, and c) 3D crustal density model.

the surface (lateral) density model. There is no difference in geometry x and y directions for 1D and 2D cases.

The most realistic case, for 3D prisms representation is shown on subfigure *c*. In 3D case, prisms are divided according to the available layers of depths and densities. Geometry of each prism in z direction is determined by the depth taken from the input 3D density model. The example is given for three layers, but they can be divided in as much additional layers as there are available. Layers correspond to the crustal layers, for example sediments, upper crust, lower crust, mantle, etc. Slightly idealized example is given for this case as all prisms have the same value in z direction, that would mean that the prisms have the same depth in all layers, which is not the case in reality. For example, sediment thickness layer may be somewhere much smaller than the upper crust layer. It can be seen that prisms in the same layer have similar density values (for example in layer 1 they have slightly different values) compared to the density values of prisms in layer 2.

3.2.4 Complete Bouguer anomaly

Correcting for the terrain effect yields the complete Bouguer or the terrain-corrected gravity field (Hofmann-Wellenhof and Moritz 2005):

$$g_{cB} = g + \delta g_{FA} - \delta g_B + \delta g_{TC}. \quad (3.17)$$

Starting from free-air gravity anomalies Δg_{FA} , complete Bouguer gravity anomalies are obtained as:

$$\Delta g_{cB} = g_{cB} - \gamma_0, \quad (3.18)$$

where: Δg_{cB} is the complete (refined) Bouguer gravity anomaly, δg_{TC} is terrain correction.

Bouguer anomalies indicate variations in the underlying density structure. They are smooth in shorter spatial scales, but due to the isostatic compensation have large systematic bias in spectral lengths of 50 to 100 km. Therefore, they are systematically negative over the continents

and positive over the oceans. In mountain areas, can easily be negative by hundreds of mGal. Much smoother than FA anomalies they are suitable for interpolation and prediction of gravity anomalies, in situations where the available gravimetric material is sparse. However, because of aforementioned large systematic bias they are not used in geoid determination (Heiskanen and Moritz 1967).

3.3 Isostasy

Already in the 18th and 19th centuries it was asserted that a certain compensation with a negative density contrast has to exist below the topography. This led to the concept of isostasy which assumes equilibrium of the Earth down to a certain level of compensation. The word *isostasy* comes from Greek meaning *equal pressure* or *equal standing* or *equilibrium* (Bowie 1927, Banks 1968). According to Brkić (2016) Croatian scientist Ruđer Bošković used term *compensation* for the first time to describe the state of equilibrium. The general equation for equilibrium condition reads:

$$\int_{-T}^H \rho dz,$$

where T stands for the depth of compensation.

Observations performed later showed that topographic masses of the Earth are 85-90 % isostatically compensated. In reality however, due to the strength of the Earth's crust, complete equilibrium is not possible for any topographic feature (Heiskanen and Vening Meinesz 1958). Two simple, and in large scope idealistic, hypothesis' emerged almost simultaneously: Pratt-Hayford (Pratt 1855, Hayford 1909) and Airy-Heiskanen (Airy 1855, Heiskanen 1931). Models assume that topographic masses are divided in vertical columns, whereas each column is independent unit from all other columns in surrounding (Heiskanen and Vening Meinesz 1958).

3.3.1 Pratt-Hayford topographic-isostatic model

According to the Pratt-Hayford model isostatic equilibrium exists because topography is compensated on some constant compensation depth and topographic columns have variable densities (figure 3.7). Thus isostatic condition for each topographic column is (Hofmann-Wellenhof and Moritz 2005):

$$\begin{aligned} \text{continent: } (D + H) \rho_c &= D\rho_0, \\ \text{ocean: } (D - H') \rho_c + H' \rho_w &= D\rho_0, \end{aligned} \tag{3.19}$$

where D is the depth of compensation, ρ_c is crustal density of the column, ρ_0 standard crustal density in the absence of topography, ρ_w sea water density. Topographic masses in mountainous have smaller densities, than masses on the ocean. Compensation depth D according to Hayford (1909) is supposed to be 113.7 km for the territory of United States, but other values are supposedly more suitable for different areas around the world.

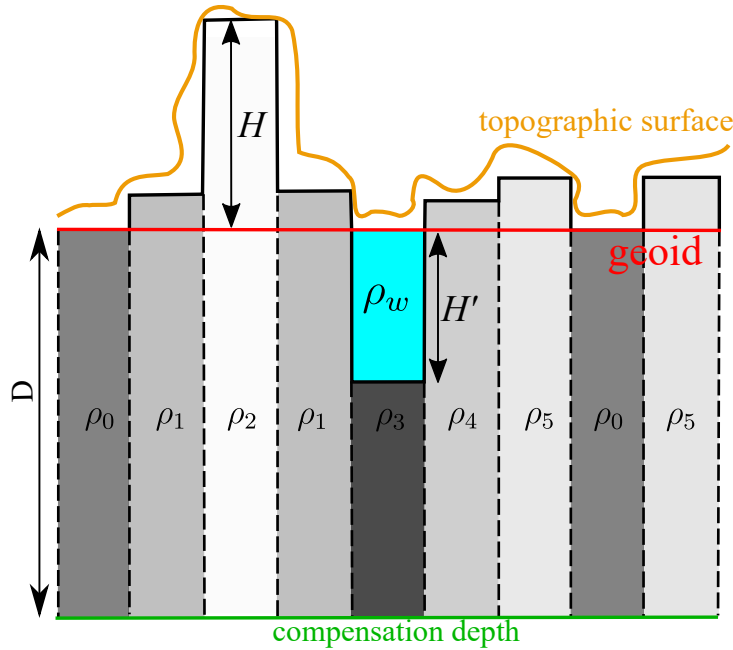


Figure 3.7: Pratt-Hayford topographic-isostatic model: constant depth of compensation D and variable column density ρ_i (after Hofmann-Wellenhof and Moritz 2005).

Density contrast between actual crustal density of the column ρ_c and crustal density in absence of topography ρ_0 is:

$$\begin{aligned} \text{continent: } \Delta\rho &= \rho_0 - \rho_c = \frac{H}{D+H}\rho_0, \\ \text{ocean: } \Delta\rho &= \rho_0 - \rho_c = -\frac{H'}{D-H'}(\rho_0 - \rho_w). \end{aligned} \quad (3.20)$$

As (Heiskanen and Vening Meinesz, 1958, p. 166) stated: "the common opinion today is that isostatic compensation seldom occurs according to the Pratt-Hayford assumption".

3.3.2 Pratt-Hayford reduction

The reduction in P-H model can be divided on two effects, a) effect of topographical masses above geoid, b) effect of compensated masses below geoid down the depth of compensation:

$$\delta g_{P-H} = \delta g_{P-H}^{top} - \delta g_{P-H}^{comp} = G \int \int \int_0^{H(x,y)} \frac{\rho(x,y,z)(H_P - z)}{l^3} dx dy dz - G \int \int \int_{-D-H_P}^{-H_P} \frac{\Delta\rho(x,y,z)(H_P - z)}{l^3} dx dy dz, \quad (3.21)$$

where $\Delta\rho$ comes from the eq. 3.20.

Pratt-Hayford topographic-isostatic gravity is given as:

$$g_{P-H} = g + \delta g_{FA} - \delta g_{P-H}, \quad (3.22)$$

and finally anomaly:

$$\Delta g_{P-H} = g_{P-H} - \gamma_0. \quad (3.23)$$

3.3.3 Airy-Heiskanen topographic-isostatic model

For describing Airy-Heiskanen topographic-isostatic model (A-H), Earth's crust floating on a mantle layer can be compared to an iceberg on a sea. If there is a root (mountain) above the geoid with the height H , there must be a corresponding anti-root sticking into the mantle with the height t . Since crustal material is lighter than the mantle there will be an upward buoyant force that balances the downward gravity force of the mountains. A similar mechanism will take place underneath oceans. The lighter sea water will induce a negative root with height, i.e. a thinner crust below the oceans (Banks 1968, Sneeuw 2006). The principle of A-H model is shown in figure 3.8. A layer, with a normal thickness of the Earth's crust T_0 separates crust and mantle. This layer is not involved in the isostatic condition.

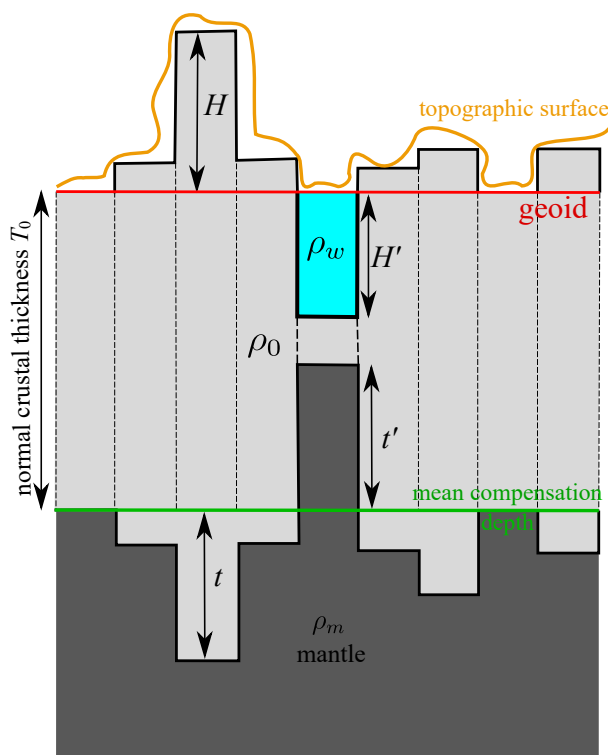


Figure 3.8: Airy-Heiskanen topographic-isostatic model (after Hofmann-Wellenhof and Moritz 2005).

From the explanation above it follows that isostatic equilibrium exists (Hofmann-Wellenhof and Moritz 2005):

$$\begin{aligned} \text{continent: } t(\rho_m - \rho_c) &= H\rho_c, \\ \text{ocean: } t'(\rho_m - \rho_c) &= H'(\rho_c - \rho_w), \end{aligned} \quad (3.24)$$

where t is thickness of the root, t' is the thickness of the anti-root. The Earth's crustal thickness T is equal to (Heiskanen and Vening Meinesz 1958, p. 137):

$$\begin{aligned} \text{continent: } T &= T_0 + H + t, \\ \text{ocean: } T &= T_0 - H' - t'. \end{aligned} \quad (3.25)$$

where t and t' are thicknesses of the roots and anti-roots, and T_0 normal thickness of the crust (Moho depth).

After rearranging equation 3.24 expressions are obtained for roots t and anti-roots t' (Hofmann-Wellenhof and Moritz 2005):

$$\begin{aligned} \text{continent: } t &= \frac{\rho_c}{(\rho_m - \rho_c)} H, \\ \text{ocean: } t' &= \frac{(\rho_c - \rho_w)}{(\rho_m - \rho_c)} H', \end{aligned} \quad (3.26)$$

where ρ_m is mantle density, H and H' are topographic height and depth. Both roots and anti-roots are linearly dependent on the height and depth of topography.

Usually standard values are used for parameters in equations: $T_0 = 30$ km, $\rho_c = 2670$ kgm⁻³, $\rho_m = 3270$ kgm⁻³, $\rho_w = 1030$ kgm⁻³. The density of $\rho_c = 2670$ kgm⁻³ for the Earth's crust is an arithmetic mean of six estimates that were made between 1811 and 1882 (Harkness 1891, Hayford and Bowie 1912, Hinze 2003).

3.3.4 Airy-Heiskanen reduction

The reduction in A-H model consists from two effects: a) effect of topographical masses above geoid, b) effect of compensated masses below geoid down to the depth of compensation:

$$\delta g_{A-H} = \delta g_{A-H}^{top} - \delta g_{A-H}^{comp} = G \int \int \int_0^{H(x,y)} \frac{\rho(x,y,z)(H_P - z)}{l^3} dx dy dz - G \int \int \int_{-T_0-t-H_P}^{-T_0-H_P} \frac{\Delta\rho(x,y,z)(H_P - z)}{l^3} dx dy dz, \quad (3.27)$$

Pratt-Hayford topographic-isostatic gravity is:

$$g_{A-H} = g + \delta g_{FA} - \delta g_{A-H}, \quad (3.28)$$

and anomaly:

$$\Delta g_{A-H} = g_{A-H} - \gamma_0. \quad (3.29)$$

In terms of computation of topographic effects, Airy-Heiskanen topographic-isostatic reduction is nearly similar to Pratt-Hayford. The difference is in the depth of compensation which causes z limits in the integral slightly change; in Pratt-Hayford compensation depth is D with values around 100 km, while in Airy-Heiskanen compensation depth is T_0 with values around 30 km corresponding to the crustal thickness of the Earth (Moho depths).

If isostatic models were completely true, isostatic reduction would result in perfectly regularized homogeneous earth's crust. However, isostatic models are simplification of reality in the

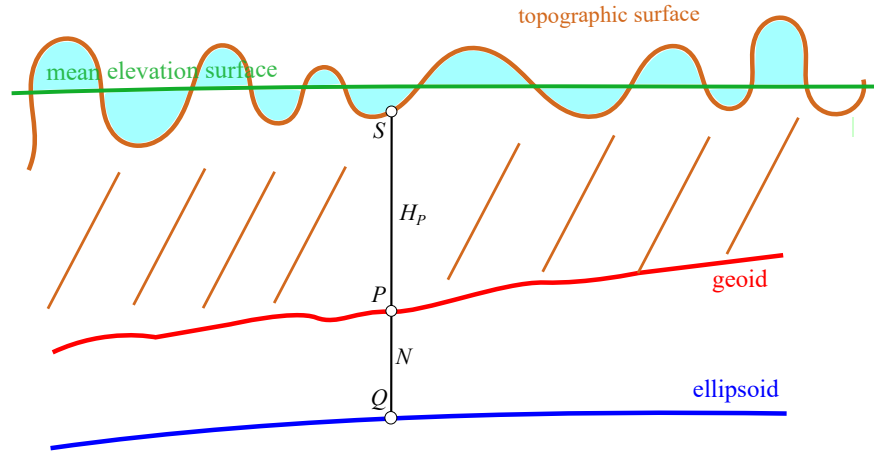


Figure 3.9: Geometry of the RTM reduction.

Earth's interior so isostatic gravity anomalies are not zero. Positive or negative anomalies mean that topography is or is not compensated at assumed compensation depth. Anyway, if correct parameters for depth of compensation and crustal density are used topographic-isostatic gravity anomalies are smooth. If used values of compensation depths and densities are different from true values errors in derivation of anomalies emerge. Probably the largest error in the corrections is due to the assumed density structure of the isostatic concepts used (Banks 1968).

3.4 Residual Terrain Model

RTM reduction is the most common terrain reduction method for quasi-geoid determination in RCR approach. It was designed by R. Forsberg and C.C. Tscherning (Forsberg and Tscherning 1981, Forsberg 1984). General methodology is to remove topographic masses above mean (reference) elevation surface and fill space below it. The reference surface can be constructed from DEM of finer resolution by averaging and low-pass filtering. The principle of the RTM reduction is illustrated on fig. 3.9.

The RTM effect on gravity is given by equation:

$$\delta g_{RTM} = G \int \int \int_{H_{ref}}^H \frac{\rho(x,y,z)(H_P - z)}{l^3} dx dy dz, \quad (3.30)$$

where H_{ref} is the height of the mean (reference) elevation surface. Closed analytic expression of the equation 3.30 is very similar as in computation of terrain correction, with different limits in z direction.

Approximative equation of the RTM reduction, which can be used if mean elevation surface

adequately approximates long-wavelengths is:

$$\delta g_{RTM} = 2\pi G\rho(H_P - H_{ref}) - G \int \int \int_{H_{ref}}^H \frac{\rho(x,y,z)(H_P - z)}{l^3} dx dy dz, \quad (3.31)$$

where the first term in 3.31 is the difference between two Bouguer plates with different thicknesses: the first one with the thickness equal to the height of the computation point H_P , and the second one with the thickness equal to the height of the reference surface H_{ref} (see, e.g. [Bajracharya 2004](#)).

RTM gravity anomalies are then:

$$\Delta g_{RTM} = g - \delta g_{RTM} - \gamma_0. \quad (3.32)$$

Main advantages of the RTM gravity anomalies is in removing only short wavelengths of the topographic masses are removed and residual anomalies are smoother than in other methods. Reference mean elevation surface serves as the approximation of the long-wavelengths surface, so they are not computed twice. Magnitude of the RTM effect decreases with increase of resolution of the mean reference surface. Resolution of the mean or reference elevation surface (h_{ref}) corresponds to the resolution of the maximum degree (n_{max}) of the global geopotential model ([Forsberg 1984](#)).

Properties of the RTM gravity anomalies are: a) its non-physical meaning, and b) need for computing corrections for the truncation bias ([Sjöberg 2005](#)) and harmonic correction ([Tziavos and Sideris 2013](#), p. 368).

3.5 Review

The main properties of topographic reductions are indirect effects, smoothness and geophysical meaning (table 3.1). For gravity determination, topographic reductions are important for: 1) point gravity anomalies gridding, 2) removal of all masses inside geoid as the boundary. For 1) the most important property is that reduced gravity data are as smooth as possible. For 2) reduced gravity field should not produce indirect effect on computed geoid undulations N . Therefore, only two topographic reduction methods are useful: Faye and RTM. The summary of formulas for obtaining gravity values, topographic reduction and anomalies are given in appendix E, table 9.4.

Table 3.1: Properties of gravity anomalies for different topographic reduction schemes (after [Bajracharya 2004](#))

Gravity anomaly	Symbol	Indirect effects on N	Smoothness	Geophysical interpretation
Free-Air	Δg_{FA}	large	very rough	yes
Bouguer	Δg_B	very large	smooth	yes
Faye	Δg_{Faye}	very small	rough	no
Airy-Heiskanen	Δg_{A-H}	small	smooth	yes
Pratt-Hayford	Δg_{P-H}	small	smooth	yes
RTM	Δg_{RTM}	very small	smooth	no

Chapter 4

Geoid Determination

“All models are wrong, but some are useful.”

George Box, 1919-2013

Theoretical foundations related to geoid determination are presented in this chapter. More detailed information can be found in many available references, such as [Denker \(2013\)](#) and [Sansó and Sideris \(2013\)](#).

4.1 Introduction

Along with Earth’s topographic surface and ellipsoid, the *geoid* is one of the three main surfaces in geodesy; it is the main reference surface for physical heights. *Geoid* can be described in different ways, so a large number of definitions have been given in the last two centuries. Some of them are:

Gauss (1828). “What we call in the geometric sense the surface of the Earth is nothing else but that surface which intersects the direction of gravity at right angles and from which the surface of the world ocean is a part.”

Stokes (1849). Geoid is the... “surface of the Earth’s original fluidity...”

Listing (1873). “According to our opinion we have to determine numerically in the future the derivations of the plumb line as long as they have visible origin, namely by a topographic surface of the continental relief, by a geological determination of the mass density of its constituents and by a systematic survey of the oceans according to well-established method. We shall call the previously defined mathematical surface of the earth, of which the ocean surface is a part, geoidal surface of the Earth or the geoid.”

Gauss-Listing geoid is... ”a best approximation of the mean sea level.”

Jensen (1950). “The equipotential surface, through a given point, chosen near MSL, that would exist if only the rotation of the Earth and the Earth’s gravitational field affected the potential as a function of the position of the chosen point.”

Einstein (1950), Bjerhammar (1962). “In relativistic geodesy, the geoid is the surface nearest to mean sea level on which precise clocks run with the same speed.”

- Heiskanen and Moritz (1967).** “The geoid as a fundamental surface of physical geodesy is defined as an equipotential surface that is closest to mean sea level; it is usually used as a mathematical model to represent the physical feature of the Earth. (...) The surface of the ocean, after some slight idealization is part of a certain level surface.”
- Nakiboglu (1979).** “Non-hydrostatic geoid is the shape that the Earth should have if gravity and rotation were in equilibrium.”
- Burkhard (1985).** “The geoid, coincides with that surface to which the oceans would conform over the entire earth if free to adjust to the combined effect of the Earth’s mass attraction and the centrifugal force of the Earth’s rotation. As a result of the uneven distribution of the Earth’s mass, the geoidal surface is irregular. (...) The geoid is a surface along which the gravity potential is everywhere equal and to which the direction of gravity is always perpendicular.”
- Torge (1993).** “About 2/3 of the Earth’s surface (oceans) approximately coincide with the geoid, the rest (continents) can be easily referred to it by leveling and gravity measurements. The geoid thus is a natural reference for describing the heights of the topography on land (continental topography) as well as on sea (sea surface topography). ”
- Vaníček and Martinec (1994).** “One of the equipotential surfaces of W , the one that approximates the mean sea level most closely, is given a special significance. We denote it by $W = W_0 = W_{const}$ and call it the geoid.”
- Petit and Luzum (2010).** “Geoid is equipotential surface of Earth’s gravity field with value $W_0 = 62,636,856.0 \pm 0.5 \text{ m}^2\text{s}^{-2}$.”
- Sansó and Sideris (2013).** “The geoid, (...), is plainly an equipotential surface of the gravity field of the earth, identified by a conventional value of the potential, such that it runs close to the surface of the ocean, within meters, but then well inside the continental masses specially in mountainous areas.”(...) “Geoid is a geometrical entity, usually described by the height of its points over the earth ellipsoid, the so called geoid undulation.”
- Vaníček and Krakiwsky (2015).** “The geoid is defined as the equipotential surface of the Earth’s attraction and rotation, which on the average coincides with mean sea level of the Earth in the absence of external influences such as wind and ocean current.”
- Sánchez et al. (2016).** “Per definition, W_0 is understood as the value of the gravity potential of the real Earth on a particular equipotential surface called *the geoid*. Since the Earth’s gravity potential field contains an infinite number of equipotential surfaces, the geoid is to be defined arbitrarily by convention.”(...) Geoid is: “the potential value obtained for the epoch 2010.0 ($62,636,853.4 \text{ m}^2\text{s}^{-2}$) recommended as the present best estimate for the W_0 value.”
- Sjöberg and Bagherbandi (2017b)** “The geoid is the equipotential surface (level surface) of the Earth’s gravity field that most closely coincides with the undisturbed mean sea level (and its continuation through the continents). Disturbances are caused by ocean tides, streams, winds, variations in salinity and temperature, etc, of the order of $\pm 2 \text{ m}$.”

Geoid in its full meaning is a physical surface, and its best approximation is *gravimetric geoid model* (usually referred as *geoid model* or simply *geoid*). Geoid models have many engineering and scientific applications, such as:

- reference surface for leveling,

- vertical datum for orthometric heights,
- transformation of ellipsoidal (geometrical) to orthometric (physically meaningful) heights,
- local and regional vertical datum unification,
- satellites orbits prediction,
- studies of the Earth interior and ocean,
- hydrographic surveying and marine navigation,
- finding deposits of ores, oil and gas.

One of the main usages of geoid models is in conversion of geometric ellipsoidal heights h , obtained by Global Navigation Satellite System (GNSS), to physical orthometric heights H :

$$H \approx h - N. \quad (4.1)$$

Geoid undulations N may be geometrically interpreted as the differences between orthometric heights, measured along the real plumb line from the geoid, and ellipsoidal heights, measured along the ellipsoidal normal (4.2). These differences are mainly caused by topographic masses and density anomalies which can seize up to ± 100 m in some areas in the world. Equation 4.1 can be used either for obtaining heights in absolute positioning or height differences in relative positioning. Measurement method for obtaining height differences is known as GNSS/levelling, which consists from measuring ellipsoidal heights h using GNSS and geoid undulation N from geoid model. If these two quantities are known, height differences between a all pairs of points are obtained in a straightforward manner as $\Delta H = (h_1 - N_1) - (h_2 - N_2)$. Therefore, if GNSS and geoid model are sufficiently accurate they can replace classical levelling using two ropes. Due to inaccuracies in GNSS (ellipsoidal) heights and geoid model GNSS/levelling cannot replace classical levelling in transfer of the heights on short distances of up to few kilometers, although on larger distances than 100 km GNSS/levelling can even give more accurate results. Another advantage of of GNSS/levelling is when heights are needed to be transfered across long and complex mountainous chains, where levelling is known to be inefficient and time-consuming. Comprehensive information about heights and height systems may be found in [Jekeli \(2000\)](#) or [Meyer et al. \(2007\)](#).

4.2 Stokes' theorem

In 1849. Stokes found solution to the 3rd BVP which satisfies boundary condition, i.e. Laplace's equation:

$$\nabla^2 V = 0. \quad (4.2)$$

The equation 4.2 is an analytic harmonic function in a mass-free space having continuous derivatives of any order. Stokes' solution later became known as the Stokes' theorem [Stokes \(1849\)](#). It explains that if on a boundary surface S the value of a potential function V is known, there will be at most one harmonic function V in the whole exterior space that satisfies boundary condition.

The integral equation of Stokes' solution is known as the Pizzetti formula ([Pizzetti 1911](#),

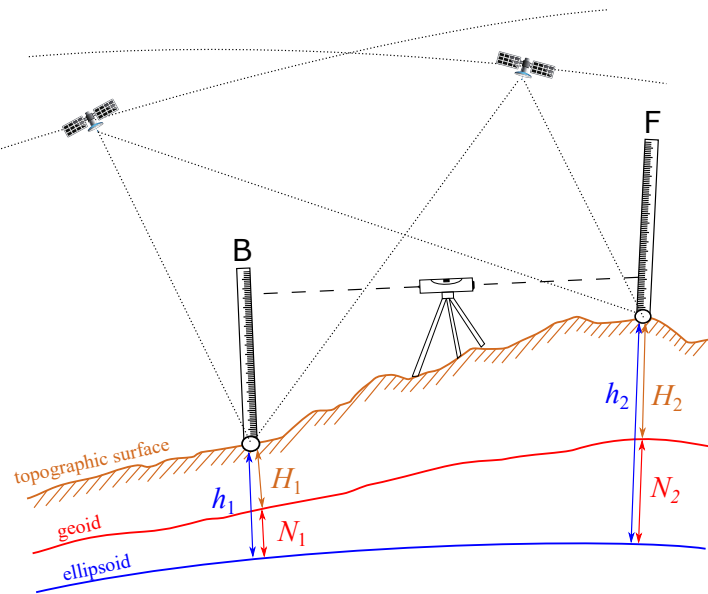


Figure 4.1: Determination of heights and height differences using two methods: classical levelling and GNSS/levelling (after Gerlach 2003)

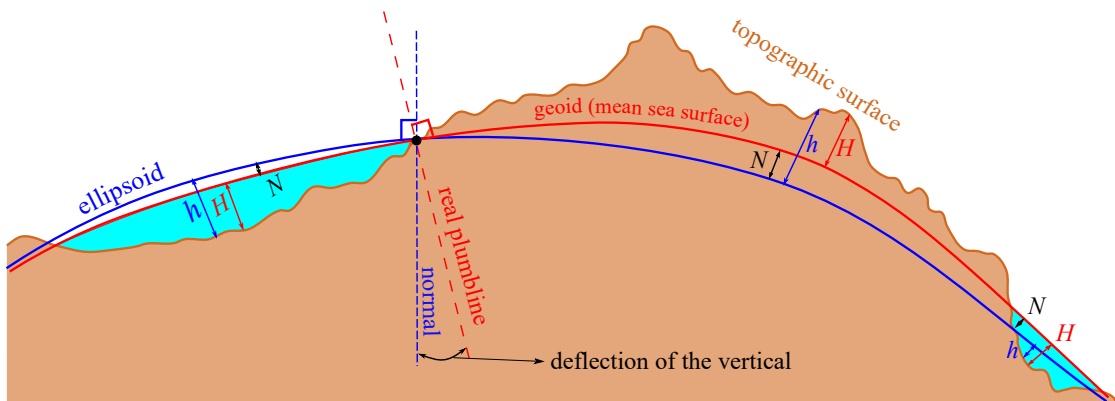


Figure 4.2: Geoid undulation depending on the mass distributions of the Earth's crust (after Burkhard 1985)

Hofmann-Wellenhof and Moritz 2005, eq. 2-304):

$$T = \frac{R}{4\pi} \iint_{\sigma} S(\psi) \Delta g d\sigma, \quad (4.3)$$

where R is the mean radius of the Earth, Δg are gravity anomalies on geoid, $S(\psi)$ the Stokes function (see, section 4.7.5), ψ the spherical distance (geocentric angle) between the computation and data point, $d\sigma$ is an infinitesimal surface element of the unit integration sphere σ . The above equation for disturbing potential T is a solution of the FEPG in the spatial domain (see, table 4.1).

Table 4.1: The relation between fundamental equation of physical geodesy (FEPR) and Stokes integral

FEPR	Stokes
$T \rightarrow \Delta g$	$\Delta g \rightarrow T$
$\Delta g = -\left(\frac{2}{R} + \frac{\partial}{\partial r}\right) T$	$T = \frac{R}{4\pi} \iint_{\sigma} S(\psi) \Delta g d\sigma$

The Stokes equation is in theoretical sense very elegant allowing computation of geoid surface in spherical approximation from the measurements reduced from the Earth's topographic surface to geoid. In practice, Stokes' equation is valid only under if (Jekeli 1981, Moritz 1989):

- The Earth is approximated with a sphere.
- Total masses, the centers of mass, and the constant surface potential of the ellipsoid and geoid are identical.
- No masses exist outside of the geoid.
- Measurements are available all over the sphere.
- All gravity measurements have to be reduced from the Earth's surface to the boundary surface, geoid, which is unknown before evaluation of the Stokes integral.

4.2.1 Molodenskii's theory

Practical computation of the geoid model using the Stokes' integral has the problem related to the unknown crustal structure between Earth's topographic surface and geoid as a boundary surface. As data have to be reduced through the crust down to the geoid, some approximations must be included, limiting strict theoretical foundation of the Stokes integral. In 1945, Molodenskii proposed modification and found new solution of the BVP. He introduced a *quasi-geoid* boundary surface, instead of geoid surface in the classical approach. Molodenskii proved that the classical approach had no solution for a non-spherical Earth and solved the BVP on the Earth's surface (Molodenskii 1962). His solution avoids reduction of the data from the Earth's surface to the geoid because no masses exist above Earth's topography surface. Solution of the Molodenskii's integral results in derivation of quasi-geoid surface through calculation of normal-heights ζ :

$$\zeta = \frac{R}{4\pi\gamma} \iint_{\sigma} (\Delta g_{FA} + g_1) S(\psi) d\sigma, \quad (4.4)$$

where the Δg_{FA} are Molodenskii's free-air gravity anomalies referring to the Earth's surface (equation 3.5). The expression g_1 is the first term in the Molodenskii series and for practical purposes can be approximated with the terrain correction term $g_1 \approx \delta g_{TC}$, where δg_{TC} is obtained by equation 3.10 in section 3.2.2 (Heiskanen and Moritz 1967).

Some authors detected theoretical and practical deficiencies in Molodenskii's solution and determination of quasi-geoid. According to Bjerhammar (1969) this approach is elegant but very complicate. In Vaníček et al. (2012) it is emphasized that quasi-geoid determination has a problem with the geometry of the Earth's surface. Integrating gravity over the surface of the Earth, which is much rougher than the geoid is not possible in certain areas, and in other areas will result in unpredictable errors. Furthermore, it is written that vertical rock surfaces represent

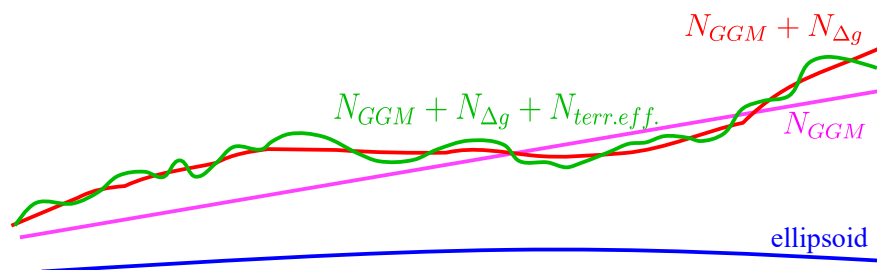


Figure 4.3: Contribution of different data types in gravimetric geoid determination (after Schwarz et al. 1987).

locations of discontinuity, and there are other areas where the surface of the Earth cannot be described as a mathematical function of horizontal positions. In such locations, the Molodenskii approach will not give results. In their opinion, the geoid which is a fairly smooth and convex surface, without any kinks, edges or other irregularities, is a better surface for integration.

In many cases in the past, when accuracy of developed geoid and quasi-geoid models was larger than few centimeters, the differences between the Stokes' and Molodenskii's solution were not so obvious, especially in the areas of simple and flat topography as the differences were not visible in the full error budget of computed geoid or quasi-geoid model.

4.3 Data for gravimetric geoid determination

Data are integral part of the process of development of gravimetric geoid model. Several data types are used for this purpose, including:

- **Global geopotential models** developed from satellite orbit, altimetry and terrestrial data, and delivered in the form of spherical harmonic (SH) coefficients with corresponding standard deviations.
- **Gravity data** obtained from the terrestrial, marine or airborne measurements. They are usually distributed as the free-air gravity anomalies.
- **Digital elevation and bathymetry models** derived from photogrammetric, Light Detection and Ranging (LiDAR) or Synthetic Apertur Radar (SAR) measurements. They are usually distributed in the gridded form with alternative spacings (1'', 3'', or 30''). Mostly used DEMs include different versions of SRTM, ASTER GDEM, GTOPO30 or ETOPO1.
- **Crustal models** derived from geodetic, geophysical, and geological data, and usually distributed in the gridded form. At this moment, crustal models are rarely available and used.

Figure 4.3 shows contributions of different data types in computation of the gravimetric geoid. Spectral sensitivity of different data types is given in table 4.2. Geoid undulation N_{GGM} contribute to the long wavelength features which change smoothly on spatial scales of more than 50 km. Geoid undulation $N_{\Delta g}$ obtained from gravity data contribute to regional part of the geoid undulation with wavelengths between 20 and 200 km. Geoid undulation $N_{terr. eff.}$ derived from digital elevation and bathymetric models which contribute to local short-scale features of the geoid undulation with wavelengths smaller than 20 km (Forsberg 1993).

Table 4.2: Spectral sensitivity of the gravity field functionals (after Schwarz 1984, Kuhn 2000 and Kern 2003)

Structure	Spectral resolution		Gravity field functional			
	Wavelength [km]	degree (n_i-n_j)	N [m]		Δg [mGal]	
long wavelength	20000 - 4000	2 - 10	± 29.72	95.6%	± 12.62	8.9%
	4000-1100	11 - 36	± 5.98	3.9%	± 15.82	13.9%
medium wavelength	1100-220	37 - 180	± 2.15	0.5%	± 22.50	28.2%
short wavelength	220-20	181-2000	± 0.47	0.02%	± 27.20	41.2%
ultra-short wavelength	220	2001 - 20000	± 0.03	0.0%	± 11.80	7.76%
	< 2	20001 - ∞	± 0.02	0.0%	± 0.15	0.001%
total	20000 - 0	2 - ∞	± 30.394	100%	± 42.37	100%

All data types have specific errors which propagate into the solutions of computed models. Some of the errors can be safely ignored, some may be modeled using different algorithms and approximations, and some are removed by filtering procedures.

4.4 Surface crustal density models

Due to the unknown structure of the Earth, especially Earth's lithosphere, practical geoid determination is mostly performed by using constant globally-estimated crustal parameters. Crustal density, density contrast between crust and mantle, and depth of compensation are arbitrarily chosen in the reduction step, such as for computation of the terrain or topographic-isostatic correction. However, globally estimated crustal parameters may be different from real values for as much as 10 or 20% in local and regional study areas.

Modelling of topographic and density effects may be improved using crustal models which can be created from different types of data using inversion methods and procedures. Several methods may be used for development of 2D (lateral, surface) or 3D (with horizons or layers) crustal models, such as: 1) isostatic models, 2) Parasnis-Nettleton's inversion method, 3) digitizing existing geological maps (see, Vaníček 1976, Pagiatakis et al. 1999, Kuhn 2000, Rózsa 2002b, Kuhn 2003, Bajracharya 2004, Bagherbandi 2011, Tziavos and Sideris 2013).

In this thesis surface (2D) crustal density models are developed by inversion method's according to Pratt-Hayford, Airy-Heiskanen, and Parasnis-Nettleton. These method's are not originally formulated for the purposes of development of crustal density. Thereafter, for implementation of these methods original formulations had to be slightly modified. Density values are computed for all cells (nodes) of the defined grid shown in figure 4.4 left. As data are used for larger area than Croatia (figure 4.4 right), actual borders of the computed density grids are wider than shown in figure. The resolution (spacing between adjacent cells) of developed models is

Table 4.3: Input parameters for development of surface crustal density models according to inversion by Airy-Heiskanen, Pratt-Hayford and Parasnis-Nettleton's topographic-isostatic models

Method	Section	Symbol	Input value
Pratt-Hayford	4.4.1	ρ_0 [kgm ⁻³]	2300, 2400, ..., 3000
		D [km]	80, 90, ..., 150
Airy-Heiskanen	4.4.2	ρ_m [kgm ⁻³]	2700, 2800, ..., 3400, 3500
		T [km]	from CRUST1.0 model
Parasnis-Nettleton	4.4.3	RS [°]	0.05, 0.1, ..., 2.0
		n_{max}	0, 5, 10, ..., 400, 500

5' in both latitude and longitude directions. All input parameters for development of developed models are given in table 4.3, and are explained in more details in the following three subsections.

4.4.1 Pratt-Hayford

Starting from equation 3.19, the surface crustal density is computed using:

$$\rho_c^{P-H} = \frac{D\rho_0}{D+H}, \quad (4.5)$$

for continent and:

$$\rho_c^{P-H} = \frac{D\rho_0 - H'\rho_w}{D - H'} \quad (4.6)$$

for ocean, where D is compensation depth, ρ_0 reference (mean) crustal density, H height and H' depth of topography taken from DEM/DBM. Compensation depths D and reference density ρ_0 can be provisionally selected, estimated or fixed. Compensation depth D is equal to the sum of crustal and upper mantle thickness which corresponds to the values around 100 km.

4.4.2 Airy-Heiskanen

In the A-H model crustal density ρ_c is known whereas crustal thickness t is unknown. The value of ρ_c has to be chosen, e.g. 2670 kgm⁻³. Original formulation of the A-H model can be modified in order to be able to calculate crustal density value for each column. This is possible under assumption that input parameters crustal thickness t , mean (normal) crustal thickness T_0 , height H , depth H' and mantle density ρ_m are assumed, fixed or taken from external models. Surface crustal density according to modified A-H model is computed as:

$$\rho_c^{A-H} = -\frac{\rho_m(H - T + T_0)}{T - T_0}, \quad (4.7)$$

for continental areas and,

$$\rho_c^{A-H} = -\frac{H'\rho_w - \rho_m(H' + T - T_0)}{T - T_0}, \quad (4.8)$$

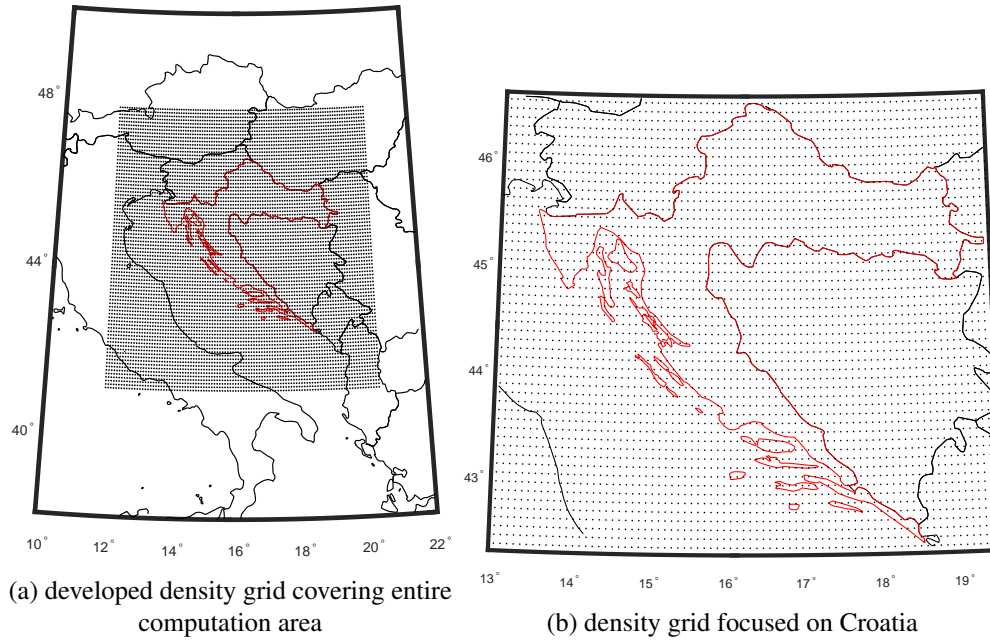


Figure 4.4: Grid points of the developed lateral density models

for ocean areas, where: ρ_c crustal density, ρ_w water density, ρ_m density of the mantle, T Earth's crustal thickness, T_0 normal Earth's crustal thickness, H and H' heights and depths of topography and bathymetry. Several values for ρ_m are chosen ($\rho_m = 3000, \dots, 3500 \text{ kgm}^{-3}$), T is taken from model of Moho depths (such as CRUST1.0 or EPcrust), T_0 is mean of the crustal thickness on some area (mean value of Moho depths on some area), and H and H' are taken from digital elevation models.

4.4.3 Parasnis-Nettleton

The idea in Parasnis-Nettleton's inversion method (P-N) follows from the property that correlation between Bouguer anomalies and elevation of topography is caused by density anomaly. Therefore no correlation should exist between Bouguer anomalies and elevations (Nettleton 1939) in case 'correct' crustal density value ρ_c is selected for computation in some area. Examples of the publications in which surface density models are created using Parasnis-Nettleton's (P-N) method are Mankhemthong et al. (2012) and Toushmalani and Rahmati (2014). Starting from the equation for derivation of Bouguer anomalies from free-air anomalies:

$$\Delta g_{sB} = \Delta g_{FA} - 2\pi G\rho H = \Delta g_{FA} - 0.04193\rho H, \quad (4.9)$$

it follows that crustal density ρ_c may be calculated by determination of the parameters of linear regression a between free-air anomalies and elevations. Gradient of the regression line a is obtained for n free-air anomalies (Rózsa 2002b, Rózsa 2002a):

$$a = \frac{\sum_{i=1}^n (H_i - \bar{H})(\Delta g_i - \bar{\Delta g})}{\sum_{i=1}^n (H_i - \bar{H})^2}, \quad (4.10)$$

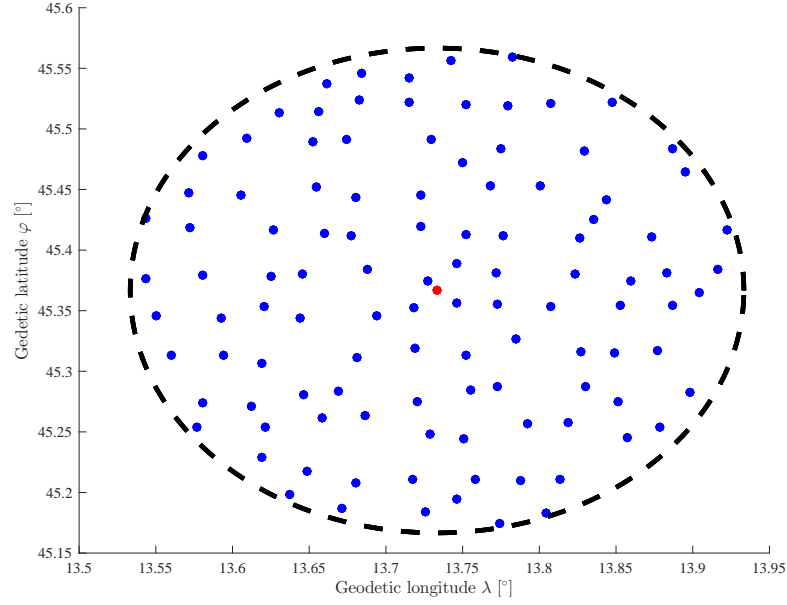


Figure 4.5: Selected point gravity anomalies (blue dots) within the radius (black circle) of computing point (red dot) as input data for determination of ρ_c .

where Δg_i are free-air anomalies, H_i orthometric heights, $\overline{\Delta g}$ mean value of free-air anomalies on computing area and $\overline{\Delta H}$ mean value of orthometric heights on some computation area. From the determined coefficient a , ρ_c is calculated as:

$$\rho_c = \frac{a}{0.04193}. \quad (4.11)$$

Computation of the crustal density models starts by division of the wanted computation area in cells, where cell sizes are defined by the wanted resolution of the model. Density value for each cell is derived by selecting free-air anomalies within chosen radius around center of the cell (RS) (figure 4.5), and utilizing equations 4.10 and 4.11 for computation of the density. Density values are obtained for all cells of the defined grid (see fig. 4.4).

Free-air gravity anomalies are used as input data. In this case, when density is determined for regional area, not global, it seems reasonable to filter long-wavelength (global) effects included in input free-air anomalies. Therefore, input values Δg_i from the equation 4.10 are derived as:

$$\Delta g'_i = \Delta g_i - \Delta g_{GGM}^{n_{max}}, \quad (4.12)$$

where $\Delta g_{GGM}^{n_{max}}$ for some n_{max} values are computed and subtracted from each free-air gravity anomaly Δg_i .

4.5 Geoid determination approaches and methods

Gravimetric geoid models are mostly determined using three approaches:

- Remove-Compute-Restore (RCR),
- Least Squares Modification of Stokes' formula with Additive corrections (LSMSA),
- Stokes-Helmert (UNB).

RCR approach is designed at the University of Copenhagen (Denmark), Least Squares Modification of Stokes' formula with Additive corrections (LSMSA) approach at the Royal Institute of Technology (KTH), and Stokes-Helmert at the University of New Brunswick.

Approaches share some similar steps and mostly use the same input data, but vary in computation steps. Minimally three obvious differences exist between them. First difference emerges in the processing of point gravity data prior to geoid computation in terms of selection of the topography reduction method. The next difference is in the way how three main types of data (gravity data, GGM and DEM) are treated and combined. The last difference is in the method of transformation from gravity data to geoid undulation which can be stochastic or deterministic.

There is no consensus which approach provides optimal results, as only few studies have been conducted so far over same study area and using same input data (section 1.4). [Sjöberg and Bagherbandi \(2017a\)](#) report KTH approach, compared with other approaches, provides better agreement with control GNSS/levelling data. However, in many areas worldwide it was shown that each approach can produce a *1 centimeter* geoid. It is also possible that scientists from three geoid modelling *schools* are biased and prefer only *their's* approach. As gravimetric geoid development is a complex process, consisting from many steps, it will probably not be possible to finally converge and make conclusion about optimal approach in all cases.

Apart from the three major approaches, geoid computation method (GCM) has to be selected in computation of gravimetric geoid starting from the input data. Traditionally, two main GCMs are Stokes' (analytic or spectral) method, and LSC. Some other attempts have been used most recently such as spherical base functions ([Schmidt et al. 2007](#)), or RBFs (see, e.g. [Ophaug and Gerlach 2017](#)).

4.5.1 Types of geoid models

The term *geoid* is commonly used for few different surfaces. In some applications differences are not so important and do not have to be emphasized, but in more strict, theoretical, context, they have to be distinguished. The main reference surfaces of physical geodesy are shown in figure 4.6.

First, the difference between *gravimetric* and *hybrid* geoid model shall be addressed:

Gravimetric geoid is a surface derived in a global reference system from gravimetric data as the solution of the 3rd BVP. It is purely related only to the gravimetric data and it has no practical geodetic application in the MSL-based vertical reference system, as it does not have connection with the local or national height networks (4.7). It may however have a geophysical and oceanographic application and interpretation.

Hybrid geoid model is a gravimetric geoid model fitted (adjusted) to regional, national, or local levelling network. As such it is used as transformation surface between ellipsoidal and physical height and always relates to the specific vertical datum (W_0) as the origin point of the height reference systems, e.g. national local vertical datum (LVD) related to the mean sea level (MSL) ([Forsberg and Strykowski 2005](#)).

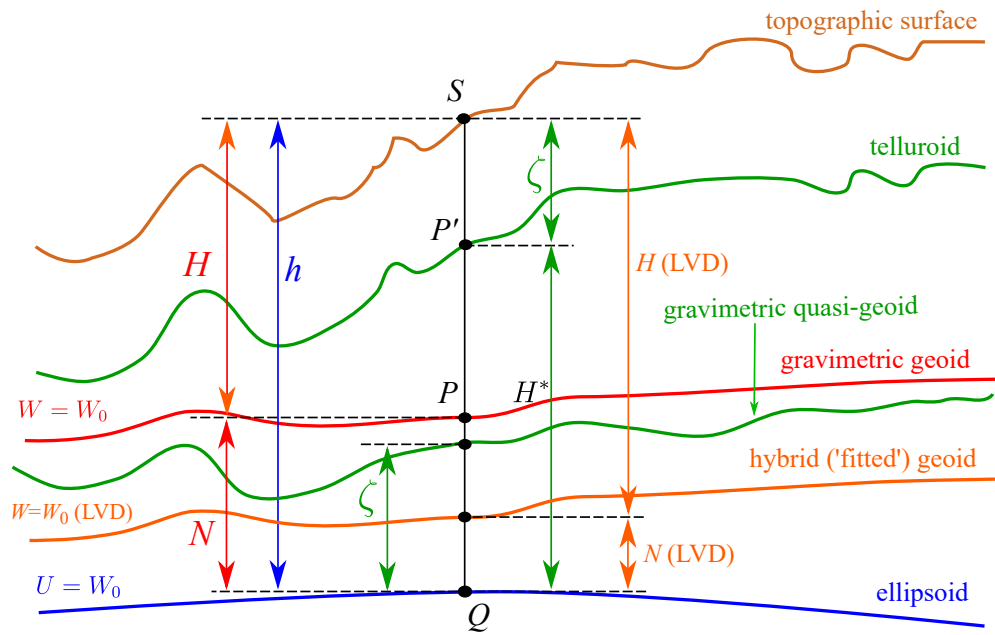


Figure 4.6: The concept of the main surfaces in geodesy

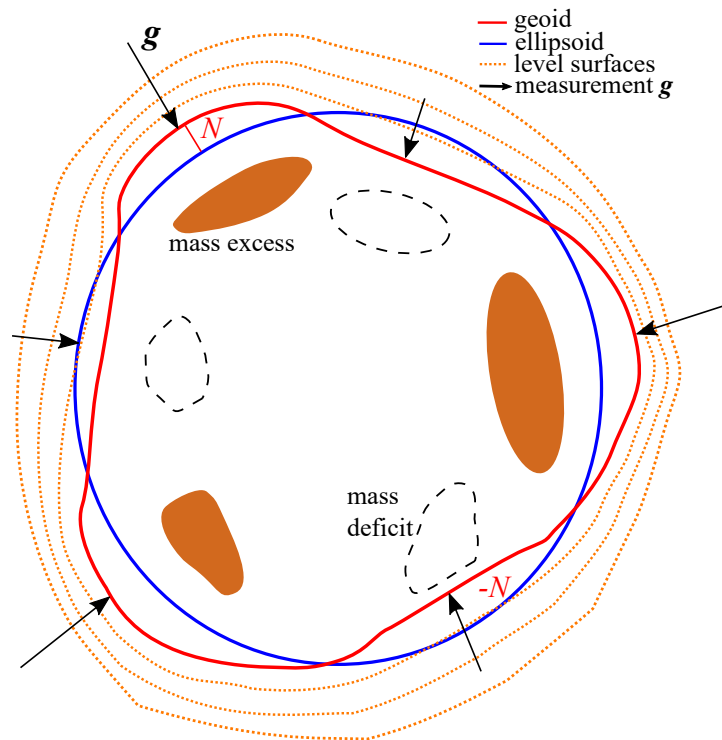


Figure 4.7: The principle of gravimetric geoid determination (after Vermeer 2018)

Procedure of gravimetric geoid model transformation to hybrid geoid models is shown in figure 4.8.

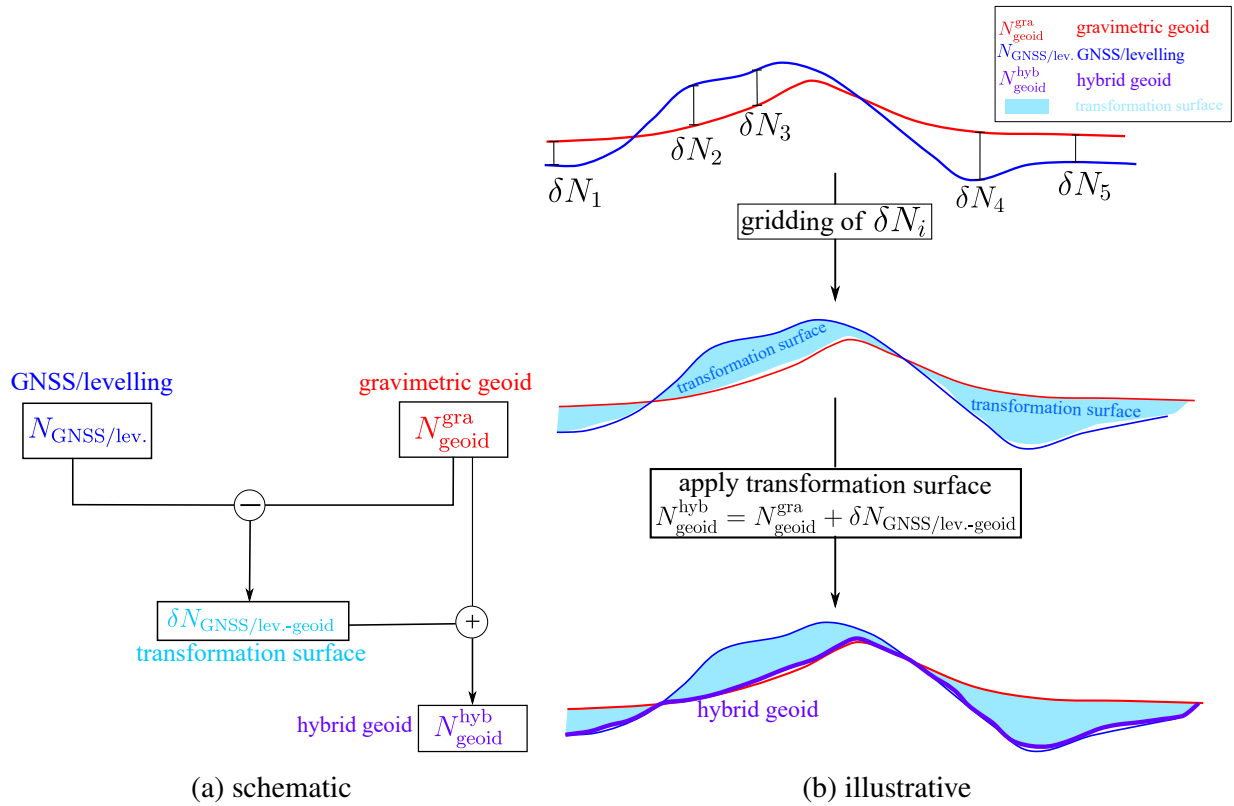


Figure 4.8: Transformation of gravimetric to hybrid geoid model (after Arana et al. 2017)

Table 4.4: The main characteristics of the orthometric and normal heights (after Marti and Schlatter 2002)

characteristics	H	H^N
rigorous system with dependency on the potential	+	+
system without a mass distribution hypothesis	-	+
easy computation	-	+
physical meaning of the reference surface	+	-
geometrical relationship with ellipsoidal heights	+	+

Second, the difference between *quasi-geoid* and *geoid* needs to be explained. Geoid is a reference surface for orthometric heights, and quasi-geoid is a reference surface for normal heights. The main characteristics of the orthometric and normal-orthometric heights are given in table 4.4. Characteristics of other height types are given in appendix E, table E.1. Geoid model is related to the Earth’s topographic surface via geoid undulations N , while quasi-geoid

via height anomalies ζ . Both surfaces may be obtained with Bruns' equation, however \bar{g} is computed at the geoid level ($H = 0$), while $\bar{\gamma}$ is evaluated at the Earth's topographic surface. The quasi-geoid is upward continued geoid to the terrain through the topographic masses (Forsberg 1993).

Inside topography disturbing potential T is not harmonic so $N \neq \zeta$. Quasi-geoid to geoid correction (separation) is (Heiskanen and Moritz 1967, section 8, Sansó and Sideris 2013, eq. 2.71):

$$\zeta - N = \frac{\bar{g} - \bar{\gamma}}{\bar{\gamma}} H = \frac{2\pi G\rho}{\gamma_0} H^2 - \frac{\Delta g_P}{\gamma_0} H, \quad (4.13)$$

where mean gravity along the plumb line \bar{g} and mean normal gravity $\bar{\gamma}$ are:

$$\bar{g} \approx g - \left(\frac{1}{2} \frac{\partial \gamma}{\partial H} + 2\pi G\rho \right) H, \quad (4.14)$$

$$\bar{\gamma} \approx \gamma - \left(\frac{1}{2} \frac{\partial \gamma}{\partial H} \right) H. \quad (4.15)$$

In practice the difference between height anomaly and geoid undulation $\zeta - N$ is computed using simpler approximate expression:

$$\zeta - N \approx -\frac{\Delta g_B H}{\bar{\gamma}}, \quad (4.16)$$

where Δg_B is the simple or complete Bouguer anomaly. In the ocean areas geoid and quasi-geoid coincide.

Due to historical reasons and geoid accuracies of several centimeters, the difference between geoid and quasi-geoid was not so rigorously computed nor specifically addressed in the past. Nowadays however for achieving highest accuracies the $\zeta - N$ difference has to be properly accounted for.

Indirect effect and co-geoid

Co-geoid is another term which has to be described more closely. By applying topographic reduction on the gravity measurement performed on the Earth's topography surface the station is shifted down to the geoid surface. Shift induces *indirect effect*, as the equipotential surface with potential W_0 changes to some value W'_0 . Therefore, co-geoid with potential W'_0 is obtained instead of geoid with potential W_0 as a result of geoid computation using topography-reduced gravity measurements. Transformation from co-geoid with potential W'_0 to geoid with potential W_0 is performed by applying correction (Wichiencharoen 1982):

$$N(W_0) = N(W'_0) + \delta N_{ind}, \quad (4.17)$$

where δN_{ind} is indirect effect on N calculated by:

$$\delta N_{ind} = \frac{\delta W}{\gamma} = -\frac{\pi G\rho H_P^2}{\gamma} - \frac{G\rho R^2}{6\gamma} \int_{\sigma} \frac{H_Q^2 - H_P^2}{l^3} d\sigma, \quad (4.18)$$

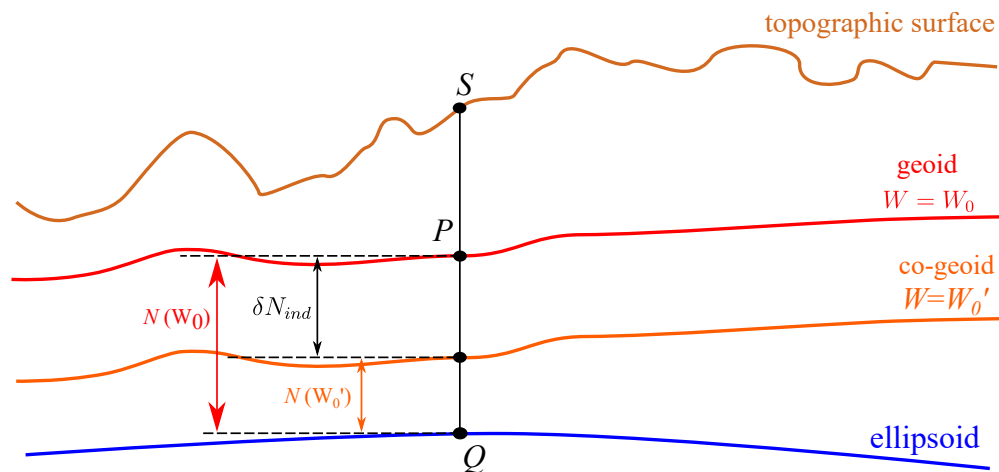


Figure 4.9: Difference between geoid and co-geoid

where δW is the change of geoid potential caused by gravity reduction.

Indirect effect depends on the used gravity reduction method (table 3.1). Generally, reduction method shall aim to produce small indirect effect on geoid undulation, as reduction method that causes large indirect effect will also produce larger errors on the computed geoid (see, table 3.1 in section 3.5). In this context, the best reduction scheme for geoid determination is RTM which is known to produce small indirect effect.

4.6 KTH approach

Least Squares Modification of Stokes' formula with Additive corrections (LSMSA) approach (more often referred as KTH approach) has been developed from 2000s at the Royal Institute of Technology (KTH), University in Stockholm, Sweden by professor Lars Erik Sjöberg. Throughout the years it was additionally improved by several other scholars, mainly during their research within doctoral studies.

In the KTH approach, terrestrial Molodenskii's free-air gravity anomalies and global geopotential model are used for calculation of approximate geoid undulation. Afterwards, all other effects influencing geoid undulations are computed separately and added to the approximate geoid undulation. The basic equation of the KTH approach is:

$$N = \tilde{N} + \delta N_{\text{top}}^{\text{comb}} + \delta N_{\text{DWC}} + \delta N_{\text{atm}} + \delta N_{\text{ell}}, \quad (4.19)$$

where \tilde{N} represents the approximate geoid undulation, $\delta N_{\text{top}}^{\text{comb}}$ combined topographic correction, δN_{DWC} downward continuation correction, δN_{atm} atmospheric correction and δN_{ell} ellipsoidal correction. The approximate geoid undulation \tilde{N} is computed from Sjöberg's modification of the Stokes' kernel (Sjöberg 2003b):

$$\tilde{N} = \frac{R}{4\gamma\pi} \iint_{\sigma_0} S_L(\psi) \Delta g \sigma + \frac{R}{2\gamma} \sum_{n=2}^M b_n \Delta g_n^{\text{GGM}}, \quad (4.20)$$

where Δg is Molodenskii's free-air gravity anomaly, σ_0 a cap with spherical radius ψ_0 of integration around the computations point, S_L modified Stokes' kernel, Δg_n^{GGM} gravity anomaly calculated from GGM using equation 4.55. Stochastic modification of the Stokes' kernel S_L as a function of the integration radius ψ is (Heiskanen and Moritz 1967, eq. 2-169):

$$S_L(\psi) = S(\psi) - \sum_{n=2}^L \frac{2n+1}{2} s_n P_n \cos \psi, \quad (4.21)$$

where s_n are arbitrarily chosen modification parameters, n is the modification degree of the Stokes function. The first term in equation 4.21 is unmodified spherical Stokes function (eq. 4.82, Heiskanen and Moritz 1967), and the second term is Sjöberg's modification with maximal degree $n < L$. Arbitrarily selected upper limit L is generally not equal to the maximal degree of expansion of the selected GGM n_{max} . Solution of the equation 4.20 is obtained after obtaining the parameters b_n from (Sjöberg 1991, Sjöberg 2003d):

$$b_n = (Q_n^L + s_n^*) \frac{c_n}{c_n + dc_n}, \quad (4.22)$$

for $2 \leq n \leq M$.

The Molodenskii's truncation coefficients Q_n^L is given as (Sjöberg 1991):

$$Q_n^L = Q_n - \sum_{k=2}^{\infty} \frac{2k+1}{2} s_k e_{nk}, \quad (4.23)$$

and the Q_n from (Heiskanen and Moritz 1967):

$$Q_n = \int_{\psi_0}^{\pi} S(\psi) P_n \cos \psi \sin \psi d\psi, \quad (4.24)$$

where e_{nk} are Paul's coefficients (Paul 1973):

$$e_{nk}(\psi_0) = \int_{\psi_0}^{\pi} P_n \cos \psi P_k \cos \psi \sin \psi d\psi. \quad (4.25)$$

4.6.1 Approximate geoid undulation

Approximate geoid undulation \tilde{N} , given by equation 4.20, written in the spectral form is (Sjöberg 2003b, eq. 2.7):

$$\tilde{N} = c \sum_{n=2}^{\infty} \left(\frac{2}{n-1} - Q_n^L - s_n^* \right) (\Delta g_n + \varepsilon_n^T) + c \sum_{n=2}^M (Q_n^L + s_n^*) (\Delta g_n^{GGM} + \varepsilon_n^S), \quad (4.26)$$

where $c = \frac{R}{2\gamma}$. The above equation includes error estimates of the input gravity Δg_n and GGM Δg_n^{GGM} data; terms ε_n^T , and ε_n^S are predicted spectral errors of terrestrial and GGM gravity anomalies in spectral form. The modification parameters s_n are defined as:

$$s_n^* = \begin{cases} s_n, & \text{is } 2 \leq n \leq L, \\ 0, & \text{otherwise,} \end{cases} \quad (4.27)$$

where the s_n parameters should minimize errors of truncation, gravity anomaly data and GGM in the least square sense (Sjöberg 1991, Sjöberg 2003a). The expected global Mean Square Error can be written in general form where E represents the statistical expectation estimator (Hofmann-Wellenhof and Moritz 2005):

$$m_{\tilde{N}}^2 = E \left\{ \frac{1}{4\pi} \iint_{\sigma} (\tilde{N} - N)^2 d\sigma \right\}. \quad (4.28)$$

By combining the estimated geoid undulation from equation 4.26 and geoid undulation N in the spectral form defined as (Heiskanen and Moritz 1967, p. 97):

$$N = c \sum_{n=2}^{\infty} \frac{2\Delta g_n}{n-1}, \quad (4.29)$$

with the expression 4.28, the expected Global Mean Square Error (GMSE) of the \tilde{N} takes the form (Sjöberg 2003d):

$$m_{\tilde{N}}^2 = c^2 \sum_{n=2}^M b_n^2 d c_n + c^2 \sum_{n=2}^{\infty} \left[(b_n^* - Q_n^L - s_n^*)^2 c_n + \left(\frac{2}{n-1} - Q_n^L - s_n^* \right)^2 \sigma_n^2 \right], \quad (4.30)$$

and consists from the GGM, terrestrial data and truncation errors. The modification parameters b_n^* are:

$$b_n^* = \begin{cases} b_n, & \text{is } 2 \leq n \leq M, \\ 0, & \text{otherwise,} \end{cases} \quad (4.31)$$

while c_n are gravity anomaly degree variances, σ_n^2 and $d c_n$ are error degree variances of point gravity (Δg_{FA}) and GGM (Δg_{GGM}) anomalies.

4.6.2 Signal and error (noise) degree variances

Errors of the terrestrial and GGM gravity anomalies in spectral form are described through variances. Gravity anomaly signal degree variances c_n are computed by (Sjöberg 2003d, eq. 12, 11a, 12b):

$$c_n = \frac{1}{4\pi} \iint_{\sigma} \Delta g_n^2 d\sigma, \quad (4.32)$$

error degree variances of terrestrial gravity anomalies:

$$\sigma_n^2 = E \left\{ \frac{1}{4\pi} \iint_{\sigma} (\varepsilon_n^T)^2 d\sigma \right\}, \quad (4.33)$$

whereas error degree variances computed from GGMs dc_n are computed by:

$$dc_n = E \left\{ \frac{1}{4\pi} \iint_{\sigma} (\varepsilon_n^S)^2 d\sigma \right\}. \quad (4.34)$$

Values c_n and dc_n are calculated from spherical harmonic coefficients C_{nm} and S_{nm} of the GGM model after equations 4.61 and 4.70.

4.6.3 Terrestrial data error degree variances

Gravity measurements should be known and measured at every point on the Earth's topography surface in order to determinate the global covariance function. Apparently this is not the case, so local covariance model and empirical covariance functions is estimated from the available terrestrial data for particular study area. The covariance function $C(\psi)$ is completely described with two parameters: error variance $C(0)$ and correlation length ψ_0 . In order to define local covariance model, these two parameters have to be assumed and chosen. The error variance is the value of covariance function for $\psi = 0$, while the correlation length ψ_0 is a value where $C(\psi)$ achieves half of the value $C(\psi_0) = 0.5 \cdot C(0)$. Elements of the covariance function are shown in figure 4.10.

Error degree variances of the terrestrial data σ_n^2 may be obtained from the reciprocal distance covariance model (Sjöberg 1986, section 7):

$$\sigma_n^2 = c_T (1 - \mu) \mu^n, 0 < \mu < 1, \quad (4.35)$$

for which parameters c_T and μ are unknowns.

First, a value of parameter μ is found using the isotropic covariance function $C(\psi)$ according to Moritz (1978) and (Sjöberg, 1986, eq. 7.2):

$$C(\psi) = c_T \left\{ \frac{1 - \mu}{\sqrt{1 - 2\mu \cos \psi + \mu^2}} - (1 - \mu) - (1 - \mu) \mu \cos \psi \right\}. \quad (4.36)$$

After calculation of μ , and $C(\psi)$ for $\psi = 0$ from the equation 4.36, parameters of the covariance function are (Ellmann 2004, Ellmann 2005b):

$$C(0) = c_T \mu^2, \quad (4.37)$$

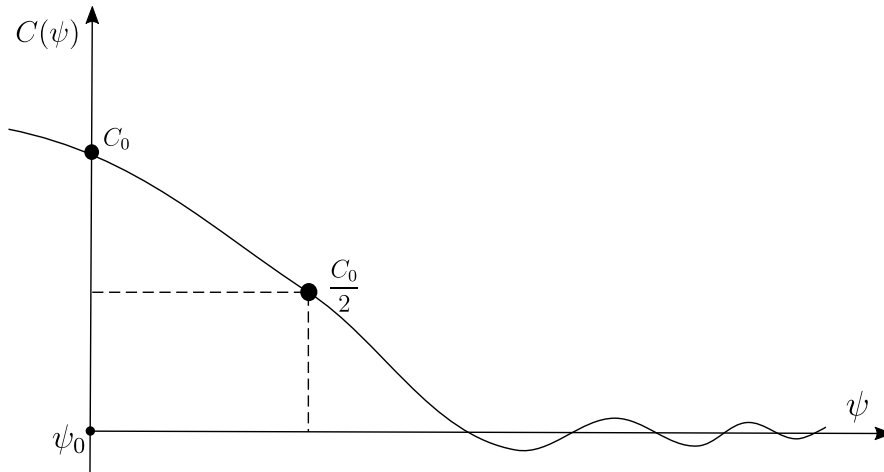


Figure 4.10: Elements of the covariance function

and correlation length $C(\psi_{1/2})$:

$$C(\psi_{1/2}) = \frac{1}{2}C(0). \tag{4.38}$$

After C_0 and $C(\psi_{1/2})$ are known, terrestrial gravity anomaly degree variances σ_n^2 can be computed using equation 4.35.

4.6.4 Least-squares modification parameters

Modification parameters s_n and b_n have to be determined for evaluation of equation 4.30. This is done by the solution of the linear system of equations (Sjöberg 1991, Ellmann 2004):

$$\sum_{r=2}^L a_{kr} s_r = h_k, k = 2, 3, \dots, L, \tag{4.39}$$

where a_{kr} and h_k are modification coefficients. Three possible solutions of the equation 4.39 are biased, unbiased and optimum. The difference between solutions is due to the choice of the parameter b_n . Optimum and biased solutions are ill-conditioned and can produce unexpected results. The issue may be overcome by using Singular Value Decomposition (SVD) method (Press et al. 1992).

Table 4.5: Parameters of the stochastic and deterministic modifications of the Stokes' kernel

parameter	stochastic modifications			deterministic modifications		
	biased	optimum	unbiased	no modification	WG	VK
s_n	$\sum_{n=2}^L a_{kn} s_n = h_k, k = 2, 3, \dots, L$			0	$\frac{2}{n-1}$	$\frac{2}{n-1} + t_n$
b_n	s_n	$\frac{Q_n^L - s_n}{c_n + d c_n}$	$Q_n^L + s_n$	Q_n	$Q_n^L + s_n$	

As given in table 4.5, the choice of the parameters in the KTH approach influences s_n modification parameters, unlike in deterministic approaches where the s_n coefficients have to be *a priori* defined. More detailed info about determination of modification parameters may be found in Ågren (2004) and Ellmann (2004).

4.6.5 Additive Corrections

Computation of approximate geoid undulation \tilde{N} represents a first term in the basic equation (eq. 4.19) of the KTH approach. Apart from this term, final gravimetric geoid model is obtained only after topographic, downward continuation, atmospheric, ellipsoidal effects are accounted for.

4.6.5.1 Topographic correction

Combined topographic correction account for the effect of topographic masses between Earth's topography surface and geoid which have to be removed to satisfy the 'mass-free' condition of the Stokes integral. It consists from direct and indirect effect which are computed through (Sjöberg 1977, Sjöberg 2007):

$$\delta N_{\text{top}}^{\text{comb}} = \delta N_{\text{top}}^{\text{dir}} + \delta N_{\text{top}}^{\text{ind}} = -\frac{2\pi G\rho}{\gamma} \left(H^2 + \frac{2H^3}{3R} \right). \quad (4.40)$$

Equation 4.40 includes also the zero- and the first- degree order effect. The topographic correction has the biggest contribution of all additive corrections in the KTH approach. It can reach up to several meters value in the mountainous areas. Topographic correction is independent of any topographic reduction method (Sjöberg and Hunegnaw 2000).

4.6.5.2 Downward Continuation correction

When topographic masses are filtered in topographic correction (eq. 4.40), effect caused by downward continuation of gravity anomaly to the geoid surface still remains. A downward continuation effect is the sort of a buffer to the topographic effect due to its counteracted influence. DWC effect may be computed for either gravity anomalies as in RCR approach, or for geoid undulations as in KTH approach. Few methods exist for calculation of the Downward Continuation (DWC) effect on gravity anomalies (see, e.g. Martinec (1996) and Hofmann-Wellenhof and Moritz (2005)). The correction for DWC effect on geoid undulation consists from three parts (Sjöberg 2003c, Ågren 2004, sec. 5.4):

$$\delta N_{\text{DWC}} = \delta N_{\text{DWC}}^{(1)} + \delta N_{\text{DWC}}^{L1,Far} + \delta N_{\text{DWC}}^{L2}, \quad (4.41)$$

where

$$\delta N_{\text{DWC}}^{(1)} = H_P \left(\frac{\Delta g}{\gamma} + 3 \frac{N_P^0}{r_P} - \frac{1}{2\gamma} \frac{\partial \Delta g}{\partial r} \Big|_P H_P \right), \quad (4.42)$$

$$\delta N_{\text{DWC}}^{L1,Far} = c \sum_{n=2}^M (s_n^* + Q_n^L) \left[\left(\frac{R}{r_P} \right)^{n+2} - 1 \right] \Delta g_n, \quad (4.43)$$

$$\delta N_{\text{DWC}}^{L2} = \frac{c}{2\pi} \iint_{\sigma_0} S_L(\psi) \left(\frac{\partial \Delta g}{\partial r} \Big|_P \right) (H_P - H_Q) d\sigma_Q, \quad (4.44)$$

where $r_P = R + H_P$, σ_0 spherical cap with radius of integration ψ centered in P , and $\frac{\partial \Delta g}{\partial r}$ is gravity gradient in point P that can be computed by (Heiskanen and Moritz 1967):

$$\frac{\partial \Delta g}{\partial r} \Big|_P = \frac{R^2}{2\pi} \iint_{\sigma_0} \frac{\Delta g_Q - \Delta g_P}{l_0^3} d\sigma_0 - \frac{2}{R} \Delta g, \quad (4.45)$$

where $l_0 = 2R \sin \frac{\psi_{PQ}}{2}$.

4.6.5.3 Atmospheric Correction

The effect of the atmospheric masses existing outside of the geoid is accounted for by applying atmospheric correction (Sjöberg and Nahavandchi 2000, Sjöberg 2001):

$$\begin{aligned} \delta N_{\text{atm}} = & -\frac{2\pi R \rho_0}{\gamma} \sum_{n=2} M \left(\frac{2}{n-1} - s_n - Q_n^L \right) H_n - \\ & \frac{2\pi R \rho_0}{\gamma} \sum_{n=M+1}^{\infty} \left(\frac{2}{n-1} - \frac{n+2}{2n+1} Q_n^L \right) H_n, \end{aligned} \quad (4.46)$$

where ρ_0 is the density of the atmosphere at the sea level, H_n is the Laplace harmonic of degree n for the topographic height. The elevation H of the arbitrary power v can be computed to any surface point with latitude and longitude as (e.g. Kiamehr 2006a):

$$H^v = \sum_{m=0}^{\infty} \sum_{m=-n}^n H_{nm}^v Y_{nm}, \quad (4.47)$$

where H_v^{nm} are the normalized spherical harmonic coefficients of degree n and order m that can be determined by the spherical harmonic analysis:

$$H_{nm}^v = \frac{1}{4\pi} \iint_{\sigma} H^v Y_{nm} d\sigma. \quad (4.48)$$

4.6.5.4 Ellipsoidal correction

First studies of the ellipsoidal correction occurred in 1962 (see, Molodenskii 1962), followed by the studies of other authors, such as Martinec and Grafarend (1997), Fei and Sideris (2000), and Heck and Seitz (2003). Ellipsoidal correction on geoid undulation is computed as (Sjöberg 2004a):

$$\delta N_{\text{ell}} \approx \psi_0 \left[(0.12 - 0.38 \cos^2 \theta) \Delta g + 0.17 \tilde{N} \sin^2 \theta \right]. \quad (4.49)$$

Simplified equation may also be used (Ellmann and Sjöberg 2004):

$$\delta N_{\text{ell}} \approx \psi_0 \left[(0.0036 - 0.0109 \sin^2 \varphi) \Delta g + 0.0050 \tilde{N} \cos^2 \varphi \right] Q_0^L, \quad (4.50)$$

where Q_0^L is the Molodenskii truncation coefficient.

4.7 Remove-compute-restore approach

Remove-Compute-Restore (RCR) approach has been developed at The National Survey and Cadastre of Denmark (KMS) and the Geophysics Department of the Neils Bohr Institute of University of Copenhagen by professors Carl Christian Tscherning (1942-2014) and René Forsberg. Geoid is obtained in three steps:

Remove long and short wavelength contributions from the gravity data and obtain residual gravity anomaly:

$$\Delta g_{FA-GGM-RTM} = \Delta g_{FA} - \Delta g_{GGM} - \Delta g_{terr. eff.}, \quad (4.51)$$

where Δg_{FA} is the free-air anomaly, Δg_{GGM} is obtained from the spherical harmonic coefficients of the GGM by eq. 4.55 and $\Delta g_{terr. eff.}$ is computed from digital elevation models.

Compute residual geoid height $N_{\Delta g}$ either by Stokes' integral or LSC using residual gravity anomalies obtained in remove step.

Restore long and short wavelength contributions and add them to computed residual geoid heights:

$$N = N_{GGM} + N_{\Delta g} + N_{terr. eff.} (+\delta N_{ind}), \quad (4.52)$$

N_{GGM} is computed using eq. 4.56 from GGM, $N_{\Delta g}$ is residual geoid height obtained in *compute* step, $N_{terr. eff.}$ is restore terrain effect, and δN_{ind} is indirect effect. The magnitudes of N_{GGM} are typically a few dozens of meters, $N_{\Delta g}$ decimeters, and $N_{terr. eff.}$ centimeters (Schwarz et al. 1987, Forsberg 1984). Quasi-geoid with height anomalies ζ are obtained if Molodenskii's integral is used instead of the Stokes integral:

$$\zeta = \zeta_{GGM} + \zeta_{\Delta g} + \zeta_{terr. eff.}. \quad (4.53)$$

In the latter case geoid to quasi-geoid correction $\zeta - N$ has to be applied in order to compute geoid from the computed quasi-geoid (see equation 4.16).

The flowchart of geoid determination by RCR approach is given in appendix A, figure A.2.

4.7.1 'Pure RTM' variation

Different variations of the RCR approach exist, as one can choose between several topographic reduction methods. Input data may be Faye or RTM anomalies, and gridding may be done before or after remove step. In this thesis the *pure RTM* method is used which consists from the following steps (Omang and Forsberg 2000):

1. Start from gravity observations on the Earth's surface Δg_{FA} .
2. Compute long-wavelength contribution to the gravity Δg_{GGM} .
3. Compute RTM terrain effect on gravity $\Delta g_{terr. eff.} = \Delta g_{RTM}$.
4. Obtain residual gravity anomalies $\Delta g = \Delta g_{FA-GGM-RTM} = \Delta g_{FA} - \Delta g_{GGM} - \Delta g_{RTM}$.
5. Interpolate (grid) residual gravity anomalies $\Delta g_{FA-GGM-RTM}$.
6. Compute residual quasi-geoid; height anomalies $\zeta_{\Delta g}$.
7. Compute restore height anomaly contributions ζ_{GGM} and ζ_{RTM} .
8. Obtain gravimetric quasi-geoid by summing up all contributions $\zeta = \zeta_{GGM} + \zeta_{\Delta g} + \zeta_{RTM}$.
9. Obtain gravimetric geoid $N = \zeta + \text{quasi-geoid to geoid correction}$.

More details about possible variations in geoid computation by RCR approach may be found in (Sansó and Sideris, 2013, section 8.4.5).

4.7.2 Global geopotential models

Global geopotential models (GGM) represent the solution of the boundary value problem for the global approach. In regional gravity field modelling, GGMs are used for computation of global, long-wavelength, contributions of different functionals of the disturbing potential T using (e.g. Barthelmes 2009, Bucha and Janák 2013, Barthelmes 2014):

$$T(\varphi, \lambda, r) = \frac{GM}{r} \sum_{n=n_{min}}^{n_{max}} \left(\frac{R}{r}\right)^n \sum_{m=0}^n (\bar{C}_{nm} \cos m\lambda + \bar{S}_{nm} \sin m\lambda) \bar{P}_{nm}(\sin \varphi), \quad (4.54)$$

where: \bar{C}_{nm} and \bar{S}_{nm} are fully normalized geopotential coefficients of the anomalous potential, P_{nm} are fully normalized Legendre functions, n_{max} is the maximum degree of expansion, $r = R + H$, and R is the mean radius of the Earth.

Gravity anomalies are computed using the equation:

$$\Delta g_{GGM}(\varphi, \lambda, r) = \frac{GM}{r^2} \sum_{n=n_{min}}^{n_{max}} \left(\frac{R}{r}\right)^n (n-1) \sum_{m=0}^n (\bar{C}_{nm} \cos m\lambda + \bar{S}_{nm} \sin m\lambda) \bar{P}_{nm}(\sin \varphi). \quad (4.55)$$

Geoid undulation is obtained by:

$$N_{GGM}(\varphi, \lambda) = \frac{T - 2\pi G\rho H^2}{\gamma}, \quad (4.56)$$

and:

$$H(\varphi, \lambda) = \sum_{n=0}^{n_{max}} \sum_{m=0}^n (\overline{HC}_{nm} \cos m\lambda + \overline{HS}_{nm} \sin m\lambda) \bar{P}_{nm}(\sin \varphi), \quad (4.57)$$

where \overline{HC}_{nm} and \overline{HS}_{nm} are the coefficients of the expansion of topography taken from the SH DTM, such as DTM2006.0 (see, Pavlis et al. 2007 and GFZ 2017b).

In a similar manner height anomaly is obtained as:

$$\zeta_{GGM} = \frac{T - \Delta g_{GGM} h}{\gamma}, \quad (4.58)$$

Additional measures may also be computed from spherical harmonic coefficients and their error estimates, such as degree variances or commission errors. They provide additional information about stochastic behavior of GGMs for all wavelengths. This is important in many cases, e.g when GGM and n_{max} has to be selected in gravimetric geoid determination, or in definition of the stochastic model between terrestrial gravity data and GGM.

Fundamental statistical measures of GGMs are signal degree variances or power spectrum, and error degree variances or error of the power spectrum. The signal degree variances denote the amount of the signal, while the error degree variances denote the error of the GGM up to a specific degree (Rapp 1982, Tsoulis and Patlakis 2013, eq. 19):

$$c_n = \sigma_n^2 = \sum_{m=0}^n (\bar{C}_{nm}^2 + \bar{S}_{nm}^2), \quad (4.59)$$

are dimensionless and describe total signal power of a degree n . Estimation of the accuracy of the SH coefficients is obtained as:

$$\varepsilon_{\sigma_n}^2 = \sum_{m=0}^n (\sigma_{C_{nm}}^2 + \sigma_{S_{nm}}^2), \quad (4.60)$$

$\sigma_{C_{nm}}^2$ and $\sigma_{S_{nm}}^2$ being standard deviations of the SH coefficients.

Usually degree variance and error degree variance are calculated for particular functional, then (e.g. Vergos et al. 2006):

$$c_n = \sigma_n^2 = \alpha \sum_{m=0}^n (\bar{C}_{nm}^{*2} + \bar{S}_{nm}^{*2}), \quad (4.61)$$

$$dc_n = \varepsilon_{\sigma_n}^2 = \alpha \sum_{m=0}^n (\varepsilon_{C_{nm}}^{*2} + \varepsilon_{S_{nm}}^{*2}), \quad (4.62)$$

where auxiliary parameter α depends on the computed functional:

- disturbing potential

$$\alpha = \left(\frac{GM}{a} \right)^2 \left(\frac{a^2}{R^2} \right)^{n+1}, \quad (4.63)$$

- gravity anomaly

$$\alpha = \left(\frac{GM}{a} \right)^2 \left(\frac{a^2}{R^2} \right)^{n+1} (n-1)^2, \quad (4.64)$$

- geoid undulation

$$\alpha = \left(\frac{GM}{a\gamma} \right)^2 \left(\frac{a^2}{R^2} \right)^{n+1}. \quad (4.65)$$

When the spectrum of the gravity field functionals has to be known beyond the maximal SH harmonic degree n_{max} of the used GGM, degree and error-degree variances can be extended synthetically using existing global analytic covariance models, such as Kaula (Kaula 1966), Rapp (Rapp 1972), Tscherning-Rapp (Tscherning and Rapp 1974), or Jekeli and Moritz (Jekeli 1978). Degree variances for several models are given in table 4.6. Example of the degree variances for different gravity field functionals is given on figure 4.11. For specific study areas, such global covariance models may provide rather questionable results for high-degrees n . The solution is in fitting of the analytic covariance models to the available data (see, e.g. Ellmann 2005a).

According to the simplest Kaula's model, degree variance of degree n and order m is (Rapp 1973, Kaula 2013):

$$\sigma_n = \frac{2n+1}{n^4} 10^{-10} \approx \frac{1}{n^2} 10^{-5}, \quad (4.66)$$

and for gravity anomaly degree variances:

$$\sigma_n^2(\Delta g) = \gamma^2 (n-1)^2 (2n+1) \sigma_{C_{nm}, S_{nm}}^2. \quad (4.67)$$

Table 4.6: Global analytic empirical degree-variance models for gravity anomalies (after Wenzel 1985, p. 147 and Kern 2003)

Reference	$c_n(\Delta g)$ [mGal ²]
Kaula (1966)	$(9.7983 \cdot 10^5)^2 (n-1)^2 \frac{1.6 \cdot 10^{-10}}{n^3}$
Rapp (1972)	$\frac{251.6468(n-1)}{(n-2)(n+12.9287+0.000715n^2)}$
Tscherning and Rapp (1974)	$\frac{425.28(n-1)}{(n-2)(n+24)} 0.999617^{n+2}$
Jekeli (1978)	$\frac{18.3906(n-1)}{n+100} 0.9943667^{n+2} + \frac{658.6132(n-1)}{(n-2)(n+20)} 0.9048949^{n+2}$
Rapp (1979)	$\frac{3.404(n-1)}{n+1} 0.998006^{n+2} + \frac{140.03(n-1)}{(n-2)(n+2)} 0.914232^{n+2}$
Flury (2006)	$\frac{6.8 \cdot 10^7 \cdot 3.09}{n+0.5}$
Rexer and Hirt (2015)	$\frac{1.79 \cdot 10^{-7} \cdot 0.9999995^n}{(n-1)(n-2)(n+4)(n+17)}$

Rapp's model is:

$$\sigma_n^2(\Delta g) = \frac{A}{n+1.5}, \quad (4.68)$$

and Tscherning-Meissl's:

$$\sigma_n^2(\Delta g) = \frac{C(n-1)}{(n-2)(l+D+\epsilon l^2)}, \quad (4.69)$$

with A, B, C, D, ϵ are numerical constants defining the model.

Tscherning and Rapp's degree variance model is most often used for obtaining degree variances for larger n (Tscherning and Rapp 1974):

$$c_n = A \frac{(n-1)}{(n-2)(n+B)} \left(\frac{R_B}{R} \right)^{2n+2}, \quad (4.70)$$

R_B is the radius of the Bjerhammar sphere, A is a constant in units [m/s⁴], B an integer. Parameters A and R_B have to be computed from empirical covariance function using measurement on the area of integration. If a spherical harmonic series expansion is used, B is typically put equal to a small number like 4, while in the original work it was put equal to 24, so that the low-degree degree-variances could be modeled appropriately.

Crucial parameter when computing any GGM-related quantity is maximal spherical harmonic degree of expansion n_{max} . It determines upper limit of summation and is always $n_{max} < \infty$. With increasing n_{max} number of coefficients \bar{C}_{nm} and \bar{S}_{nm} exponentially increases (subfigure *a*, figure 4.12), and is also related to the spatial resolution of the functional at the Earth's surface. In other words, n_{max} of each GGM determines spatial resolution (level of detailedness) of gravity field (subfigure *b*, figure 4.12). Spatial resolution is spherical distance derived by using expression (Barthelmes 2009, p. 20, eq. 114):

$$\psi_{\min}(n_{max}) = 4 \arcsin \left(\frac{1}{n_{max} + 1} \right), \quad (4.71)$$

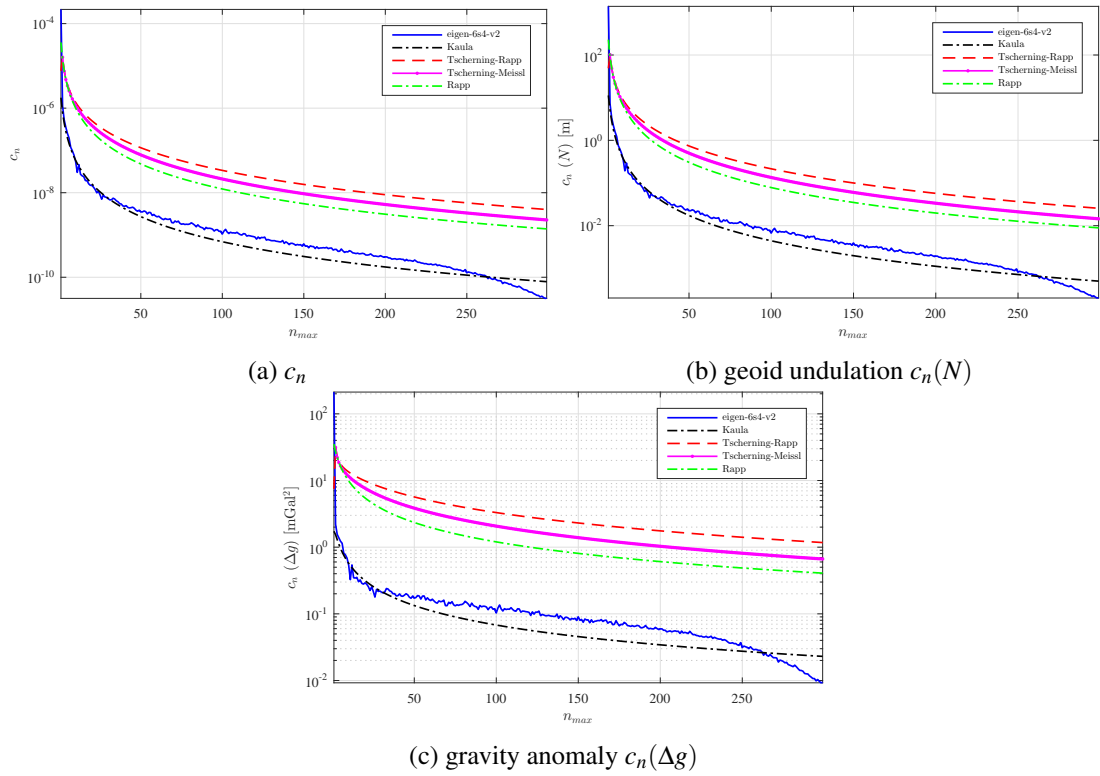


Figure 4.11: Degree variances for EIGEN-6s4 and several analytic covariance models (Kaula, T-R, TM, Rapp)

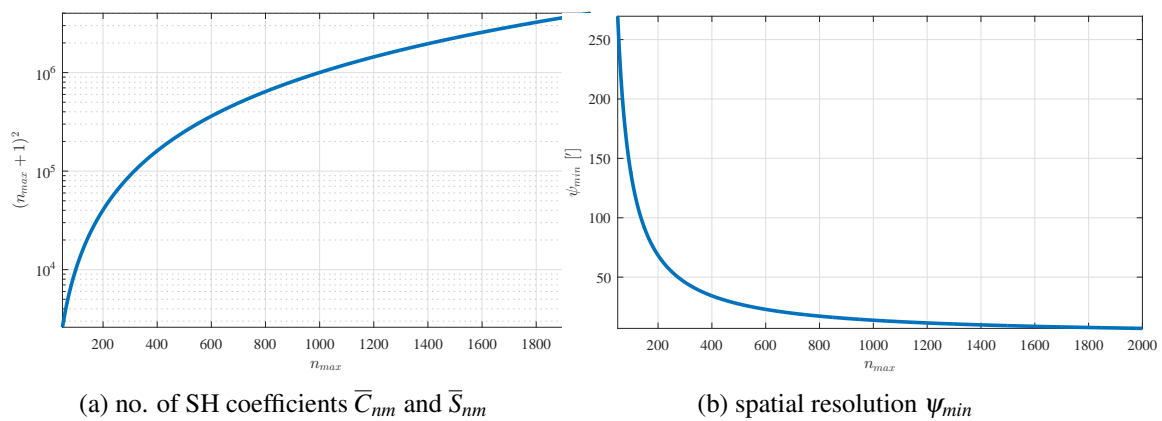


Figure 4.12: Number of SH coefficients and spatial resolution of the GGMs as a function of the maximal SH degree of expansion n_{max}

where $\psi_{min}(n_{max})$ is given in degrees $[\circ]$. E.g. for $n_{max} = 50$ functionals are computed with the spatial resolution of around 4° , while for $n_{max} = 360$ it is $0.5^\circ \approx 60$ km.

4.7.3 Compute

In RCR approach *compute* step follows after *remove* step in which residual gravity field is obtained by subtraction of global and local gravity effects. Input data in the *compute* step are residual gravity field data; usually the data are gravity anomalies. There are mainly two methods for conversion of residual gravity data to residual geoid, and thesea are:

- Least squares collocation,
- Stokes integration.

4.7.4 Least Squares Collocation

In the broadest sense, collocation is a method for prediction of the unknown variables by least-squares adjustment. It has different formulations (Krarup 1969, Moritz 1978, Moritz 1989):

- A mathematical method for solving ordinary and partial differential equations.
- A combination technique of least squares adjustment and prediction. The solution is the minimum mean square error with the used data on the specific area.
- The solution of a geophysical inverse problem.
- Analytic approximation of the Earth's potential with harmonic functions.
- A form of linear regression - estimating output stochastic quantities from other input stochastic quantities by using their statistical correlations.

In geodesy, LSC is most often used for geoid determination, interpolation, and spherical harmonic coefficients determination. The main advantage of LSC is possibility to combine different input data types, and to obtain error predictions for the resulting quantities. Its main limitation is that there has to be solved as many equations as the number of data, which can be problematic if there are larger number of input data. Some methods, such as Fast Spherical

Collocation (FSC), have been proposed to address the problem, but can only be used under some conditions and approximations (see, e.g. [Bottoni and Barzaghi 1993](#), [Sansò and Tscherning 2003](#)).

Mathematical formulation of the the LSC is given in table 4.7. l is a set of observed quantities (e.g. gravity data), x is a vector of predicted quantities (e.g. geoid height at wanted locations). C_{ss} , C_{ls} , C_{ll} are cross- and autocovariance matrices of prediction signals and observations according to selected covariance model.

Table 4.7: Summary of least-squares collocation (after [Moritz 1989](#) and [Kern 2003](#))

Name	Formulas	
Model	l	$= Ax + s + n$
	l	observation vector
	A	design matrix
	x	parameter vector
	s	signal vector
	s'	signals to be predicted
	n	noise vector
	t	$= (s, s')^T$
Covariance functions	C_{ss}	$= \bar{E}(ss^T)$
	C_{nn}	$= \bar{E}(nn^T)$
	C_{ls}	$= C_{sl}^T = \bar{E}(ls^T)$
	C_{ll}	$= \bar{E}(ll^T) = C_{ss} + C_{nn}$
Assumptions	$\bar{E}(s)$	$= \bar{E}(n) = \bar{E}(sn^T) = \bar{E}(tn^T) = \mathbf{0}$
	$\bar{E}(l)$	$= Ax$
Minimum principle	$t^T C_{tt}^{-1} t + n^T C_{nn}^{-1} n = \min$	
Solutions	\hat{x}	$= (A^T C_{ll}^{-1} A)^{-1} A^T C_{ll}^{-1} l$
	\hat{s}	$= C_{ss} C_{ll}^{-1} (l - A\hat{x})$
	\hat{s}'	$= C_{s's} C_{ll}^{-1} (l - A\hat{x})$
	\hat{n}	$= C_{nn} C_{ll}^{-1} (l - A\hat{x})$
Error covariances	$E_{\hat{x}\hat{x}}$	$= (A^T C_{ll}^{-1} A)^{-1}$
	$E_{\hat{s}\hat{s}}$	$= C_{ss} - C_{ss} C_{ll}^{-1} (I - A (A^T C_{ll}^{-1} A)^{-1} A^T C_{ll}^{-1}) C_{ss}$
	$E_{\hat{s}'\hat{s}'}$	$= C_{s's'} - C_{s's} C_{ll}^{-1} (I - A (A^T C_{ll}^{-1} A)^{-1} A^T C_{ll}^{-1}) C_{ss'}$

Input data in geoid determination by LSC should be isotropic (have random behavior in all directions) and non-biased, which means they shall have small standard deviation and mean value. In RCR approach this is achieved in the *remove* step where input data are filtered for GGM and RTM contributions. Residual height anomalies are then obtained from residual data using:

$$\tilde{\zeta}_P = \left\{ C_{P_1}^{Ng}, C_{P_2}^{Ng}, \dots, C_{P_n}^{Ng} \right\} \left(\left[\begin{array}{cccc} C_{11} & C_{12} & \cdot & C_{1n} \\ C_{21} & \cdot & \cdot & \cdot \\ \cdot & \cdot & \cdot & \cdot \\ C_{n1} & \cdot & \cdot & C_{nn} \end{array} \right] + \left[\begin{array}{cccc} v_{11} & v_{12} & \cdot & v_{1n} \\ v_{21} & \cdot & \cdot & \cdot \\ \cdot & \cdot & \cdot & \cdot \\ v_{n1} & \cdot & \cdot & v_{nn} \end{array} \right] \right)^{-1} \cdot \begin{pmatrix} L_1 \\ L_2 \\ \dots \\ L_n \end{pmatrix}, \quad (4.72)$$

where L_1, L_2, L_n can be heterogeneous data if they are functionals of the disturbing potential T (e.g. gravity anomalies, gravity gradients or deflections of the vertical), where variance cross-covariance matrices C^{Ng} , C_{nn} are calculated from equation 4.75.

A basic prerequisite in using LSC is cross-covariance matrix C_{ij}^{Ng} between input and output data, which can be obtained by determination of covariance function using covariance propagation (Moritz 1989, p. 87, Sansó and Sideris 2013, ch. 5, pp. 217).

If some functional of disturbing potential is T then global covariance function is equal to:

$$C(P, Q) = \frac{1}{8\pi^2} \int_0^{2\pi} \int_{-\pi/2}^{\pi/2} \int_0^{2\pi} T(P)T(Q)d\alpha \cos \varphi d\varphi d\lambda, \quad (4.73)$$

where α is azimuth between points each points P and Q .

The global integral from 4.73 may be rewritten in spectral form, i.e. as a Legendre series. The covariance between anomalous potential T in the points $P(\varphi, \lambda)$ and $Q(\varphi', \lambda')$ becomes (Andersen 2013, pp. 423):

$$C(P, Q) = \sum_{n=2}^{\infty} c_n^T P_n(\cos \psi), \quad (4.74)$$

where c_n^{TT} are degree variances and ψ is spherical distance between points P and Q , P_n are the Legendre polynomials. This kernel is homogeneous and isotropic which means it depends only on the distance of the points, not location or azimuth. Mutual relationship between geoid height and gravity anomalies follow from covariance propagation on $C(P, Q)$:

$$\begin{aligned} C_{NN} &= \sum_{n=2}^{\infty} \left(\frac{1}{\gamma} \right)^2 c_n^T P_n(\cos \psi), \\ C_{\Delta g \Delta g} &= \sum_{n=2}^{\infty} \left(\frac{n-1}{r} \right)^2 c_n^T P_n(\cos \psi), \\ C_{N \Delta g} &= \sum_{n=2}^{\infty} \left(\frac{n-1}{\gamma r} \right)^2 c_n^T P_n(\cos \psi). \end{aligned} \quad (4.75)$$

where c_n are signal degree variance computed from SH coefficients of the GGM up to n_{max} and extended with selected analytic empirical degree-variance model (see equations from 4.59 to 4.70).

Determination of the above matrices from equations 4.75 fully determines LS adjustment process. Practically, empirical local covariances are determined from the input data, then fitted to the global covariance model, such as Tscherning-Rapp model. Therefore complete covariance

models is (Tscherning 2013, pp. 323, eq. 7.17):

$$C(\psi, r, r') = \alpha \sum_{n=2}^N (\sigma_n^{err})^2 \left(\frac{\bar{R}^2}{rr'} \right)^{n+1} P_n(\cos \psi) + \sum_{n=N+1}^{\infty} \frac{A}{(n-1)(n-2)(n+4)} \left(\frac{R_B^2}{rr'} \right)^{n+1} P_n(\cos \psi). \quad (4.76)$$

Parameters α , A and R_B are obtained from fitting of the empirically determined covariance function.

4.7.4.1 Planar logarithmic covariance model

The planar logarithmic covariance model is the approximation of the Tscherning-Rapp spherical covariance model (Tscherning and Rapp 1974) which was firstly described and used by prof. R. Forsberg (Forsberg 1987). It closely approximates Kaula's rule, and describes spatial correlation between all disturbing (anomalous) potential functionals. Covariance function is defined by three parameters: empirical variance of data C_0 , and high and low frequency attenuation factors D and T . Parameter C_0 is used for description of the gravity field variability. Parameter D corresponds to double (twice) value of Bjerhammar depth in harmonic downward continuation. Parameter T is used for obtaining finite values for gravity and geoid variances while modelling the singularity of the planar logarithmic model. Attenuation of long-wavelengths in the covariance model is generally needed as GGM is used in RCR approach. All parameters characterize the correlation and power of gravity anomalies in a study area.

Covariance between gravity anomalies at heights H_1 and H_2 is (Forsberg 1987):

$$C(\Delta g^{H_1}, \Delta g^{H_2}) = -f \sum_{k=0}^3 \alpha_k \ln \left[D_k + \left[s^2 + (D_k + H_1 + H_2)^2 \right]^{\frac{1}{2}} \right], \quad (4.77)$$

where α_k is a weight factor with values $\alpha_0 = 1$, $\alpha_1 = -3$, $\alpha_2 = 3$, and $\alpha_3 = -1$, s is the horizontal distance between points, D_k is:

$$D_k = D + kT, \quad (4.78)$$

scale factor f from equation 4.77 is:

$$f = \frac{C_0}{\frac{\ln D_1^3 D_3}{D_0 D_2^3}}. \quad (4.79)$$

Closed expressions for covariances between gravity anomalies and geoid undulations are:

$$C(N^{H_1}, \Delta g^{H_2}) = -0.00102f \sum_{k=0}^3 \alpha_k [r - z \ln(z + r)], \quad (4.80)$$

for $z = (D_k + H_1 + H_2)$, $r = (s^2 + z^2)^{\frac{1}{2}}$.

4.7.5 Stokes integration

The main method for calculation of geoid undulations in RCR approach is Stokes integration. Stokes' integral, the central equation of physical geodesy, is a result of combination of Pizzetti's (eq. 4.3) and Bruns' equation (eq. 2.17) (Heiskanen and Moritz 1967, p. 94, Hofmann-Wellenhof and Moritz 2005, p. 104, eq. 2-307):

$$N = \frac{R}{4\pi\gamma} \iint S(\psi)\Delta g d\sigma, \quad (4.81)$$

where Δg are gravity anomalies on the geoid surface, $S(\psi)$ is a Stokes' kernel, γ is Earth's mean gravity, R is Earth's mean radius. Stokes' integral (equation 4.81) can be rewritten in spherical (ψ, α) or geodetic coordinates (θ or φ, λ):

$$\begin{aligned} \text{geodetic: } N &= \frac{R}{4\pi\gamma} \int_{\lambda=0}^{2\pi} \int_{\theta=0}^{\pi} S(\psi_{PQ})\Delta g_Q \sin \theta d\theta d\lambda, \\ \text{spherical: } N &= \frac{R}{4\pi\gamma} \int_{\alpha=0}^{2\pi} \int_{\psi=0}^{\pi} S(\psi_{PQ})\Delta g_Q \sin \psi d\psi d\alpha, \end{aligned}$$

where P is computation point, Q is integration point on the unit sphere σ . In practical computations, gravity anomalies Δg are integrated within a limited area or spherical cap (figure 4.14). The area of integration is often a rectangular area around the country. Figure 4.13 demonstrates the principle of integration.

In Stokes' integration, geoid heights are obtained by:

- reduction of all input data (gravimetric measurements) on the geoid as boundary surface,
- calculation of the spherical distance ψ_{PQ} between computational point P and surrounding points Q_i within the chosen spherical cap ψ_0 ,
- multiplication of the Δg_Q with the Stokes function, and
- integrate over the spherical cap.

4.7.5.1 Original 'analytic' Stokes kernel

In the Stokes integration each gravity anomaly Δg from the grid within the integration radius is multiplied with the Stokes' function $S(\psi)$. Stokes' integral can be computed spectrally (using Legendre polynomial series) or analytically (using closed expressions) according to (Heiskanen and Moritz 1967):

$$\text{spectral: } S(\psi) = \sum_{n=2}^{\infty} \frac{2n+1}{n-1} P_n \cos \psi, \quad (4.82)$$

$$\text{closed: } S(\psi) = \frac{1}{s} - 6s + 1 - 5 \cos \psi - 3 \cos \psi \ln(s + s^2), s = \sin \frac{1}{2} \psi, \quad (4.83)$$

where n is degree of expansion, $s = \sin \frac{\psi}{2}$, P_n are Legendre polynomials. Legendre polynomials for different values of n are shown in figure 4.15. The ψ is the central angle between computation

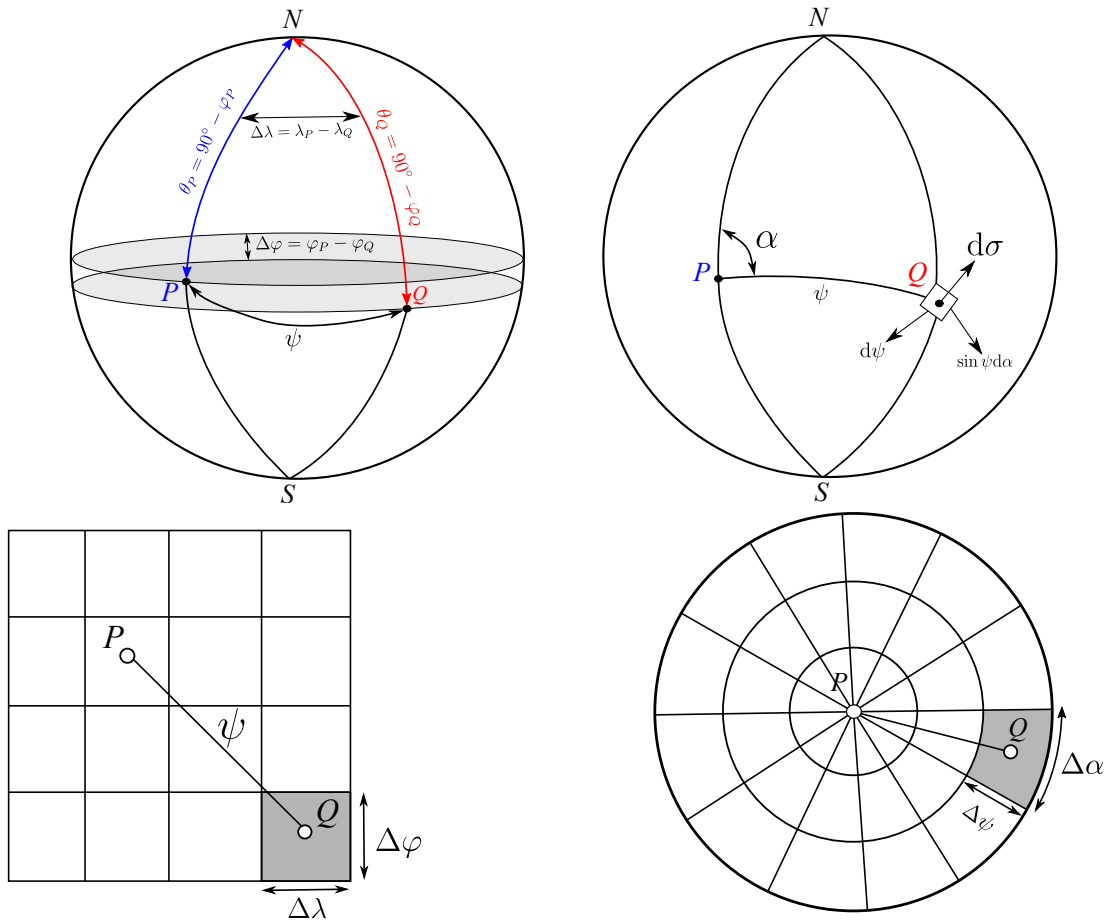


Figure 4.13: Stokes integration using: a) geographic θ , λ (left) and b) spherical ψ , α (right) coordinates (after Kuhn 2000).

point P and integration point Q :

$$\cos \psi = \cos \theta_P \cos \theta_Q + \sin \theta_P \sin \theta_Q \cos \Delta \lambda_{PQ}. \quad (4.84)$$

Stokes kernel may also be written in planar form (Heiskanen and Moritz 1967):

$$S(\psi) \approx \frac{1}{\sin \frac{\psi}{2}} \approx \frac{2}{\psi} \approx \frac{2R}{l} \quad (4.85)$$

where x and y are planar coordinates in local reference system, $l(x, y) = \sqrt{(x - x_P)^2 + (y - y_P)^2}$.

4.7.5.2 Kernel modifications

By its definition Stokes integral should be computed by continuous integration of gravity anomalies over the whole sphere. Gravity anomalies are not available for integration over the whole

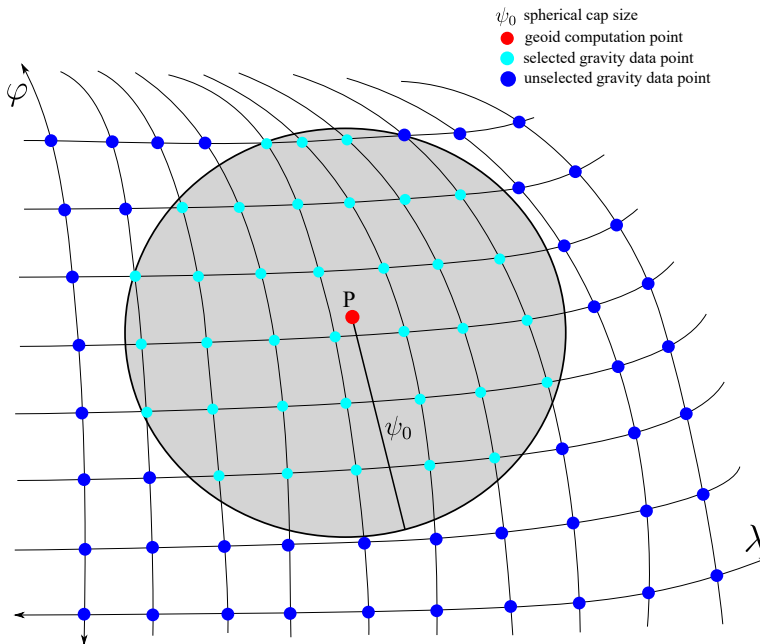


Figure 4.14: Stokes' integration of point gravity data within spherical cap size ψ_0 around computation point P .

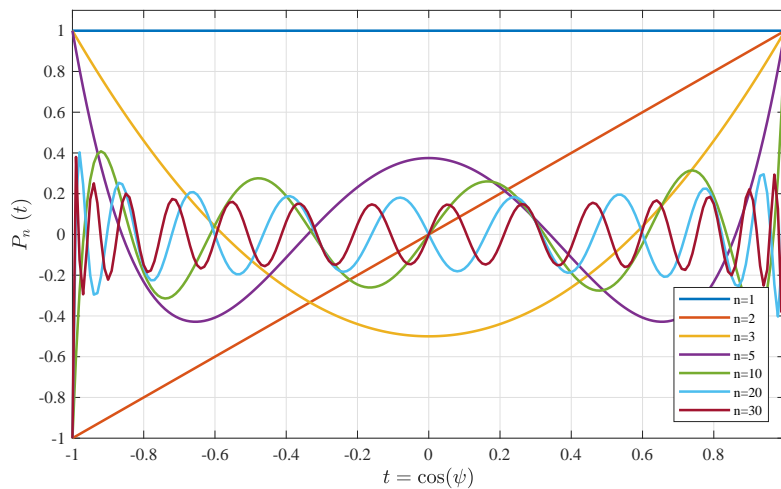


Figure 4.15: Legendre polynomials for $n = 1, 2, 3, 5, 10, 20, 30$ as an argument of $t = \cos(\psi)$.

sphere, especially in regional gravity field modelling. Therefore, the integration cannot be performed over the entire sphere (σ), but only inside the limited area defined by spherical cap (σ_0). Information is lost in the remote zone where data are not integrated ($\sigma - \sigma_0$), inducing long-wavelength truncation errors, as 'local' gravity data are known to have errors in long-wavelengths. Therefore, long-wavelength errors from gravity measurements propagate into resulting geoid undulations. Molodenskii showed that the truncation error of the remote zone can

be reduced by using modified Stokes' kernel (function), which combines the terrestrial gravity measurements and the long wavelength contribution in the form of low-degree coefficients (up to degree L) from satellite-derived GGMs (Molodenskii 1958, Molodenskii 1962). Apart from this, Stokes' kernel modifications modify decay rate of the far-zone contribution, filter the kernel function, and smooth the error kernel so outside of the integration cap σ_0 , gravity anomaly Δg is small and rapidly diminishes (Vaníček and Featherstone 1998, Kern 2003).

Modified Stokes' kernels S^L have general form (e.g. Heck and Grüninger 1987, Ellmann 2005a):

$$S^L(\psi) = \sum_{n=2}^{\infty} \frac{2n+1}{n-1} P_n(\cos \psi) - \sum_{n=2}^L \frac{2n+1}{2} s_n P_n(\cos \psi), \quad (4.86)$$

where first term is unmodified Stokes function $S(\psi)$ (as in eq. 4.82, figure 4.16), L is a modification limit, Legendre polynomials $P_n(\cos \psi)$. The modification coefficients $s_n, n = 2, \dots, L$ and modification degree limit L are chosen by various criteria. The main idea is to modify low-degree Legendre polynomials ($2 \leq n \leq L$) so $\|S^L(\psi)\| < \|S(\psi)\|$. In that way Stokes' kernel tappers off faster for increasing values of radiuses of integration σ_0 compared to unmodified Stokes' function (figure 4.16), so contribution of distant gravity anomalies is smaller.

Various modifications of the Stokes' integral have been proposed in many references, including: Molodenskii (1962), Wong and Gore (1969), Meissl (1971), Vincent and Marsh (1974), Wenzel (1981), Wenzel (1982), Vaníček and Kleusberg (1987), Heck and Grüninger (1987), Vaníček and Sjöberg (1991), Sjöberg (1991), Featherstone et al. (1998), Sjöberg and Hunegnaw (2000), Sjöberg (2003b), Ellmann (2004), Ågren (2004), Sjöberg and Joud (2017). Modifications can be divided in few groups: deterministic, stochastic, combined and band-limited. Deterministic modifications change Stokes function by removing the low degree terms (i.e. the long-wavelength part) of Stokes' kernel and high-pass filtering of gravity anomalies (e.g. Wong and Gore 1969, Kiamehr 2006a). Their's disadvantage is that errors of GGM and terrestrial data are not accounted for (Ellmann 2005b). The problem is partially solved in stochastic modifications where predictions of errors of GGMs and terrestrial data are used to minimize GMSE. More details may be found in cited references, here only main equations are given for kernel modifications, which are latter used in Part II of the thesis.

Wong and Gore (1969) removed low degree Legendre polynomials from the unmodified Stokes' function:

$$S^{WG}(\psi) = S(\psi) - \sum_{n=2}^L \frac{2n+1}{n-1} P_n \cos(\psi), \quad (4.87)$$

where n is the modification degree which has to be smaller than maximal degree of expansion n_{max} of the GGM ($2 \leq n \leq n_{max}$). When $n = n_{max}$, the kernel is called spheroidal Stokes kernel. The size of the evaluation area σ_0 is chosen to be compatible with n_{max} .

Meissl (1971) modified kernel by subtraction of the value of the Stokes' kernel at the truncation radius $S(\psi_0)$ from the unmodified kernel $S(\psi)$:

$$S^M(\psi) = \begin{cases} S(\cos \psi) - S(\cos \psi_0), & 0 \leq \psi \leq \psi_0, \\ 0, & \psi_0 < \psi \leq \pi, \end{cases} \quad (4.88)$$

so that truncation error series diminishes to zero when values n are increased.

Heck and Grüniger (1987) modified Meissl's kernel by combining Wong-Gore's and Meissl's modifications. The spheroidal kernel at the truncation radius is subtracted from the spheroidal Stokes kernel inside the truncation radius:

$$S^{HG}(\psi) = \begin{cases} S^{WG}(\cos \psi) - S^{WG}(\cos \psi_0), & 0 \leq \psi \leq \psi_0, \\ 0, & \psi_0 < \psi \leq \pi. \end{cases} \quad (4.89)$$

Vaniček and Kleusberg (1987) modification is:

$$S^{VK}(\psi) = \begin{cases} S^{WG}(\cos \psi) - \sum_{n=2}^L \frac{2n+1}{2} t_n(\psi) P_n(\cos \psi), & 0 \leq \psi \leq \psi_0, \\ 0, & \psi_0 < \psi \leq \pi, \end{cases} \quad (4.90)$$

where t_n are the modification coefficients. In order to minimize the upper bound of the truncation error in a least squares sense a series of modifying coefficients are subtracted from the Molodenskii's spheroidal integration kernel (eq. 4.87).

Featherstone et al. (1998) combined Meissl's and Vaniček-Kleusberg's solutions to obtain:

$$S^{FEO}(\psi) = \begin{cases} S^{VK}(\cos \psi) - S^{VK}(\cos \psi_0), & 0 \leq \psi \leq \psi_0, \\ 0, & \psi_0 < \psi \leq \pi. \end{cases} \quad (4.91)$$

In such way the upper bound is modified to decrease the truncation error while the function shall converge faster to zero. Comparison of the properties of the deterministic modifications of Stokes' kernel are given in table 4.8.

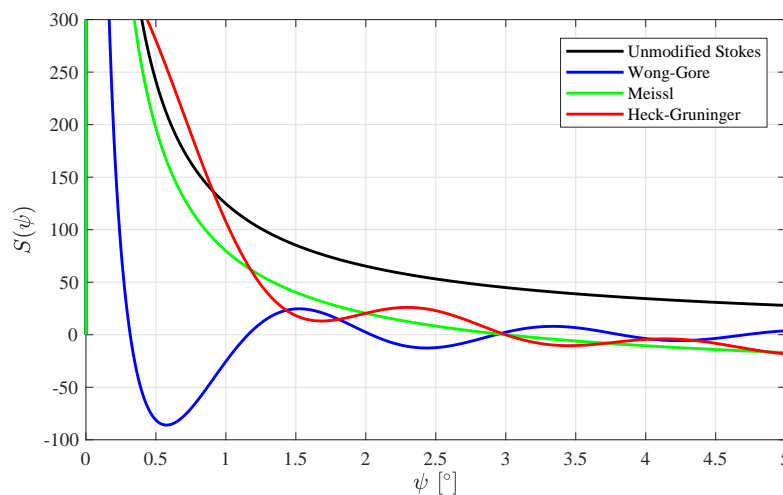


Figure 4.16: Stokes' kernel $S(\psi)$ modifications as a function of the spherical distance ψ .

Table 4.8: Comparison of deterministic modifications of the Stokes' integral according to Kern (2003) (small ○; medium ◐; large ●)

Name	Computation time	Implementation complexity	Far-zone contribution	Inclusion of inconsistencies
Heiskanen and Moritz (1967)	○	○	◐	●
Molodenskii (1962)	●	●	○	●
Wong and Gore (1969)	○	◐	○	○
Meissl (1971)	○	○	○	●
Heck and Grüniger (1987)	○	◐	◐	○
Vaniček and Kleusberg (1987)	●	●	○	○
Featherstone et al. (1998)	●	●	○	○

4.7.6 Spectral methods

Analytic Stokes integration is time-consuming and inefficient for large number of data and computation points, as is the case when geoid is computed for the continental areas or larger countries. This problem can be addressed with FFT methods, which have been used in physical geodesy since the beginning of the 1990s for computation of the regional and continental geoid models (see, e.g. Forsberg 1991, Forsberg 1985). Some examples of geoid models computed using FFT methods are European Gravimetric Quasigeoid (EGG) (Denker and Torge 1998) in Europe, Germany (Liebsch et al. 2006), USA (Wang et al. 2012), Canada (Huang and Véronneau 2013). The main advantage of using FFT is their's speed and efficiency, whereas drawbacks are the requirement to interpolate (grid) point data, unpredictable periodicity effects, and flat-earth approximation (Forsberg and Sideris 1993).

Several spectral methods for the Stokes' integral evaluation have been developed in the last few decades including:

- planar FFT,
- spherical FFT,
- spherical multi-band FFT,
- spherical 1D FFT.

4.7.6.1 Planar FFT

Stokes integral (equation 4.81) in planar approximation may be rewritten into the two-dimensional convolution integral for computation of geoid height N_P (Kearsley et al. 1985, Schwarz et al. 1990, Sideris 2013):

$$N_P(x_p, y_p) = \frac{1}{2\pi\gamma} \iint_{\sigma} \frac{\Delta g(x, y)}{\sqrt{(x_p - x)^2 + (y_p - y)^2}} dx dy = \frac{1}{\gamma} \Delta g(x_p, y_p) * l_N(x_p, y_p), \quad (4.92)$$

where symbol $*$ stands for convolution operation, l_N is the planar distance of the Stokes' kernel function:

$$l_N(x, y) = (2\pi)^{-1} (x^2 + y^2)^{-\frac{1}{2}}, \quad (4.93)$$

γ is mean gravity on computation area, σ is the area of integration.

In the spectral domain, convolution integral from eq. 4.92 is computed using two direct and one inverse Fourier transform with spectral functions $\Delta G(u, v)$ and $L_N(u, v)$ according to (Schwarz et al. 1987, Haagmans et al. 1993):

$$N_{\Delta g}(x, y) = \frac{1}{2\pi\gamma} \{\mathbf{F}\{\Delta g(x, y)\}\mathbf{F}\{L_N(x, y)\}\} = \frac{1}{2\pi\gamma} \mathbf{F}^{-1} \{\Delta G(u, v)L_N(u, v)\}, \quad (4.94)$$

where F is inverse direct or continuous Fourier transform, u and v are frequencies of the x and y and $L_N(u, v)$ is $\frac{1}{\sqrt{u^2+v^2}}$. ΔG and L_N are computed using discrete Fourier transform (DFT) and continuous Fourier transform (CFT).

4.7.6.2 Spherical FFT

Planar approximation may create unwanted errors for computation areas larger than few hundred kilometers, which can be avoided if spherical Stokes integral is implemented (Sideris 2013):

$$N(\varphi_P, \lambda_P) = \frac{R}{4\pi\gamma} \iint_{\sigma} \Delta g(\varphi, \lambda) S(\varphi_P, \lambda_P, \varphi, \lambda) \cos \varphi d\varphi d\lambda, \quad (4.95)$$

or in another form using gridded gravity anomalies:

$$N(\varphi_l, \lambda_k) = \frac{R}{4\pi\gamma} \sum_{j=0}^{N-1} \sum_{i=0}^{M-1} \Delta g(\varphi_j, \lambda_i) \cos \varphi_j S(\varphi_l, \lambda_k, \varphi_j, \lambda_i) \Delta\varphi\Delta\lambda. \quad (4.96)$$

Convolution form of the above equation is (Van Hees 1991):

$$\begin{aligned} N(\varphi_l, \lambda_k) &= \frac{R}{4\pi\gamma} \sum_{j=0}^{N-1} \sum_{i=0}^{M-1} \Delta g(\varphi_j, \lambda_i) \cos \varphi_j S(\varphi_l - \varphi_j, \lambda_k - \lambda_i, \bar{\varphi}) \Delta\varphi\Delta\lambda = \\ &= \frac{R}{4\pi\gamma} [\Delta g(\varphi_l, \lambda_k) \cos \varphi_l] * S(\varphi_l, \lambda_k, \bar{\varphi}), \end{aligned} \quad (4.97)$$

which can be computed using one or two dimensional DFT (Sideris 2013):

$$N(\varphi_l, \lambda_k) = \frac{R}{4\pi\gamma} \mathbf{F}^{-1} \{\mathbf{F}\{\Delta g(\varphi_l, \lambda_k) \cos \varphi_l\} \mathbf{F}\{S(\varphi_l, \lambda_k, \bar{\varphi})\}\}. \quad (4.98)$$

4.7.6.3 Spherical multi-band FFT

Errors in spherical kernel increase when moving from the centre towards the north and south edges of the computation area. Forsberg and Sideris (1993) proposed to split computation area in several zones by adopting mean reference latitudes $\bar{\varphi}_i$. The principle is shown in figure 4.17. Reference latitudes divide computation area in several areas along parallels. Geoid undulations are computed for ν number of reference latitudes $\bar{\varphi}_i$ while unified solution is obtained by interpolation between neighboring latitudes $\bar{\varphi}_i$ and $\bar{\varphi}_{i+1}$ (Sideris 2013):

$$N(\varphi) = \frac{\varphi - \varphi_{i+1}}{\bar{\varphi}_i - \bar{\varphi}_{i+1}} N_i + \frac{\bar{\varphi}_i - \varphi}{\bar{\varphi}_i - \bar{\varphi}_{i+1}} N_{i+1}. \quad (4.99)$$

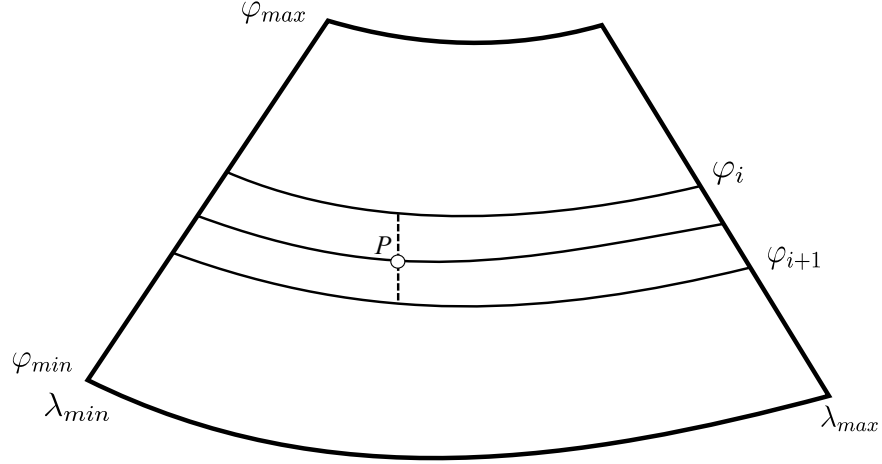


Figure 4.17: Reference latitude bands for spherical multi-band kernel (after Forsberg and Sideris 1993)

4.7.6.4 Spherical 1D FFT

Inconvenience of the above 2D FFT solutions was solved by Haagmans et al. 1993 using the spherical 1D FFT (SP1D) method. Geoid is computed for all the computation points along each latitude without planar approximation. Therefore the results of analytical numerical integration and 1D FFT shall be the same. Advantage is also that the zero padding has to be applied only to the parallels, which allows speeding up computations. Geoid undulation using this method is obtained:

$$N(\varphi_l, \lambda_k) = \frac{R}{4\pi\gamma} \mathbf{F}_1^{-1} \left\{ \sum_{j=0}^{N-1} \mathbf{F}_1 \{ \Delta g(\varphi_j, \lambda_k) \cos \varphi_j \} \mathbf{F}_1 \{ S(\varphi_l, \varphi_j, \lambda_k) \} \right\}, \quad (4.100)$$

for $\varphi_l = \varphi_1, \varphi_2, \dots, \varphi_N$, where \mathbf{F}_1 and \mathbf{F}_1^{-1} are 1D Fourier transform operator and its reverse.

4.7.7 Restore

Restore step follows after residual geoid $N_{\Delta g}$ or quasi-geoid $\zeta_{\Delta g}$ is obtained in the compute step. GGM and RTM contributions on the height anomalies ζ_{GGM} and ζ_{RTM} are computed using the same input parameters that were used in remove step for computation of Δg_{GGM} and Δg_{RTM} contributions on gravity anomalies. ζ_{GGM} and ζ_{RTM} are added to the computed residual geoid undulation $N_{\Delta g}$.

The RTM terrain effect on the quasi-geoid is computed by using equation:

$$\zeta_{\text{terr. eff.}} = \zeta_{RTM} = \frac{G\rho}{\gamma} \iint_{h_{ref}} \int^h \frac{1}{r} dx dy dz, \quad (4.101)$$

where $r = \left[(x_p - x)^2 + (y_p - y)^2 + (H_p - z)^2 \right]^{\frac{1}{2}}$, which can be obtained by numerical integration (Forsberg 1984) or FFT (Forsberg 1985).

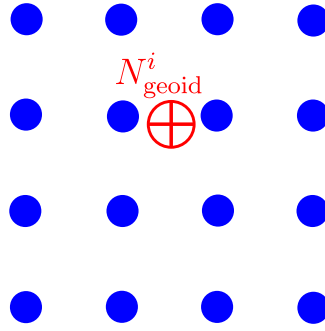


Figure 4.18: Interpolation of N_{geoid}^i from the geoid model for each GNSS/levelling point.

4.8 Accuracy validation and fitting of geoid models

Accuracy validation is a final stage of gravimetric geoid model development. Usually a number of different models will be computed and only one has to be selected as *the geoid*. The selected model shall be the one which is the most accurate and has the best agreement with the control data. Reference data for validation of geoid models are GNSS/levelling points as they are obtained using independent measurement methods. GNSS/levelling point is the point with the known geoid undulation N computed as the difference between ellipsoidal h and orthometric height H : $N = h - H$. Although, GNSS/levelling points are not error-free data, they are supposed to have at least one magnitude higher accuracy than computed and validated geoid model, and are taken as reference or *true*. Such presumption can be problematic if quality of either levelling or GNSS measurements is unknown.

The main quantity used in validation are geoid undulation differences, also called residuals, derived by subtraction of the geoid undulations from *reference* GNSS/levelling points and those *interpolated* from the validated geoid model:

$$\delta N_{\text{GNSS/lev.-geoid}}^i = N_{\text{GNSS/lev.}}^i - N_{\text{geoid}}^i, \quad (4.102)$$

where i is the index of control GNSS/levelling point. After this, statistical measures, such as mean and standard deviation, are computed for all the geoid undulation difference $\delta N_{\text{GNSS/lev.-geoid}}^i$. Mean values provide information about the offset (shift) between geoid based on MSL- GNSS/levelling and validated gravimetric geoid model, whereas standard deviation indicates accuracy.

Different errors are coherent in residuals computed by equation 4.102. Some of the main error sources are: a) random and systematic errors in derived heights h , H , and N , b) datum inconsistencies, c) theoretical and empirical approximations made in processing observed data, d) movement of the vertical reference frame due to geodynamical, and e) other effects (Fotopoulos 2005). Modelling of these errors is performed by fitting differences to parametric models in a least squares adjustment (Kotsakis and Sideris 1999, Kiamehr and Sjoberg 2005, Fotopoulos 2013). Initial no-fit parametric model is based on equation:

$$\delta N_{\text{GNSS/lev.-geoid}}^i = N_{\text{GNSS/lev.}}^i - N_{\text{geoid}}^i = \mathbf{A}_i^T \mathbf{x} + \mathbf{v}_i, \quad (4.103)$$

where i is the index of GNSS/levelling points, \mathbf{x} is the $n \times 1$ vector of unknown adjusting parameters, \mathbf{A} is the $n \times 1$ vector of known coefficients, and \mathbf{v}_i are residuals as random noise term.

Possible fitting parametric models A_i^T are (Kotsakis and Sideris 1999, Daho et al. 2006):

Polynomial model

$$A_i^T x = \sum_{r=0}^P \sum_{q=0}^{P-r} x_{rq} \Delta \varphi^r \Delta \lambda^q \quad (4.104)$$

where P is the order or degree of the polynomial, x_{rq} the coefficients of the polynomial. $\Delta \varphi$ and $\Delta \lambda$ are scaled coordinates which can be obtained for each point as (Bilker-Koivula 2010):

$$\Delta \varphi = \frac{2\varphi_i - (\varphi_{\max} + \varphi_{\min})}{\varphi_{\max} - \varphi_{\min}} \quad \Delta \lambda = \frac{2\lambda_i - (\lambda_{\max} + \lambda_{\min})}{\lambda_{\max} - \lambda_{\min}} \quad (4.105)$$

or simply (Daho et al. 2006):

$$\Delta \varphi = \varphi_i - \varphi_0 \quad \Delta \lambda = \lambda_i - \lambda_0, \quad (4.106)$$

φ_0, λ_0 being the mean values of the coordinate vectors.

Three-parameteric model

$$A_i^T x = \cos \varphi_i \cos \lambda_i x_1 + \cos \varphi_i \sin \lambda_i x_2 + \sin \varphi_i x_3, \quad (4.107)$$

Four-parameteric model

$$A_i^T x = \cos \varphi_i \cos \lambda_i x_1 + \cos \varphi_i \sin \lambda_i x_2 + \sin \varphi_i x_3 + x_4, \quad (4.108)$$

Five-parameteric model

$$A_i^T x = \cos \varphi_i \cos \lambda_i x_1 + \cos \varphi_i \sin \lambda_i x_2 + \sin \varphi_i x_3 + \sin^2 \varphi_i x_4 + x_5, \quad (4.109)$$

Seven-parameteric model

$$A_i^T x = \cos \varphi_i \cos \lambda_i x_1 + \cos \varphi_i \sin \lambda_i x_2 + \sin \varphi_i x_3 + \frac{\cos \varphi_i \sin \varphi_i \cos \lambda_i}{W_i} x_4 + \frac{\cos \varphi_i \sin \varphi_i \sin \lambda_i}{W_i} x_5 + \frac{\sin^2 \varphi_i}{W_i} x_6 + x_7, \quad (4.110)$$

where φ_i and λ_i are geodetic coordinates of control points, e is the eccentricity of reference ellipsoid and $W_i = \sqrt{1 - e^2 \sin^2 \varphi_i}$. Vector of unknown parameters x is determined in the least squares adjustment of the geoid undulation differences ΔN_i .

Validation procedure

1. define initial GNSS/levelling dataset (latitude, longitude, ellipsoidal height, orthometric height or geoid undulation),
2. split initial GNSS/levelling dataset on two subsets:
 - (a) subset for determination of unknown parameters x ,
 - (b) subset for independent control,

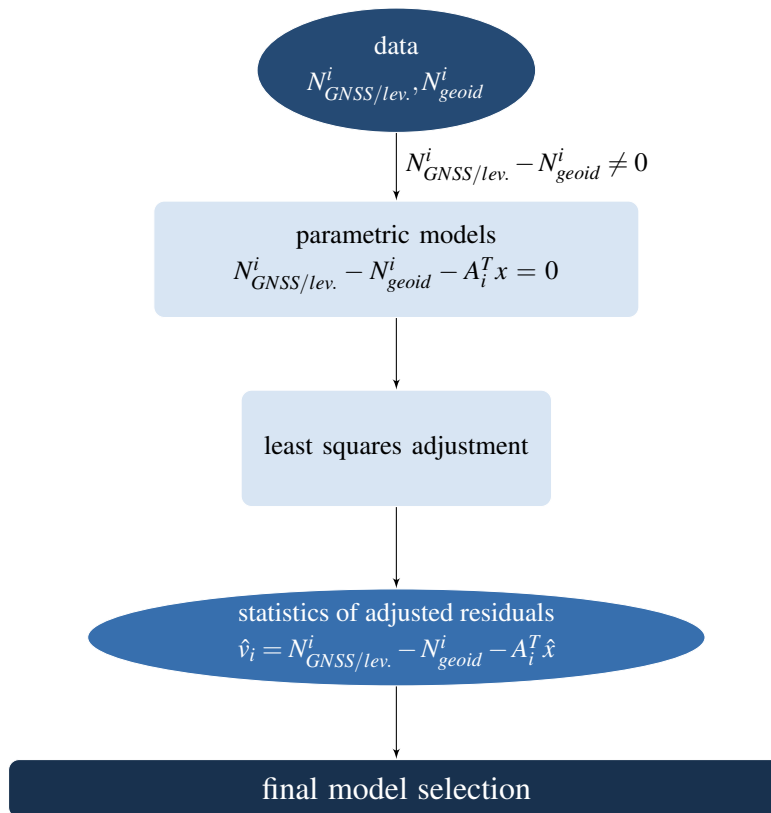


Figure 4.19: Flowchart of geoid model accuracy validation.

3. interpolate geoid undulations from geoid model,
4. perform least squares adjustment of differences with selected parametric model; determine vector of unknowns \boldsymbol{x} ,
5. use points of control dataset and corresponding undulations interpolated from geoid model to fit differences: $v_j = Ax - L_j$, where $L_j = N_{GNSS/levelling} - N_{geoid}$, and j are all control points that have not been included in determination of parameters,
6. statistical measures of the fitted differences indicate external accuracy of gravimetric geoid model,
7. fitting of the gravimetric geoid model and obtaining hybrid geoid model.

Criterion for selection of the most accurate geoid between all computed candidate solutions is the best fit between the GNSS/levelling points and fitted undulations from gravimetric geoid. Mostly used statistical measures for comparison of the geoid model accuracy are standard deviation and mean, or root mean square, along with minimum, maximum (definitions given in table E.3).

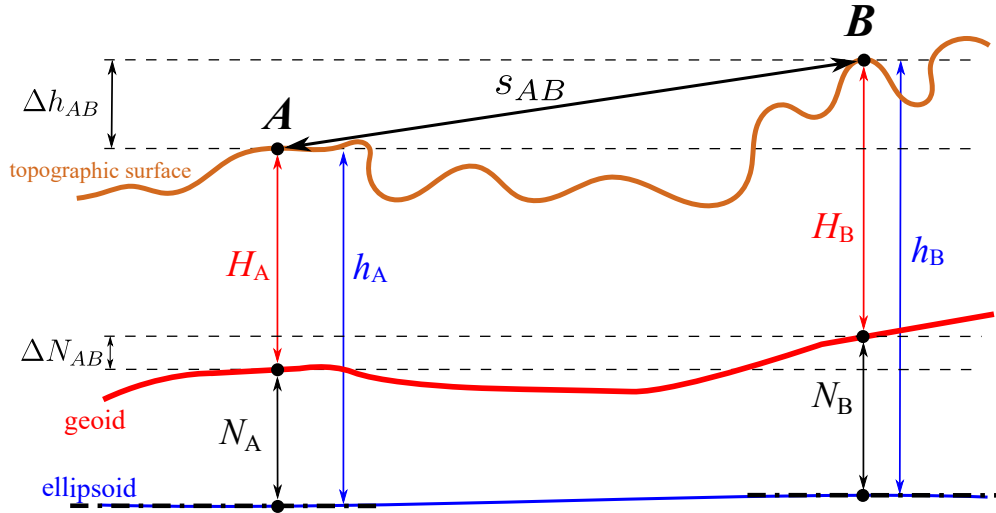


Figure 4.20: The principle of relative geoid accuracy validation between two points A and B .

4.8.1 Relative geoid accuracy validation

Validation of relative accuracy is performed to assess the potential of geoid models for transfer of the heights over some distance. In absolute geoid accuracy validation the goal is to determine how accurate will be orthometric height H , if ellipsoidal height h is measured, and geoid undulation N is taken from the hybrid geoid model. In relative geoid accuracy validation the goal is to determine accuracy for the differences between orthometric and ellipsoidal heights from one side, and geoid undulation differences from geoid models on another side. The advantage of such procedure is that some errors, such as vertical datum biases, which affect absolute measures of accuracy will cancel out in the differences as they are the same on each side of the baseline (Kearsley 1988). The principle of relative geoid accuracy validations is shown in figure 4.20.

Initial data for validation are differences between ellipsoidal and orthometric heights from GNSS/levelling, and geoid undulations for each pair of points A, B (e.g. Fotopoulos et al. 2003, eq. 2-4):

$$\begin{aligned}\Delta h_{AB} &= h_A - h_B, \\ \Delta H_{AB} &= H_A - H_B, \\ \Delta N_{AB} &= N_A - N_B,\end{aligned}\tag{4.111}$$

where A and B are pairs of available GNSS/levelling points over the distance s_{AB} .

Number of baselines for n points is $N = n(n - 1)/2$. The baseline distance (length) s_{AB} may be calculated from the geodetic latitudes and longitudes for each pair of points using formulas of Vincenty (1975). These distances are given along the geodesic, which is the shortest distance between two points on the reference ellipsoid.

In theoretical *error-free* case, for all baselines s_i between each pair of points A or B stands

(e.g., Featherstone 2001):

$$\begin{aligned} h_A - H_A - N_A &= 0, \\ h_B - H_B - N_B &= 0, \\ \Delta N_{AB} &= N_A - N_B, \end{aligned} \quad (4.112)$$

and:

$$\Delta h_{AB} - \Delta H_{AB} - \Delta N_{AB} = 0, \quad (4.113)$$

where i is the index of baseline. In practice, the above condition (equation 4.113) is not fulfilled, so misclosure values l_i for each baseline are:

$$l_i = \Delta h_{AB} - \Delta H_{AB} - \Delta N_{AB}. \quad (4.114)$$

Mean relative accuracy \bar{a}_r is obtained (e.g. Schwarz et al. 1987):

$$\bar{a}_r = \frac{1}{N} \sum_{i=1}^N \frac{\delta l_i}{s_i}, \quad (4.115)$$

where s_i is the distance between each pair of points in *ppm* units.

4.9 Gridding and interpolation

Before performing Stokes integration scattered point gravity data have to be either gridded or averaged. Therefore interpolation has to be performed. One should typically choose the method which gives the best predicted values at the needed locations of grid nodes. If the data are equally distributed on the interpolation area, without gross or biased errors and gapes, choosing of the interpolation method is not so demanding. Usually however, data are non-randomly distributed with containing unknown errors so interpolation procedure has to be properly taken care of.

Traditionally, least squares collocation was mostly used in gridding as it gives reasonable results under assumption that input data are isotropic and non-biased, and especially if stochastic properties of the input data are known. Other possible interpolation methods are (Surfer 2016, Grgić et al. 2015):

Inverse Distance to a Power. Weighted average interpolator that can be either an exact or a smoothing interpolator. Data is weighted during interpolation such that the influence of one point relative to another declines with distance from the grid node. It does not extrapolate elevation values beyond those found in the source data (Franke 1982).

Kriging. A method for constructing a minimum-error-variance manifestation. It attempts to express trends suggested in the data that can be fitted to any dataset by specifying the appropriate variogram model and anisotropy (Cressie 1990, Journel and Huijbregts 1978).

Minimum Curvature. A method that fits linear elastic plate through the data values with a minimum amount of bending. It produces the smooth surface and consequently, source data is not always treated exactly; each pass over the grid applying method equation is counted as a single iteration (Smith and Wessel 1990).

Modified Shepard's Method. A method that uses an inverse distance weighted least squares method and it can be either an exact or a smoothing interpolator. It computes a local least squares fit of a quadratic surface around each observation (Shepard 1968, Franke and Nielson 1980).

Natural Neighbour. A method estimates grid values by finding the closest subset of input data points to a grid node and then applying heightening to each. The method does not extrapolate grid values beyond the range of data and it does not generate nodes in areas without data (Sibson 1981).

Nearest Neighbour. An exact interpolator where the interpolated value of each grid node is a value of the nearest original data point. It does not take anisotropy into account. Polynomials of different orders allow fit the data using weighted least squares.

Polynomial Regression. A method used to define large-scale trends and patterns in source data and is not an interpolator. The method may extrapolate elevation values beyond the range of the source data (Draper and Smith 2014).

Radial Basis Function. An exact interpolator where the real-value specified function depends on the distance to the origin. It is similar to Kriging in terms of flexibility and usually produces a smooth grid (Powell 1992, Carlson and Foley 1991).

Triangulation with Linear Interpolation. A method that draws lines between data points to create triangles, none of the triangle edges are intersected by other triangles. It does not extrapolate outside source data range (Lee and Schachter 1980).

Moving Average. A method that assigns values to grid nodes by arithmetic averaging the data within the grid node's search ellipse (the identified neighboring data). It does not extrapolate outside the source data range.

Local Polynomial. A method that assigns values to grid nodes by using a weighted least squares fit with data within the grid node's search ellipse (Fan and Gijbels 1996).

Validation of gridding methods may be done efficiently by performing cross-validation. The process starts by removing a random point from some location in a validated dataset. Then an interpolation with gridding method in a location of the removed points is performed. Afterward, interpolated value is compared with the measurement value of removed point. Error of interpolation is considered as difference (residual) between these two values ($\text{error}(\varepsilon) = \text{measurement value of removed point} - \text{interpolated value}$).

The process is repeated for previously defined number of random points for each gridding methods. Statistical measures are computed from $\text{error}(\varepsilon)$, such as Root Mean Square Error (RMSE) or R^2 .

Part II
Research

Chapter 5

Data, study area, and software

“The ultimate purpose of geodetic measurements can be expressed in this way: We want to compute the coordinates of all points of the physical surface of the earth in a universal system, the origin of which is the center of gravity of the earth and the principal axis of which is the rotational axis.”

Reino Antero Hirvonen (1908-1989)

In this chapter data used in the thesis are described with their main characteristics and references. Data used in computations are:

- gravity anomalies,
- GNSS/levelling points,
- global geopotential models,
- digital elevation models,
- crustal density models.

5.1 Terrestrial and marine gravity anomalies

The main dataset used for all computations is a database of free-air gravity anomalies Δg_{FA} covering the study area. The database consists from approximately 16500 terrestrial free-air anomalies. The database was already used in computations of geoid models over Croatia in the past, such as HRG2000 (Bašić and Hećimović 2006), HRG2009 (Bašić 2009, Bašić and Bjelotomić 2014) and HRG2015 (Bjelotomić 2015).

Most of the data were collected from 1970s to 1995 across the territory of the Socialist Federal Republic of Yugoslavia (SFRJ). Positional coordinates are given in the Croatian Terrestrial Reference System 1996 (HTRS96) which is a realization of the European Terrestrial Reference System 1989 (ETRS89) and refers to the GRS80 ellipsoid. Heights of the points in the database are normal-orthometric in the Croatian Height Reference System 1971.5 (HVR571) (Rožić and Feil 2001, Tir et al. 2013). Gravity data refer to the International Gravity Standardization Net-

work 1971 (IGSN71). There are no reliable information about the external accuracy of these data neither for position, height, or gravity values. Estimated accuracy of the data are: positional from 0.1 m to 3 m, vertical from 0.1 to 0.5 m and gravimetric from 1 to 5 mGal.

Spatial distribution of the points in gravity database is shown on figure 5.1a. The data are more-or-less equally distributed across wider territory of Croatia. On the continental part of Croatia data are denser, whereas in mountainous areas and on islands data are sparser. As it will be shown later, the biggest issue in computations will be in the coastal and near-coastal areas for which no new and reliable shipborne gravimetric measurements exists.

Filling gaps in the original gravity anomaly database

Data gaps exist in few regions over the study area so the existing database was filled with gravity anomalies from other sources. Database was filled for land areas using gravity anomalies computed from global geopotential model EGM2008 (Pavlis et al. 2008), while sea areas are filled with gravity anomalies from global gravity field model DTU15 created from the satellite altimetry data (Andersen and Knudsen 2016).

The principle of filling the existing database with data from other sources is shown in figure 5.2. Red circles are existing points in the database. Grey and blue points are obtained from the filling grid which was created from the data of other sources. Such 'filling' grid is overlaid with the points from the existing database. Grey points are candidates for filling, but have existing points inside the circle within the radius ψ therefore have not been selected for filling. Blue points are grid nodes that have been included in the database because they do not have any point within the radius ψ . Points were added in all areas where there was neither one point data inside the radius of $\psi = 0.01^\circ$. Filled data used are shown in figure 5.1b.

Most of the points were added in the Hungarian area at the north-eastern part of the study area and in areas near the coastline where no data exist. The area along the coastline is known to be the most problematic area for geoid determination if there are no terrestrial data exist on islands, whereas satellite altimetry data near the coastline are not reliable. Besides filling holes in the data, additional data were included outside of the borders of available terrestrial data. In such way data coverage area is extended in order to minimize geoid computation errors which emerge on the borders of computation area.

Advantage of filling the database in the areas where no data exist is to increase accuracy in computations as it cannot be expected that any predicted or modeled quantity in computations will be reliably determined in the blank-data areas. Disadvantage of filling is that possible unknown and undocumented errors between different datasets, such as differences between reference systems or systematic biases, are possibly included. In this case, filled data from other sources are used without investigation of the consistency and discrepancies between data from different sources. This issue will be investigated more closely in the future.

Filtering and outliers detection

Prior to geoid computation, filled gravity database was visually and statistically analysed in order to find and eliminate suspected outliers, systematic biases and co-linear points. After performing filtering procedure, filtered gravity database is created.

Gravity database before filtering is shown in figure 5.4a, having 24471 points in total. Schematic diagram of creating the filtered gravity database is shown in figure 5.3. Initial input data are free-air gravity anomalies Δg_{FA} which are converted to residual gravity anomalies $\Delta g_{FA-GGM-RTM}$, that were smooth and non-biased (small st. dev. and mean value), which are wanted properties for outliers detection. $\Delta g_{FA-GGM-RTM}$ by subtraction of GGM Δg_{GGM} and RTM Δg_{RTM} contributions from the Δg_{FA} . Δg_{GGM} are computed using EGM2008 until maximal degree ($n_{max} = 2190$), while Δg_{RTM} are computed with SRTM 3'' global digital elevation model (global DEM) and 'default' TC input parameters: $r_1 = 20$ km, $r_2 = 20$ km, $\rho_c = 2670$ kgm⁻³. After subtraction long and short contributions from the Δg_{FA} , under assumption that no errors exist in the database, residual gravity anomalies $\Delta g_{FA-GGM-RTM}$ should have smooth changes without spikes. Spikes are values of residual anomalies that are different than surrounding points by more than few mGal. On the other hand, areas where errors exist should be detectable on the map of residual gravity anomalies or filtered using some statistical normality test.

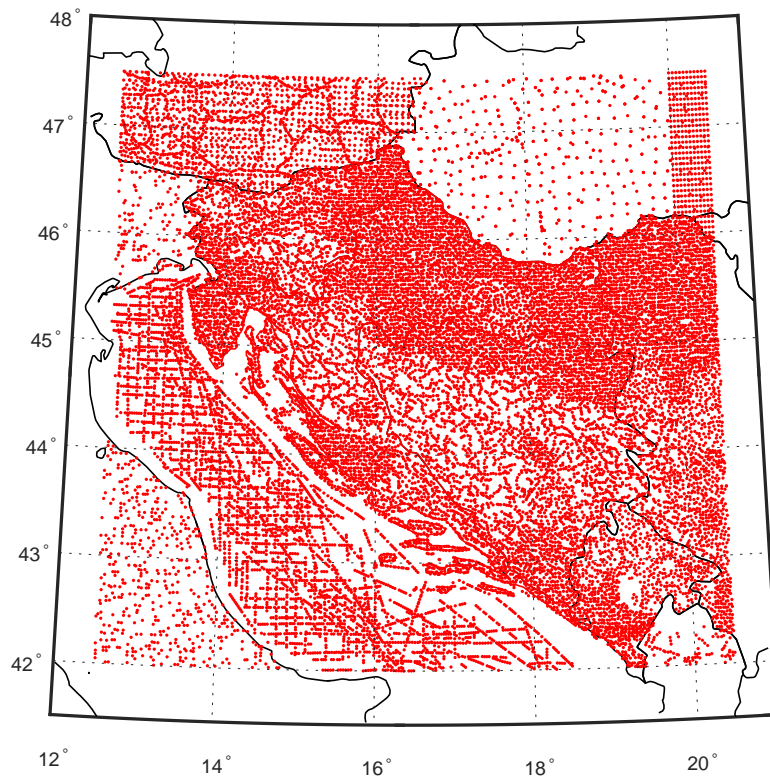
Map of gridded residual anomalies $\Delta g_{FA-GGM-RTM}$ before and after filtering is shown in figure 5.5. First, suspected outliers were eliminated visually by finding spikes and evident large discrepancies from all surrounding areas. On subfigure *a* values with values larger than 100 mGal are easily detectable outliers. They are mostly located in the Alpine region. Some other problematic areas are along the Dinarides mountains (SE part of the study area). After visual filtering, Grubbs' test for outliers (Grubbs 1969) was performed with the significance level $\alpha = 0.05$. Grubbs' test is a statistical test for outliers detection in a univariate sample which should be normally distributed. Test was performed in n iterations where in each iteration value that is either highest or lowest from the sample mean is removed from the sample. The procedure is repeated until all suspected outliers are filtered from the database.

From the filled database having 24471 points, in total 498 points were filtered, which is 2%. Spatial distribution of the filtered points is shown in figure 5.4b.

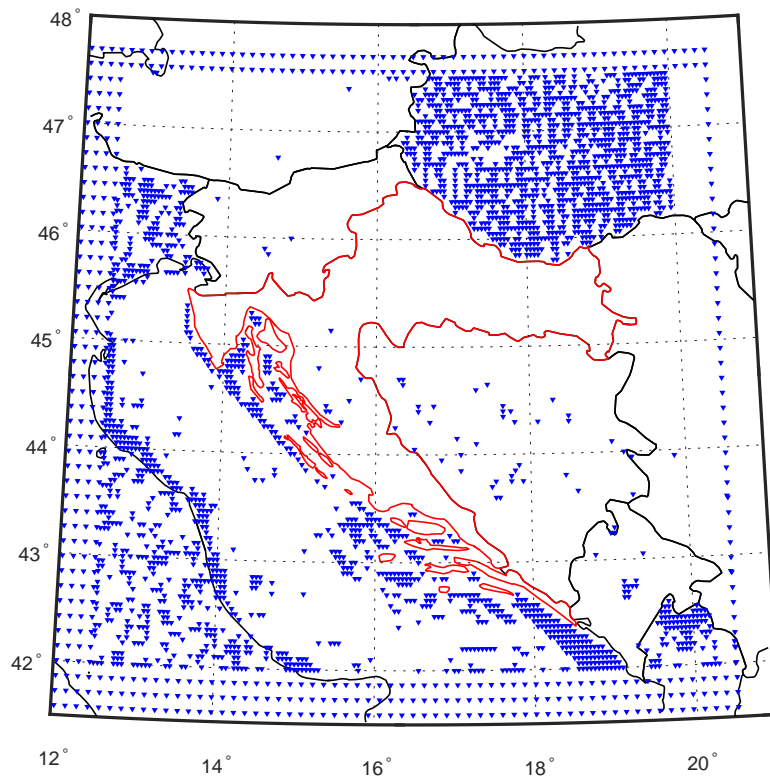
On the subfigure *b* of figure 5.5 it seems that residual gravity anomalies are smoother, more equally distributed around the mean and not having local outliers over the problematic mountainous areas of the test areas. Statistics of four types of gravity anomalies before and after filtering of the database is shown in table 5.1. Overall statistics are given for free-air, simple and complete Bouguer, and residual gravity anomalies. Concerning free-air anomalies there is no change of any statistical measure. The effect of filtering is better seen in simple and complete Bouguer gravity anomalies where standard deviation is smaller by 1 mGal. As outliers are more evident in $\Delta g_{FA-GGM-RTM}$ where minimum, maximum and range are smaller in the filtered gravity database, for example range is reduced from 238.8 mGal. Mean is almost the same -0.7 before filtering compared to 0.9 mGal after filtering, while standard deviation is reduced from 7.4 to 6.5 mGal.

Table 5.1: Statistics of different types of gravity anomalies before and after filtering/outlier detection of the database. Units: [mgal].

	Δg_{FA}		Δg_{sB}		Δg_{cB}		$\Delta g_{FA-GGM-RTM}$	
	before	after	before	after	before	after	before	after
min	-131	-131	-232	-207	-203	-177	-52.2	-32.2
max	217	217	109	109	111	111	186.5	30.1
range	347	347	341	316	314	288	238.8	62.2
mean	10	10	-28	-28	-25	-25	-0.7	-0.9
st. dev.	35	35	39	38	36	35	7.4	6.5



(a) Initial gravity database



(b) Filled points from EGM2088 and DTU15

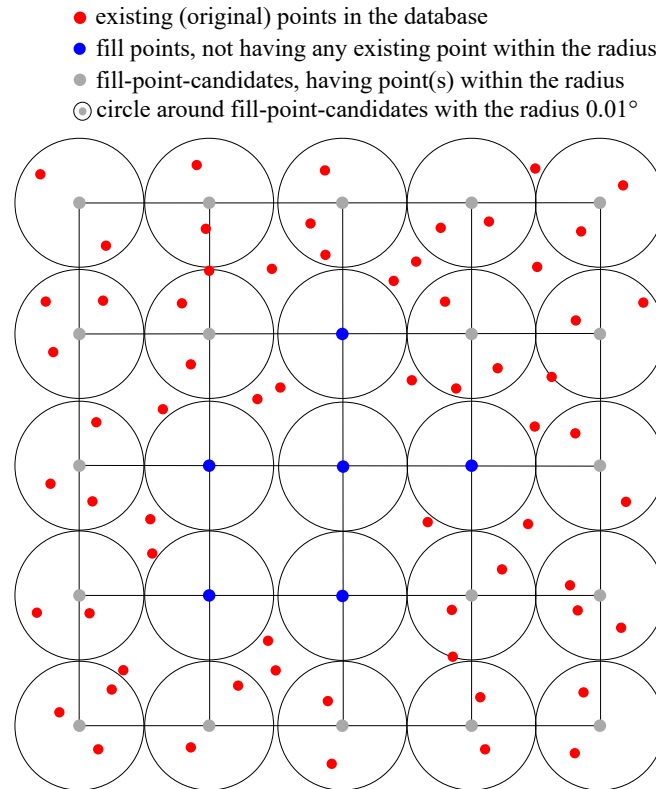


Figure 5.2: The principle for filling gaps in the gravity database

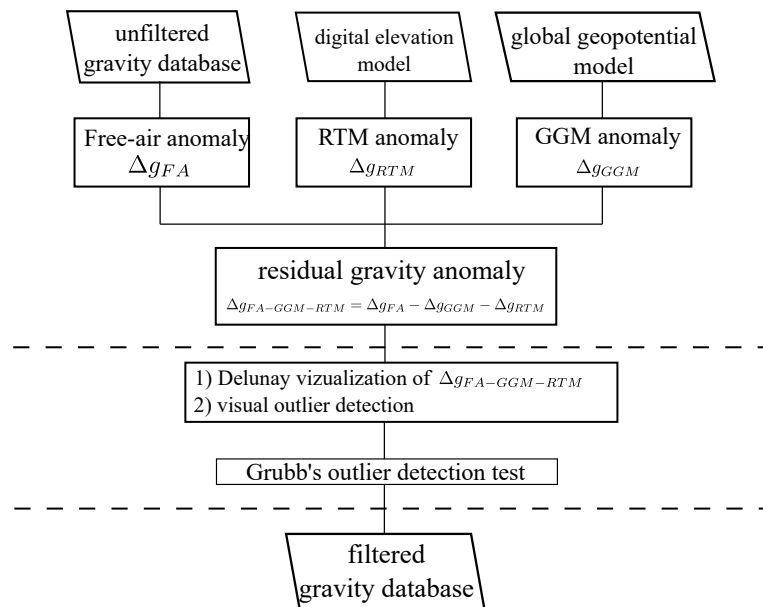
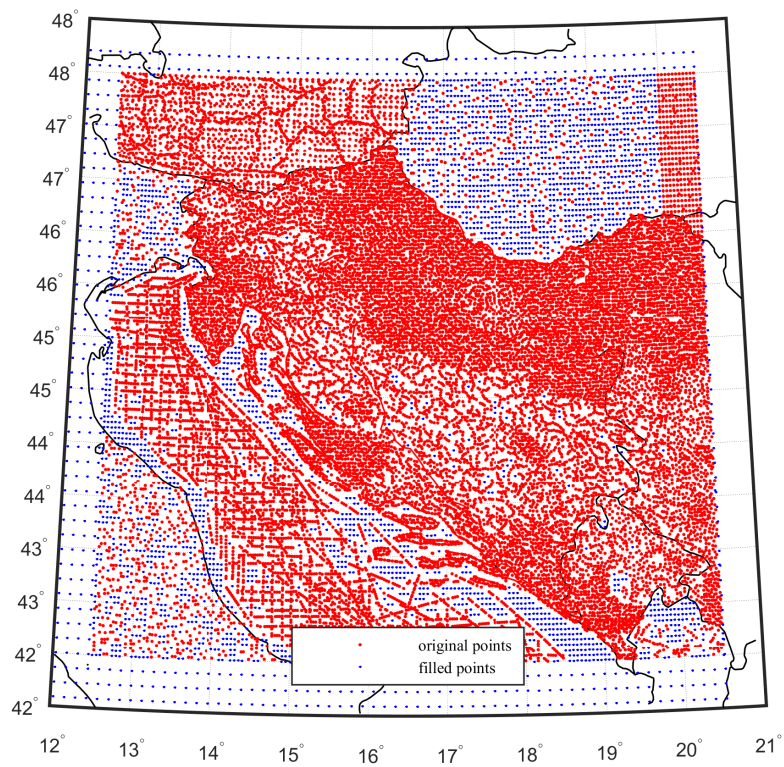
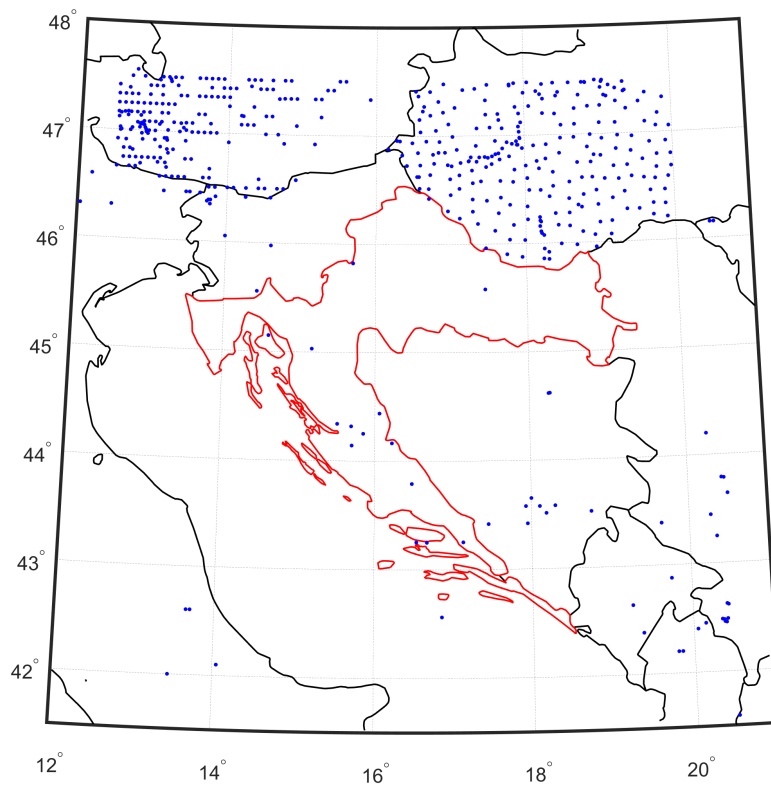


Figure 5.3: Schematic diagram of the procedure for detection and filtering of outliers from the database



(a) Gravity database before filtering and outliers detection



(b) Filtered points

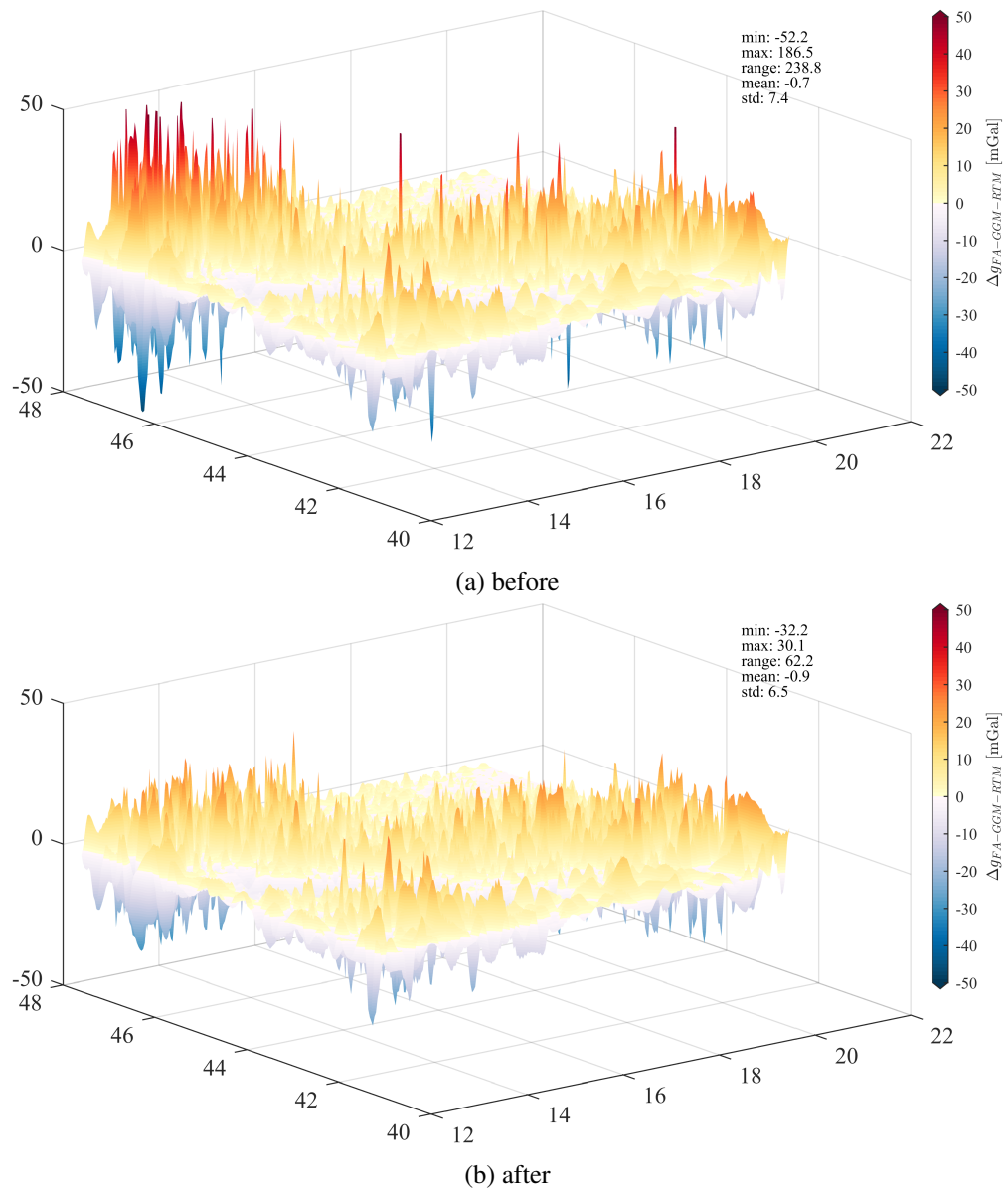


Figure 5.5: Map of residual anomalies $\Delta g_{FA-GGM-RTM}$ before and after filtering

5.2 Validation of gridding methods using different types of gravity anomaly

Geoid computation usually requires gravity anomalies in a gridded form (figure 5.6). As most of the data are not measured in 'gridded' way, some gridding method has to be applied for interpolation in grid nodes. This is a required and unavoidable step for all geoid computation approaches and methods, except for LSC in some cases when number of data does not exceed few thousand points. Accuracy of the measured point gravity data may be superior, but gridding as a mathematical procedure of calculation of the unknown value at some location, can always be done with limited accuracy. It is preferable that in this step as much as possible of raw accuracy is preserved after gridding. One wants to interpolate with best possible gridding method. The problem is even more serious because there is no way to model or filter gridding induced errors, they will simply modify and affect all afterward results and final geoid solutions.

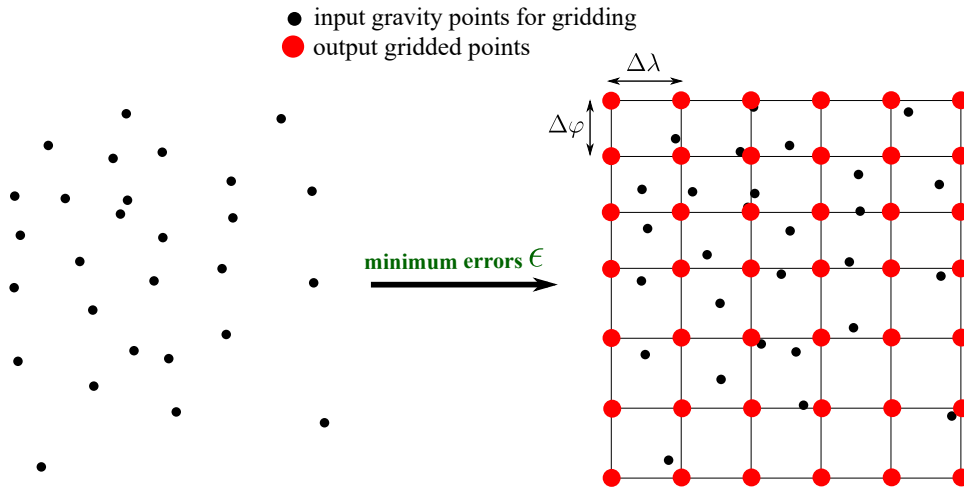


Figure 5.6: Transformation of point gravity to the gravity grid

General objectives of this section are to:

- find best possible gridding methods,
- investigate gridding accuracy of different types of anomalies.

Input data for gridding are different types of point gravity anomalies: free-air Δg_{FA} , simple Bouguer Δg_{SB} , complete Bouguer Δg_{CB} and residual $\Delta g_{FA} - \Delta g_{GGM} - \Delta g_{RTM}$. It is known that some types of anomalies have fast, and some slow fluctuations in the space. If gravity anomalies are changing fast, as it is the case with free-air gravity anomalies which depend of the topography, they will be more demanding for interpolation. Generally, it is preferable to interpolate input data which is smooth as it will probably result in the smaller errors.

Methodology of validation and gridding methods are briefly described in section 4.9. Schematic diagram of the complete process is shown in figure 5.7. Selected gridding methods for validation are: Inverse Distance to a Power (IDW), Kriging, Minimum Curvature, Modified Shepard's, Natural Neighbour, Nearest Neighbour, Polynomial Regression, Radial Basis Function (RBF), Triangulation with Linear Interpolation (TIN), Moving Average, Local Polynomial. Each grid-

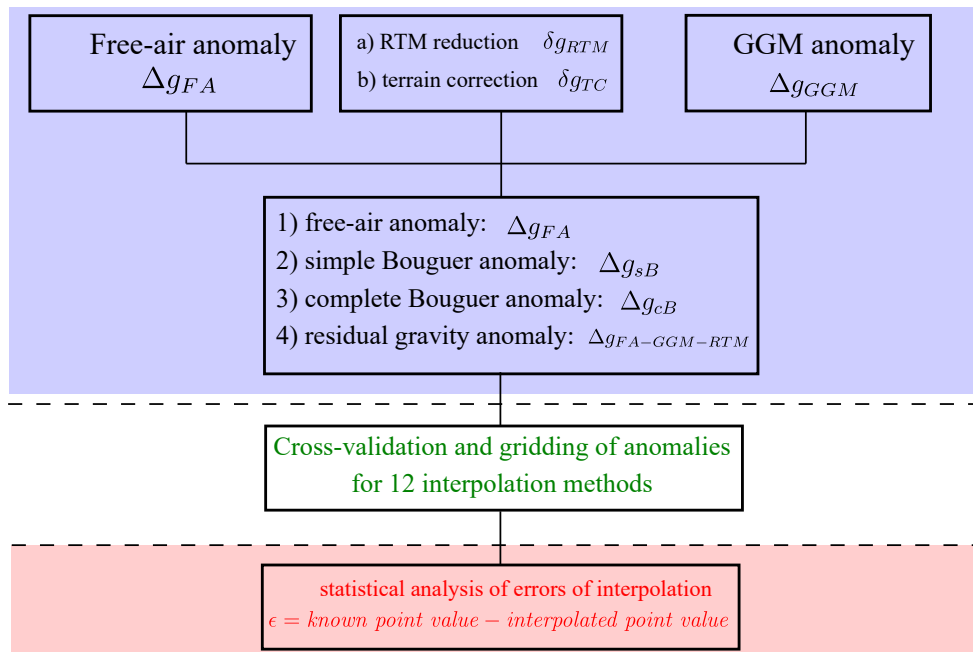


Figure 5.7: Schematic diagram of gridding methods validation

ding method has specific parameters which have to be selected for gridding. A list of input parameters for each gridding method is given in table 5.2. Results may significantly differ depending of the selected parameters, e.g. in Kriging method variogram model can be defined in several dozens ways. As for each gridding method many several solutions are obtained for each gridding method using many different parameters.

The main criteria of the accuracy of gridding method is statistical parameter RMS derived from the differences (residuals) between original (true) and interpolated (gridded) gravity anomaly value.

in tables 5.3 and 5.4 statistics of the accuracy of different gridding methods for different types of anomalies is given. Generally, there are differences of more than 10 mGal for free-air, 2 mGal for $\Delta g_{FA-GGM-RTM}$, 20 mGal for Bouguer anomalies between best and worse gridding method. For example, Kriging of Δg_{FA} resulted in 7.8 mGal RMS, whereas for Moving Average is 28.8 mGal. Kriging is the best possible method for all types of gravity anomalies. The selection of variogram model is crucial for this method. For variograms that do not describe trend of data, its accuracy can be degraded by several mGal. Minimum Curvature, Radial Basis Function and Inverse Distance to a Power are worse by around 1 mGal compared to Kriging. These three methods gave very similar results for gridding of all gravity anomaly types. The differences between them are less than 1 mGal for all gravity anomaly types. Another property of Kriging and these three gridding methods is that they do not interpolate gravity anomalies with bias, except for gridding of free-air gravity anomalies. Biased gravity anomalies are known to cause long to medium wavelengths errors in compute geoid models.

Gridding methods which largest RMS are Moving Average, Polynomial Regression and

Table 5.2: List of input parameters for different gridding methods (GS Surfer software).

Gridding method	Input parameter
All	Longitude and Latitude Spacing
	Number of Random Points
	Anisotropy Ratio
	Anisotropy Angle
IDW	Smoothing Power
Kriging	Drift Type
	Type
	Variogram
Minimum Curvature	Internal Tension
	Boundary Tension
	Relaxation Factor
Radial Basis Function	Basis Type
Polynomial Regression	MaxXOrder
	MaxYorder
	Max Total Order
Local Polynomial	Order
	Power

Table 5.3: Interpolation accuracy of different gridding methods for free-air Δg_{FA} (left) and residual gravity anomalies $\Delta g_{FA} - \Delta g_{GGM} - \Delta g_{RTM}$ (right). Sorted by RMS, units: [mGal].

Gridding method	min	max	mean	st.dev.	rms	Gridding method	min	max	mean	st.dev.	rms
Kriging	-34.3	21.8	1.6	7.7	7.8	Kriging	-5.9	9.4	0.1	3.3	3.3
Minimum Curvature	-36.1	34.1	-0.1	10.0	10.0	Minimum Curvature	-11.2	10.9	-0.3	3.7	3.6
Inverse Distance to a Power	-25.9	28.7	1.6	10.5	10.6	Radial Basis Function	-9.3	15.5	0.2	3.7	3.7
Radial Basis Function	-60.7	25.9	0.1	10.8	10.8	Inverse Distance to a Power	-11.3	11.5	-0.1	3.8	3.8
Nearest Neighbour	-38.2	56.4	-0.5	11.2	11.2	TIN	-19.0	17.0	0.2	4.4	4.4
Modified Shepard's	-33.5	33.9	1.1	11.3	11.3	Natural Neighbour	-17.0	24.6	-0.2	4.8	4.8
Natural Neighbour	-45.6	48.6	2.7	11.3	11.6	Local Polynomial	-14.1	12.8	-0.0	4.8	4.8
Local Polynomial	-52.7	50.3	1.5	11.7	11.8	Polynomial Regression	-14.9	12.9	-0.1	4.9	4.8
TIN	-69.9	40.5	1.2	12.0	12.0	Nearest Neighbour	-19.8	17.1	0.3	5.0	5.0
Polynomial Regression	-83.9	92.1	2.5	22.9	22.9	Modified Shepard's	-14.1	24.7	0.5	5.3	5.3
Moving Average	-94.0	76.5	2.5	28.9	28.8	Moving Average	-22.2	14.0	-1.2	5.7	5.8

Modified Shepard's; these gridding methods should not be used in interpolation of gravity anomalies. The results indicate that differences between accuracy of interpolation of different types of anomalies are smaller when anomalies are smoother; for free-air gravity anomaly difference between Kriging and Minimum Curvature as first and second best methods for gridding is 2.2 m Gals, whereas for residual gravity anomalies $\Delta g_{FA} - \Delta g_{GGM} - \Delta g_{RTM}$ the difference is 0.3 mGal. This mean that if smooth anomalies, such as complete Bouguer anomalies are selected

Table 5.4: Interpolation accuracy of different gridding methods for simple Δg_{sBoug} (left) and complete Bouguer anomalies Δg_{cBoug} (right). Sorted by RMS, units: [mGal].

Gridding method	min	max	mean	st.dev.	rms	Gridding method	min	max	mean	st.dev.	rms
Kriging	-5.8	8.8	0.0	2.3	2.3	Kriging	-6.3	8.4	0.0	2.1	2.1
Radial Basis Function	-7.0	8.1	-0.1	2.4	2.4	Inverse Distance to a Power	-13.7	6.5	-0.2	2.8	2.8
Natural Neighbour	-6.2	7.0	0.2	2.4	2.4	Radial Basis Function	-10.0	8.0	0.5	2.8	2.8
TIN	-8.5	8.0	-0.4	2.8	2.8	TIN	-11.2	6.4	-0.1	2.9	2.9
Minimum Curvature	-11.2	11.7	-0.0	3.1	3.1	Minimum Curvature	-6.7	9.8	0.3	3.1	3.1
Inverse Distance to a Power	-10.4	11.4	0.2	3.3	3.3	Natural Neighbour	-13.7	11.6	0.2	3.1	3.1
Local Polynomial	-7.9	11.4	0.6	3.6	3.6	Nearest Neighbour	-11.3	10.7	0.5	3.4	3.4
Nearest Neighbour	-16.3	14.5	-0.5	4.6	4.6	Local Polynomial	-10.9	10.2	0.3	3.5	3.5
Modified Shepard's	-18.3	20.7	0.2	7.8	7.8	Modified Shepard's	-22.0	31.0	0.2	7.1	7.1
Polynomial Regression	-37.5	59.2	0.9	21.2	21.1	Polynomial Regression	-57.0	46.5	-3.4	19.0	19.2
Moving Average	-94.9	102.0	-4.5	32.0	32.1	Moving Average	-48.2	84.8	1.6	32.4	32.3

for gridding the importance of the selection of gridding method is important but not crucial.

Table 5.5: Comparison of the best interpolation methods for different types of gravity anomalies. Sorted by RMS. Units: [mGal].

Gravity anomaly	Symbol	Interpol.method.	min	max	mean	st.dev.	rms
complete Bouguer	Δg_{cB}	Kriging	-6.3	8.4	0.0	2.1	2.1
simple Bouguer	Δg_{sB}	Kriging	-5.8	8.8	0.0	2.3	2.3
residual	$\Delta g_{FA} - \Delta g_{GGM} - \Delta g_{RTM}$	Kriging	-5.9	9.4	0.1	3.3	3.3
free-air	Δg_{FA}	Kriging	-34.3	21.8	1.6	7.7	7.8

From the previous tables solutions which resulted in the smallest RMS are selected and written in table 5.5. Here, statistics for different gravity anomalies are compared. Free-air anomalies are not suitable for interpolation; they can be interpolated with 7.8 mGal. Residual gravity anomalies which are used as input data in geoid determination by RCR approach can be interpolated with accuracy of 3.3 mGal. The best type of anomalies for interpolation are complete Bouguer with RMS of 2.1 mGal. The difference between interpolation with simple and complete Bouguer anomalies is 0.2 mGal. Therefore, simple Bouguer anomalies may be selected for gridding if accuracy of gravity observations is larger than 1 mGal, which is mostly the case, terrain is not mountainous and data are dense.

5.3 GNSS/levelling dataset

GNSS/levelling points are independent data used for validation and fitting of gravimetric geoid and global geopotential models. Available dataset consists from 495 points distributed across the Croatian territory. This dataset originates from the 2009 year when major GNSS campaign was conducted prior to calculation of the latest official geoid solution HRG2009 (Bašić and Bjelotomić 2014). Measurements were done on eccenters in the vicinity of the benchmarks of the Croatian Height Reference Frame (II.NVT) with dual-frequency instruments, Real Time Kinematic (RTK) or static method and 15'' interval registration. The observed network was adjusted with fixed points of the CROatian POSitioning System (CROPOS) network, precise satellite ephemerides in ETRS89, epoch 1989.0. Adjusted measurement were transformed to the terrestrial reference frame HTRS96 (ITRF96 for epoch 1995.55). A posteriori accuracy of ellipsoidal heights is 0.7 mm (Grgić et al. 2010). Spatial distribution of the points is shown in figure 5.8. Average density of points is approximately 10 points/km².

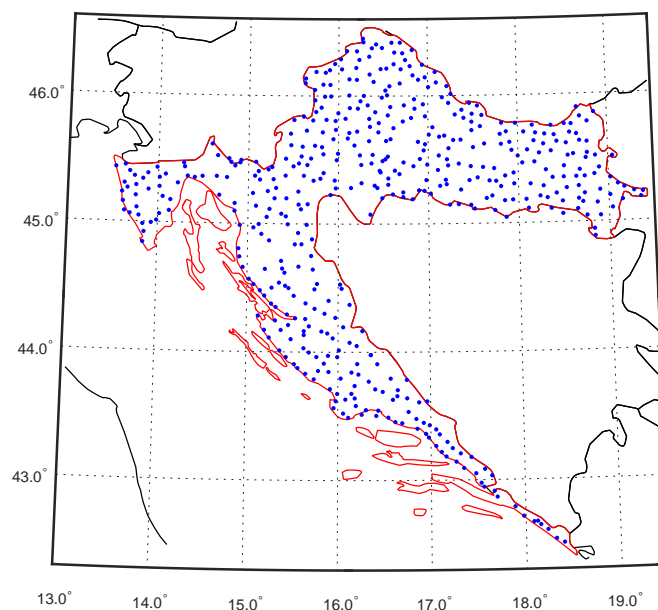


Figure 5.8: GNSS/levelling dataset

5.4 Global geopotential models

GGMs are used as the data source for modelling of the long-wavelengths of gravity potential. GGMs are models of the geopotential from which all other gravity-related quantities (functionals) are computed, such as gravity anomalies, height anomalies, deflections of vertical etc. Gravity anomalies, geoid heights, and second radial derivative, obtained from EGM2008 for n_{max} are presented in figure 5.9. These data are usually as the data source for modelling of the gravity potential of the long-wavelength spatial features of the gravity field. Three types of GGMs

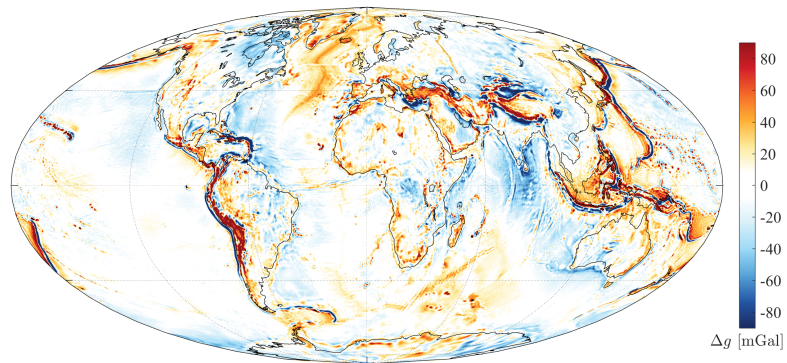
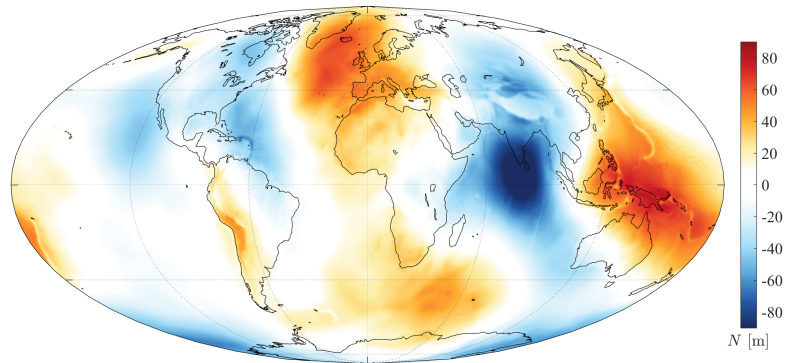
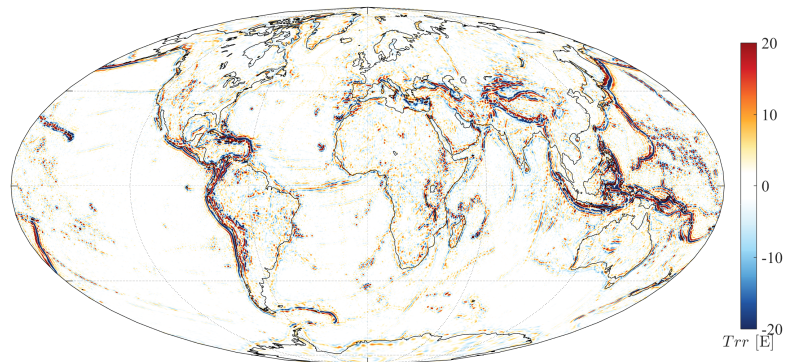
exist, depending on the type of data used for GGM development: satellite-only, combination satellite-terrestrial and tailored.

GGMs are developed since 1960s and first satellite missions, although their renaissance started with the beginning of the 21st century after satellite gravity mission CHAMP had started. Afterwards, (GRACE and GOCE) missions started which allowed scientists to collect, process and model huge amount of data about Earth's gravity field. As the result of these mission more than 80 GGMs have been published from the 2000. Distribution of GGMs goes through the website of the International Centre for Global Earth Models (ICGEM)).

GGMs have two major roles in this thesis:

1. validation of the gravity database and GNSS/levelling dataset,
2. geoid determination.

The objective of 1) is acquiring information about the accuracy of GGMs over the selected study-area by validation using the gravity database and GNSS/levelling dataset. The objective of 2) is to calculate and use gravity anomalies and geoid undulations from GGMs in the gravimetric geoid determination. There are two main uses of functional computed from GGMs in geoid determination. In RCR approach, gravity anomalies Δg_{GGM} and ΔN_{GGM} are computed for wanted degree of expansion n . contributions are computed before and after residual geoid computation, whereas in KTH approach approximate geoid undulation is computed from GGMs.

(a) gravity anomaly Δg (b) geoid height N (c) second radial derivative T_{rr} Figure 5.9: Gravity anomalies, geoid heights, and gravity gradients from EGM2008 for $n_{max} = 360$

5.4.1 Validation of global geopotential models

Global geopotential models have increased their quality in the past two decades, and are currently used in large number of applications. Validation step and mutual GGM comparison is therefore needed for obtaining information about the accuracy which they represent geopotential of the Earth. Validation results is important in geoid determination for: finding the most optimal GGM for the study area, selection of the most appropriate maximal degree of expansion, and for quality analysis, cross-checking, detection of outliers and systematic errors in gravity or GNSS/levelling datasets.

In this section GGMs are validated on available GNSS/levelling and gravity datasets. Validation of GGMs on GNSS/levelling is done in numerous studies in many different part of the world. In such studies GNSS/levelling and gravity data are used as reference (*true*) data and are considered to have higher order of accuracy than GGM. Data used for validation are described in chapter 5, sections 5.1 and 5.3.

Two functionals of gravity field potential, geoid undulation N_{GGM} and free-air gravity anomalies Δg_{GGM} , are computed from spherical harmonic coefficients for each GGM using equations 4.55 and 4.56 given in section 4.7.2. More detailed info about calculation of other functionals may be found in many references, such as Barthelmes (2009) and Bucha and Janák (2013). After computation of functionals, validation is done following procedure in section 4.8. Validation of GGMs and gravimetric geoid models coincide. Input data for analysis are differences (residuals) between gravimetric or GNSS/levelling points as control (reference) and functionals N_{GGM} and Δg_{GGM} that are computed using simple relations:

$$\begin{aligned}\delta N &= \delta N_{\text{GNSS/lev.-GGM}} = N_{\text{GNSS/lev.}} - N_{\text{GGM}}, \\ \delta g &= \delta g_{\text{grav. point-GGM}} = \Delta g_{\text{grav. point}} - \Delta g_{\text{GGM}},\end{aligned}\tag{5.1}$$

for all available points. Note that δ symbol stands for *difference* between two datasets, whereas Δ symbol usually for *gravity anomaly*.

A list of selected GGMs for validation is shown in table 5.6. They are selected by three criteria:

1. recently published (not older than 15-20 years),
2. satellite-only (e.g. GOCE, GRACE) and combination satellite-terrestrial-altimetry data GGMs (e.g. EGM2008),
3. have the best agreement on GNSS/levelling data on several areas of the world according to the GFZ 2017a validation.

Models are downloaded from the website of ICGEM (GFZ 2017a). More details about development of selected models may be found in the references given in table 5.6.

In the following subsections, validation is done in several steps:

- statistical analysis of the differences δN and δg computed with maximal degree of expansion n_{max} without and with using fitting parametric models,
- graphical analysis of the differences δN and δg computed with maximal degree of expansion n_{max} as a function of different variables (e.g. geodetic latitude or simple Bouguer anomaly),
- graphical analysis of δN and δg RMS as a function of the maximal degree of expansion n_{max} , where n_{max} values are provisionally selected values from 50, 100, ..., 2190.

Table 5.6: A list of the validated GGMs. Sorted descending by the publishing year (source: GFZ 2017a).

no.	Model	Year	n_{max}	Data source	Reference
1	XGM2016	2017	719	S, G, A	Pail et al. 2016
2	Tongji-Grace02s	2017	180	S	Chen et al. (2016)
3	NULP-02s	2017	250	S	Marchenko et al. (2017)
4	HUST-Grace2016s	2017	160	S	Zhou et al. (2016)
5	ITU-GRACE16	2016	180	S	Akyilmaz et al. (2016b)
6	eigen-6s4	2016	300	S	Förste et al. (2015)
7	ITU-GGC16	2016	280	S	Akyilmaz et al. (2016a)
8	goco05c	2016	720	S, G, A	Fecher et al. (2015)
9	goco05s	2015	280	S	Mayer-Gürr (2015)
10	GECO	2015	2190	S, G, A	Gilardoni et al. (2016)
11	ggm05c	2015	360	S, G, A	Ries et al. (2016)
12	eigen-6c4	2014	2190	S, G, A	Förste et al. (2014)
13	itsg-grace2014s	2014	200	S	Mayer-Gürr et al. (2014)
14	go-cons-gcf-2-tim-r5	2014	280	S	Brockmann et al. (2014)
15	gif48	2011	360	S, G, A	Ries et al. (2011)
16	egm2008	2008	2190	S, G, A	Pavlis et al. (2008), Pavlis et al. (2012)
17	egm96	1996	360	S, G, A	Lemoine et al. (1998)

S: satellite, G: gravity, A: altimetry data

It should be emphasized here that solutions with the smallest RMS are selected for each tested GGM in tables 5.7 and 5.9. Therefore n_{max} column in these tables does not necessarily correspond to the actual maximal degree of expansion of GGM. For example, in table 5.7 smallest RMS for EGM2008 was found for $n_{max} = 1900$ and not for 2190 which is its maximal degree.

5.4.1.1 Validation on GNSS/levelling points

Statistical comparison of the differences between GNSS/levelling points and undulations computed from GGM is given in table 5.7. EGM2008 resulted in the smallest RMS, followed by EIGEN-6C4, GECO and XGM2016. These are all GGMs created from combined-data. For the no-fit solution of the EGM2008 standard deviation of 4.8 cm, which is even comparable to regional geoid model solutions in some parts of the world. Mean error of 4.9 cm indicates existence of bias between GGM and GNSS/levelling. Mean error is eliminated in the fitting procedure 5.7, right. When third (3rd) polynomial fitting parametric model is used the bias is completely eliminated whereas standard deviation is decreased; EGM2008 agrees with the GNSS/levelling without mean value and with standard deviation of 4.3 cm. Except for EGM2008, in all other GGMs, the mean error is almost eliminated (less than 1 cm), and standard deviation decreases for more than 3 centimeters.

From satellite-only GGMs models, ITU-GGC16 results in the best agreement by RMS of 24.4 cm, followed by go-cons-gcf-2-tim-r5 with RMS of 24.8 cm. The difference between the

Table 5.7: Statistics of geoid undulation differences $\delta N_{GNSS/lev.-GGM}$ for validated GGMs. Fitting parametric model: no fit (left) and 3rdpoly (right), sorted by RMS, units: [cm].

GGM	n_{max}	min	max	range	mean	st. dev.	rms	GGM	n_{max}	min	max	range	mean	st. dev.	rms
egm2008	1900	-12.5	23.6	36.1	4.9	4.8	6.9	egm2008	1900	-16.8	17.5	34.3	-0.1	4.3	4.3
eigen-6c4	1700	-8.6	29.7	38.3	6.6	4.7	8.1	eigen-6c4	1700	-18.5	20.1	38.6	0.1	4.4	4.4
geco	2100	-6.4	22.0	28.4	6.7	5.1	8.4	geco	2100	-14.8	18.5	33.3	-0.4	4.9	4.9
XGM2016	650	-20.8	41.5	62.3	6.6	8.8	10.9	XGM2016	650	-28.4	37.2	65.5	-0.4	8.8	8.8
goco05c	700	-20.2	41.1	61.3	7.1	8.4	11.0	goco05c	700	-28.2	33.9	62.1	0.2	8.4	8.4
gif48	360	-39.8	63.4	103.2	6.1	17.1	18.2	gif48	360	-45.8	58.7	104.5	-0.1	15.5	15.5
ggm05c	350	-32.6	62.0	94.6	7.0	17.7	19.0	ggm05c	350	-45.4	63.8	109.2	0.3	16.6	16.6
ITU-GGC16	260	-61.0	77.6	138.6	6.4	23.6	24.4	ITU-GGC16	260	-53.9	75.8	129.7	-0.5	21.0	21.0
go-cons-gcf-2-tim-r5	260	-62.2	76.1	138.3	5.7	24.1	24.8	go-cons-gcf-2-tim-r5	260	-52.5	74.3	126.8	0.5	21.7	21.7
goco05s	260	-61.6	78.5	140.1	6.8	24.4	25.3	goco05s	260	-53.9	73.1	127.0	-0.4	21.8	21.8
NULP-02s	220	-75.5	84.8	160.3	6.5	24.9	25.7	NULP-02s	220	-92.6	78.1	170.7	-0.8	23.0	23.0
eigen-6s4-v2	270	-60.3	77.5	137.8	7.0	25.0	26.0	eigen-6s4-v2	270	-55.8	77.2	133.0	-0.7	22.7	22.7
egm96	360	-92.3	99.8	192.1	-23.2	24.9	34.0	egm96	360	-54.9	77.3	132.1	-0.2	17.6	17.6
Tongji-Grace02s	170	-99.7	96.5	196.2	3.0	35.4	35.5	Tongji-Grace02s	170	-94.5	69.0	163.4	-0.4	22.3	22.3
ITSG-Grace2014s	180	-101.1	112.4	213.5	-2.8	36.9	37.0	ITSG-Grace2014s	180	-93.1	74.9	168.0	-0.5	22.7	22.7
HUST-Grace2016s	160	-112.4	140.0	252.4	11.0	37.1	38.7	HUST-Grace2016s	160	-90.5	75.5	166.0	1.0	24.7	24.7
ITU-GRACE16	150	-123.5	168.8	292.3	2.0	44.9	45.0	ITU-GRACE16	150	-81.1	108.7	189.7	-0.7	28.8	28.7

best satellite-only solution ITU-GGC16 and best combined data solution EGM2008 is almost 20 cm. This is an omission error of the much smaller n_{max} for the satellite-only GGM. Satellite-only models derived from GOCE and GRACE missions or those computed only from GOCE satellite mission agree more closely with terrestrial data than GRACE-only GGMs.

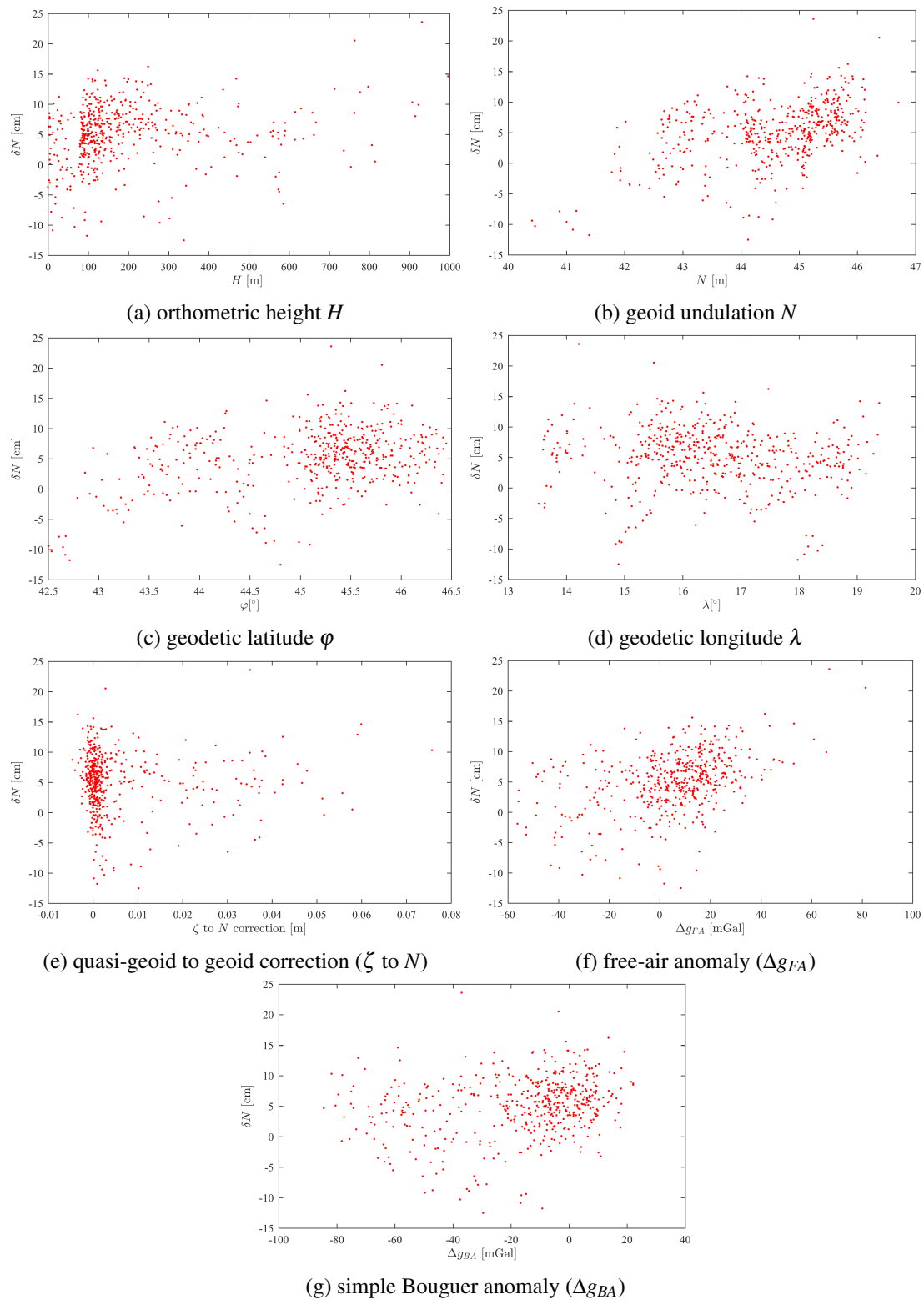


Figure 5.10: Geoid undulation differences ($\delta N = N_{GNSS/lev.} - N_{GGM}$) as a function of different variables. EGM2008, $n_{max} = 2190$

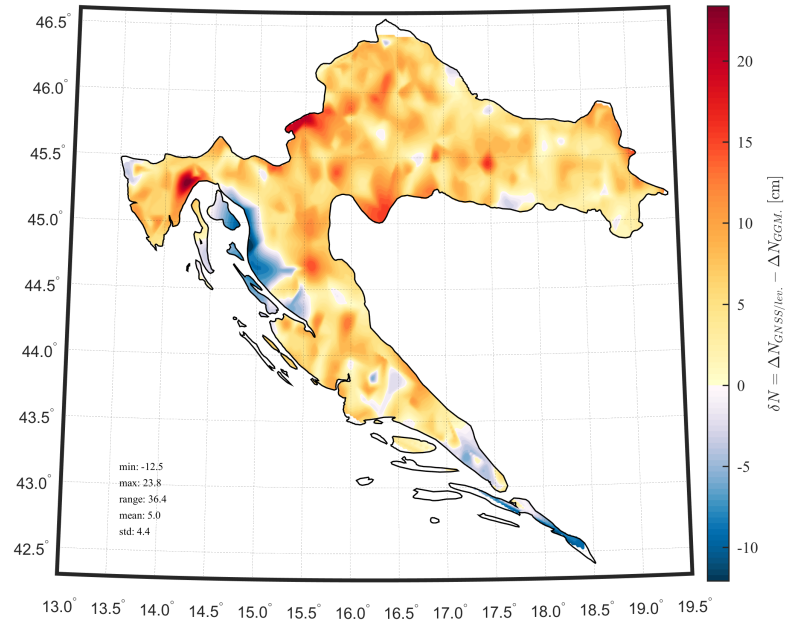


Figure 5.11: Gridded geoid undulation differences $\delta N = N_{GNSS/lev.} - N_{GGM}$, EGM2008, no fit, $n_{max} = 2190$

Geoid undulation differences δN as a function of different variables are shown in figure 5.10. On the subfigure *a* differences δN start to increase for points when orthometric height is larger 300 m. There are very few GNSS/levelling points which are situated in mountainous areas; only around 40 points from the original dataset of 495 points have elevations higher than 300 m making it harder to make reliable validation of GGMs (and gravimetric geoid models) in mountainous. The dispersion of differences for elevations from 0 to 30 m which are situated along the coast, suggest discrepancies in quality of GGM in the near-coastal zones. If geoid undulation differences δN are analysed as a function of N in subfigure *b*, it is seen that differences have large negative values of around -10 cm for N around 41 m. For increasing N , differences ΔN start to increase values and change sign to positive. The reason is that probably geoid surface computed from GGM is inclined (tilted) in some direction. Several areas can be detected with larger differences than points in surrounding from the subfigures *c* and *d*. E.g. few points with latitude and longitude $\varphi \approx 42.5^\circ$ and $\lambda \approx 18^\circ$. Subfigure *e* shows no evident correlation between quasi-geoid to geoid correction with differences δN . Subfigures *f* and *g* show that larger differences may be expected in the areas where larger free-air and Bouguer anomalies exist.

Gridded geoid undulation differences δN over the territory of Croatia are shown in figure 5.11. Only 495 point values were used which are not homogeneously distributed over the study area, so reliability is questionable in some areas where only few points are used for gridding. Few areas exist where systematic bias exists between EGM2008, especially in the continental central area of the Croatia where positive differences are larger than 10 cm. Other than this, near-coastal area in the northern Adriatic have negative values less than -10 cm.

Statistics of the differences δN computed using different fitting parametric models are shown in table 5.8 for egm2008 with $n_{max} = 1900$ which is the solution that resulted in the smallest

Table 5.8: Statistics of differences $\delta N_{\text{GNSS/lev.}-\text{GGM}}$ using different fitting parametric models. Units: [cm].

fit model	min	max	range	mean	st. dev.
nofit	-12.5	23.6	36.1	4.9	4.8
bias	-17.5	18.7	36.3	-0.2	4.9
linear	-17.7	17.1	34.8	-0.1	4.4
2ndpoly	-18.3	18.1	36.4	-0.2	4.3
3rdpoly	-16.8	17.5	34.3	-0.1	4.3
3pfit	-17.7	17.1	34.8	-0.1	4.4
4pfit	-17.9	18.3	36.3	-0.2	4.3
5pfit	-18.3	18.0	36.3	-0.2	4.3
7pfit	-17.4	17.9	35.3	-0.2	4.3

RMS compared to gravity points (see, table 5.7). Differences δN have mean error of 4.9 cm for no-fitting. The bias between GNSS/levelling and GGM is removed even with the simplest parametric models, such as with bias or linear fitting parametric model. More complex parametric models do not improve agreement more than few centimeters by means of standard deviation. For example 3rd polynomial fitting model results in standard deviation of 4.0 cm, while bias parametric model is 4.5 cm.

5.4.1.2 Validation on gravity points

Statistical comparison of the differences between point gravity anomalies and gravity anomalies computed from GGM is given in tables 5.9. Sorted by the RMS, the order of GGMs is nearly similar as in comparison of GNSS/levelling data with GGMs in table 5.7; GGMs which agree the best with GNSS/levelling, mostly agree the best with gravity data.

Table 5.9: Statistics of gravity anomaly differences $\delta g = \Delta g_{\text{gravim.point}} - \Delta g_{\text{GGM}}$ for validated GGMs. Fitting parametric model: nofit and 3rdpoly, sorted by RMS, units: [mGal].

GGM	n_{max}	min	max	range	mean	st. dev.	rms	GGM	n_{max}	min	max	range	mean	st. dev.	rms
eigen-6c4	2190	-150.9	76.1	227.0	-5.8	18.2	19.1	eigen-6c4	2190	-131.5	114.3	245.8	0.3	16.5	16.5
geco	2190	-138.7	73.1	211.8	-6.2	18.2	19.2	geco	2190	-110.5	107.7	218.2	-0.3	16.3	16.3
egm2008	2050	-151.9	72.8	224.7	-5.9	18.7	19.6	egm2008	2050	-133.2	104.2	237.4	0.1	16.7	16.7
XGM2016	650	-187.8	134.7	322.5	-7.3	24.4	25.4	XGM2016	650	-135.6	145.2	280.8	0.1	22.4	22.4
goco05c	700	-186.7	139.0	325.6	-7.0	24.7	25.7	goco05c	700	-136.0	140.3	276.2	0.3	22.6	22.6
egm96	340	-149.9	136.0	285.9	-8.5	26.5	27.8	egm96	340	-140.1	146.2	286.3	0.2	25.4	25.4
gif48	350	-165.5	104.0	269.5	-7.5	27.0	28.0	gif48	350	-153.6	154.2	307.8	0.0	25.2	25.2
ggm05c	360	-167.8	154.2	322.0	-7.9	27.3	28.4	ggm05c	360	-130.7	156.8	287.5	-0.4	25.4	25.4
ITU-GGC16	230	-168.0	112.8	280.8	-7.3	28.4	29.4	ITU-GGC16	230	-127.6	152.0	279.6	0.5	26.9	26.9
go-cons-gcf-2-tim-r5	260	-179.1	169.8	348.9	-7.9	28.4	29.4	go-cons-gcf-2-tim-r5	260	-123.0	172.8	295.7	-0.1	26.5	26.5
NULP-02s	230	-169.8	110.2	280.1	-7.9	28.6	29.6	NULP-02s	230	-137.7	134.3	272.0	-0.5	26.9	26.9
goco05s	280	-183.5	112.9	296.4	-7.1	28.8	29.7	goco05s	280	-132.0	140.7	272.8	0.5	27.1	27.1
eigen-6s4-v2	210	-166.2	167.6	333.8	-7.4	28.9	29.9	eigen-6s4-v2	210	-138.7	169.6	308.3	-0.1	27.0	27.0
HUST-Grace2016s	160	-143.5	127.8	271.4	-6.0	29.3	29.9	HUST-Grace2016s	160	-132.5	142.7	275.2	0.3	28.2	28.2
ITSG-Grace2014s	170	-146.8	119.6	266.4	-7.0	29.2	30.1	ITSG-Grace2014s	170	-136.6	155.4	292.0	-0.7	27.7	27.7
ITU-GRACE16	150	-141.7	121.8	263.5	-5.9	30.0	30.6	ITU-GRACE16	150	-129.7	131.0	260.7	0.5	28.9	28.9
Tongji-Grace02s	160	-143.3	115.5	258.9	-5.8	30.0	30.6	Tongji-Grace02s	160	-134.6	124.7	259.3	0.2	28.8	28.8

EIGEN-6c4 agrees the best with point gravimetric data with standard deviation of 18.2 and mean -5.8 mGal. GECO and EGM2008 are almost the same to EIGEN-6c4. The best satellite-

only GGM are ITU-GGC16 and go-cons-gcf-2-tim-r5 being almost the same with RMS of 29.4 mGal. In all models mean error has negative values, which means GGM models systematically overestimate real gravity values. This is an error of long-wavelength character.

After using 3rd polynomial fitting parametric model mean error is completely removed from differences. Standard deviation is reduced for around 2 mGal, which is only 10% of the complete gravity anomaly value. Otherwise, a drawback of this comparison is that high-frequency signal contained in gravity anomaly is ignored; free-air anomalies contain topographic signal and masks real differences between gravimetric dataset and GGM.

Gravity anomaly differences δg as a function of different variables are shown in figure 5.12. Differences δg increase visible with increase of orthometric height (subfigure *a*). Most of the points are located below height of 1000 m, so these areas should be densified with increase reliability. From subfigure *b* it can be seen that differences are starting to increase with increase of N above 46 m. For the geoid undulations of 50 m differences have highest values. Dependency of differences from latitude and longitude (subfigures *c* and *d*) reveal larger discrepancies in the areas around $\varphi \approx 47^\circ$ and $\lambda \approx 13^\circ$ with values of more than -50 mGal. From subfigures *e, f, g, h* as a general rule it follows that if gravity anomaly is larger, the differences or disagreement of the gravimetric point data with GGM will increase. Large gravity anomalies are found in the mountainous areas of the Alps at the north-western part and Dinarides at the south-central part of the study area. In these areas δg values are also larger than in low terrain areas.

Gridded gravity anomaly differences δg over the territory of Croatia are shown in figure 5.13. Over the continental part of Croatia differences are rarely larger than 20 mGal. However, for the Alpian area, and mountainous areas in Bosnia and Herzegovina differences have strong negative values of more than -30 mGal. If there were GNSS/levelling data for these areas, such differences would probably show up also in gridded geoid undulation differences, if we had points for testing. This can be explained with the lack of reliable the data in the mountainous areas and not inclusion of terrain and RTM effects in computation of Δg_{GGM} . Over the whole Adriatic sea area, differences are smaller compared to the continental area with values of few mGal. It has to be noted that Croatian gravity database was included in $5' \times 5'$ gravity anomaly grid used for creation of EGM2008 (and EIGEN-6c4), so good agreement in terms of δg differences are probably due to the equality in input data.

Statistics of the differences δg computed using different fitting parametric models are shown in table 5.10 for eigen-6c4 with $n_{max} = 2190$ which is the solution that resulted in the smallest RMS compared to gravity points (see, table 5.9). Such analysis not standard in a literature but can provide insights in propagation of errors. Mean error is -6.2 mGal with standard deviation of 18.2 mGal for no fitting. After elimination of the bias in all parametric models standard deviation decreases for around 2 mGal.

5.4.1.3 Validation with varying maximal degree of expansion

Here graphical analysis of the statistics of the differences between gravity anomaly and GNSS/levelling as reference data and GGM as validated data is performed. Input data for this analysis are differences computed by equation 5.1, where N_{GGM} and Δg_{GGM} are computed for different $n_{max}=5, 10, 15, \dots, 100, 150, 200, \dots, 500, 2000, 2190$. Mean and standard deviations are computed and visualized with all point differences for each computed n_{max} . As GGMs based on

Table 5.10: Statistics of differences $\delta g_{\text{grav. point-GGM}}$ using different fitting parametric models. Model: GECO. Units: [mGal].

fit model	min	max	range	mean	st. dev.
nofit	-138.7	73.1	211.8	-6.2	18.2
bias	-132.8	79.0	211.8	-0.2	18.2
linear	-125.9	78.3	204.2	-0.2	17.9
2ndpoly	-115.4	89.6	205.0	-0.4	16.9
3rdpoly	-110.5	107.7	218.2	-0.3	16.3
3pfit	-126.2	78.2	204.4	-0.2	17.9
4pfit	-120.9	81.5	202.4	-0.3	17.8
5pfit	-121.1	81.8	202.9	-0.3	17.8
7pfit	-112.6	96.2	208.8	-0.3	16.7

satellite-only data (e.g. GOCO05s) and those from combined data (e.g. EGM2008) might have large differences the figures are done separately for satellite-only and combined GGMs. Except this, not all GGMs are visualized but only those that showed better agreement with GNSS/levelling and gravity data according to the results in tables 5.7 and 5.9.

Statistical measures mean and standard deviation derived from the differences for satellite-only GGMs are shown in figures 5.14. EGM2008 is also included in figure as a reference solution. In terms of geoid undulation differences, all GGMs show similar trends with changing n_{max} . Generally, there is no GGM which gives consistently lower mean and standard deviation for all computed maximal degrees n_{max} .

Mean of δN for n_{max} from 30 to 100 show fluctuations from almost -60 cm to 60 cm. For $n_{max} > 150$ mean error for all GGMs stabilizes around values from 5 to 10 cm. It is smallest for $n_{max} = 175$. Generally, NULP-02s have smallest mean error. Standard deviation of δN , as opposite to mean value, decreases for increasing maximal degree. For maximal degree around 250 standard deviation is smallest compared to all other degrees and has values of around 20 to 22 cm.

Mean of δg for n_{max} from 30 to 100 changes from around -11 to -6 mGal. For $n_{max} > 200$ mean values has values of around -7.5 mGal. Standard deviation of differences δg decreases with increasing n_{max} .

It is interesting that for both mean and standard deviation and differences δN and δg and all GGMs for different n_{max} have similar trend.

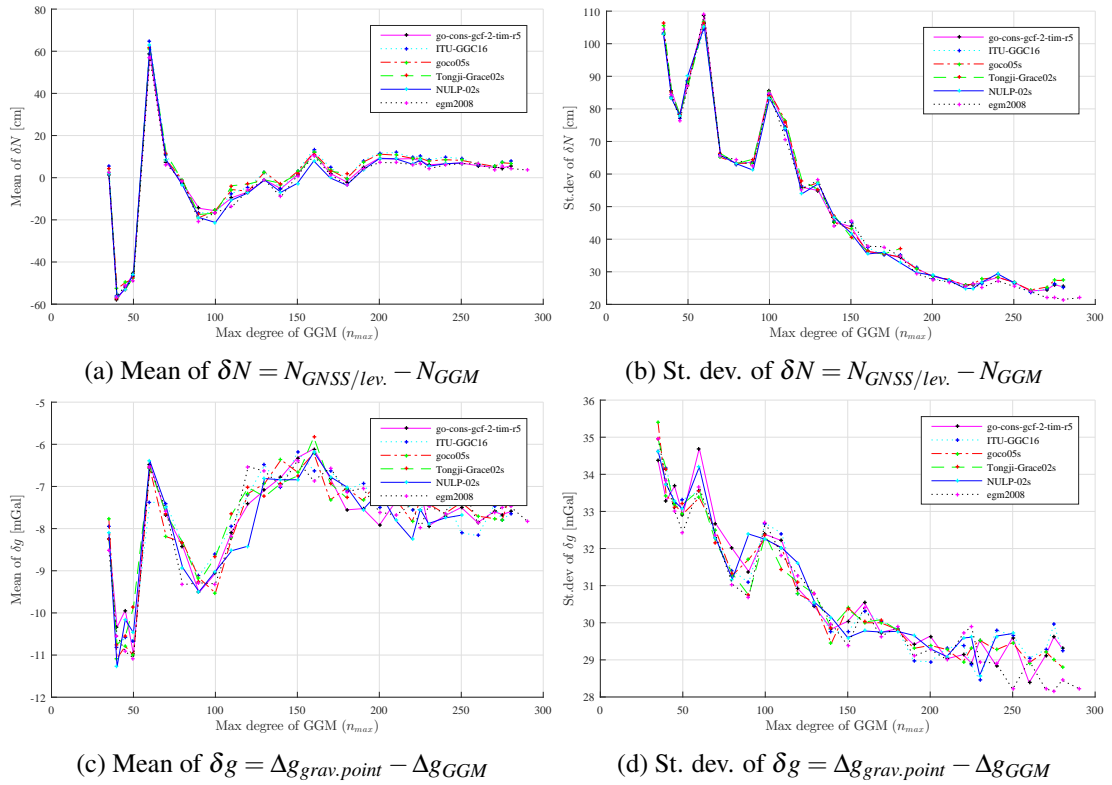


Figure 5.14: Statistics of the differences between gravity and GNSS/levelling data, and GGM models as a function of maximal degree of expansion. For $30 < n_{max} < 300$. Fitting parametric model: nofit.

Statistical measures mean and standard deviation derived from the differences for combined GGMs are shown in figures 5.15. Results are given only for n_{max} 200 to 2190, as this part of the spectrum comes from the non-satellite data. Some differences between combined GGMs are in satellite-part of the spectrum, from n_{max} 200 to 360. Considering mean value of geoid undulation differences δN , EGM2008 has the smallest values. However, it is unexpected that mean value is larger for increase of n_{max} . For example, mean values for EGM2008 $n_{max} = 250$ mean value is around 2.3 cm, while for 2190 it is more than 5 cm. This means that systematic bias between GNSS/levelling and GGMs increase after $n_{max}=360$ as terrestrial gravimetric data for computation of the GGM. Contrary to mean value, standard deviation of δN decreases with increasing maximal degree of expansion. EIGEN-6C4 has consistently smallest standard deviation of all GGMs and n_{max} . For $n_{max} = 2190$ standard deviation of EIGEN-6C4 is 4.3 cm.

For statistical measures of the gravity anomaly differences δg , with increasing maximal degree both mean and standard deviation decrease. EIGEN-6C4, EGM2008 and GECO are for the most part of the spectrum very similar in terms of gravity anomalies. From n_{max} 300 to 2190 mean value is decreased from around -8 to -6 mGal, whereas standard deviation from 28 to less than 19 mGal.

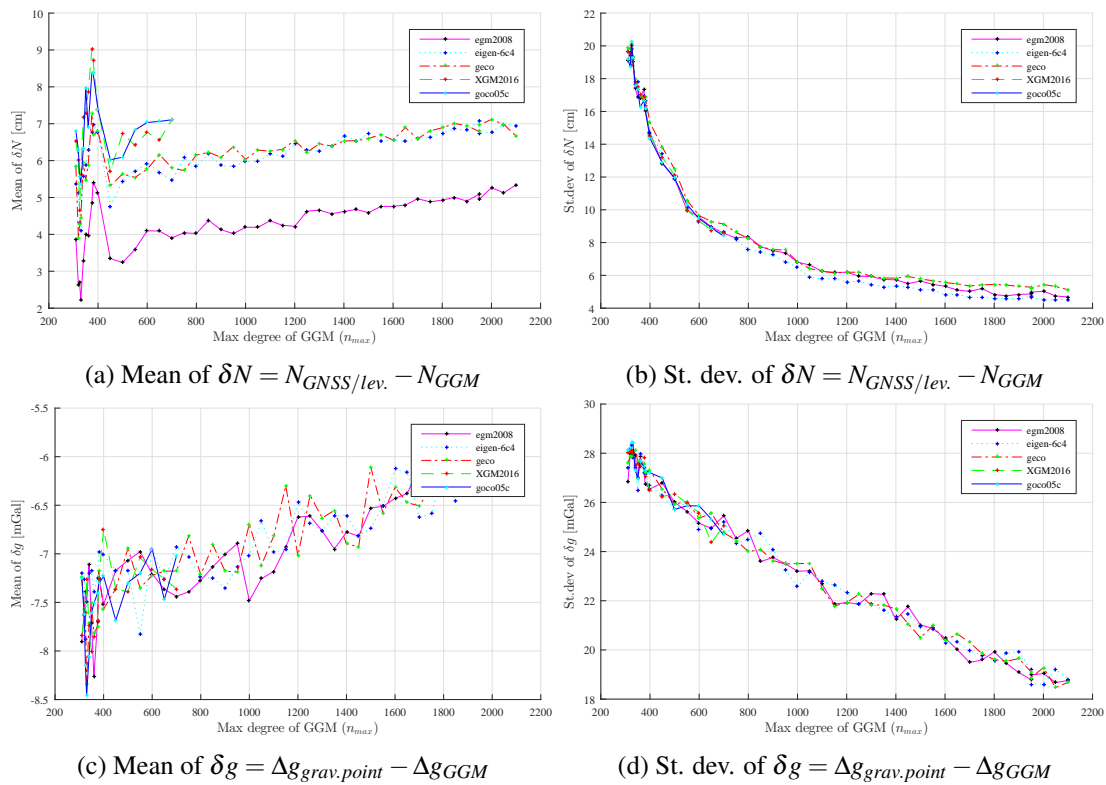


Figure 5.15: Statistics of the differences (residuals) between gravity and GNSS/levelling data, and GGM models as a function of maximal degree of expansion. For $200 < n_{max} < 2190$. Fitting parametric model: nofit.

5.4.1.4 Review

Based on the obtained results following conclusion may be drawn: EGM2008 and eigen-6c4 for the combined GGMs, and ITU-GGC16 and go-cons-gcf-2-tim-r5 for satellite-only GGMs should be used for Croatian area. EGM2008 shows better agreement for geoid undulations, whereas eigen-6c4 for gravity data.

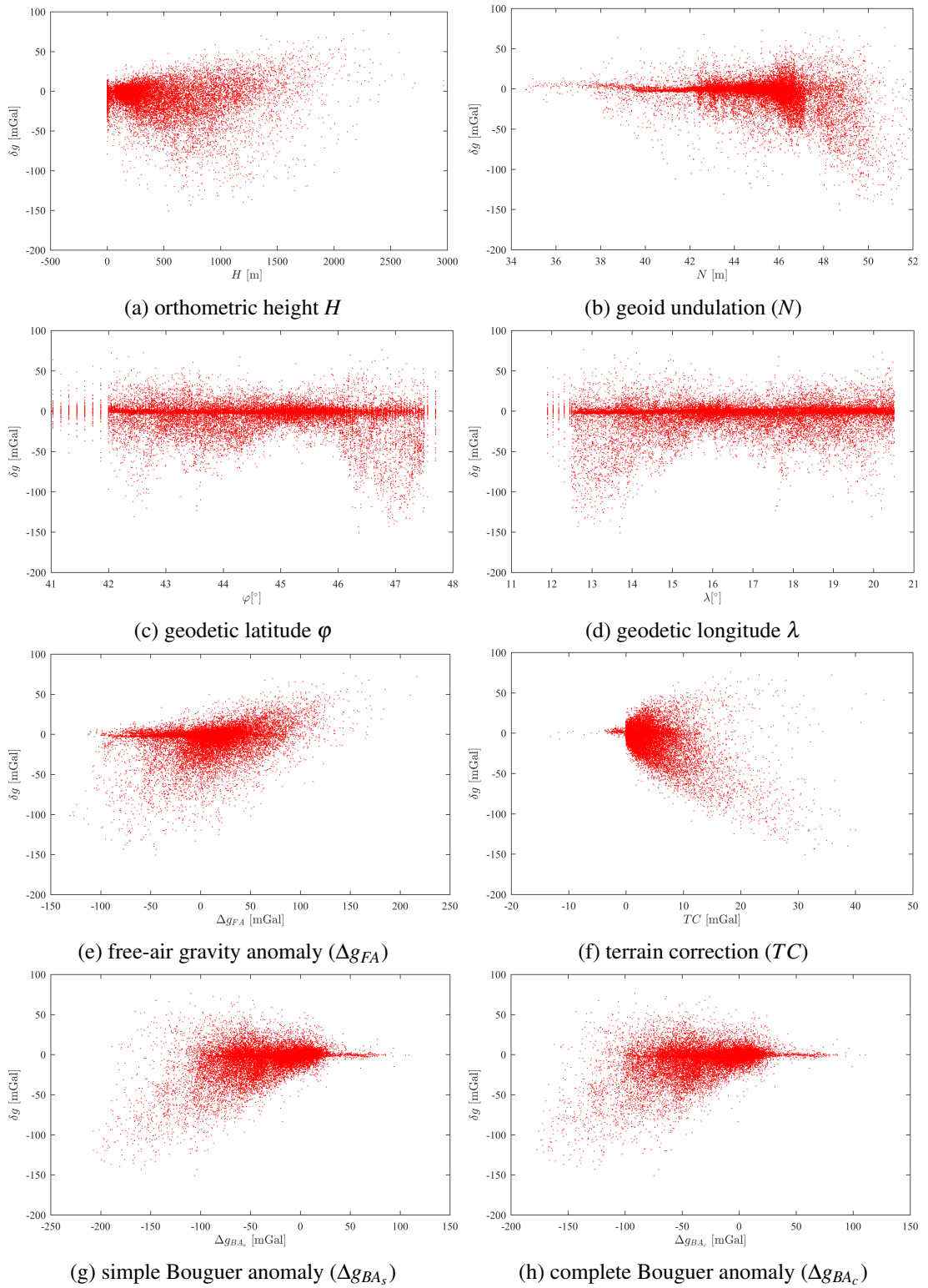


Figure 5.12: Gravity anomaly differences ($\delta g = \Delta g_{grav.point} - \Delta g_{GGM}$) as a function of different variables. EGM2008, $n_{max} = 2190$.

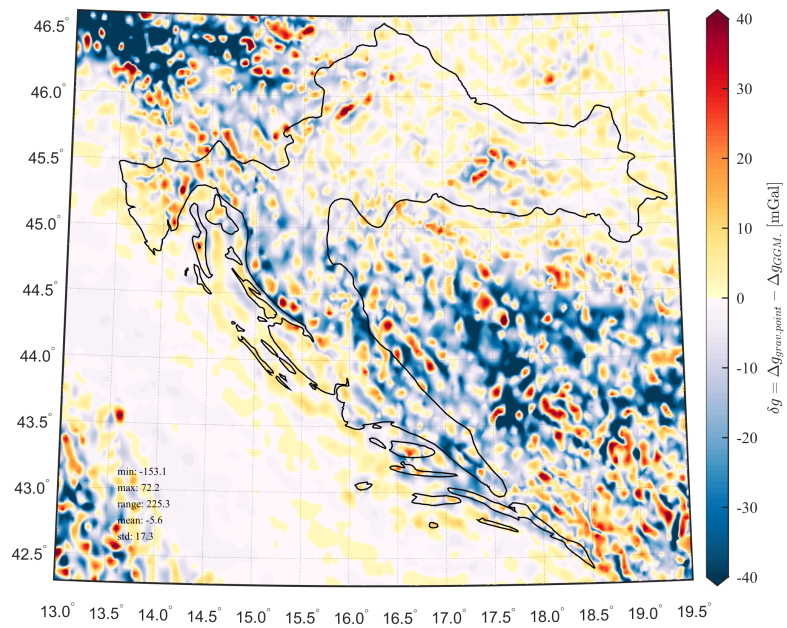


Figure 5.13: Gravity (free-air) anomaly differences $\delta g = \Delta g_{grav.point} - \Delta g_{GGM}$, EGM2008, no fit, $n_{max} = 2190$

5.5 Digital elevation models

DEMs describe Earth's topography surface and may be either: I) digital terrain model (DTM) which represent surface with vegetation, land cover and built features, or II) digital surface model (DSM) that represent bare Earth's surface without any objects (see, figure 5.16). Although both types of models are applied in geosciences, DSMs are mostly available and used, as the process of DTMs development is much more complex.

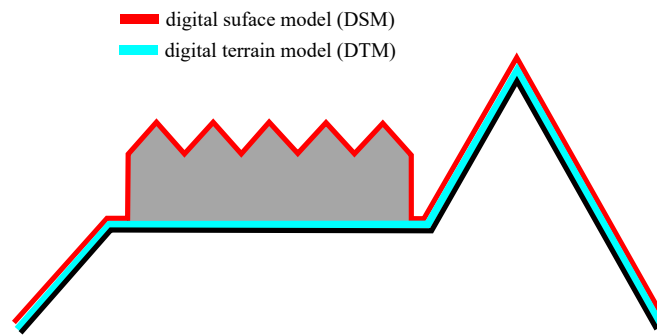


Figure 5.16: Digital elevation model (DEM) can be either digital surface model (DSM) or digital terrain model (DTM) (after [LINK](#))

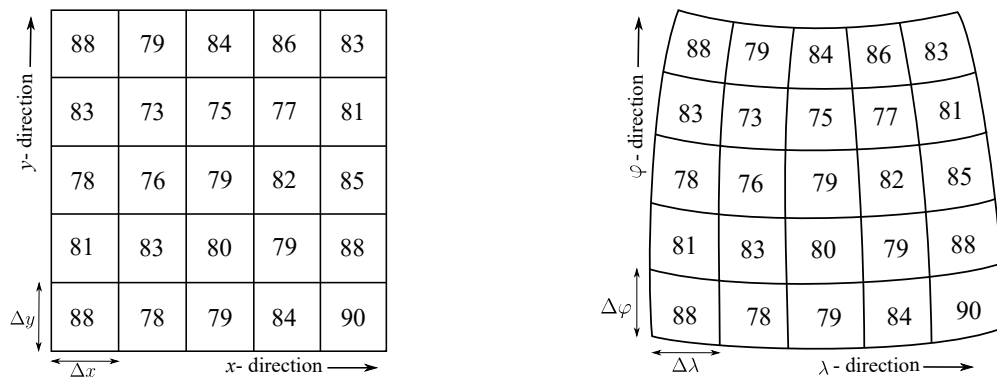
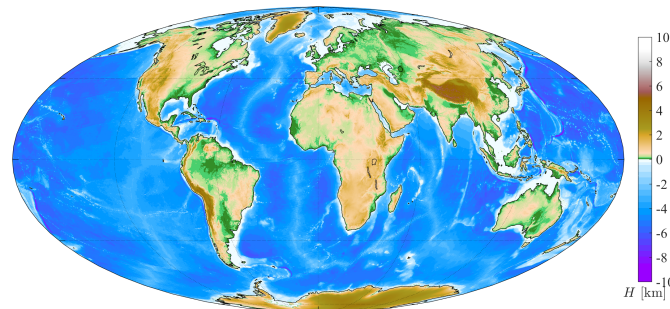


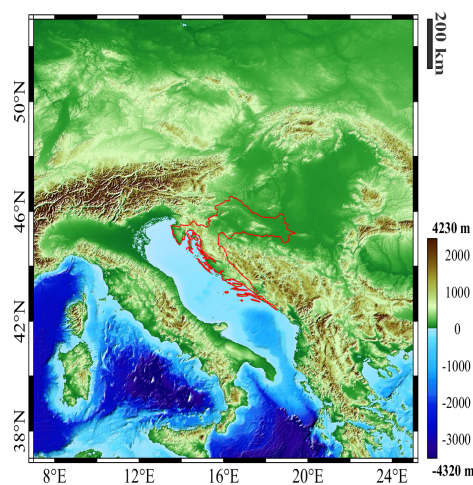
Figure 5.17: DEM referenced to planar (left) and geographic coordinate (right) systems (after [Kuhn 2000](#))

DEMs are created from different types of data, such as photogrammetric, interferometric, ground and laser surveying, and other types of data. DEMs can be distributed in either vector (TIN) or raster (grid) format. Grid may be planar-referenced in map projection, or geographic-referenced to sphere (figure 5.17). DEMs coverage can seize from local or national areas to global. If no DEM exist for a country, as it is the case in Croatia, one of the options is to use available global DEMs. They are represented in the form of georeferenced grid with equally spaced points. Major breakthrough in both detailedness and accuracy of the global DEMs came as a result of SRTM and ASTER missions back in years 2000 and 2011 ([Yamaguchi et al. 1998](#), [Farr et al. 2007](#), [Abrams et al. 2015](#)). They are nowadays freely available in resolution up to 1", which means that elevation in our areas is available for every 30 m. Example of topography

worldwide according to the ETOPO1 GDEM is visualised in figure 5.18a, and over the Croatian territory according to the SRTM15 GDEM in figure 5.18b.



(a) ETOPO1 GDEM worldwide



(b) SRTM15 GDEM over the wider territory of the Republic of Croatia

Figure 5.18: Earth's topography surface represented by two GDEMs

Evaluation of the accuracy of global DEMs is an on-going research topic with many published studies in the past few years. Each GDEM needs to be evaluated for a particular study area as accuracy may vary by more than 10 m compared to global estimates of the DEMs accuracy (Farr et al. 2007). The most recent analysis' of the vertical accuracy of GDEMs over Croatian area is in Bašić and Buble (2007), Varga and Bašić (2013), Varga and Bašić (2015) and Bjelotomić (2015). Most oftenly used GDEMs were used in these studies, including different versions of SRTM GDEMs (SRTM1, SRTM3, SRTM15, SRTM30), ASTER GDEM, GTOPO30, ETOPO1, ACE2, GMTED2010, etc. Bašić and Buble (2007) tested SRTM GDEM version 2 over Croatia with the benchmark set and found a standard deviation of 27.5 m. Varga and Bašić (2013) inspected grid differences between DEMs and found the best agreement between the ASTER, SRTM (CGIAR-CSI, version 4.1), ACE2, and GMTED2010 models, where the smallest percentage of absolute values of differences is over 20 m, indicating the lower presence of major errors in those models. However, differences between the global DEMs indicated the obvious and potentially significant presence of outliers in all models. According to Varga

Table 5.11: Basic characteristics of global digital elevation models selected for geoid modelling

Model	Institutions	Reference	Web page	Download	DSM, DTM	Coverage	Resolution	Datum
ETOPO1	NOAA	Amante and Eakins (2009)	[4]	[2]	DSM	World, bathymetry	1'	WGS84, MSL
GTOPO30	USGS		[5]	[2]	DTM	World, bathymetry	30''	WGS84, MSL
SRTM1 Arc-Second Global	NASA, NGA, JPL		[6]	[2]	DSM	World	1''	
SRTM Void Filled	NASA, NGA, JPL		[7]	[2]	DSM	World	3''	WGS84, EGM96
SRTM15	JPL	Smith and Sandwell (1997)	[8]		DSM	World	15''	
SRTM30+	JPL		Becker et al. (2009)	[9]		DSM	World	30''
ASTER	NASA, NGA, METI	JPL (2017)	[10]	[2]	DSM	World	1''	WGS84, MSL

[1] Amante and Eakins (2009), [2] USGS (2017a), [3] Farr et al. (2007), [4] NOAA (2017), [5] USGS (2017b), [6] USGS (2017c), [7] USGS (2017d), [8] USGS (2017e), [9] UCSD (2017), [10] JPL (2017)

and Bašić 2015, mean values and standard deviation of the differences between levelling benchmarks as reference data and heights interpolated from evaluated DEMs, high-resolution model SRTM3 showed to be the most accurate with 0.2 ± 3.8 m, followed by ACE2 0.4 ± 4.5 m, ASTER -1.7 ± 7.1 m (table 5.12). All DEMs have worse accuracy in the mountainous and forest areas, whereas in flat and bare-lands SRTM and ASTER GDEMs are usually accurate within 3 m.

Basic characteristics of the GDEMs used in this thesis are shown in table 5.11. For more information, readers should check references and links given in table.

From the perspective of application of DEMs in geoid determinations, they represent a data source for modelling of the high frequencies (short wavelength) of the gravity signal and are used in all equations related to the computation of the topographic effects in gravity reductions for both RCR and KTH geoid determination approaches. Only one DEM is used in computations by KTH approach, whereas in RCR approach three different models have to be prepared from the initial DEM: fine, coarse and reference. Fine DEM is used for calculation of effects in the nearest surrounding of the point (up to 20 km), coarse for far terrain effects (up to around 200 km), while reference (mean) DEM is used in calculation of RTM effects, as the approximation of long-wavelength gravity field after subtraction of GGM effects. Geographic limits of these DEMs are shown in figure 5.19.

5.6 Crustal density models

Gravity data (terrestrial, shipborne, airborne), global geopotential models and digital elevation models have been standard data in regional gravity field modelling and geoid determination. Three parameters, including crustal density (ρ_c), mantle density (ρ_m) and Moho depths T , are relevant. More specifically, these three parameters are used in the RCR and KTH approaches for

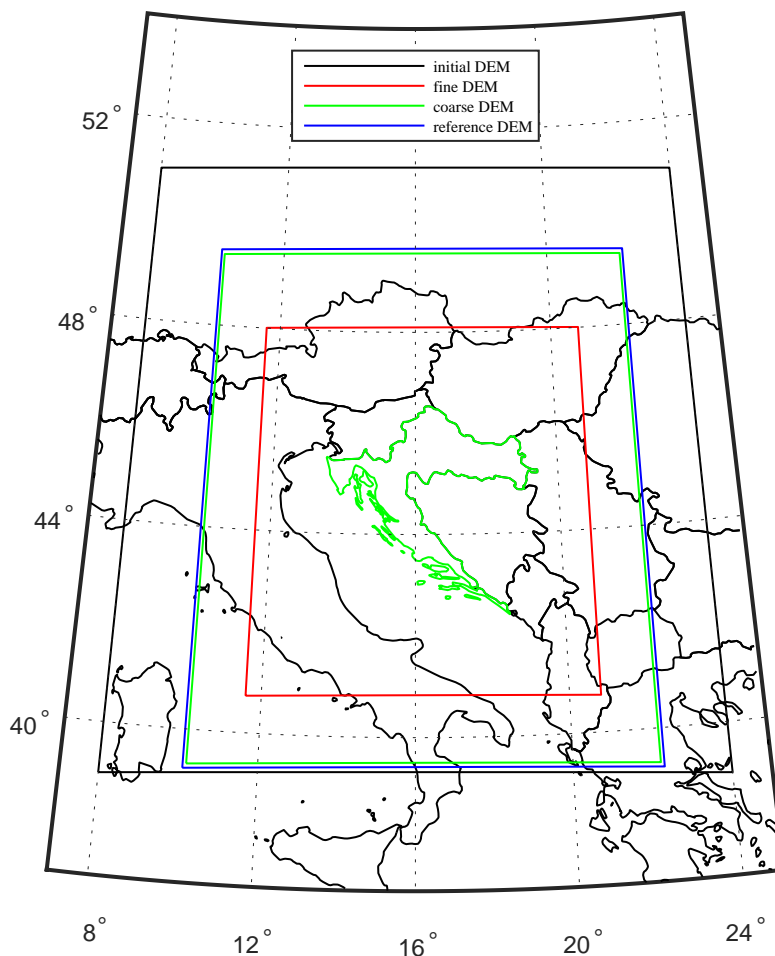


Figure 5.19: Geographic limits of the fine, coarse, and reference DEMs in the RCR approach geoid determination

gravity reduction and topographic effects on gravity anomalies and geoid undulations.

Traditionally, constant values have been used for all of these three parameters. However, constant values are somewhat rough approximation of reality therefore crustal models are possibly used in modelling. Crustal models may be two (2D) or three (3D) dimensional. For each location on some study area, two dimensional crustal models provide one value, while three dimensional crustal models provide several values, depending on the number of layers. Two-dimensional crustal models are also known as surface or lateral models, usually given as a list or grid with three quantities; two positional (φ, λ) and one parameter (e.g. crustal density). 2D crustal models have only one- surface - layer in vertical dimension, while 3D crustal model have multiple layers. Each layer corresponds to particular part of the crustal structure. For example, EPcrust model for each location provides values for three layers: sediments, upper crust and lower crust.

There are two possibilities regarding the selection of the crustal models. One can choose between using existing crustal models or creating new models from available data. Several

Table 5.12: Vertical accuracy of GDEMs across Croatia (Varga and Bašić 2015). Units: [m].

GDEM	min	max	mean	rms
ETOPO1	-95	105	9.7	27.6
GTOPO30	-82	83	3.7	21.6
SRTM30+	-82	84	6.3	21.3
GMTED2010	-29	31	1.2	7.4
ACE2	-17	18	0.4	4.5
SRTM	-17	17	0.2	3.8
ASTER	-26	27	-1.7	7.1

Table 5.13: The main properties of used 3D crustal models

model	parameter	layers	coverage	resolu- tion	reference
CRUST1.0	Moho, V_s , V_p , ρ	water, ice, upper sedim, middle sedim, lower sedim, upper crust, middle crust, lower crust	world	1°	Laske et al. (2013b), Laske et al. (2013a)
EPcrust	V_s , V_p , ρ	sediments, upper crust, lower crust	Europe	30'	Molinari and Morelli (2011a), Molinari and Morelli (2011b)

existing global or regional crustal models are available, although their coarse resolution is a major drawback in its implementation in geoid determination. Except this, if user does not have geophysical data for validation, which is usually a case, reliability of these models are not verified. The second possibility is to create a model based on from the available data by using some inversion algorithm or hypothesis' with constraining parameters. Development of the 3D crustal model is complex and demanding both from theoretical and practical point of views. First, many types of data, such as geological, geophysical and geodetic, have to be collected and combined together. Second, inversion procedures by itself are known to be ill-conditioned resulting in unreal and uninterpretable values. Although 2D crustal models are not as realistic as 3D, their development is simpler (as in section 4.4).

Two existing 3D models, and three types of newly-created 2D models are used in this thesis. Global 3D models CRUST1.0 and EPcrust are used for calculation in this thesis. Their main properties are listed in table 5.13 and shown in figures 5.20 and 5.21.

Global crustal model CRUST1.0 was developed in 2013 from different seismic databases (surface waves, free oscillation, body wave travel times). It consists from the eight layers: water, ice, 3-layer sediment cover and upper, middle and lower crystalline crust (see, Tenzer et al. 2015). In addition with these eight layers sediment and crustal thickness is available. Shear wave velocity (V_s), pressure wave velocity (V_p) and density (ρ) is given for each layer. It is distributed in 1° resolution. In each 1-degree cell, boundary depth, compressional and shear velocity as well as density is given for 8 layers: water, ice, 3-layer sediment cover and upper, middle and lower crystalline crust. The principal crustal types are adopted from CRUST5.1 (Mooney et al. 1996) and CRUST2.0 (Bassin 2000, Naliboff et al. 2012, Bagherbandi and Sjöberg 2012, Reguzzoni

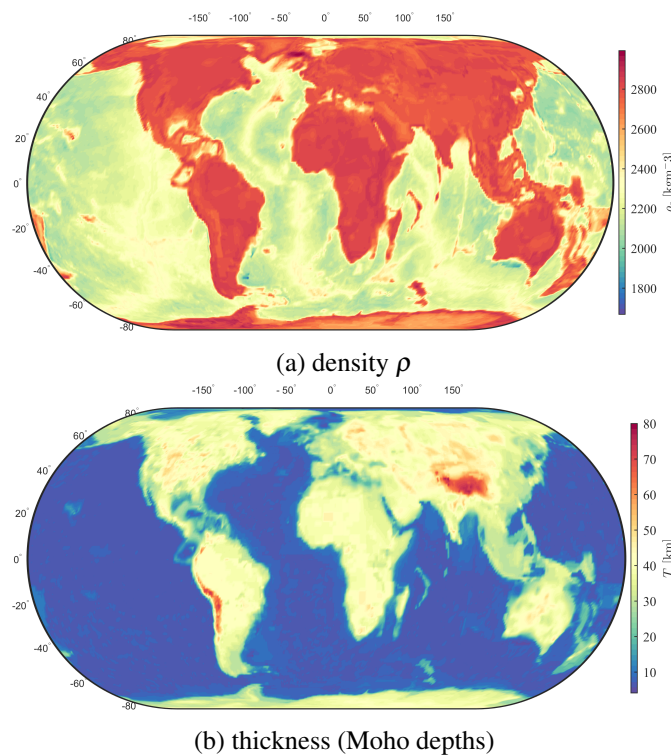


Figure 5.20: Density and thickness models according to CRUST1

et al. 2013).

EPcrust is a crustal model for the European continent in the 0.5° resolution. It was compiled in 2011 from different data sources such as CRUST2.0 (Bassin 2000), EuCRUST-07 (Tesauro et al. 2008), ESC Moho (Grad et al. 2009), ETOPO1 (Amante and Eakins 2009), etc. The crust is described by three layers, sediments, upper crust and lower crust, with three parameters, isotropic P- and S- wave velocities and crustal density (more in Molinari and Morelli 2011a).

5.6.1 Development of the crustal density models

Two-dimensional crustal density models are developed using three inversion methods: Airy-Heiskanen, Pratt-Hayford and Parasnis-Nettleton. Theoretical background of the methods are described in section 4.4. Input parameters used for development of the methods for all three inversion methods are given in table 5.14. The values of parameters are selected in order to obtain various solutions and to observe how the density values is affected by using different parameters. General objective is to find and select the most realistic crustal density model for the study area. The main criteria for finding and selection of one solution for each inversion method from the variety of computed solutions is based on the analysis of statistics obtained from: a. residual gravity anomalies $\Delta g_{FA-GGM-RTM}$ (section 6), and b. developed gravimetric geoid models using RCR and KTH approaches. The assumption is that the most realistic models results in the smallest standard deviation and mean value of residual gravity anomalies $\Delta g_{FA-GGM-RTM}$

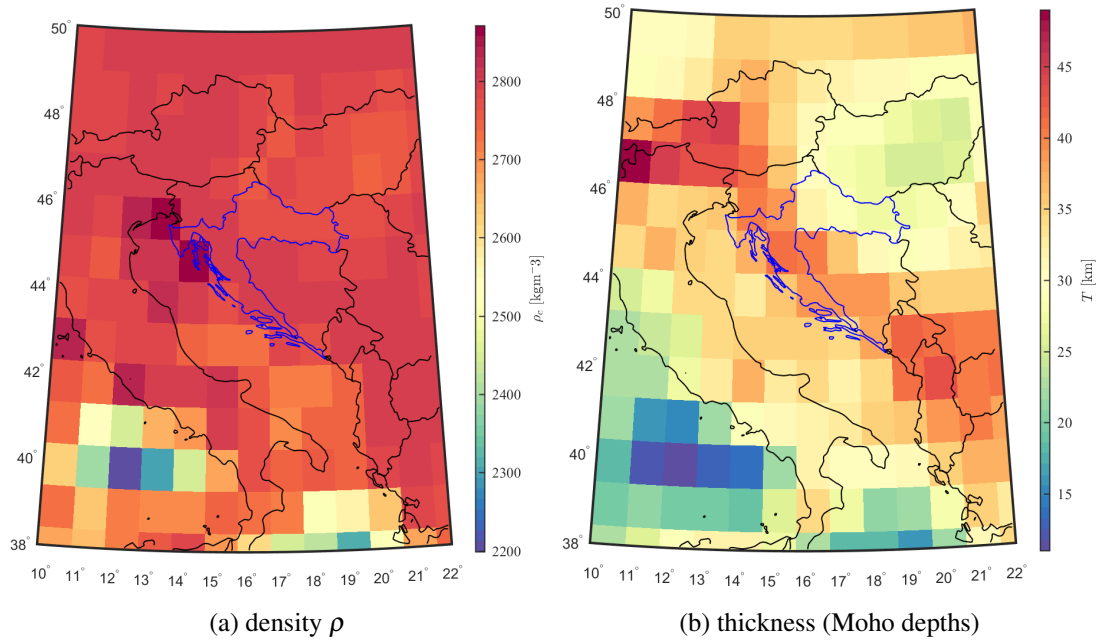


Figure 5.21: Crustal model CRUST1: Croatia

Table 5.14: Input parameters for calculation of crustal density models using three inversion methods

Inversion method	Equations in section	Parameter symbol	Input values
Pratt-Hayford	4.4.1	ρ_0	2300, 2400, 2500, 2670, 2800, 2900, 3000
		D	80, 90, 100, 110, 120, 130, 150
Airy-Heiskanen	4.4.2	ρ_m	2700, 2800, 2900, 3000, 3100, 3200, 3270, 3400, 3500
		T	from CRUST1 model
Parasnis-Nettleton	4.4.3	RS	0.05, 0.1, 0.2, 0.3, 0.5, 0.7, 1.0, 2.0
		n_{max}	0, 5, 10, 30, 50, 100, 200, 500

for case a. and differences between GNSS/levelling and geoid undulations $\delta N_{GNSS/lev.-geoid}$ for case b. Approximately one hundred crustal density models are developed for the area between $41.0^\circ N - 47.7^\circ N$ and $11.9^\circ E - 20.5^\circ E$ in $0.083^\circ (\approx 5')$ resolution. Schematic representation of developed grids of crustal density models grid is shown in figure 5.22. One node (blue circle) corresponds to the density value ρ_c of one cell.

In the Airy-Heiskanen inversion method input parameters are mantle density ρ_m and compensation depth T used in equations 4.7 and 4.8 from section 4.4.2. Different variations models were developed using ρ_m values from 2600 to 3500 kgm^{-3} . Values for T were taken from the crustal thickness layer of the CRUST1 model. In the Pratt-Hayford's inversion method input parameters are reference crustal density ρ_0 and compensation depth D used in equations 4.5 and 4.6 given in section from 4.4.1. For ρ_0 values from 2000 to 3100 kgm^{-3} and compensation depths from 80 to 120 km were used. In Parasnis-Nettleton's inversion method input parameters are radius search RS and n_{max} . Radius search RS is a parameter which determines radius in degrees for selection of the gravity anomalies within each computation cell. Therefore for each cell in a

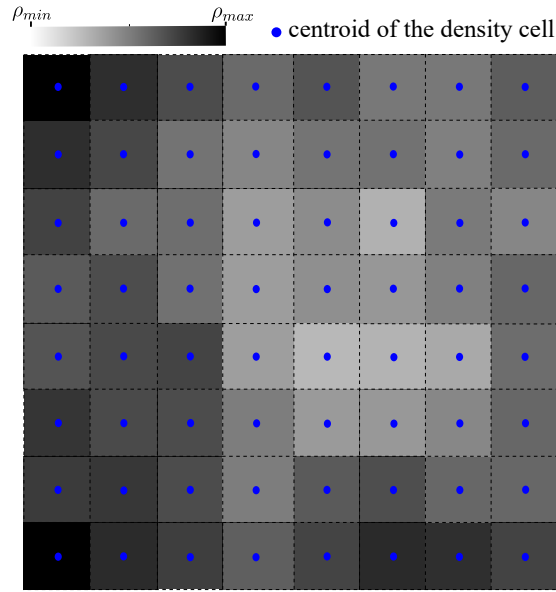


Figure 5.22: Schematic representation of the crustal density grid

grid of density model, all point gravity anomalies Δg_{FA} are selected inside radius RS . Parameter n_{max} is a maximal degree of the EGM2008 model where $\Delta g_{GGM}^{n_{max}}$ term is computed to eliminate long-wavelength effects from the selected gravity anomalies Δg_{FA} . These anomalies for each cell of the density grid model are used in equation 4.10 from section 4.4.3 for computation of the density ρ_c .

Developed crustal density models are shown in figure 5.23. Model developed by Pratt-Hayford's method indicated small variation in density across the study area; most of the values are around 2300 kgm^{-3} . Smaller values are shown in the areas of higher mountains (south-east part). Model developed by Airy-Heiskanen's method shows larger variability; at the sea area (south-west part) and lowlands (north-east) crustal density values have values around 3000 kgm^{-3} . In some areas there are evident artificial and granulated density values. In most parts of the study area, density varies with topography, having smaller values in higher mountains. Compared to Pratt-Hayford's model it seems to be much more realistic. Model developed by Parasnis-Nettleton's method indicates greatest reliability. It is smoother than P-H and A-H methods, and has larger range of densities from 1500 to 3500 kgm^{-3} . Its reliability is questionable over the sea area due to the unknown quality of the satellite-altimetry gravity data.

Differences between models are visualized in figure 5.24, and statistics of the differences are given in table 5.15. A-H model is largely different from the P-H and P-N models. Mean difference between P-H and P-N models is -45 kgm^{-3} which is much smaller than differences between other two combinations of models. From subfigure *c*, figure 5.24, differences between P-H and P-N models are largest in the south central area with values larger than 1500 kgm^{-3} , and smallest in the low-lands (north-east part).

Overall, Parasnis-Nettleton's model was selected as the optimal model for the study area, although the most realistic model would be developed using other geophysical and geological

Table 5.15: Statistics and differences between developed crustal density models. Units: $[\text{kgm}^{-3}]$.

Density	min	max	range	mean	st. dev.
ρ_c^{P-H}	2220	2300	84	2290	13
ρ_c^{A-H}	1800	3200	1400	2900	309
ρ_c^{P-N}	1090	3640	2540	2330	613
$\rho_c^{P-H} - \rho_c^{A-H}$	-925	494	1420	-617	300
$\rho_c^{P-H} - \rho_c^{P-N}$	-1350	1200	2550	-45	610
$\rho_c^{A-H} - \rho_c^{P-N}$	-835	2010	2840	571	581

data.

5.7 Study area

Study area is the wider territory of the Republic of Croatia shown in figure 5.25. Croatia is situated in Central to South-East Europe, at the northwestern part of the Balkan Peninsula, and covers 56.594 km^2 . It has borders with Slovenia, Hungary, Serbia, Bosnia and Herzegovina and Montenegro in continent and Italy on the sea.

Geographic borders of the geoid computation are $42.0^\circ N - 46.5^\circ N$ and $13.0^\circ E - 19.5^\circ E$. Green line shows borders of the area which cover point gravity anomaly data (described in section 5.1), red line shows borders of the anomalies grid, and black line shows borders of computed geoid solutions. Gravity anomalies cover largest area, while grids of anomalies is slightly smaller to minimize effects of anomaly gridding prior to geoid computations. Geoid computation area is approximately 1° smaller than grids of anomalies. Borders shown in figure are fixed in all computations of geoid models.

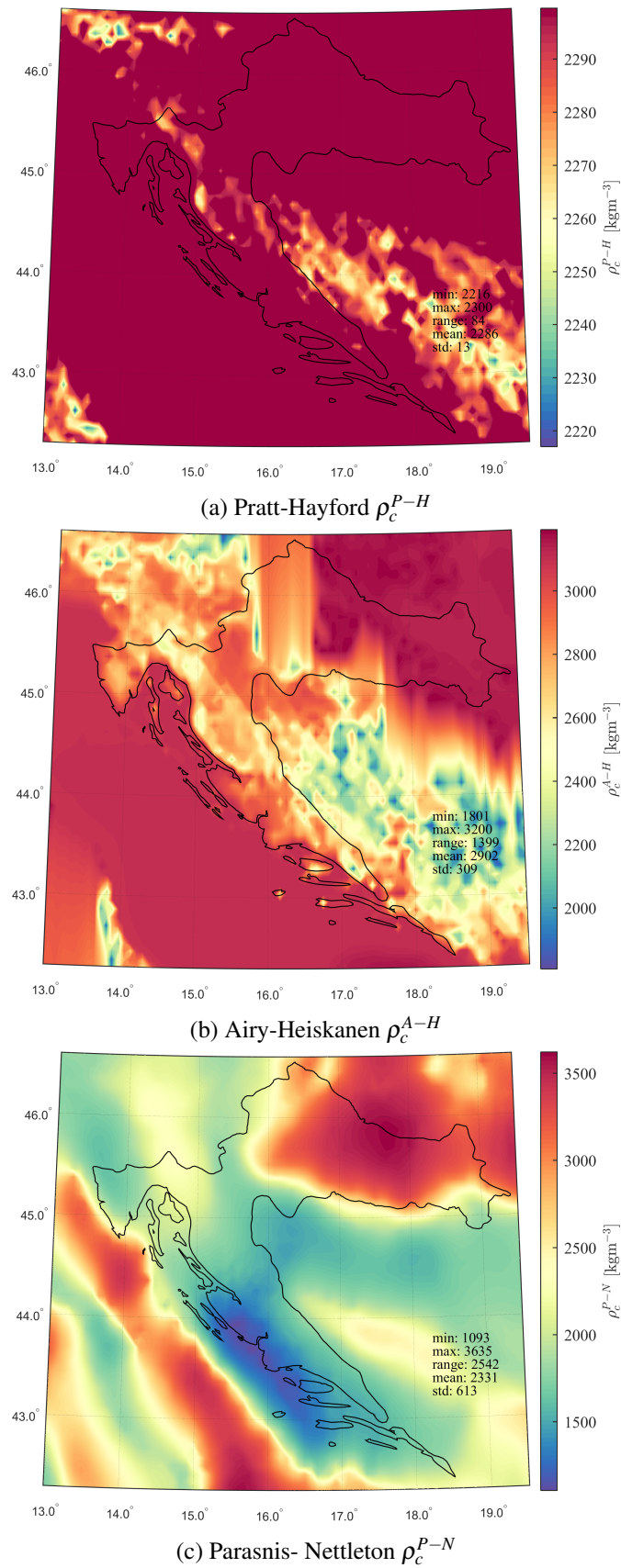


Figure 5.23: Crustal density models for the Republic of Croatia

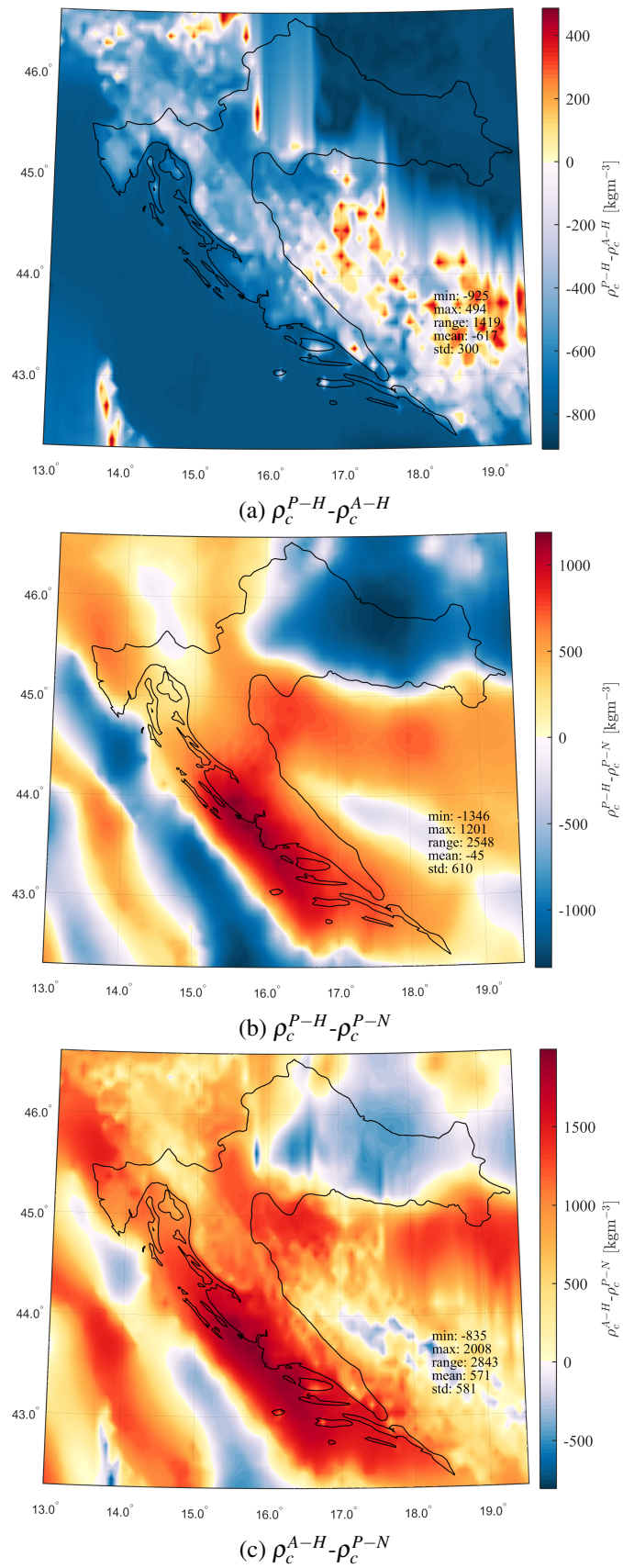


Figure 5.24: Differences between crustal density models ($\rho_c^{grid_1} - \rho_c^{grid_2}$)

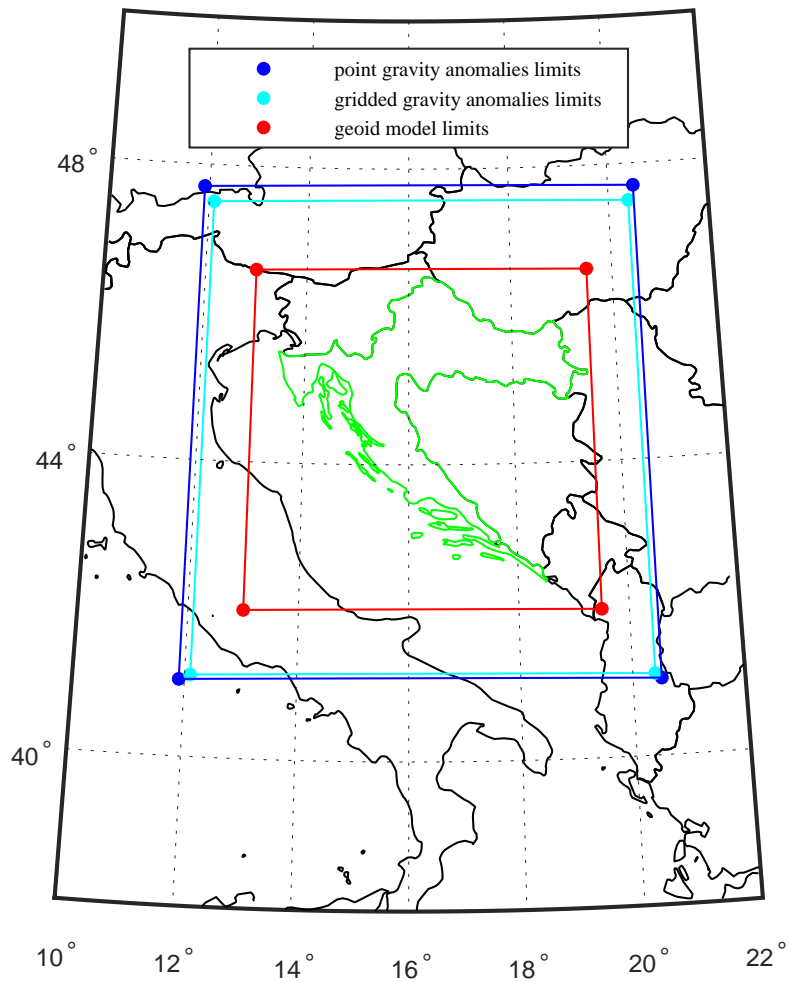


Figure 5.25: Study area

5.8 Software

Results in this thesis are obtained by using more than two hundred different software routines written mainly in Fortran, Matlab, and C++. One of the goals of this thesis was to maximally automatize geoid determination process for both RCR and KTH approaches. Gravsoft, as a well-known geoid determination package, has Graphical User Interface (GUI) and batchin options, but it does not allow computation of the geoid in one step starting from input data and models until the final geoid model along with the evaluated accuracy. Users have to manually define input data and parameters for each programming routine. Single geoid solution may be obtained using several different unconnected routines which means that efforts and time are needed. Another option is to exploit benefits of batch programming, although one has to manually define parameters and then start and run several scripts. Anyway, Gravsoft is not suitable in the cases where large number of geoid solutions have to be computed, or when input models and parameters have to be changed and tested in order to find optimal geoid model solution.

For this purpose, various *connective* scripts have been programmed for modelling, computational, statistical and visualization tasks. The scripts allow seamless determination of large number of solutions by combining different input parameters and models. The complete procedure of geoid computation has been automatized, with all steps from the beginning until end have been connected through scripts, starting from selection of input models and parameters, then outliers detection, gridding, geoid computation, accuracy validation and fitting, until visualization and advanced statistical analysis of solutions. The result is the ability to find the best possible geoid model on the study area based on available data with minimal or almost no manual work. A list of all developed routines is given in appendix D in table D.1.

The routines that were the starting point for computations are listed in table 5.16. Global geopotential model functionals, such as gravity anomalies and geoid undulations, are computed using Harmsynth and Graflab routines. GRAVSOFTE and LSMSSOFT packages were used for geoid determination. Terrain reduction is done with Fortran script TC provided by R. Forsberg and TC3 routines provided by Mario Brkić. Routines for DWC were used from Huang (2002) and Goli and Najafi-Alamdari (2011). Stokes' integration for unmodified and modified kernels is performed using scripts made by Featherstone (2003) and Ellmann (2005a). Fitting of the gravimetric solutions is based on Featherstone (2001) and Daho et al. (2006) routines.

Commercial software, MATLAB and GS Surfer, are ownership of the University of Zagreb. All other software routines were received from their authors, usually scientists which developed and published them as part of their own research.

Table 5.16: A list of the existing software packages and routines used in computations

Software name	Authors	Reference
Global geopotential model analysis		
Harmsynth	Holmes S. A., Pavlis, N. K.	Holmes et al. 2006
Graflab	Bucha, B., Janák, J.	Bucha and Janák 2013
Geoid modelling		
GRAVSOF	Forsberg, R., Tscherning, C. C.	Forsberg and Tscherning 2008
LSMSSOF	Abbak, R. A., Ustun, A.	Abbak and Ustun 2015
Analytic Stokes' integration		
Stokes' kernel modifications	Ellmann, A.	Ellmann 2005a
Stokes' kernel modifications	Featherstone, W.E.	Featherstone 2003
Terrain effects on gravimetric quantities		
TC (3D)	Brkić, M.	Brkić 1994b
DWC	Huang, J.	Huang 2002
DWC	Goli, M., Najafi-Alamdari, M.	Goli and Najafi-Alamdari 2011
Gravimetric geoid fitting		
ADJGLG	Daho, B.	Daho et al. 2006
GEOID_TESTER	Featherstone, W.E.	Featherstone 2001
other (gridding, visualization, statistics)		
MATLAB	MathWorks	MATLAB 2016
Surfer	Golden Software	Surfer 2016
GGM	Bezděk, A., Sebera, J.	Bezděk and Sebera 2013

Chapter 6

Residual gravity field modeling

Gravity measurements contain gravity signal of all spectral wavelengths, from long to short. Residual gravity field modelling is a procedure when gravity reduction scheme is applied in order to reduce effects of long or short wavelengths from the gravity measurements. After gravity is reduced for such effects, it is said that only *residual* gravity field signal is left. Reduction may apply to all types of measurement, such as deflections of vertical or geoid undulations, although gravity anomalies are used most often.

Residual gravity field functionals are used in many tasks, such as: a) input data in RCR approach, b) interpolation and gridding, c) elimination of outliers and systematic errors from the dataset, d) derivation of anomaly maps, for example Bouguer or topographic-isostatic anomalies maps. In this chapter, the objective is to remove GGM and RTM contributions and obtain residual gravity anomalies $\Delta g_{FA-GGM-RTM}$ prior to geoid determination. As $\Delta g_{FA-GGM-RTM}$ are used as input data in RCR approach, it is crucial that after reduction they are smooth and unbiased. Mean value indicate potential biases in data, whereas standard deviation indicates smoothness or dispersion of the data around the mean value. It is preferable that residual gravity field quantities have both standard deviation and mean error close to zero. The problem is to find the best combination of available input data and parameters as there are many different possibilities for their selection. It is not clear which combination of input data and parameters should be used to obtain residual gravity anomalies which would be used in further computations. For example, one has to select one GGM among all published GGMs, or decide which resolution of the reference DEM to use to match maximal degree of expansion n_{max} of the GGM.

Initial data for residual gravity field modelling are free-air anomalies Δg_{FA} described in section 5.1. All other input data are described in chapter 5. List of all tested input data and parameters for GGM and RTM contribution are given in table 6.1 and table 6.2. Δg_{GGM} contribution is computed for selected global geopotential models and maximal degrees of expansion. Δg_{RTM} contribution is computed using digital elevation and crustal models with varying values of input parameters: crustal density value, resolution of fine, coarse and reference DEM, radius of integration and DEM gridding method.

More than five thousand solutions of residual gravity anomalies $\Delta g_{FA-GGM-RTM}$ are obtained using variety of combinations of input models and parameters. Results provide detailed insight on the significance of each model and parameter in modelling of residual gravity field.

Table 6.1: Input data and parameters for computation of Δg_{GGM} contribution

Name	Acronym	Values
Data		
Global geopotential model	GGM	Tongji Grace02s, NULP 02s, HUST Grace2016s, ITSG Grace2014s, ITU GRACE16, goco05s, egm96, gif48, geco, goco05c, XGM2016, ggm05c, EGM2008, eigen 6c4
Parameters		
Maximal degree of expansion	n_{max}	100, 150, ..., 700, 2100

Table 6.2: Input data and parameters for computation of Δg_{RTM} contribution

Name	Acronym	Values
Data		
digital elevation model	<i>DEM</i>	SRTM3, SRTM30, GTOPO30, ETOPO1
digital density model 2D	<i>DDM2</i>	Airy-Heiskanen, Pratt-Hayford, Parasnis-Nettleton, CRUST1 (2D)
digital density model 3D	<i>DDM3</i>	CRUST1, EPcrust
Parameters		
radius of inner zone integration	r_1	1, 2, 5, 10, 20 [km]
radius of outer zone integration	r_2	0, 10, ..., 100, 150, 200 [km]
crustal density dimension	ρ_{dim}	constant, 2D or 3D
constant crustal density	ρ_c	2000, 2100, ..., 3000, 3100 [kgm ⁻³]
resolution of the detailed DEM	$DMR_{fine_{res}}$	3, 5, 10, 15, 20 ["]
resolution of the coarse DEM	$DMR_{coarse_{res}}$	10, 20, ..., 60 ["]
low-pass filter of the coarse DEM	$DMR_{coarse_{LPF}}$	0, 10, ..., 50 ["]
resolution of the reference DEM	$DMR_{ref_{ref}}$	30, 40, ..., 200, 300, ..., 3600 ["]
low-pass filter of the coarse DEM	$DMR_{ref_{LPF}}$	0, 10, 20, ..., 200, 300, 400 ["]

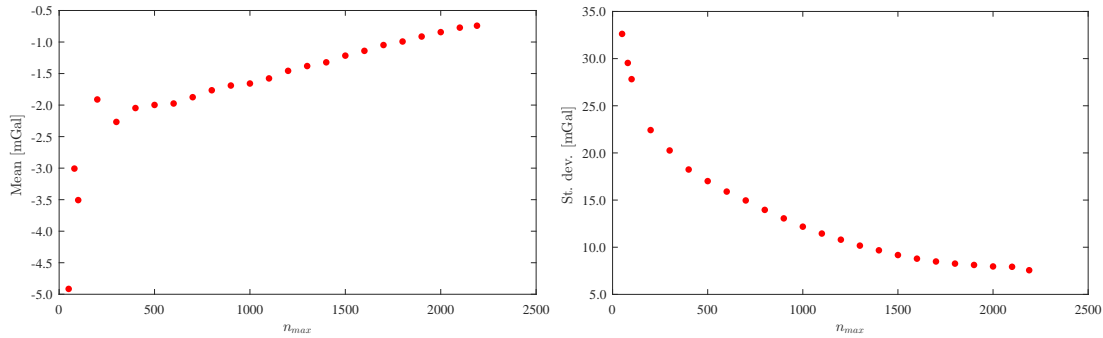


Figure 6.2: Mean and st. dev. of $\Delta g_{FA-GGM-RTM}$ as a function of maximum degree n_{max} for EGM2008

6.1 Residual gravity anomalies as a function of different parameters or models

Mean value and standard deviation of residual anomalies $\Delta g_{FA-GGM-RTM}$ using different global geopotential models is shown in figure 6.1. Maximum degree n_{max} is 180 for all selected GGMs. The differences in residual anomalies are almost the same depending on the used GGM, except for TongjiGrace02s and EGM96, suggesting that differences between new-generation GGMs are very small for the selected n_{max} . Very similar result is obtained in GGM comparison and validation, see section 5.4.1.2, figures 5.14.

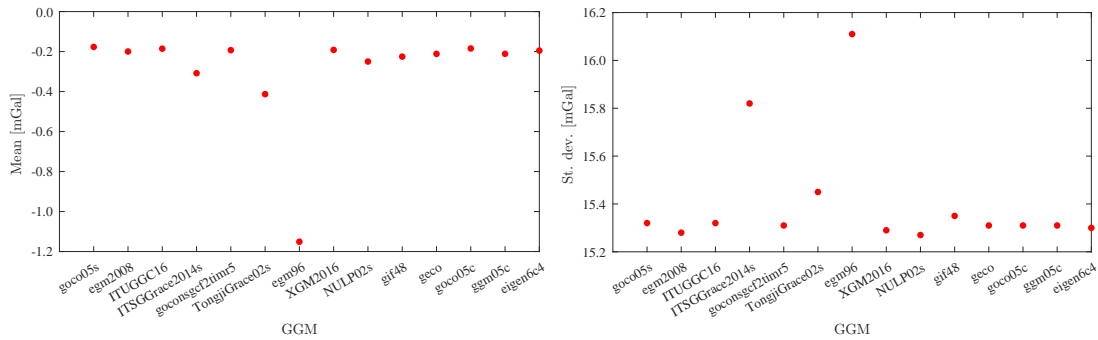


Figure 6.1: Mean and st. dev. of $\Delta g_{FA-GGM-RTM}$ as a function of GGM up to $n_{max} = 250$

Mean value and standard deviation of $\Delta g_{FA-GGM-RTM}$ using different maximal degrees of GGM is shown in figure 6.2. EGM2008 was used in this case, with fixed reference DEM resolution of approximately $1'$. It can be seen that for low degrees of GGM both mean value and standard deviation have high values. When n_{max} is increased mean value and standard deviation of anomalies decrease. In other words, anomalies become smoother and have smaller bias with larger n_{max} . For satellite-only part of the GGM (up to $n_{max} = 250$) residual anomalies are still rough (st. dev. 25 mGal) with significant mean value around -3 mGal. Along with the resolution of the reference DEM (figure 6.5), proper selection of this parameter seem to be one of the most important in residual gravity field modelling.

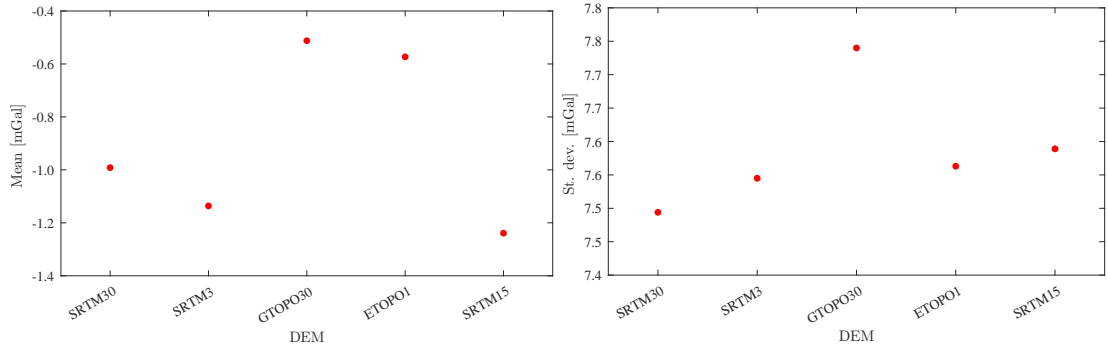


Figure 6.3: Mean and st. dev. of $\Delta g_{FA-GGM-RTM}$ as a function of digital elevation model (DEM)

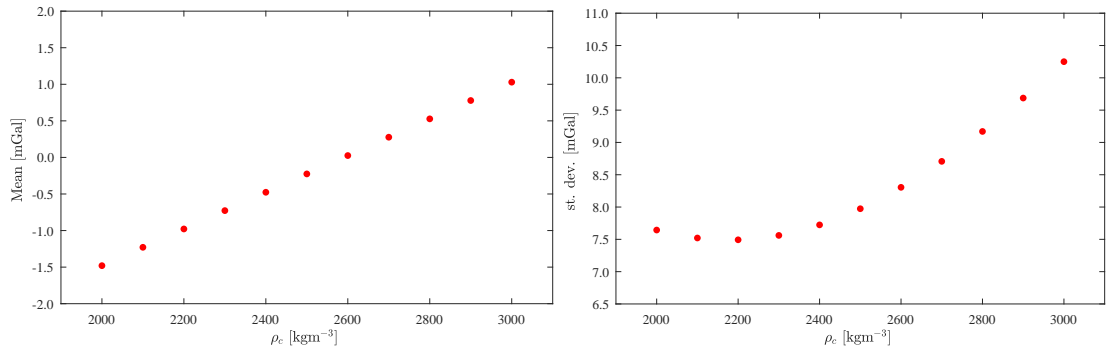


Figure 6.4: Mean and st. dev. of $\Delta g_{FA-GGM-RTM}$ as a function of constant crustal density (ρ_c)

Mean value and standard deviation of $\Delta g_{FA-GGM-RTM}$ using different digital elevation models is shown in figure 6.3. SRTM3, SRTM15, SRTM30, GTOPO30 and ETOPO1 are used in this case, while all other input parameters are fixed: EGM2008, $n_{max} = 2190$, fine DEM resolution $5''$, reference DEM resolution $30''$, LPF resolution $80''$, $\rho_c = 2200 \text{ kgm}^{-3}$. The differences using different digital elevation models seem to be in the range of 1 mGal for both mean and standard deviations. This indicates that differences between digital elevation models when modelling topographic effects are not huge. However, SRTM30 model provides anomalies with smallest standard deviation.

Mean value and standard deviation of $\Delta g_{FA-GGM-RTM}$ using different constant crustal density values ρ_c is shown in figure 6.4. Values ρ_c from 2000 to 3000 kgm^{-3} are used. Here mean values of residual anomalies are smallest for $\rho_c = 2650 \text{ kgm}^{-3}$, while standard deviation is smallest for $\rho_c = 2200 \text{ kgm}^{-3}$. Mean values have linear trend and are increasing when ρ_c increases. In both standard deviation and mean values RMS changes around 3 mGal, indicating the importance of using the most realistic crustal density for the particular study area.

Mean value and standard deviation of $\Delta g_{FA-GGM-RTM}$ using different fine DEM resolution is shown in figure 6.5. Fine DEM is a DEM used for modelling of the nearest (inner) zone effects of topographic masses. For all tested values from $5''$ to $40''$, mean values change between -1.4 and -2.8 mGal, while standard deviation changes between 8.0 and 10.5 mGal. Mean value has non-expected trend, from $5''$ to $20''$ it increases their values, than from $30''$ to $40''$ has completely

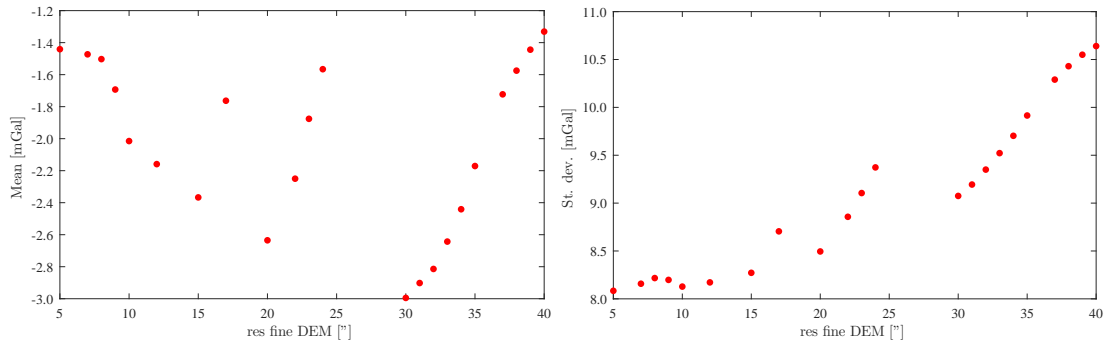


Figure 6.5: Mean and st. dev. of $\Delta g_{FA-GGM-RTM}$ as a function of resolution of the fine DEM (res fine DEM)

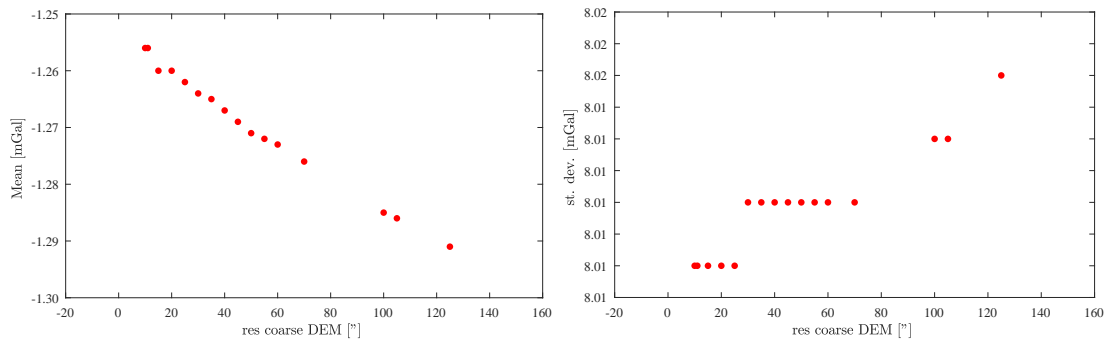


Figure 6.6: Mean and st. dev. of $\Delta g_{FA-GGM-RTM}$ as a function of resolution of the coarse DEM (res coarse DEM)

another trend. The reason may be in that resolution of the fine DEM should match (fit) with the resolution of the coarse and reference DEMs. Standard deviation decreases with increase of DEM fine resolution. Until around $15''$ it is very similar around 8.2 mGal, while for resolution larger than $15''$ it starts to increase its values, e.g. for the resolution of $40''$ its values is 10.5 mGal. In any case, the finest resolution of $5''$ produces smallest values for both mean and standard deviation, which means that high-resolution DEM should be used whenever possible.

Mean value and standard deviation of $\Delta g_{FA-GGM-RTM}$ using different resolution of the coarse DEM is shown in figure 6.6. Several values of the resolution of coarse DEM from $5''$ to $130''$ have been used. The results show both mean and standard deviation are not changing for more than 0.01 mGal depending on the resolution. Therefore, residual gravity anomalies are not sensitive to the resolution of the coarse DEM in opposite to their higher change and sensitivity on the resolution of the fine and reference DEMs (see figures 6.5 and 6.7). Resolution of the coarse DEM may be chosen arbitrarily in range from $15''$ to $60''$ and will not affect results. The reason is that topographic effects in the near zone, represented by the fine DEM, are known to have much larger impact on residual anomalies than far-zone effects, represented by the coarse DEM.

Mean value and standard deviation of $\Delta g_{FA-GGM-RTM}$ using different resolution of the reference DEM is shown in figure 6.7. Reference DEM resolution shall match to the resolution of the used n_{max} of GGM. Maximal spherical harmonic degree of expansion n_{max} of the GGM

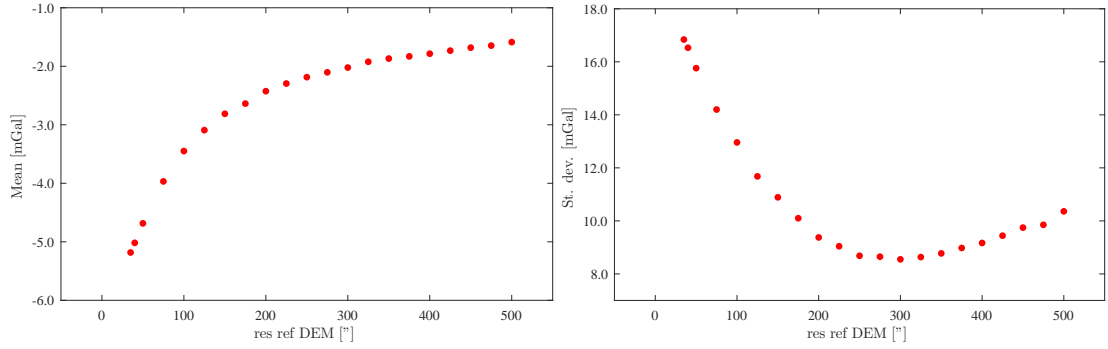


Figure 6.7: Mean and st. dev. of $\Delta g_{FA-GGM-RTM}$ as a function of resolution of the reference DEM (res ref DEM)

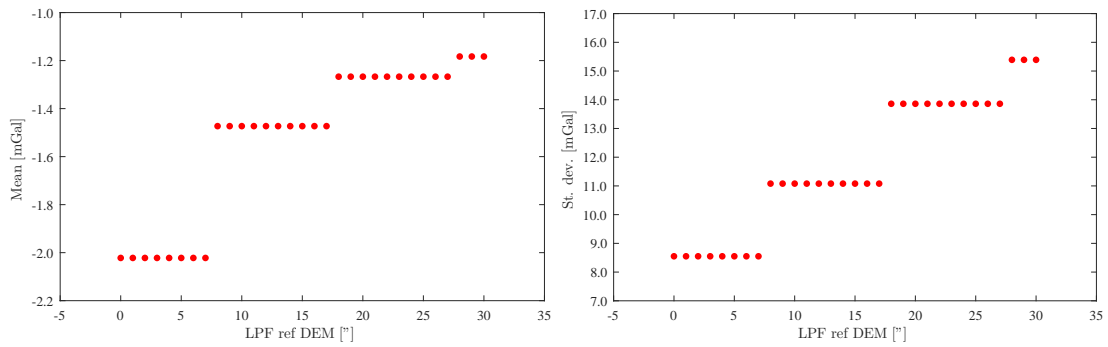
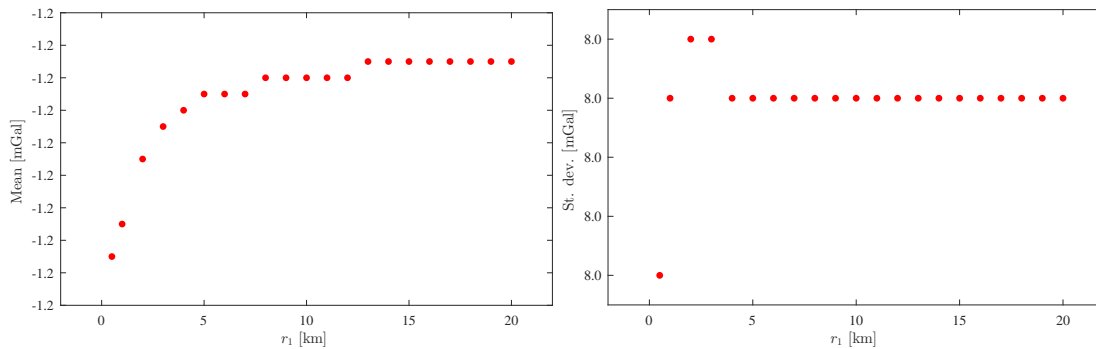
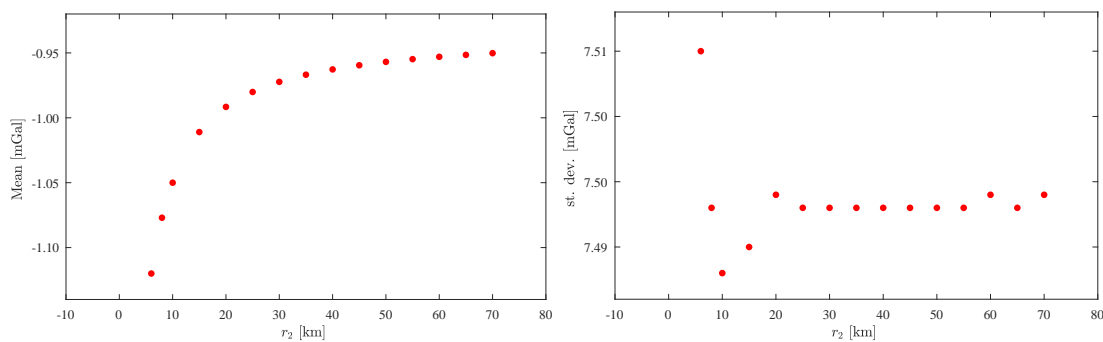


Figure 6.8: Mean and st. dev. of $\Delta g_{FA-GGM-RTM}$ as a function of low pass filter of the reference DEM (LPFref DEM)

corresponds to the spatial resolution at the Earth’s surface (according to the equation 4.71). It can be seen that resolution of the reference DEM affects to both mean value and standard deviation for up to 10 mGal. Mean values exponentially decrease, when reference DEM resolution is increased. Standard deviation of anomalies seem to be smallest for resolution of the reference DEM around 300". This is also related to the n_{max} of GGM which is 2190 in this case. Finally, mean and standard deviation of residual anomalies seem to be not related at all, but both have large changes depending on the resolution of the reference DEM.

Mean value and standard deviation of $\Delta g_{FA-GGM-RTM}$ using different resolution of the reference DEM by low pass filtering is shown in figure 6.8. Modifying resolution of DEM by low pass filter has the same effect as changing resolution of the reference DEM. Mean values are changing up to 4 mGal, while standard deviation changes up to 8 mGal for selected values. Mean values of anomalies are exponentially increasing with increase of the resolution; for values that are higher than 200" mean value is less than 1 mGal. Standard deviation seem to be around 8 mGal for resolution of the reference DEM of 100". By increasing resolution standard deviation also increases.

Mean value and standard deviation of $\Delta g_{FA-GGM-RTM}$ using different radiuses of integration of the inner (near) zone is shown in figure 6.9. Values from 0 to 20 km were selected. It is seen that both mean values and standard deviation do not change more than 0.1 mGal depending on

Figure 6.9: Mean and st. dev. of $\Delta g_{FA-GGM-RTM}$ as a function of radius of inner zone r_1 (r_1)Figure 6.10: Mean and st. dev. of $\Delta g_{FA-GGM-RTM}$ as a function of radius of outer zone r_2 (r_2)

the radius r_1 , although probably values less than 5 km should not be selected.

Mean value and standard deviation of $\Delta g_{FA-GGM-RTM}$ using different integration radiuses of the outer (far) zone is shown in figure 6.10. Values from 8 to 80 km were selected. Figures look the same as for the radius r_1 . For standard deviation of anomalies it is irrelevant which radius is chosen, but in case of mean value increase of radius decreases mean value. It seems reasonable to select values between 10 and 30 km for r_2 .

Mean value and standard deviation of $\Delta g_{FA-GGM-RTM}$ using different gridding methods of DEMs is shown in figure 6.11. Nearest neighbor, bilinear, bicubic and moving average with different box sizes are used. Nearest neighbor, bilinear and bicubic method give reasonable mean value and standard deviation whereas Moving average with box size 3x3 results in smallest standard deviation.

6.2 Residual gravity anomalies as a function of two different parameters

Statistical parameters, mean and standard deviation, of residual gravity anomalies as a function of one parameter are analysed in the previous section. In the same way, statistical parameters may be analysed as a function of two (or even more) different parameters, as it is the case here.

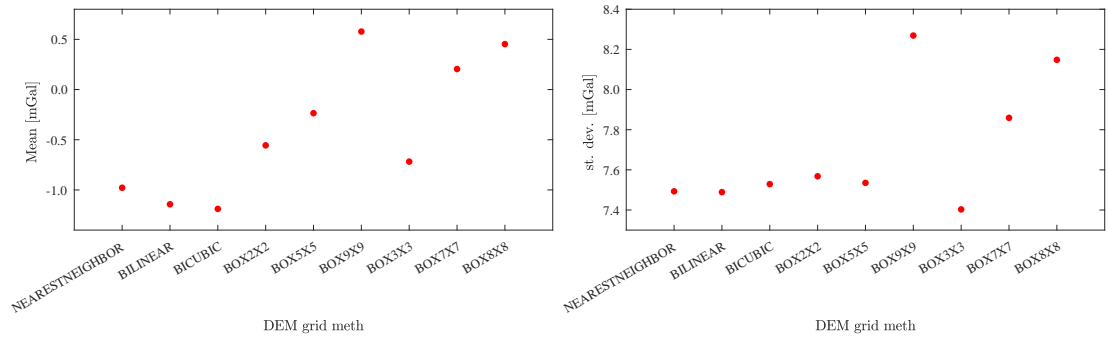


Figure 6.11: Mean and st. dev. of $\Delta g_{FA-GGM-RTM}$ as a function of gridding method of the digital elevation model (DEM grid meth)

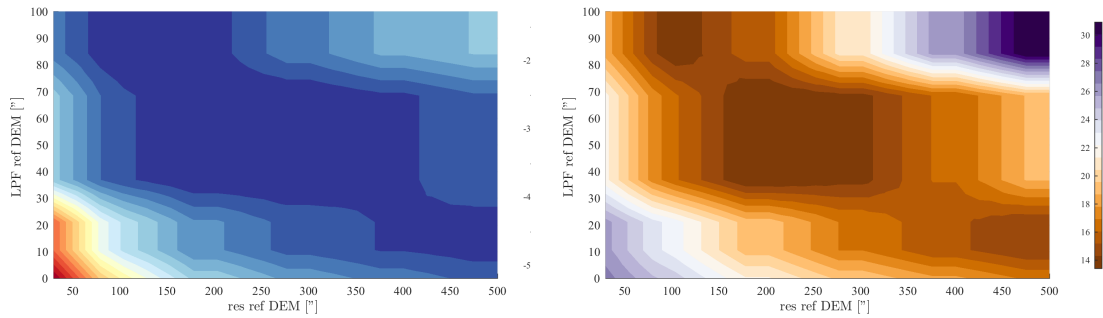


Figure 6.12: Mean and st. dev. of $\Delta g_{FA-GGM-RTM}$ as a function of reference DEM resolution (res ref DEM and reference DEM low pass filtering (LPF ref DEM)). EGM2008, with $n_{max} = 2190$. Units: [mGal].

All input parameters are fixed, whereas two input parameters change values. With each pair of values of two input parameters, residual gravity anomalies are calculated.

From the practical perspective, this is a more realistic case, because in real calculations, two or more parameters can depend on each other. For example, it is well known that n_{max} of the GGM and resolution of the reference DEM have to be changed simultaneously to achieve small residual anomalies.

Mean and st. dev. of $\Delta g_{FA-GGM-RTM}$ as a function of reference DEM resolution (res ref DEM) and reference DEM low pass filtering (LPF ref DEM) are shown in figure 6.12. Reference DEM resolution and LPF are reciprocal. If reference DEM resolution is increased reference DEM LPF has to be decreased in order to have smaller mean and standard deviation. Smallest residual gravity anomalies are achieved for res. ref. of 400'' and LPF 30''.

Mean and st. dev. of $\Delta g_{FA-GGM-RTM}$ as a function of maximum degree of GGM (n_{max}) and reference DEM resolution (res ref DEM) are shown in figure 6.13. The situation is more complex, because mean and standard deviation have different trends and are not having smallest values for the same n_{max} . For increasing n_{max} resolution of the reference DEM should be around 400''.

Mean and st. dev. of $\Delta g_{FA-GGM-RTM}$ as a function of inner zone radius (r_1) and outer zone radius (r_2) are shown in figure 6.14.

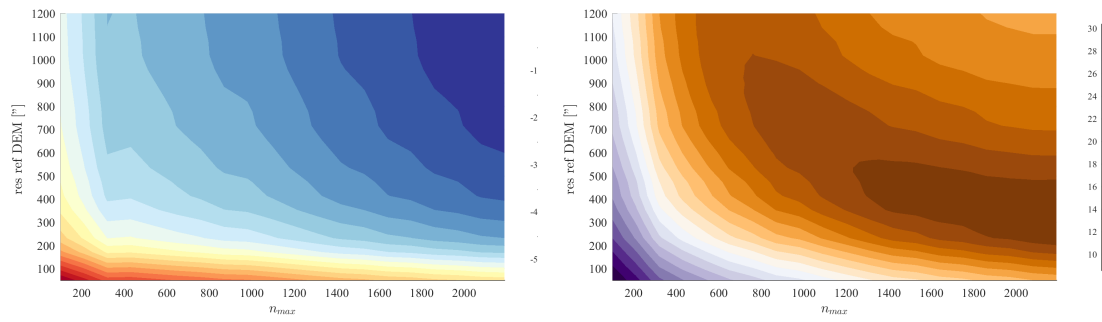


Figure 6.13: Mean and st. dev. of $\Delta g_{FA-GGM-RTM}$ as a function of maximum degree of GGM (n_{max}) and reference DEM resolution (res ref DEM). Units: [mGal].

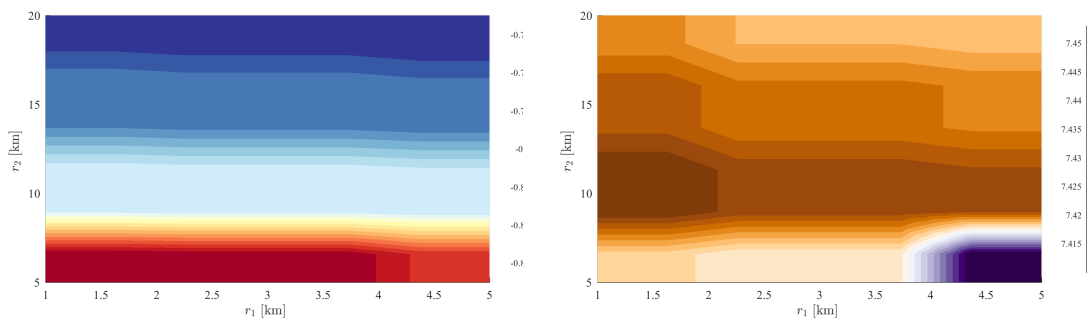


Figure 6.14: Mean and st. dev. of $\Delta g_{FA-GGM-RTM}$ as a function of inner zone radius (r_1) and outer zone radius (r_2). Units: [mGal].

6.3 Review

The combination of input models and parameters which will provide smallest standard deviation and mean value is important task prior to geoid determination. These statistical measures largely depend on several factors: study area, number and quality of gravity anomalies, availability of the DEMs and crustal models, etc. Up to some point, computation of the most suitable residual gravity anomalies $\Delta g_{FA-GGM-RTM}$ for particular area seems to be trial-error type of work. However, results in the previous section allow making few generalizations.

The influence of input parameters (from tables 6.1 and 6.2) on residual gravity anomalies may be divided into general categories. Categories are defined provisionally depending on the change of mean value and standard deviation as: 1) strong influence: parameter influences mean value or standard deviation more than 3 mGal; 2) moderate influence: parameter influences mean value or standard deviation between 1 and 3 mGal; 3) low influence: parameter influences mean value or standard deviation less than 1 mGal.

Based on the above defined categories it follows that following parameters have:

1. strong influence:
 - maximum degree of expansion of GGM,
 - resolution of fine DEM,
 - resolution of reference DEM,
 - low pass filtering of reference DEM,
 - crustal density ρ_c ,
2. moderate influence:
 - global geopotential model,
 - digital elevation model,
 - gridding method of digital elevation model,
3. low influence:
 - inner zone radius r_1 ,
 - outer zone radius r_2 ,
 - resolution of coarse DEM.

From the above results few recommendations can be drawn for easier selection of parameters and models in residual gravity field modelling:

- global geopotential model: satellite only GGM based on GOCE satellite mission for geoid determination, and EGM2008 for gravity anomaly maps or outlier detection,
- n_{max} : satellite only GGM from 200 to 250 for geoid determination, combined GGM with maximal degree (e.g. EGM2008 up to 2190),
- digital elevation model: SRTM3 or SRTM30,
- crustal density ρ_c : depending of study area; for this study area $\rho_c=2200 \text{ kgm}^{-3}$,
- fine DEM resolution: smaller than $10''$,
- coarse DEM resolution: any value from $10''$ to $60''$; lower resolution will increase speed of computations and will not affect results,
- reference DEM resolution and low pass filtering: depends on the parameter n_{max} ; e.g. for $n_{max} = 2000$ resolution of reference DEM around $300''$. One can choose either to change resolution or to low pass filter,

- inner r_1 and outer r_2 zone: for r_1 5 to 10 km, for $r_2 = 20$ km; smaller value r_2 decreases computation time.
- DEM gridding method: moving average with smaller box size (e.g. 3x3), nearest neighbor, bilinear, bicubic.

It must be emphasized that this is a numerical experiment on one study area, and results may be much different in other areas and input data. However, results are indicative and can point towards proper treatment of each input model or parameter.

Chapter 7

KTH geoid

Results of geoid determination over Croatia using KTH approach are presented in this chapter. The theory of KTH approach is comprehensively explained in section 4.6.

The main objectives of this chapter are the following:

1. Computation of gravimetric and hybrid geoid models using KTH approach.
2. Investigation of geoid model accuracy depending of different constant crustal density values ρ_c and surface crustal density models.
3. Investigation of geoid model accuracy all input data, models and parameters.

Table 7.1: Input data and parameters for geoid model determination using KTH approach

Data and parameter name	Acronym	Input values
free air gravity anomalies	Δg_{FA}	*gridded gravity database, see section: 5.1
global geopotential model	GGM	ITU GRACE16, goco05s, ITUGGC16, goconsgecf2timr5 egm2008, eigen 6c4
digital elevation model	DEM	SRTM3, SRTM15, SRTM30, GTOPO30, ETOPO1
constant crustal density (1D) density model (2D)	ρ_c $DDM2$	2000, 2100, ..., 3000 [kgm ⁻³] Airy-Heiskanen, Pratt-Hayford, Parasnis-Nettleton, CRUST1 (2D), EPcrust (2D)
variance of terrestrial gravity anomalies	C_0	1, 2, 3, ..., 20 [mgal]
kernel type of stochastic Stokes' integral	ν	1: optimum, 2: biased, 3: unbiased
spherical cap size	ψ_0	0.1, 0.2, ..., 2.0 [°]
integration radius of gravity gradients in DWC	ψ_{DgR}	0.1, ..., 1.0 [°]
input models (gravity, DEM) resolution	inp mod res	0.01, 0.02, ..., 0.1 [°]
output geoid resolution	geoid res	0.01, 0.02, 0.03, ..., 0.2 [°]
gridding method of digital elevation model	DEM grid meth	nearest neighbour, bilinear, bicubic, boxN×N for N = 1, 2, ..., 9
gridding method of gravity anomalies	anmly grid meth	bilinear, cubic, nearest neighbour, Greens' function approach

Input data and parameters are listed in table 7.1. More details about input data are described in chapter 5, sections 5.1 and 5.3. Filtered gravity database is used in all computations. Other used data for computation are GGM and DEM models. Several GGM models which showed best agreement with GNSS/levelling data are selected (see, 5.4.1). For topographic effects three SRTM-based DEMs, GTOPO30 and ETOPO1 are used. For crustal density in 1D case different

constant values from 2000 to 3100 kgm^{-3} are selected. In 2D case, surface crustal density models are used; CRUST1 and EPcrust, transformed from 3D to 2D by averaging of layers, and three additional models created by inversion methods according to the Airy-Heiskanen, Pratt-Hayford and Parasnis-Nettleton's models. Parameters in computation of geoid using KTH approach are: a) variance of terrestrial gravity anomalies C_0 , b) kernel type of stochastic Stokes' integral v , c) spherical cap size ψ_0 , and d) integration radius of gravity gradients Δg_{Trr} in DWC. These are crucial parameters in geoid determination by KTH approach, under assumption that the best possible gravity anomalies, GGM and DEM models are used. Few additional parameters may also affect solution such as resolution and gridding method of the input data and geoid model. Several values for geoid grid resolution, from 0.01° to 0.2° , are used in computations.

7.1 HRG2018-KTH: new gravimetric and hybrid geoid models

Around 3000 different geoid solutions are computed as a result of using many combinations of different input models and parameters. Statistics of the geoid solution that resulted in the smallest standard deviation when fitted to the GNSS/levelling is given in table 7.2. These models are named HRG2018-KTH-gra for gravimetric and HRG2018-KTH-hyb for hybrid (fitted) solution. Gravimetric (no-fit) solution has mean bias of almost -9 dm compared to GNSS/levelling. Bias is removed after fitting, while standard deviation is reduced to 3.5 cm. As it was the case in RCR geoid and GGM validation applying the 3rd polynomial parametric model resulted in smallest standard deviation when gravimetric geoid is fitted. Seven parametric model showed very similar results with 3.6 cm.

Table 7.2: Statistics of the geoid undulation differences $\delta N_{GNSS/lev.-geoid}$ for HRG2018-KTH geoid. Units: [cm].

fit model	min	max	range	mean	st. dev.
no fit	-99.5	-71.4	28.0	-87.3	4.8
bias	-12.2	15.7	27.9	0.0	4.8
linear	-12.8	13.8	26.6	0.0	4.0
2nd poly	-11.0	14.3	25.3	-0.0	3.9
3rd poly	-11.9	13.0	24.8	-0.0	3.5
3-p	-12.7	13.8	26.5	0.0	4.0
4-p	-11.0	14.4	25.4	-0.0	3.9
5-p	-10.9	14.5	25.4	-0.0	3.9
7-p	-11.5	14.1	25.6	0.0	3.6

The best gravimetric and the best hybrid solutions are selected after ascended sort of all computed geoid solutions by RMS values. Statistics of them are showed in table 7.3. However, difference between the best gravimetric and hybrid solution is in several dozens of centimeters implying that if gravimetric geoid solution has smallest standard deviation, it does not mean it will also have the smallest standard deviation after fitting to GNSS/levelling. This stands as one of unresolved problems of the computation with KTH approach. It is completely counterintuitive that these two solutions differ in mean values by 85 cm and in standard deviations around 27

Table 7.3: Statistics of the gravimetric and hybrid geoid solutions giving smallest RMS compared to GNSS/levelling. Selected among more than 3000 different solutions. Units: [cm].

selected solution by RMS	fitting parametric model	min	max	range	mean	st. dev.
best gravimetric solution	no fit	-96	97	193	-3.9	31.8
	3rdpoly	-90	74	164	1.2	22.9
best hybrid solution (HRG2018-KTH-gra and HRG2018-KTH-hyb)	no fit	-99	-71	28	-87.3	4.8
	3rdpoly	-12	13	25	0.0	3.5

cm (no fit rows in table 7.3). Gravimetric geoid which results in the smallest RMS compared to GNSS/levelling data should also agree well after fitting. Best gravimetric geoid solution has very small mean error but large standard deviation, while best hybrid ('fitted') geoid solution has the opposite, large mean value and small standard deviation. The best gravimetric solution after fitting does not improve agreement with GNSS/levelling. Even the mean value (bias) is not completely filtered in fitting procedure. After fitting it still has mean bias of 1.2 cm with standard deviation of 22.9 cm. Solution with such standard deviation is not reliable and much worse than the best gravimetric solution computed by RCR approach. It is even worse when compared to the geoid that could be computed from satellite-only GGM, not to say from the best GGM like EGM2008. The problem might be in computation of the approximate geoid undulation by the stochastic modification of the Stokes' kernel. It is known that hybrid geoid models are used in practical applications and are fixed to the national or continental MSL based vertical datum.

On figures 7.1 geoid undulation differences are visualized. As it can be seen from the left figure, the bias is so large that it cannot be visualized with the same scale as after fitting. On the right figure differences are mostly distributed around zero, without areas with evidently larger discrepancies. HRG2018-KTH-hyb for the largest part of the Croatian area has smaller differences than 3 cm. The issue with reliability of gridded δN differences on this figure is that only 495 GNSS/levelling points were used for the whole study area.

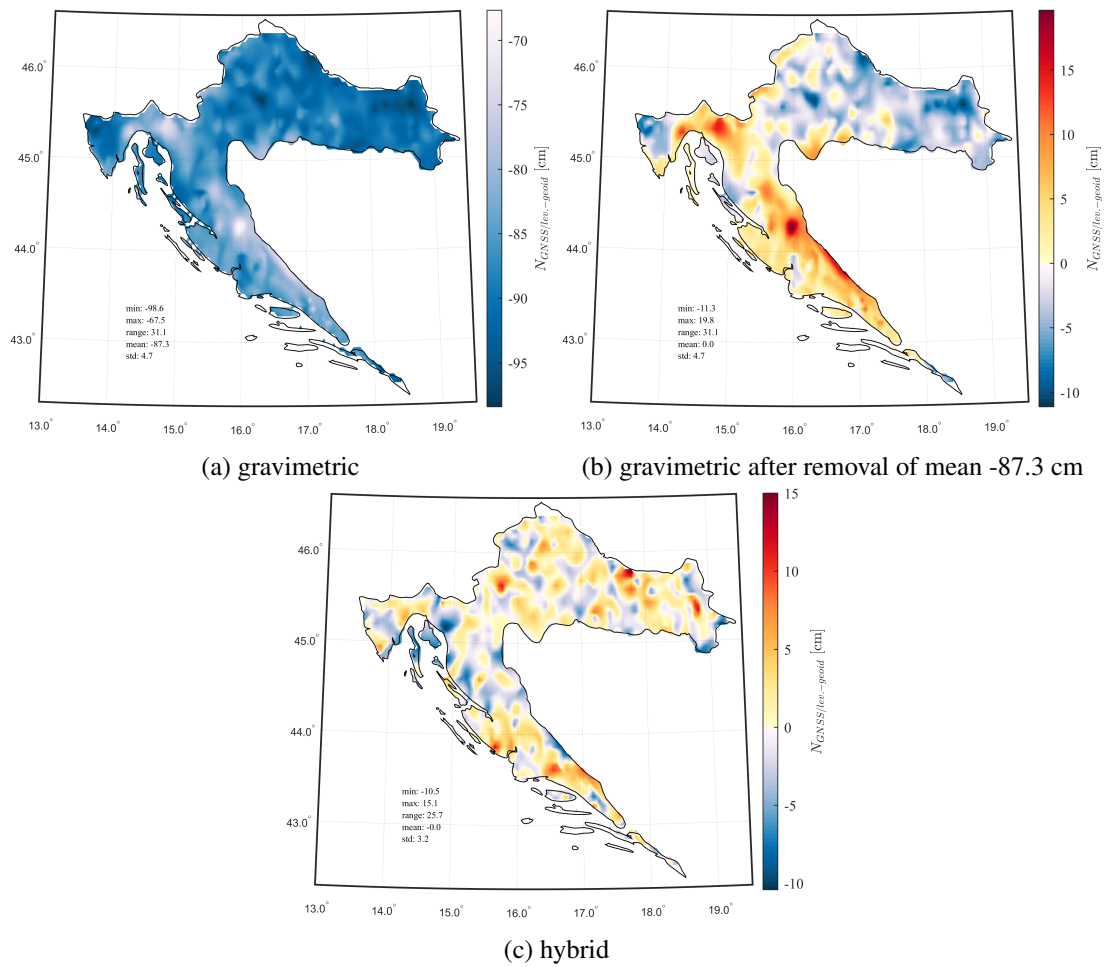


Figure 7.1: Gridded geoid undulation differences $\delta N_{GNSS/lev.-geoid}$ for gravimetric and hybrid KTH geoid models

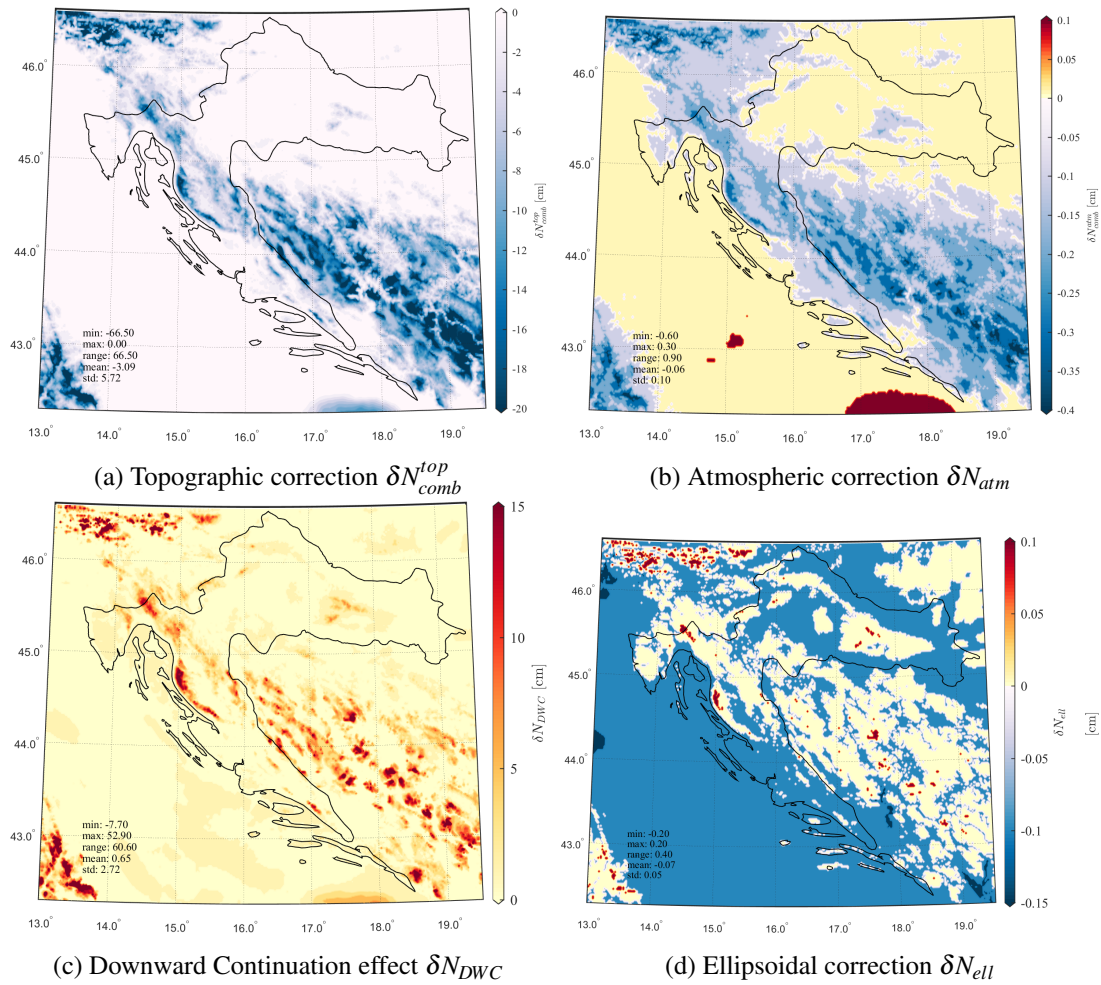


Figure 7.2: Additive correction of on geoid undulation in KTH approach

7.2 Additive corrections

The statistics of approximate geoid undulation and additive corrections are given in table 7.4. Approximate geoid undulation \tilde{N} has the largest values of all components in KTH approach ranging from 37.5 to 50.5 m. Topographic correction N_{comb}^{top} has most values around 3 cm with minimum of -66 cm. This correction reduces all approximated geoid undulations as it has only negative values. Atmospheric correction δN_{comb}^{atm} has almost all values smaller than 1 cm. Downward correction δN_{DWC} has strong contribution on the geoid undulation which ranges from -8 cm to 53 cm. Ellipsoidal effect δN_{ell} achieves values from -0.2 to 0.2 cm, which is for one order smaller than other corrections. Finally, geoid undulation N , after summing up all additive corrections, have values from 37.5 to 50.43 cm with mean value of 44.98 m.

Approximate geoid undulations \tilde{N} are shown in figure 7.3a. They are smooth and have visible correlation with topography. Computation of this contribution is the most crucial for

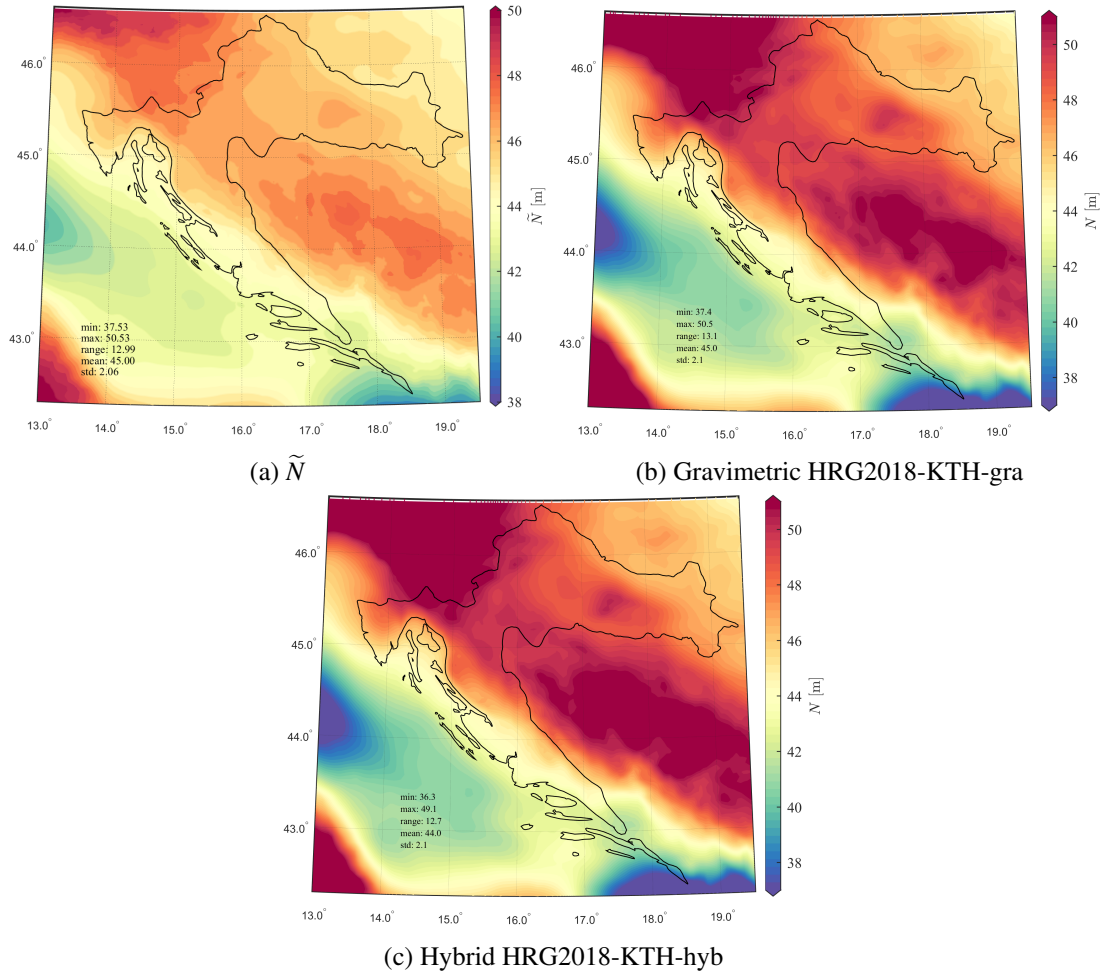
Figure 7.3: Approximate geoid undulation (\tilde{N}), gravimetric and hybrid geoid models HRG2018-KTH-gra

Table 7.4: KTH approach additive corrections

	Units	min	max	range	mean	st. dev.
\tilde{N}	[m]	37.53	50.53	12.99	45.00	2.06
δN_{top}	[cm]	-66.50	0.00	66.50	-3.09	5.72
δN_{atm}	[cm]	-0.60	0.30	0.90	-0.06	0.10
δN_{DWC}	[cm]	-7.70	52.90	60.60	0.65	2.72
δN_{ell}	[cm]	-0.20	0.20	0.40	-0.07	0.05
N	[m]	37.54	50.43	12.89	44.98	2.05

computation of final geoid undulation. Largest geoid undulation values, more than 46 m, are in the northern Alps area and along Dinaric Alps mountain chain. Smallest values are found along the coastline and in Adriatic Sea. Topographic effect δN_{comb}^{top} is shown on fig. 7.2a. It has a strong correlation with the topography. Over the sea and flat area it is almost zero, whereas in high mountainous it can have values of more than 60 cm. δN_{comb}^{top} has negative values everywhere, to compensate the effect of topographic masses which cause increasing the geoid undulation. Here selection of DEM strongly affects computed values of geoid undulations. Atmospheric effect N_{atm} is shown on fig. 7.2b. At this level of geoid accuracy (which is still not at the level of 1 cm) it should be taken care although it does not exceed values of more than 0.5 cm. Atmospheric effect is negative in high mountains, and positive value in sea areas and flat terrain.

According to Molodenskii free-air gravity anomalies refer to the topographic surface. Stokes integral requires gravity anomalies are given on the geoid therefore DWC has to be performed. In KTH approach this is not accounted for on gravity anomalies, so the error emerges in computation of approximated geoid undulation. According to Sjöberg DWC error can be accounted for after geoid computation in correction δN_{DWC} (shown on fig. 7.2c). DWC has a correlation with topography, as in δN_{comb}^{top} , with largest values where larger masses exist. It has mostly positive values which are almost everywhere less than 5 cm. In extreme cases values may have larger than 20 cm. Over the sea DWC effect is smaller with values achieving maximally 2 to 3 cm. Ellipsoidal effect on geoid undulation δN_{ell} is smaller than 0.2 cm over the entire study area, as it can be seen from figure 7.2d.

Final HRG2018-KTH gravimetric and hybrid geoid models are shown in figure 7.3.

7.3 Influence of input parameters and models on geoid solutions

Analysis of various input data and parameters on the accuracy of geoid models using KTH approach is performed using following procedure:

1. selection of the geoid solution which showed the best agreement with GNSS/levelling data (solution in table 7.2),
2. select and alter (change) each input data and parameter (all parameters given in table 7.2),
3. compute geoid solutions with altered selected data and parameter,
4. validate computed geoid solution on GNSS/levelling points and obtain standard deviation of δN differences,
5. analyze differences between geoid solution as a function of each altered data or parameter.

The same procedure is repeated for all input parameters and models from table 7.2.

Standard deviation of δN differences as a function of the selected global geopotential model is shown on figure 7.4. Models EGM2008, ITUGGC16, GOCONSGCF2TIMR5 and GOCO05s are tested. Geoid solution computed using EGM2008 model has smallest standard deviation. Coefficient of correlation is 0.5 indicating the importance of proper GGM selection. It should be emphasized only GGMs that showed the best agreement with the gravity and GNSS/levelling data on the study area were used (according to results in section 5.4.1). The differences between solutions would be much larger if GGMs which agree worse with terrestrial GNSS/levelling and gravity data would have been used.

Standard deviation of δN differences as a function of the maximal degree of GGM n_{max} is

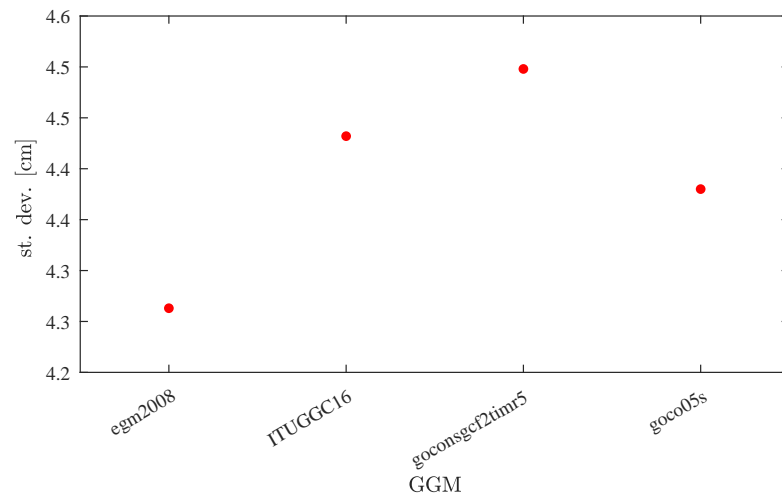


Figure 7.4: Standard deviation of $\delta N_{GNSS/lev.-geoid}$ as a function of global geopotential model (GGM)

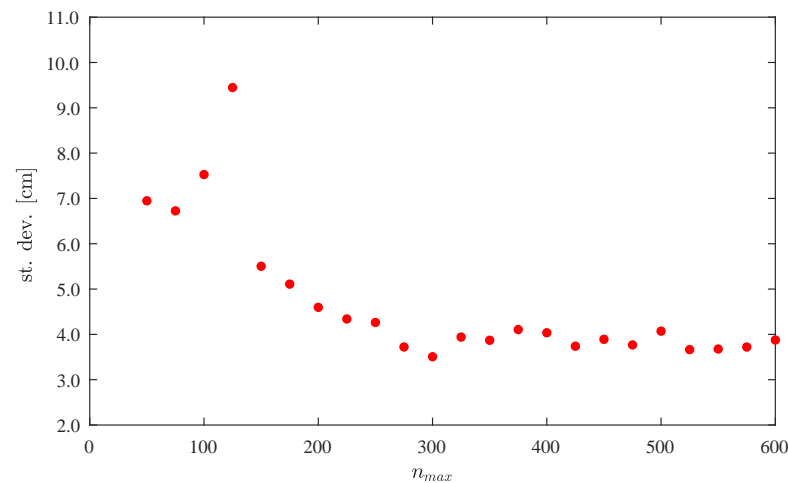


Figure 7.5: Standard deviation of $\delta N_{GNSS/lev.-geoid}$ as a function of maximum degree of GGM (n_{max})

shown on figure 7.5. Here, EGM2008 was used as input model. The importance of selection of the best maximal degree is evident as standard deviation is changed from approximately 10 cm to 3 cm for higher degrees n_{max} . For $n_{max} > 150$ standard deviation decreases rapidly until $n_{max} = 300$. For $n_{max} > 300$ standard deviation changes around 4 cm, indicating that GGMs afterwards are not ideal and well-suited for regional geoid determination. For $n_{max} > 300$ terrestrial data could improve geoid solution further. Coefficient of correlation is -0.7 which also confirms assumption that with the increase of n_{max} geoid model standard deviation decreases.

Standard deviation of δN differences as a function of the used digital elevation model is shown on figure 7.6. SRTM 3'' is the most accurate DEM over Croatia, followed by SRTM30, SRTM15, GTOPO30, ETOPO1 (according to [Varga and Bašić \(2013\)](#) and [Varga and Bašić \(2015\)](#)). DEMs are used in geoid modelling for topographic effects and downward continuation.

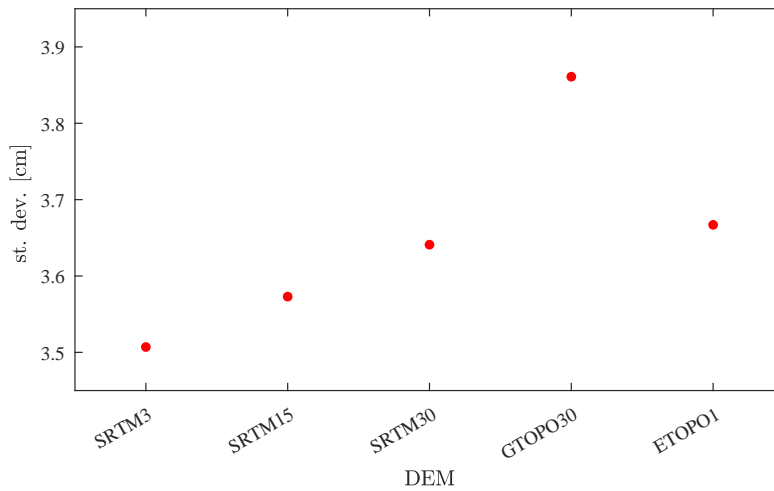


Figure 7.6: Standard deviation of $\delta N_{GNSS/lev.-geoid}$ as a function of digital elevation model (DEM)

Geoid undulation differences δN between solutions using different DEMs are few millimeters at most. This is not expected as past studies in the RCR approach have shown that DEMs have huge importance in gravimetric geoid modelling. However, such studies cannot be directly compared with result of the KTH approach as the modelling of topographic effects is largely different. However, it is indicative that even less accurate DEM models may provide accurate gravimetric geoid models. In any case, it is generally expected that the most detailed and accurate model for the particular study area shall be used for computations.

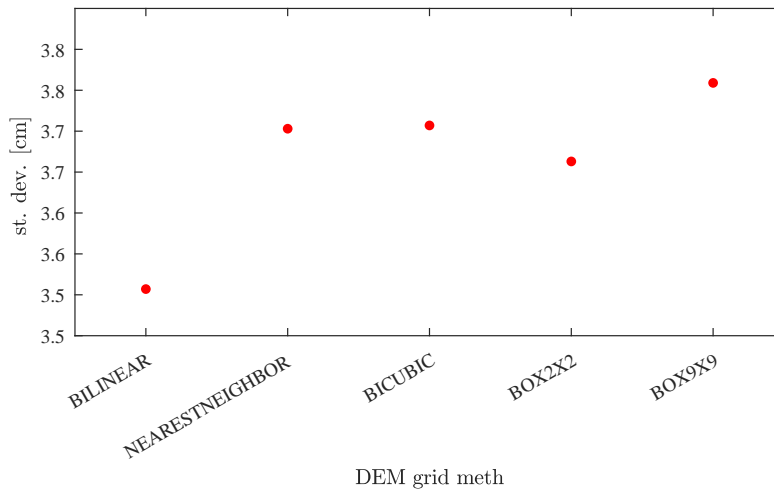


Figure 7.7: Standard deviation of $\delta N_{GNSS/lev.-geoid}$ as a function of gridding method of the digital elevation model (DEM grid meth)

Standard deviation of δN differences as a function of the gridding method of digital elevation model is shown on figure 7.7. This is a computational step in gravimetric geoid development where DEM in some cases has to be transformed from initial resolution another resolution. In

these cases appropriate interpolation method has to be selected. Tested interpolation methods are: bilinear, nearest neighbour, bicubic, and averaging using different box sizes. The results show that when DEM is gridded using bilinear interpolation the resulting geoid will result in the best agreement with GNSS/levelling. The differences between other interpolation methods are at the order of few millimeters.

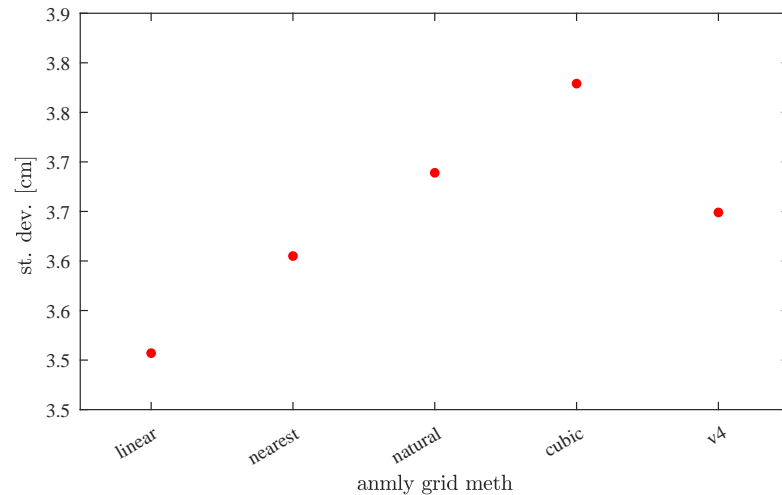


Figure 7.8: Standard deviation of $\delta N_{GNSS/lev.-geoid}$ as a function of gridding method of the anomalies (anmly grid meth)

Standard deviation of δN differences as a function of the gridding method of gravity anomalies is shown on figure 7.8. The objective is to find the best gridding method of gravity anomalies as Stokes integral require gridded gravity anomalies, whereas original gravity data are given as scattered (point) values. In this step, point free air anomalies were first transformed to complete Bouguer anomalies, then gridding was performed and finally free air anomalies (which are input data in KTH approach) are reconstructed from the gridded complete Bouguer anomalies. Tested interpolation methods are linear, nearest neighbour, natural neighbour, cubic and biharmonic spline interpolation (Matlab v4, see Sandwell 1987). Bilinear interpolation method shows smallest standard deviation compared to other methods. Overall, differences between different interpolation methods of gravity anomalies are at the order of few millimeters.

Standard deviation of δN differences as a function of the constant crustal density values ρ_c is shown on figure 7.9. Values of ρ_c from 2000 to 3100 with interval of 50 kgm^{-3} are tested. The differences between solutions are up to 5 mm. Therefore there is an small effect on geoid solution, but there is no clear indication which constant crustal density value could yield the best results. However, generally the most suitable value of the crustal density for this study area is from 2100 to 2500 kgm^{-3} .

Standard deviation of δN differences as a function of the geoid resolution is shown on figure 7.10. Tested geoid resolution values were from 0.005 to 0.2° with interval of 0.01° . Standard deviation of δN decreases with the increase of geoid resolution. Results with very highest resolution (e.g. 0.005°) indicate increase of the standard deviation. The best solution is obtained with resolution of 0.02° (or $1.2'$ or $72''$). The results indicate importance of the proper selection

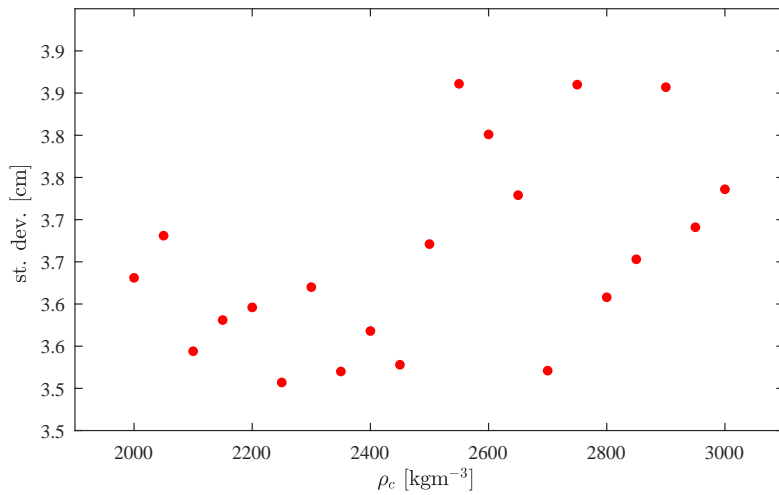


Figure 7.9: Standard deviation of $\delta N_{GNSS/lev-geoid}$ as a function of density of the crust (ρ_c)

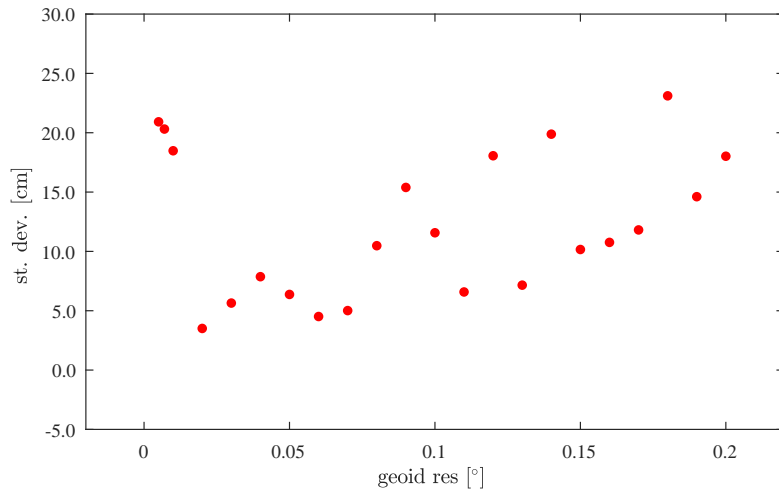


Figure 7.10: Standard deviation of $\delta N_{GNSS/lev-geoid}$ as a function of resolution of the geoid (geoid res)

of the geoid resolution.

Standard deviation of δN differences as a function of the spherical cap size ψ_0 is shown on figure 7.11 . Values of ψ_0 from 0.1° to 4° with the interval of 0.1° were tested. The differences between solutions depending of the ψ_0 are very large; difference between standard deviation of the best solution with $\psi_0 = 0.5^\circ$ and worst solution with $\psi_0 = 3.5^\circ$ is 30 cm. Generally, the solution that yielded smallest standard deviation are obtained with ψ_0 from 0.1 to 1° . It must be emphasized that these results are obtained with fixed $n_{max} = 300$ of EGM2008. Selection of the spherical cap size ψ_0 is not independent of the n_{max} so it is better to analyze changes in standard deviation as a function of both ψ_0 and n_{max} .

Standard deviation of δN differences as a function of variance of terrestrial gravity data C_0 is shown on figure 7.12. Values of C_0 from 1 mgal to 30 mgal with the interval of 1 mgal were

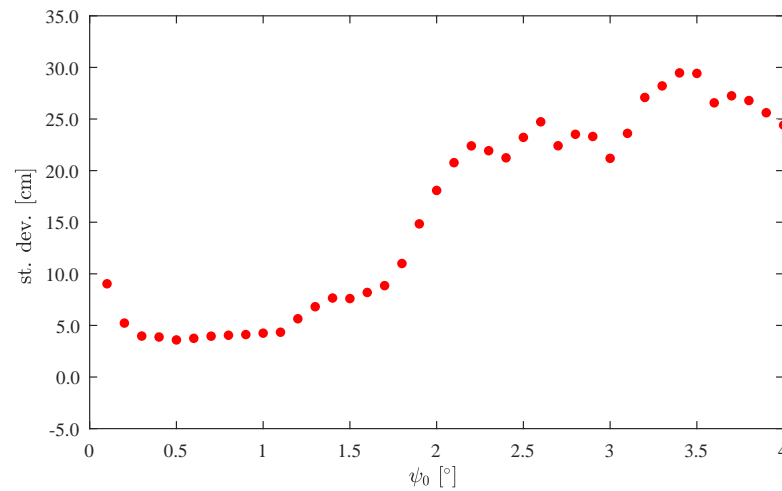


Figure 7.11: Standard deviation of $\delta N_{GNSS/lev.-geoid}$ as a function of spherical cap size (ψ_0)

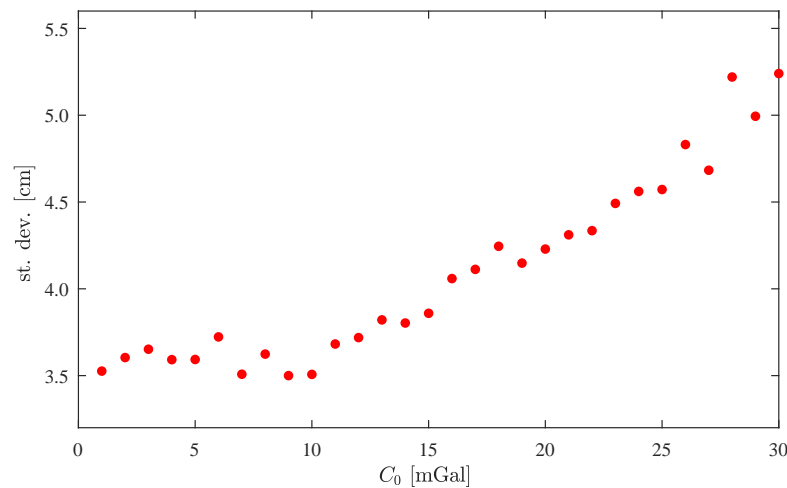


Figure 7.12: Standard deviation of $\delta N_{GNSS/lev.-geoid}$ as a function of variance of terrestrial gravity data (C_0)

tested. The differences between solutions depending of the variances C_0 are at the centimeter level. Differences between solutions with the smallest ($C_0 = 10$ mGal) and largest ($C_0 = 30$ mGal) standard deviations are 2 cm. For variances C_0 from 1 to 10 mGal the solutions are more or less identical, but for $C_0 > 10$ mGal standard deviation increases linearly. This show that in KTH approach selection of the proper stochastic prediction of input gravity data has large effect on geoid solution.

Standard deviation of δN differences as a function of Stokes integral stochastic solution is shown on figure 7.13. Tested values ν are: 1: biased. 2: unbiased, 3: optimum. Unbiased ($\nu = 2$ on x-axis of the figure) and optimum ($\nu = 3$ on x-axis on figure) have as twice as larger standard deviation compared to biased solution of the stochastic modification of Stokes' kernel. Furthermore, if all solutions of the geoid models are compared; unbiased ($\nu = 2$) and optimum

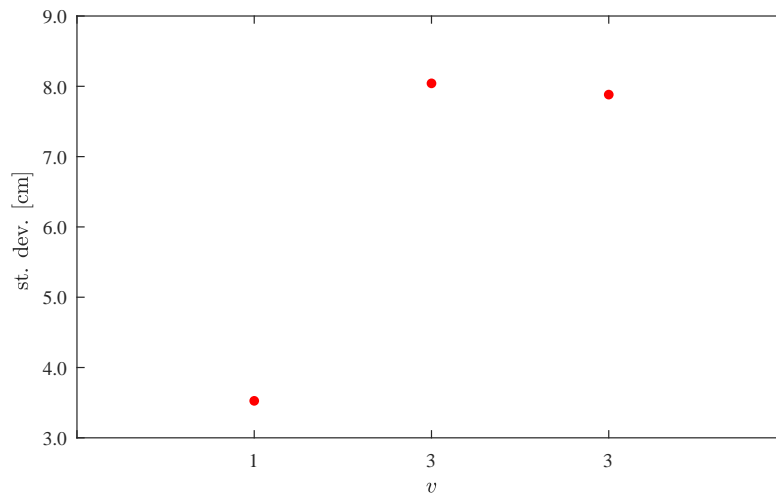


Figure 7.13: Standard deviation of $\delta N_{GNSS/lev.-geoid}$ as a function of Stokes integral stochastic solutions (v)

($v = 3$) solutions result in the smallest standard deviation for gravimetric geoid models (without fitting to the GNSS/levelling), whereas biased ($v = 1$) solutions result in the smallest standard deviation in hybrid geoid models (fitted to the GNSS/levelling with some parametric model). As on figure 7.13 fitted solutions with the 3rd parametric models are given, biased ($v = 1$) solutions have smallest standard deviation of 3.5 cm. This problem requires further investigations.

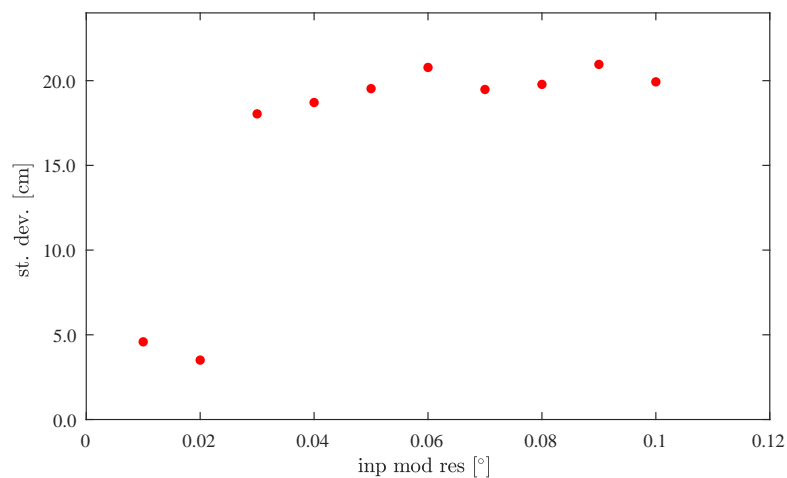


Figure 7.14: Standard deviation of $\delta N_{GNSS/lev.-geoid}$ as a function of input (gravity anomalies, DEMs) models resolution (inp mod res)

Standard deviation of δN differences as a function of input models resolution is shown on figure 7.14. As all input models have to be gridded in computations, their resolution has to be selected. Values from 0.01° to 0.1° with interval of 0.01° were tested. The differences between solutions with smallest and largest standard deviation are 15 cm. The solution with smallest standard deviation is where input models have resolution of 0.02° ($1.2'$ and $72''$) From 0.03°

to 0.1° results have values of around 20 cm.

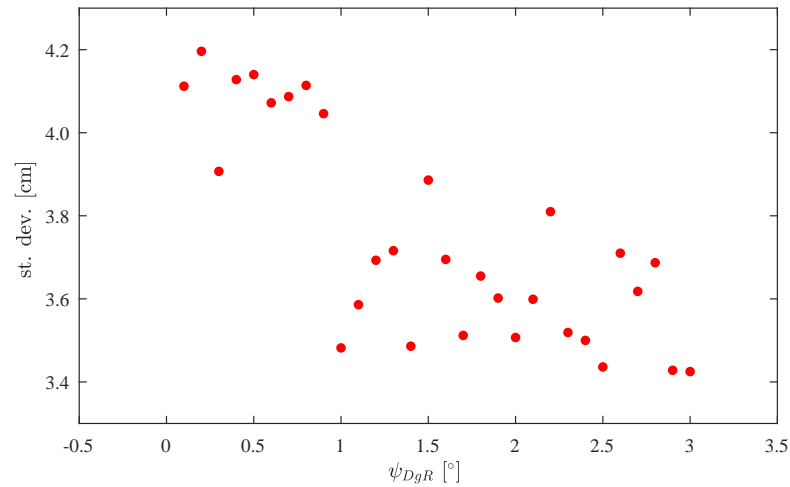


Figure 7.15: Standard deviation of $\delta N_{GNSS/lev-geoid}$ as a function of Integration radius of anomalies in DWC (ψ_{DgR})

Standard deviation of δN differences as a function of the integration radius of anomalies in DWC ψ_{DgR} is shown on figure 7.15. Contrary to the spherical cap size ψ_0 , where smallest standard deviations are obtained for $0.1^\circ < \psi_0 < 1^\circ$ (see, fig. 7.11), here smallest standard deviations are obtained for $1^\circ < \psi_{DgR} < 3^\circ$. The differences between solutions with smallest and largest standard deviation are more than 1 cm.

Chapter 8

Remove-Compute-Restore geoid

Results of geoid computations using RCR approach are presented in this section. Theoretical basis of the RCR approach is described in section 4.7.

In RCR approach geoid model can be computed using different geoid computation methods. Each method has advantages and drawbacks. Furthermore, each method has its own methodology of calculation with method-specific input parameters. For example, LSC uses point data, while Stokes uses gridded data. Stokes integration by FFT require zero padding of the input data, whereas analytic integration does not. In LSC stochastic model and covariance function has to be defined, while in Stokes integration all data have the same weight in computing geoid undulation.

Therefore, objectives of this section are:

- investigate the influence of different crustal models on resulting geoid models,
- comparison of geoid models and their's accuracy developed by different analytic and spectral geoid computation methods,
- investigate influence of different input parameters in each geoid computation method,
- find and analyze a solution which will give the best agreement with GNSS/levelling data,
- analyze fitting parametric models.

All used methods are listed in table 8.1 and these are 'classical' Stokes integration with unmodified and modified Stokes' kernel, flat-Earth and 3D collocation, and planar, spherical and spherical multi-band FFT. For each method different input parameters are used that will be listed for each method. Not all methods are discussed in details, therefore interested readers should consult references listed in table 8.1.

Input data in all methods are residual gravity anomalies $\Delta g_{FA-GGM-RTM}$. Computation of $\Delta g_{FA-GGM-RTM}$ is described in chapter 6. More than ten thousand solutions of residual gravity anomalies $\Delta g_{FA-GGM-RTM}$ were computed using different combinations of input parameters and models and only few solutions are chosen and used in geoid computations. They are selected by smallest RMS criteria and to have diversity of parameters, such as: GGM, maximal degrees of expansion, density, resolution of DEM, etc.

Table 8.1: Geoid computation methods in RCR approach

Geoid computation method	Acronym	Equations in section	Reference
Stokes integration (analytic)	Stokes	4.7.5.1	*see in section
LSC (spherical, 3D)	GEOCOL	4.7.4	Tscherning (1985), Tscherning (2013)
LSC (planar, 2D)	GPCOL	4.7.4.1	Forsberg (1987)
Planar FFT	GEOFOUR	4.7.6.1	Van Hees (1991)
Spherical multi-band FFT	SPFOUR	4.7.6.2	Forsberg and Sideris (1993)
Spherical 1D FFT	SP1D	4.7.6.4	Haagmans et al. (1993)

8.1 Solutions using different crustal density models

The statistics of geoid solutions computed using different density models is given in table 8.3. There are three groups of solutions: a) 1D using constant density values from 2000 to 3000 kgm^{-3} , b) 2D surface (lateral) density models: models computed by inversion using Pratt-Hayford, Airy-Heiskanen, and Parasnis-Nettleton methods, and crustal models CRUST1 and EPcrust which were averaged from original 3D layers to 2D, c) 3D crustal models CRUST1 and EPcrust. These crustal density models are used in all steps of geoid computation, including remove and restore steps as well as quasi-geoid to geoid correction.

Results of evaluation of hybrid (fitted) geoid solutions using different crustal density values and models are shown in table 8.4. Notable differences between solutions is in the statistical parameter mean error. Mean error increases if ρ_c is not the optimal value on computation area. In 1D case, when values of crustal density larger than 2700 kgm^{-3} are selected mean error increases for 4 to 5 cm compared to the solution with the smallest mean error -0.4 cm using $\rho_c = 2200 \text{ kgm}^{-3}$. In solutions where surface crustal density models are used, the solution where the model EPcrust is used results in the smallest mean error 0.3 cm. Where surface density crustal density models are created using inversion method, the solution where Pratt-Hayford model is used results in the smallest mean error 1.1 cm, while the biggest mean error is obtained using Airy-Heiskanen's density model.

In solutions where 3D density models are used, EPcrust model resulted in the smallest mean error 0.3 cm, where CRUST1 model resulted in 1.2 cm larger mean error. It suggests EPcrust 3D model is more appropriate on the Croatian territory. There are no big differences comparing 2D and 3D solution with CRUST1 and EPcrust models. Crustal models can improve representation of crustal structure but only up to some level. The reason lies in the coarse resolution of currently available models. CRUST1.0 is 1° and EPcrust 0.5° which means that crustal structure at this study area is represented with around 500 values when using CRUST1.0 and 1000 values when using EPcrust. If crustal models are compared to elevation models in terms detailednesses, e.g. SRTM in $3''$ resolution has around 278 million values for the same study area. This is apparently a limitation in using currently available crustal models in regional gravity field modelling and geoid determination.

Table 8.2: Statistics of residual gravity anomalies $\Delta g_{FA-GGM-RTM}$ selected for geoid computation

no.	min	max	range	mean	st. dev.	parameters
1	-60.2	194.5	254.6	-0.4	9.3	GGM= egm2008, $n_{max}=1000$, DEM= SRTM3, dens model= konst, $\rho_c=2670 \text{ kgm}^{-3}$, res fine DEM= 5'', res coarse DEM= 10'', res ref DEM= 90'', LPFref DEM= 50'', DEM grid meth= NEAREST NEIGHBOR, $r_1=5 \text{ km}$, $r_2=20 \text{ km}$
2	-83.0	177.5	260.5	-0.3	8.9	GGM= egm2008, $n_{max}=1500$, DEM= SRTM3, dens model= konst, $\rho_c=2670 \text{ kgm}^{-3}$, res fine DEM= 5'', res coarse DEM= 10'', res ref DEM= 90'', LPFref DEM= 30'', DEM grid meth= NEAREST NEIGHBOR, $r_1=5 \text{ km}$, $r_2=20 \text{ km}$
3	-52.2	186.1	238.2	-0.7	7.6	GGM= egm2008, $n_{max}=2190$, DEM= SRTM30, dens model= konst, $\rho_c=2300 \text{ kgm}^{-3}$, res fine DEM= 5'', res coarse DEM= 10'', res ref DEM= 30'', LPFref DEM= 80'', DEM grid meth= NEAREST NEIGHBOR, $r_1=5 \text{ km}$, $r_2=20 \text{ km}$
4	-52.1	186.1	238.2	-0.7	7.6	GGM= egm2008, $n_{max}=2190$, DEM= SRTM30, dens model= konst, $\rho_c=2300 \text{ kgm}^{-3}$, res fine DEM= 5'', res coarse DEM= 25'', res ref DEM= 30'', LPFref DEM= 80'', DEM grid meth= NEAREST NEIGHBOR, $r_1=5 \text{ km}$, $r_2=30 \text{ km}$
5	-71.1	167.3	238.5	-0.7	13.7	GGM= egm2008, $n_{max}=250$, DEM= SRTM3, dens model= konst, $\rho_c=2670 \text{ kgm}^{-3}$, res fine DEM= 5'', res coarse DEM= 10'', res ref DEM= 450'', LPFref DEM= 25'', DEM grid meth= NEAREST NEIGHBOR, $r_1=10 \text{ km}$, $r_2=100 \text{ km}$
6	-69.9	157.6	227.5	-0.6	13.8	GGM= ITU GGC16, $n_{max}=225$, DEM= SRTM3, dens model= konst, $\rho_c=2670 \text{ kgm}^{-3}$, res fine DEM= 5'', res coarse DEM= 10'', res ref DEM= 450'', LPFref DEM= 25'', DEM grid meth= NEAREST NEIGHBOR, $r_1=10 \text{ km}$, $r_2=100 \text{ km}$
7	-65.0	151.0	215.9	-0.7	14.4	GGM= goco05s, $n_{max}=225$, DEM= SRTM3, dens model= konst, $\rho_c=2670 \text{ kgm}^{-3}$, res fine DEM= 5'', res coarse DEM= 10'', res ref DEM= 385'', LPFref DEM= 25'', DEM grid meth= NEAREST NEIGHBOR, $r_1=10 \text{ km}$, $r_2=150 \text{ km}$
8	-53.1	186.7	239.7	-0.9	7.4	GGM= egm2008, $n_{max}=2190$, DEM= SRTM30, dens model= konst, $\rho_c=2200 \text{ kgm}^{-3}$, res fine DEM= 5'', res coarse DEM= 25'', res ref DEM= 30'', LPFref DEM= 80'', DEM grid meth= BOX 3X3, $r_1=1 \text{ km}$, $r_2=5 \text{ km}$
9	-62.7	186.2	248.9	-1.7	7.6	GGM= egm2008, $n_{max}=2190$, DEM= SRTM30, dens model= Epcrust, $\rho_c=\text{NaN kgm}^{-3}$, res fine DEM= 5'', res coarse DEM= 25'', res ref DEM= 30'', LPFref DEM= 80'', DEM grid meth= NEAREST NEIGHBOR, $r_1=5 \text{ km}$, $r_2=30 \text{ km}$
10	-53.5	185.3	238.8	-1.2	8.1	GGM= egm2008, $n_{max}=2190$, DEM= SRTM30, dens model= CRUST1, $\rho_c=\text{NaN kgm}^{-3}$, res fine DEM= 5'', res coarse DEM= 10'', res ref DEM= 30'', LPFref DEM= 80'', DEM grid meth= NEAREST NEIGHBOR, $r_1=5 \text{ km}$, $r_2=20 \text{ km}$
11	-57.4	186.4	243.8	-1.1	7.5	GGM= egm2008, $n_{max}=2190$, DEM= SRTM30, dens model= Pratt, $\rho_c=\text{NaN kgm}^{-3}$, res fine DEM= 5'', res coarse DEM= 10'', res ref DEM= 30'', LPFref DEM= 80'', DEM grid meth= NEAREST NEIGHBOR, $r_1=5 \text{ km}$, $r_2=20 \text{ km}$
12	-56.3	186.4	242.6	-1.1	7.5	GGM= egm2008, $n_{max}=2190$, DEM= SRTM30, dens model= Parasnis, $\rho_c=\text{NaN kgm}^{-3}$, res fine DEM= 5'', res coarse DEM= 10'', res ref DEM= 30'', LPFref DEM= 80'', DEM grid meth= NEAREST NEIGHBOR, $r_1=5 \text{ km}$, $r_2=20 \text{ km}$

In case of standard deviation, either in 1D, 2D or 3D cases of density models gravimetric geoid solutions among themselves have values from 5.0 cm to 8.0 cm. However, standard deviation seems to be more insensitive than mean error. For example in 3D case, when EPcrust and CRUST1 are used the difference is 1 mm. In 1D case using any value from $\rho_c = 2000 \text{ kgm}^{-3}$ to $\rho_c = 2400 \text{ kgm}^{-3}$ will bring differences of few millimeters in terms of standard deviation.

If solutions computed using 1D, 2D and 3D densities are compared, it can be concluded that there is a necessity to find and select more appropriate density values or model for geoid determination as systematic bias can be included with values that are larger than 5 cm. The differences between best solutions for the 1D, 2D and 3D cases are within 1-2 cm. For a 1 cm geoid model this effect might be crucial.

Table 8.3: Statistics of the geoid undulation differences $\delta N_{GNSS/lev.-geoid}$ for gravimetric geoid models computed with constant values, 2D surface (lateral) and 3D crustal models. Units: ρ_c in [kgm^{-3}], statistics in [cm].

crustal parameter/model		min	max	range	mean	st. dev.
1D	$\rho_c = 2000$	-14	15	29	1.6	5.7
	$\rho_c = 2100$	-14	14	29	1.0	5.1
	$\rho_c = 2200$	-15	14	28	-0.4	5.3
	$\rho_c = 2300$	-16	13	29	-1.5	5.4
	$\rho_c = 2400$	-16	13	29	-2.2	5.5
	$\rho_c = 2500$	-16	13	29	-3.2	6.1
	$\rho_c = 2600$	-17	13	29	-3.9	6.2
	$\rho_c = 2670$	-18	13	31	-4.7	6.1
	$\rho_c = 2700$	-19	13	31	-5.1	6.4
	$\rho_c = 2800$	-21	13	34	-6.0	6.9
	$\rho_c = 2900$	-24	13	36	-6.9	7.2
	$\rho_c = 3000$	-26	13	39	-8.1	7.8
$\rho_c = 3100$	-29	13	41	-9.3	8.0	
2D	CRUST1	-16	14	31	-2.0	5.6
	EPcrust	-15	15	30	0.3	5.2
	Airy-Heiskanen	-18	14	32	-4.3	6.8
	Parasnis-Nettleton	-15	15	30	1.2	5.7
	Pratt-Hayford	-14	14	29	1.1	5.2
3D	CRUST1	-16	14	31	-1.5	5.0
	EPcrust	-15	14	29	0.3	4.9

8.2 Solutions using different computation methods

8.2.1 'Classic' Stokes

Parameters for geoid computation with Stokes' method are given in table 8.5. Different Stokes' kernel modifications $Stokes_{mod}$ are used (explained in section 4.7.5.2). The basic Stokes' kernel is unmodified, whereas used modifications include Wong-Gore, Heck and Gruninger, Meissl's, spheroidal Molodenskii (Vaníček and Kleusberg) and spheroidal Molodenskii-Meissl (Featherstone). From the Stokes' kernel different degrees n_{mod} may be removed therefore values from 10 to 300 are used. Integration zone of anomalies is divided on inner and outer zone and different values of radiuses of integration in inner and outer zone are used.

More than 500 solutions using Stokes' integration were calculated using different combinations of input parameters and input residual gravity anomalies. Some selected results are given in table 8.6. The best solution is no. 3. with standard deviation 3.7 cm. It was derived using Vaníček and Kleusberg's modification with degree $n_{mod} = 400$, integration radiuses of inner and outer zone 0.1° and 1.0° .

Table 8.4: Statistics of the geoid undulation differences $\delta N_{GNSS/lev.-geoid}$ for hybrid (fitted) geoid models computed with constant values, 2D surface (lateral) and 3D crustal models. Units: ρ_c in $[\text{kgm}^{-3}]$, statistics in $[\text{cm}]$.

crustal parameter/model		min	max	range	mean	st. dev.
1D	$\rho_c = 2000$	-9	7	17	0.1	3.3
	$\rho_c = 2100$	-9	8	18	0.1	3.1
	$\rho_c = 2200$	-10	9	19	-0.2	3.3
	$\rho_c = 2300$	-10	9	18	-0.2	3.5
	$\rho_c = 2400$	-10	9	18	-0.2	3.5
	$\rho_c = 2500$	-9	9	18	-0.2	3.5
	$\rho_c = 2600$	-10	9	18	0.0	3.4
	$\rho_c = 2670$	-9	10	19	0.0	3.4
	$\rho_c = 2700$	-9	9	18	0.1	3.2
	$\rho_c = 2800$	-10	9	20	0.0	3.5
	$\rho_c = 2900$	-18	10	28	0.1	3.9
	$\rho_c = 3000$	-9	10	20	0.1	3.6
	$\rho_c = 3100$	-11	9	20	0.0	3.5
2D	CRUST1	-8	10	18	0.3	3.2
	EPcrust	-9	7	17	-0.4	3.5
	Airy-Heiskanen	-12	8	19	-0.1	3.4
	Parasnis-Nettleton	-9	8	17	0.1	3.3
	Pratt-Hayford	-8	8	16	0.3	3.1
3D	CRUST1	-8	9	18	0.3	3.0
	EPcrust	-9	7	16	-0.3	2.9

Table 8.5: Input data and parameters for computation of geoid using Stokes method

Data and parameter name	Acronym	Input values
residual gravity anomalies	$\Delta g_{FA-GGM-RTM}$	table 8.2
Stokes' kernel modification	$Stokes_{mod}$	0: no modification, 1: spheroidal (Wong and Gore), 2: Heck and Gruening, 3: Meissl, 4: spheroidal Molodensky (Vaníček and Kleusberg), 5: spheroidal Molodenski-Meissl
degree of Stokes' kernel modification	n_{mod}	10, 20, 50, 100, 200, 300, 500
inner zone integration range	ψ_{in}	0.25, 0.5, 1.0, 2.0 [$^\circ$]
outer zone integration range	ψ_{out}	3, 4, 5 [$^\circ$]

8.2.2 Planar FFT

Parameters for geoid computation with the planar FFT are given in table 8.7. Two parameters are changed in computations: tapering window width $iwndw$ and removal of the mean value from the input anomalies $lmean$. Tapering window is used for elimination of periodicity effect which

Table 8.6: Statistics of the differences between GNSS/levelling and selected geoid models computed using Stokes method. Fitting parametric model: 3rdpoly. Units: [cm].

no.	min	max	range	mean	st. dev.	input values of parameters
1	-54.2	54.0	108.2	-0.2	14.5	$Stokes_{mod}=1$, $\psi_{in}=0.3^\circ$, $\psi_{out}=3.0^\circ$, $n_{mod}=200$, GGM= goco05s, $n_{max}=225$, dens model= konst, $\rho_c=2670 \text{ kgm}^{-3}$, DEM= SRTM3, DEM grid meth= NEAREST NEIGHBOR, res fine DEM= 5'', res coarse DEM= 10'', res ref DEM= 385'', LPFref DEM= 25'', $r_1=10 \text{ km}$, $r_2=150 \text{ km}$
2	-16.2	12.9	29.0	0.0	3.8	$Stokes_{mod}=2$, $\psi_{in}=0.1^\circ$, $\psi_{out}=1.0^\circ$, $n_{mod}=200$, GGM= egm2008, $n_{max}=2190$, dens model= konst, $\rho_c=2300 \text{ kgm}^{-3}$, DEM= SRTM30, DEM grid meth= NEAREST NEIGHBOR, res fine DEM= 5'', res coarse DEM= 25'', res ref DEM= 30'', LPFref DEM= 80'', $r_1=5 \text{ km}$, $r_2=30 \text{ km}$
3	-16.9	13.4	30.3	-0.0	3.7	$Stokes_{mod}=4$, $\psi_{in}=0.1^\circ$, $\psi_{out}=1.0^\circ$, $n_{mod}=400$, GGM= egm2008, $n_{max}=2190$, dens model= konst, $\rho_c=2300 \text{ kgm}^{-3}$, DEM= SRTM30, DEM grid meth= NEAREST NEIGHBOR, res fine DEM= 5'', res coarse DEM= 10'', res ref DEM= 30'', LPFref DEM= 80'', $r_1=5 \text{ km}$, $r_2=20 \text{ km}$
4	-14.1	12.8	26.9	0.0	3.8	$Stokes_{mod}=3$, $\psi_{in}=0.1^\circ$, $\psi_{out}=1.0^\circ$, $n_{mod}=0$, GGM= egm2008, $n_{max}=2190$, dens model= CRUST1, $\rho_c=\text{NaN} \text{ kgm}^{-3}$, DEM= SRTM30, DEM grid meth= NEAREST NEIGHBOR, res fine DEM= 5'', res coarse DEM= 25'', res ref DEM= 30'', LPFref DEM= 80'', $r_1=5 \text{ km}$, $r_2=30 \text{ km}$
5	-15.0	12.9	27.9	0.1	3.8	$Stokes_{mod}=5$, $\psi_{in}=0.1^\circ$, $\psi_{out}=1.0^\circ$, $n_{mod}=400$, GGM= egm2008, $n_{max}=2190$, dens model= CRUST1, $\rho_c=\text{NaN} \text{ kgm}^{-3}$, DEM= SRTM30, DEM grid meth= NEAREST NEIGHBOR, res fine DEM= 5'', res coarse DEM= 25'', res ref DEM= 30'', LPFref DEM= 80'', $r_1=5 \text{ km}$, $r_2=30 \text{ km}$

is a problem related to the discrete Fourier transform. According to Forsberg and Tscherning (2008) this can be avoided either by zero-padding or windowing of the data on the borders (edges).

Table 8.7: Input data and parameters for computation of geoid using planar FFT method

Data and parameter name	Acronym	Input values
residual gravity anomalies	$\Delta g_{FA-GGM-RTM}$	table 8.2
tapering windowing width	<i>indow</i>	0, 1, 2, 3, 5, 10, 20, 30 [grid points]
remove mean from data	<i>lmean</i>	1: yes, 0: no

More than 1300 solutions are computed using different parameters and residual gravity anomalies. The best solution is no. 3 in which CRUST1 3D model is used (table 8.8). Windowing was used for 20 grid points, without removal of mean values from the data. Otherwise, more than 100 solutions resulted in blank or strange geoid undulation values. Comparison between solutions with and without removed mean from the data does not seem to improve results.

Table 8.8: Statistics of the differences between GNSS/levelling and selected geoid models computed using planar FFT method. Fitting parametric model: 3rdpoly. Units: [cm].

no.	min	max	range	mean	st. dev.	input values of parameters
1	-10.9	8.4	19.4	-0.0	3.0	$l_{mean}=0$, $iv_{ndow}=40$, GGM= egm2008, $n_{max}=2190$, dens model= konst, $\rho_c=2300 \text{ kgm}^{-3}$, DEM= SRTM30, DEM grid meth= NEAREST NEIGHBOR, res fine DEM= 5'', res coarse DEM= 10'', res ref DEM= 30'', LPFref DEM= 80'', $r_1=5 \text{ km}$, $r_2=20 \text{ km}$
2	-9.2	12.5	21.7	0.0	3.1	$l_{mean}=0$, $iv_{ndow}=10$, GGM= egm2008, $n_{max}=2190$, dens model= Pratt, $\rho_c=\text{NaN} \text{ kgm}^{-3}$, DEM= SRTM30, DEM grid meth= NEAREST NEIGHBOR, res fine DEM= 5'', res coarse DEM= 25'', res ref DEM= 30'', LPFref DEM= 80'', $r_1=5 \text{ km}$, $r_2=30 \text{ km}$
3	-9.7	12.3	22.0	-0.0	3.1	$l_{mean}=0$, $iv_{ndow}=34$, GGM= egm2008, $n_{max}=2190$, dens model= CRUST1, $\rho_c=\text{NaN} \text{ kgm}^{-3}$, DEM= SRTM30, DEM grid meth= NEAREST NEIGHBOR, res fine DEM= 5'', res coarse DEM= 25'', res ref DEM= 30'', LPFref DEM= 80'', $r_1=5 \text{ km}$, $r_2=30 \text{ km}$
4	-10.5	8.8	19.4	0.0	3.0	$l_{mean}=0$, $iv_{ndow}=20$, GGM= egm2008, $n_{max}=2190$, dens model= Pratt, $\rho_c=\text{NaN} \text{ kgm}^{-3}$, DEM= SRTM30, DEM grid meth= NEAREST NEIGHBOR, res fine DEM= 5'', res coarse DEM= 10'', res ref DEM= 30'', LPFref DEM= 80'', $r_1=5 \text{ km}$, $r_2=20 \text{ km}$
5	-10.8	9.7	20.5	-0.0	3.1	$l_{mean}=0$, $iv_{ndow}=20$, GGM= egm2008, $n_{max}=2190$, dens model= Parasnis, $\rho_c=\text{NaN} \text{ kgm}^{-3}$, DEM= SRTM30, DEM grid meth= NEAREST NEIGHBOR, res fine DEM= 5'', res coarse DEM= 10'', res ref DEM= 30'', LPFref DEM= 80'', $r_1=5 \text{ km}$, $r_2=20 \text{ km}$

8.2.3 LSC with flat-Earth logarithmic covariances

Parameters for geoid computation with the least squares collocation using planar logarithmic covariance function are given in table 8.9. Selected values for *splintsizeECF* are 1, 2, 5, 10, 20 km. Block computation is done using blocks with sizes from 0.5° to 3°, as computation with 22000 available point data showed to be slow. Values from 0.1 to 10 mGal are used for observation errors σ_{max} . Values of parameters C_0 , D and T are obtained from empirical covariance function (ECF).

More than 200 solutions using different parameters and residual gravity anomalies are calculated. The best solution is no. 3 where 3D model CRUST1.0 is used with standard deviation 3.1 cm and mean error 0.0 cm after fitting (table 8.10).

8.2.4 Least Squares Collocation

Parameters for geoid computation with the least squares collocation are given in table 8.11. This is the most complex method for geoid determination which has to be performed in few steps: 1) derivation of empirical covariance function, 2) fitting of ECF, 3) calculation of height anomalies.

Selected results of geoid models are given in table 8.12. The best solution is no. 4 with standard deviation 3.0 cm and mean error 0.0 cm. Under assumption that residual gravity anomalies are smooth and parameters of fitted covariance function describe their trend with small RMS it gives stable solutions. For many variations using different input parameters standard deviation does not exceed values of more than 4 cm. In comparison with FFT, where changing some of the parameters can produce differences of more than few cm's among solutions.

Table 8.9: Input data and parameters for computation of geoid using flat-Earth logarithmic LSC method

Data and parameter name	Acronym	Input values
residual gravity anomalies	$\Delta g_{FA-GGM-RTM}$	table 8.2
sample interval size of ECF	$smplintsizeECF'$	1,2, 5, 10, 20 [km]
block size	$blcksize$	0.5, 1, 2, 3 [°]
overlap of neighbour blocks	$blckovrlp$	0.5 [°]
observation error	σ_{max}	0.1, 1, 2, 5, 10 [mGal]
search ranges of attenuation factors D and T		(1 10), (10 100) [km]
variance of data	$C0$	* computed from fitting of the analytic ECF to the flat flat-earth logarithmic covariance function
high frequency attenuation factor	D	
low frequency attenuation factor	T	

Table 8.10: Statistics of the differences between GNSS/levelling and selected geoid models computed using flat-Earth logarithmic LSC method. Fitting parametric model: 3rdpoly. Units: [cm].

no.	min	max	range	mean	st. dev.	input values of parameters
1	-9.1	9.5	18.6	-0.0	3.3	$smplintsizeECF = 3$ km, $blcksize = 0.75$ °, $blckovrlp = 0.50$ °, $\sigma_{max} = 2.0$ mgal, $C0 = 6.57$ mgal, $D = 1$ km, $T = 12$ km, GGM= egm2008, $n_{max} = 2190$, dens model= konst, $\rho_c = 2200$ kgm ⁻³ , DEM= SRTM30, DEM grid meth= BOX 3X3, res fine DEM= 5'', res coarse DEM= 25'', res ref DEM= 30'', LPFref DEM= 80'', $r_1 = 1$ km, $r_2 = 10$ km
2	-17.5	16.9	34.4	0.0	4.9	$smplintsizeECF = 20$ km, $blcksize = 0.75$ °, $blckovrlp = 0.50$ °, $\sigma_{max} = 3.0$ mgal, $C0 = 13.64$ mgal, $D = 20$ km, $T = 15$ km, GGM= goco05s, $n_{max} = 225$, dens model= konst, $\rho_c = 2670$ kgm ⁻³ , DEM= SRTM3, DEM grid meth= NEAREST NEIGHBOR, res fine DEM= 5'', res coarse DEM= 10'', res ref DEM= 385'', LPFref DEM= 25'', $r_1 = 10$ km, $r_2 = 150$ km
3	-9.3	10.6	19.9	0.1	3.1	$smplintsizeECF = 10$ km, $blcksize = 0.20$ °, $blckovrlp = 0.50$ °, $\sigma_{max} = 3.0$ mgal, $C0 = 6.83$ mgal, $D = 1$ km, $T = 20$ km, GGM= egm2008, $n_{max} = 2190$, dens model= CRUST1, $\rho_c = NaN$ kgm ⁻³ , DEM= SRTM30, DEM grid meth= NEAREST NEIGHBOR, res fine DEM= 5'', res coarse DEM= 25'', res ref DEM= 30'', LPFref DEM= 80'', $r_1 = 5$ km, $r_2 = 30$ km
4	-9.6	10.3	19.8	0.0	3.3	$smplintsizeECF = 2$ km, $blcksize = 0.20$ °, $blckovrlp = 0.50$ °, $\sigma_{max} = 10.0$ mgal, $C0 = 6.95$ mgal, $D = 1$ km, $T = 17$ km, GGM= egm2008, $n_{max} = 2190$, dens model= Eprust, $\rho_c = NaN$ kgm ⁻³ , DEM= SRTM30, DEM grid meth= NEAREST NEIGHBOR, res fine DEM= 5'', res coarse DEM= 25'', res ref DEM= 30'', LPFref DEM= 80'', $r_1 = 5$ km, $r_2 = 30$ km

8.2.5 Spherical multi-band FFT

Parameters for geoid computation using spherical multi-band FFT method are given in table 8.13. In this method Wong-Gore Stokes modification is used. Method-specific parameters is number of reference parallels no_{par} . Other used parameters are: a) radiuses of integration in inner and outer zones ψ_{in} and ψ_{out} , b) degrees of modification of Wong-Gore's kernel, c) tapering

Table 8.11: Input data and parameters for computation of geoid using LSC method

Data and parameter name	Acronym	Input values
residual gravity anomalies	$\Delta g_{FA-GGM-RTM}$	table 8.2
Empirical covariance function		
sample interval size of ECF	$splintsizeECF'$	5, 10, 15 [']
Fitting of the empirical covariance function (Tscherning 1976a, Tscherning 1976b)		
type of degree variance-covariance function model used for degree-variances larger than n_{max}	$ktype$	1, 2, 3
integer in numerator of the anomaly degree-variance model	$linter$	
ratio between the Bjerhammar-sphere radius and the mean radius of the Earth R_E	R	
the depth to the Bjerhammar sphere of the radius R_B	$idepth$	
variance of gravity anomalies at zero altitude	$vargd2$	400 [mgal ²]
maximal degree for empirical degree-variances	$imax$	usually corresponds to the maximal degree of EGM
error degree variances model	$model$	computed from $\sigma_{C_{nm}}$ and $\sigma_{S_{nm}}$ of the corresponding GGM
model used from degree	$imin$	2, 50, 100
input error degree variance scale factor	vg or AA	1
number of iterations for nonlinear adjustment	$nitmax$	
apriori standard deviations of AA , A and $RB - RE$ in adjustment	τ_{AA} , τ_A , τ_{RB-RE}	1.0
no of values taken from ECF	$idat$	5, 10, 15
relative weight	$weight$	0.1, 0.5
data variance at mean altitude	cc	200, 400 [mgal ²]
standard deviation of observations	wm	0.1 [mgal]

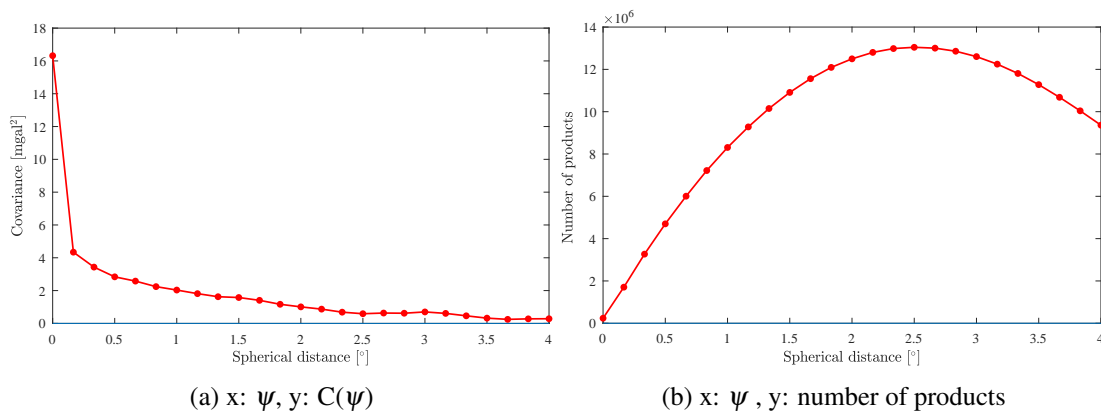


Figure 8.1: Empirical covariance function for the best solution

Table 8.12: Statistics of the differences between GNSS/levelling and selected geoid models computed using least squares collocation method. Fitting parametric model: 3rdpoly. Units: [cm].

no.	min	max	range	mean	st. dev.	input values of parameters
1	-10.9	11.4	22.4	-0.1	3.3	<i>ktype</i> = 2, <i>linter</i> = 4, <i>R</i> = -2.76 km, <i>vargd2</i> = 17.68 mGal ² , <i>imin</i> = 2, <i>imax</i> = 600, <i>nitmax</i> = 10, $\tau_1 = 1$, $\tau_2 = 1$, $\tau_3 = 1$, <i>idat</i> = 5, <i>weight</i> = 0.1, <i>cc</i> = 400, <i>vg</i> = 0.73, <i>weight</i> = 0.1, GGM= egm2008, <i>nmax</i> = 2190, dens model= konst, $\rho_c = 2200 \text{ kgm}^{-3}$, DEM= SRTM30, DEM grid meth= BOX 3X3, res fine DEM= 5'', res coarse DEM= 25'', res ref DEM= 30'', LPFref DEM= 80'', $r_1 = 1 \text{ km}$, $r_2 = 10 \text{ km}$
2	-10.2	9.4	19.6	-0.0	3.1	<i>ktype</i> = 2, <i>linter</i> = 4, <i>R</i> = -2.75 km, <i>vargd2</i> = 17.84 mGal ² , <i>imin</i> = 2, <i>imax</i> = 600, <i>nitmax</i> = 10, $\tau_1 = 1$, $\tau_2 = 1$, $\tau_3 = 1$, <i>idat</i> = 5, <i>weight</i> = 0.1, <i>cc</i> = 400, <i>vg</i> = 0.73, <i>weight</i> = 0.1, GGM= egm2008, <i>nmax</i> = 2190, dens model= konst, $\rho_c = 2300 \text{ kgm}^{-3}$, DEM= SRTM30, DEM grid meth= NEAREST NEIGHBOR, res fine DEM= 5'', res coarse DEM= 10'', res ref DEM= 30'', LPFref DEM= 80'', $r_1 = 5 \text{ km}$, $r_2 = 20 \text{ km}$
3	-10.6	9.9	20.6	-0.0	3.1	<i>ktype</i> = 2, <i>linter</i> = 4, <i>R</i> = -2.75 km, <i>vargd2</i> = 17.84 mGal ² , <i>imin</i> = 2, <i>imax</i> = 600, <i>nitmax</i> = 10, $\tau_1 = 1$, $\tau_2 = 1$, $\tau_3 = 1$, <i>idat</i> = 5, <i>weight</i> = 0.1, <i>cc</i> = 400, <i>vg</i> = 0.73, <i>weight</i> = 1.0, GGM= egm2008, <i>nmax</i> = 2190, dens model= konst, $\rho_c = 2300 \text{ kgm}^{-3}$, DEM= SRTM30, DEM grid meth= NEAREST NEIGHBOR, res fine DEM= 5'', res coarse DEM= 10'', res ref DEM= 30'', LPFref DEM= 80'', $r_1 = 5 \text{ km}$, $r_2 = 20 \text{ km}$
4	-10.5	9.0	19.5	0.0	3.0	<i>ktype</i> = 2, <i>linter</i> = 4, <i>R</i> = -2.75 km, <i>vargd2</i> = 17.84 mGal ² , <i>imin</i> = 2, <i>imax</i> = 600, <i>nitmax</i> = 10, $\tau_1 = 1$, $\tau_2 = 1$, $\tau_3 = 1$, <i>idat</i> = 5, <i>weight</i> = 0.1, <i>cc</i> = 400, <i>vg</i> = 0.73, <i>weight</i> = 1.0, GGM= egm2008, <i>nmax</i> = 2190, dens model= konst, $\rho_c = 2300 \text{ kgm}^{-3}$, DEM= SRTM30, DEM grid meth= NEAREST NEIGHBOR, res fine DEM= 5'', res coarse DEM= 10'', res ref DEM= 30'', LPFref DEM= 80'', $r_1 = 5 \text{ km}$, $r_2 = 20 \text{ km}$
5	-10.0	9.9	19.9	0.0	3.2	<i>ktype</i> = 2, <i>linter</i> = 5, <i>R</i> = -2.74 km, <i>vargd2</i> = 17.85 mGal ² , <i>imin</i> = 2, <i>imax</i> = 600, <i>nitmax</i> = 10, $\tau_1 = 1$, $\tau_2 = 1$, $\tau_3 = 1$, <i>idat</i> = 15, <i>weight</i> = 0.1, <i>cc</i> = 400, <i>vg</i> = 0.73, <i>weight</i> = 1.0, GGM= egm2008, <i>nmax</i> = 2190, dens model= konst, $\rho_c = 2300 \text{ kgm}^{-3}$, DEM= SRTM30, DEM grid meth= NEAREST NEIGHBOR, res fine DEM= 5'', res coarse DEM= 10'', res ref DEM= 30'', LPFref DEM= 80'', $r_1 = 5 \text{ km}$, $r_2 = 20 \text{ km}$

window and d) remove mean value from the data.

Few selected results are given in table 8.14. The solution which gives the smallest standard deviation is no. 4 with 3.7 cm. It was calculated with $nref = 5$ and integration radius in inner zone $\psi_{in} = 0.1^\circ$.

8.2.6 Spherical 1D FFT

Parameters for geoid computation using 1D FFT are given in table 8.15. In this algorithm Wong-Gore's kernel modification is implemented with modification degrees n_{mod_1} and n_{mod_2} . Integration area is divided in two zones inner and outer which are defined with two parameters ψ_{in} and ψ_{out} . Different values are tested for all input parameters.

More than two thousand different solutions are computed using different combination of input parameters and data. Few selected results are given in table 8.16. The best solution is no. 1 with standard deviation of 3.6 cm and mean value 0.0 cm. It was calculated with radiuses of integration of inner and outer zone of $\psi_{in} = 0.1^\circ$ and $\psi_{out} = 3.0^\circ$ and degrees of removal n_{mod_1}

Table 8.13: Input data and parameters for computation of geoid using spherical multi-band FFT method

Data and parameter name	Acronym	Input values
residual gravity anomalies	$\Delta g_{FA-GGM-RTM}$	table 8.2
number of reference parallels	nr_{par}	1, 2, 3, 4, 5
inner zone integration range	Ψ_{in}	0.25, 0.5, 1.0, 2.0 [°]
outer zone integration range	Ψ_{out}	3, 4, 5 [°]
lower range of Stokes' kernel modification	n_{mod1}	10, 20, 50, 100
upper range of Stokes' kernel modification	n_{mod2}	100, 200, 300, 400
tapering windowing width	$iwindow$	0, 1, 2, ..., 10, 20, 30 [grid nodes]
remove mean from data	$lmean$	1: yes, 0: no

Table 8.14: Statistics of the differences between GNSS/levelling and selected geoid models computed using spherical multi-band FFT method. Fitting parametric model: 3rdpoly. Units: [cm].

no.	min	max	range	mean	st. dev.	input values of parameters
1	-64.6	51.1	115.6	-0.1	16.8	$nref=2, \Psi_{in}=0.5^\circ, \Psi_{out}=3.0^\circ,$ $n_{mod1}=50, n_{mod2}=300, lmean=0,$ $iwindow=5, GGM=ITU\ GGC16, n_{max}=225, dens\ model=konst,$ $\rho_c=2670\ kgm^{-3}, DEM=SRTM3, DEM\ grid\ meth=NEAREST\ NEIGHBOR,$ $res\ fine\ DEM=5'', res\ coarse\ DEM=10'',$ $res\ ref\ DEM=450'', LPFref\ DEM=25'',$ $r_1=10\ km, r_2=100\ km$
2	-17.7	12.9	30.6	0.0	3.8	$nref=2, \Psi_{in}=0.5^\circ, \Psi_{out}=2.0^\circ,$ $n_{mod1}=200, n_{mod2}=300, lmean=0,$ $iwindow=0, GGM=egm2008, n_{max}=2190, dens\ model=Epcrust,$ $\rho_c=NaN\ kgm^{-3}, DEM=SRTM30, DEM\ grid\ meth=NEAREST\ NEIGHBOR,$ $res\ fine\ DEM=5'', res\ coarse\ DEM=10'',$ $res\ ref\ DEM=30'', LPFref\ DEM=80'',$ $r_1=5\ km, r_2=20\ km$
3	-17.8	13.2	31.0	0.1	3.8	$nref=2, \Psi_{in}=0.5^\circ, \Psi_{out}=2.0^\circ,$ $n_{mod1}=200, n_{mod2}=300, lmean=0,$ $iwindow=0, GGM=egm2008, n_{max}=2190, dens\ model=Pratt,$ $\rho_c=NaN\ kgm^{-3}, DEM=SRTM30, DEM\ grid\ meth=NEAREST\ NEIGHBOR,$ $res\ fine\ DEM=5'', res\ coarse\ DEM=10'',$ $res\ ref\ DEM=30'', LPFref\ DEM=80'',$ $r_1=5\ km, r_2=20\ km$
4	-17.9	13.2	31.2	-0.1	3.8	$nref=2, \Psi_{in}=0.5^\circ, \Psi_{out}=2.0^\circ,$ $n_{mod1}=200, n_{mod2}=300, lmean=0,$ $iwindow=0, GGM=egm2008, n_{max}=2190, dens\ model=Parasnis,$ $\rho_c=NaN\ kgm^{-3}, DEM=SRTM30, DEM\ grid\ meth=NEAREST\ NEIGHBOR,$ $res\ fine\ DEM=5'', res\ coarse\ DEM=10'',$ $res\ ref\ DEM=30'', LPFref\ DEM=80'',$ $r_1=5\ km, r_2=20\ km$
5	-17.3	13.0	30.4	0.0	3.7	$nref=2, \Psi_{in}=0.1^\circ, \Psi_{out}=2.0^\circ,$ $n_{mod1}=200, n_{mod2}=300, lmean=0,$ $iwindow=0, GGM=egm2008, n_{max}=2190, dens\ model=konst,$ $\rho_c=2200\ kgm^{-3}, DEM=SRTM30, DEM\ grid\ meth=NEAREST\ NEIGHBOR,$ $res\ fine\ DEM=5'', res\ coarse\ DEM=10'',$ $res\ ref\ DEM=30'', LPFref\ DEM=80'',$ $r_1=5\ km, r_2=20\ km$

and n_{mod2} of 200 and 250.

Table 8.15: Input data and parameters for computation of geoid using spherical 1D FFT method

Data and parameter name	Acronym	Input values
residual gravity anomalies	$\Delta g_{FA-GGM-RTM}$	table 8.2
inner zone integration range	Ψ_{in}	0.25, 0.5, 1.0, 2.0 [°]
outer zone integration range	Ψ_{out}	3, 4, 5 [°]
lower range of Stokes' kernel modification	n_{mod_1}	10, 50, 100, 200, 250
upper range of Stokes' kernel modification	n_{mod_2}	100, 200, 300, 400, 600
remove mean from data	$lmean$	1: yes, 0: no

Table 8.16: Statistics of the differences between GNSS/levelling and selected geoid models computed using spherical 1D FFT method. Fitting parametric model: 3rdpoly. Units: [cm].

no.	min	max	range	mean	st. dev.	input values of parameters
1	-13.7	13.3	27.0	-0.0	3.6	$\Psi_{in} = 0.1^\circ$, $\Psi_{out} = 3.0^\circ$, $n_{mod_1} = 200$, $n_{mod_2} = 250$, $lmean = 0$, GGM= egm2008, $n_{max} = 2190$, dens model= konst, $\rho_c = 2200 \text{ kgm}^{-3}$, DEM= SRTM30, DEM grid meth= BOX 3X3, res fine DEM= 5'', res coarse DEM= 25'', res ref DEM= 30'', LPFref DEM= 80'', $r_1 = 1 \text{ km}$, $r_2 = 5 \text{ km}$
2	-34.4	30.2	64.6	-0.0	10.0	$\Psi_{in} = 0.1^\circ$, $\Psi_{out} = 2.0^\circ$, $n_{mod_1} = 100$, $n_{mod_2} = 200$, $lmean = 0$, GGM= goco05s, $n_{max} = 225$, dens model= konst, $\rho_c = 2670 \text{ kgm}^{-3}$, DEM= SRTM3, DEM grid meth= NEAREST NEIGHBOR, res fine DEM= 10'', res coarse DEM= 20'', res ref DEM= 400'', LPFref DEM= 30'', $r_1 = 10 \text{ km}$, $r_2 = 30 \text{ km}$
3	-18.4	12.5	30.9	-0.0	3.8	$\Psi_{in} = 0.3^\circ$, $\Psi_{out} = 1.0^\circ$, $n_{mod_1} = 200$, $n_{mod_2} = 200$, $lmean = 0$, GGM= egm2008, $n_{max} = 2190$, dens model= Parasnis, $\rho_c = \text{NaN kgm}^{-3}$, DEM= SRTM30, DEM grid meth= NEAREST NEIGHBOR, res fine DEM= 5'', res coarse DEM= 10'', res ref DEM= 30'', LPFref DEM= 80'', $r_1 = 5 \text{ km}$, $r_2 = 20 \text{ km}$
4	-16.4	13.0	29.4	-0.0	3.7	$\Psi_{in} = 0.1^\circ$, $\Psi_{out} = 2.0^\circ$, $n_{mod_1} = 200$, $n_{mod_2} = 250$, $lmean = 0$, GGM= egm2008, $n_{max} = 2190$, dens model= Pratt, $\rho_c = \text{NaN kgm}^{-3}$, DEM= SRTM30, DEM grid meth= NEAREST NEIGHBOR, res fine DEM= 5'', res coarse DEM= 10'', res ref DEM= 30'', LPFref DEM= 80'', $r_1 = 5 \text{ km}$, $r_2 = 20 \text{ km}$
5	-17.7	13.3	31.0	0.0	3.8	$\Psi_{in} = 0.3^\circ$, $\Psi_{out} = 2.0^\circ$, $n_{mod_1} = 200$, $n_{mod_2} = 250$, $lmean = 0$, GGM= egm2008, $n_{max} = 2190$, dens model= CRUST1, $\rho_c = \text{NaN kgm}^{-3}$, DEM= SRTM30, DEM grid meth= NEAREST NEIGHBOR, res fine DEM= 5'', res coarse DEM= 25'', res ref DEM= 30'', LPFref DEM= 80'', $r_1 = 5 \text{ km}$, $r_2 = 30 \text{ km}$

8.2.7 Validation of geoid models computed with RCR and KTH approaches

Statistical comparison of geoid models computed using different methods and validated on GNSS/levelling points is given in table 8.17. The best fit is obtained using planar FFT (GEOFOUR) and spherical 3D LSC (GEOCOL) of 3.0 and 3.1 cm. Very similar results are obtained with analytic Stokes integration method (Stokes), spherical multi-band FFT (SPFOUR) and SP1D methods. The differences between different methods are all within 1 cm; GEOFOUR as the best, and SPFOUR as the worst solution. The results indicate that the best RCR approach hybrid geoid solution is better for 0.5 cm than the best KTH approach solution.

Table 8.17: Comparison of the statistics of geoid undulation differences ($\delta N_{GNSS/lev.-geoid}$). Geoid models are computed using different RCR methods and KTH approach. Fit: 3rdpoly, units: [cm].

Geoid computation method	min	max	range	mean	st dev
KTH	-11.4	12.1	23.5	-0.2	3.4
Stokes	-16.8	12.8	29.5	-0.0	3.7
GEOFOUR	-9.7	12.3	22.0	-0.0	3.1
GPCOL	-10.6	10.8	21.4	0.1	3.1
SPFOUR	-17.3	13.0	30.4	0.0	3.7
GEOCOL	-10.6	9.1	19.7	0.1	3.1
SP1D	-16.6	11.7	28.3	-0.0	3.6

Mean value (error) is (almost) completely removed within the fitting procedure, with maximal values of -0.2 cm in KTH.

8.2.7.1 Differences between geoid models computed using different methods

Statistics of geoid undulations (N) for models computed using different methods are shown in table 8.18. Selected solutions in this case are the ones that resulted in the best agreement with GNSS/levelling data as they are considered to be the most accurate. Geoid undulations N over study area have values between 36.6 m and 50.5 m, with mean values of 44.1 m. All RCR approach solutions have almost the same values for all statistical parameters. Geoid computed using KTH approach has differences of around 1 m in comparison with RCR approach solutions for minimum, maximum and mean.

Statistics of the differences between gravimetric geoid models computed using different methods is given in table 8.19. The differences are obtained by subtraction of gravimetric geoid grids ($grid_1 - grid_2$).

The biggest differences are obtained when geoid model derived using KTH approach is subtracted from geoid derived using RCR approach. For example, when KTH and RCR GEOCOL grids are subtracted the mean value is 1.01 m. More generally, mean differences between KTH geoid and different RCR solutions are having values from 88 to 101 cm. The differences can achieve in some areas values of 1.4 m, while minimal differences seize around 38 cm. Slightly better agreement with KTH geoid showed geoid computed using SPFOUR method. KTH and RCR approach are both unique and non-easily comparable approaches, but these differences are

Table 8.18: Statistics of gravimetric geoid models computed using different computation methods. Units: [cm].

Geoid method	min	max	range	mean	st dev
KTH	37.4	50.5	13.1	45.0	2.1
Stokes	36.6	49.7	13.0	44.1	2.1
GEOFOUR	36.7	49.8	13.1	44.1	2.1
GPCOL	36.4	49.6	13.2	44.0	2.2
SPFOUR	36.6	49.8	13.1	44.1	2.1
GEOCOL	36.7	49.5	12.8	44.0	2.2
SP1D	36.6	49.7	13.1	44.1	2.1

hard to explain and should be analysed thoroughly in the future. Currently, it looks like these are completely different surfaces.

Differences are much smaller, although they still exist, when only RCR computation methods are compared. Largest differences are between GPCOL and SP1D methods with -13.0 ± 12.4 cm. GEOCOL and GPCOL method agree within -0.6 ± 6.3 cm. However, both GEOCOL and GPCOL do not agree well with other methods. E.g. GEOCOL- SP1D results in the -12.4 ± 14.6 . SPFOUR and SP1D agree the best with -0.1 ± 1.3 cm. Stokes and SP1D differ by -3.4 ± 3.6 cm.

Gridded differences between geoid models computed using various RCR methods are given in appendix B. The scale is unique for all figures, therefore, differences which are larger than 20 cm, as between KTH and different RCR methods, are completely red.

Largest differences between methods are in the Adriatic sea where altimetric data from DTU15 model were included in the database. In order to increase reliability of future gravimetric geoid model solutions, the existing gravity database will need to be updated with new data in these areas.

Differences between GEOFOUR and GEOCOL (subfigure *n*), and GEOFOUR and GPCOL (subfigure *l*), are for the most of computation area constant although at the south of computation area there are some visible differences at the borders in FFT methods.

Table 8.19: Statistics of the differences ($\delta N = grid - grid$) between gravimetric geoid models computed using different computation methods. Units: [cm].

Geoid method	min	max	range	mean	st. dev.
KTH - Stokes	36.1	117.0	80.5	91.8	10.2
KTH - GEOFOUR	28.9	133.0	104.0	92.7	12.8
KTH - GPCOL	45.8	141.0	95.4	102.0	15.5
KTH - SPFOUR	31.7	114.0	82.2	88.3	9.7
KTH - GEOCOL	39.9	147.0	107.0	101.0	16.9
KTH - SP1D	32.0	114.0	82.1	88.4	9.6
Stokes - GEOFOUR	-14.8	25.3	40.1	0.9	7.5
Stokes - GPCOL	-8.0	34.2	42.2	9.6	9.2
Stokes - SPFOUR	-16.0	5.9	21.8	-3.5	4.1
Stokes - GEOCOL	-14.8	40.2	54.9	9.0	11.3
Stokes - SP1D	-15.6	4.0	19.6	-3.4	3.6
GEOFOUR - GPCOL	-7.0	34.5	41.5	8.8	8.8
GEOFOUR - SPFOUR	-39.4	16.5	55.9	-4.4	10.5
GEOFOUR - GEOCOL	-12.8	38.1	50.9	8.2	8.0
GEOFOUR - SP1D	-35.1	15.4	50.5	-4.3	9.8
GPCOL - SPFOUR	-47.3	9.3	56.6	-13.1	12.7
GPCOL - GEOCOL	-29.1	17.1	46.2	-0.6	6.3
GPCOL - SP1D	-46.1	7.0	53.1	-13.0	12.4
SPFOUR - GEOCOL	-13.9	54.1	67.9	12.5	15.0
SPFOUR - SP1D	-3.0	4.8	7.8	0.1	1.3
GEOCOL - SP1D	-52.4	13.5	65.9	-12.4	14.6

8.3 HRG2018-RCR: new gravimetric and hybrid geoid models

The solution which resulted in the smallest standard deviation compared to GNSS/lev. was calculated using GEOFOUR method. This can be considered as the best solution when compared to all other RCR methods and also solution obtained using KTH approach. Names are given to those models: HRG2018-RCR-gra for gravimetric and HRG2018-RCR-hyb for hybrid variant of the model. Input parameters of this solution are given in section 8.2.2, table 8.8, no. 3.

Quasi-geoid (ζ) to geoid (N) correction

Gravimetric quasi-geoid defined by height anomalies ζ is obtained as a result of computations using RCR approach and residual gravity anomalies $\Delta g_{FA-GGM-RTM}$ (as explained in subsection 4.7.1). The gravimetric geoid defined by geoid undulations is obtained by applying quasi-geoid to geoid correction ($\zeta - N$).

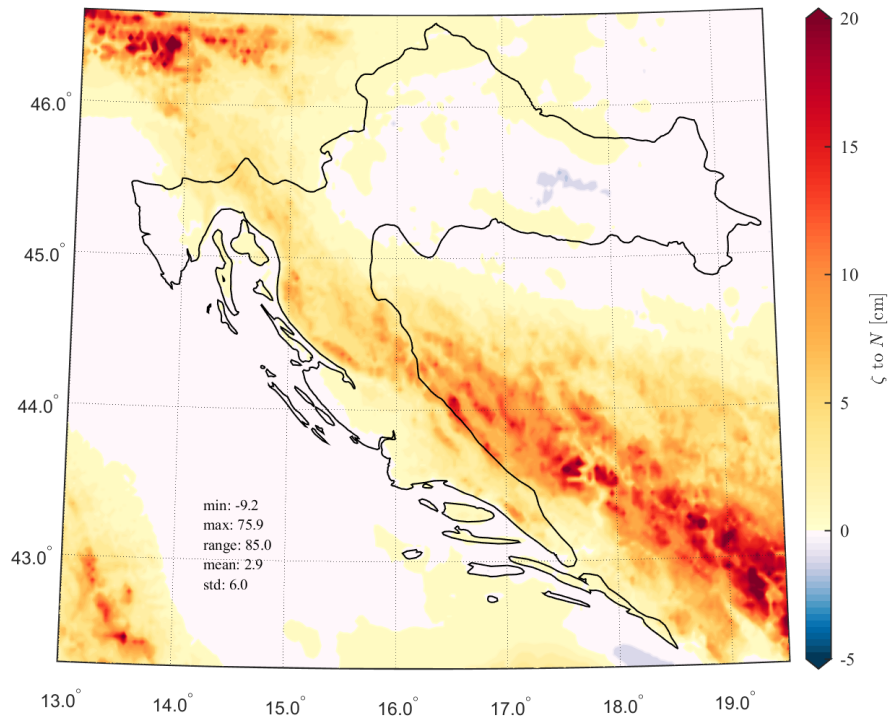


Figure 8.2: Quasi-geoid (ζ) to geoid (N) correction

The quasi-geoid to geoid correction is for the most part of the study area around 1 to 2 cm, as it can be seen from figure 8.2. It is largest in mountainous areas, such as Alps at the north, Velebit in the middle and Dinarides at the south-east of the study area. Its maximal values are larger than 15 cm. In coastal areas and in low-lands this correction is small and can sometimes be neglected.

Remove-restore contributions in gravity anomalies and geoid undulations

Statistics of the different gravity anomalies contributions in remove step and calculation of input residual gravity anomalies are given in table 8.20. Residual gravity anomalies $\Delta g_{FA} - \Delta g_{GGM} - \Delta g_{RTM}$, after subtracting GGM and RTM contribution, have standard deviation of 6.5 and mean value of -1.0 mGal. This means that input anomalies were very smooth and have no systematic biases or outliers in the data prior to geoid computation, which is a preferable property, although it can be argued whether by selection of $n_{max} = 2190$ medium wavelengths have also been filtered. The mean value is actually increased if only RTM effect Δg_{RTM} is filtered from the Δg_{FA} anomalies in remove step, which implies that gravity anomalies $\Delta g_{FA} - \Delta g_{RTM}$ have no special meaning and interpretation unless long-wavelengths are not filtered. Actually, the most important step is derivation of the reference surface (reference DEM) which replace and model short-frequency part of gravity anomalies. Statistics of the geoid undulation contributions to the

Table 8.20: Statistics of the *remove* gravity anomaly contributions of the input residual gravity anomalies $\Delta g_{FA} - \Delta g_{GGM} - \Delta g_{RTM}$. Units: [mGal].

Contribution	min	max	range	mean	st. dev.
Δg_{FA}	-130.7	216.6	347.3	9.9	34.9
Δg_{GGM}	-114.2	172.4	286.6	16.4	34.2
Δg_{RTM}	-267.6	67.8	335.4	-5.8	19.6
$\Delta g_{FA} - \Delta g_{GGM}$	-209.6	190.6	400.2	-6.5	20.0
$\Delta g_{FA} - \Delta g_{RTM}$	-112.5	182.3	294.9	15.7	34.3
$\Delta g_{FA} - \Delta g_{GGM} - \Delta g_{RTM}$	-36.4	35.0	71.4	-1.0	6.5

final geoid in restore step are given in table 8.21.

Geoid undulation N_{GGM} computed from the chosen global geopotential models has the largest contribution. Residual geoid undulation $N_{\Delta g_{FA} - \Delta g_{GGM} - \Delta g_{RTM}}$ from compute step has mean value of -12 cm with standard deviation of 14 cm. RTM geoid undulation N_{RTM} computed in restore step has small values; mean value 0.0 m, with minimal and maximal values of -11 cm and 14 cm. This is in accordance with the expected RTM anomaly property which has smallest power in high-frequencies and has small indirect effect. Statistics of the final geoid undulation for the territory of the Republic of Croatia are given in the last row of the table. Final geoid undulation has minimum and maximal values of 36.68 and 49.51 m with mean value of 43.99

Table 8.21: Statistics of the *compute* and *restore* geoid undulation contributions of the HRG2018-RCR geoid. Units: [m].

Contribution	min	max	range	mean	st. dev.
$N_{\Delta g_{FA} - \Delta g_{GGM} - \Delta g_{RTM}}$	-0.50	0.15	0.65	-0.12	0.14
N_{GGM}	36.66	49.55	12.89	44.11	2.10
N_{RTM}	-0.11	0.14	0.25	-0.00	0.02
N	36.68	49.51	12.83	43.99	2.16

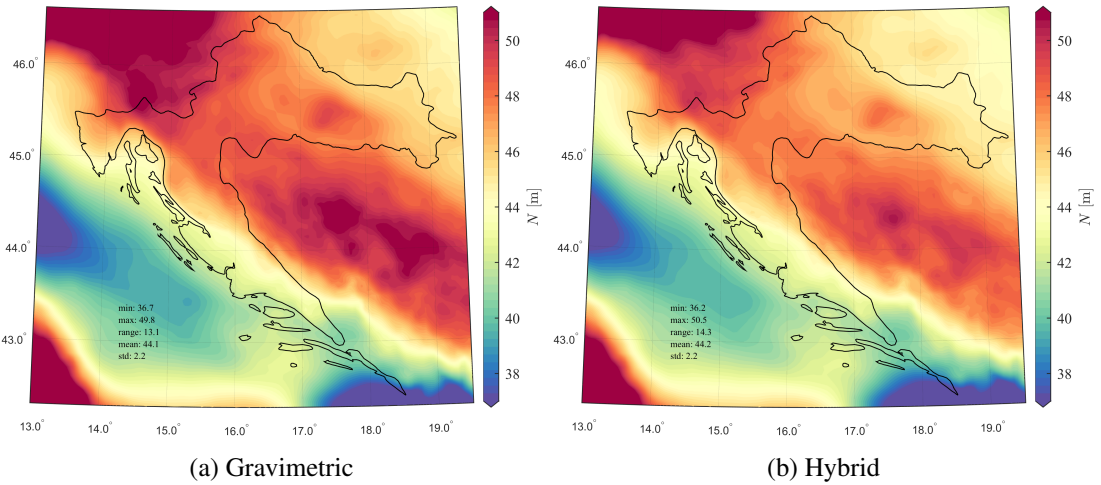


Figure 8.3: Final gravimetric and hybrid geoid models HRG2018-RCR

m.

HRG2018-RCR gravimetric and hybrid geoid models are shown in figure 8.3. Differences between gravimetric and hybrid geoid models are given in figure 8.4. The differences are smaller than 10 cm for most of the study area. In the continental (northern and north-eastern) area the differences are smaller than 5 cm. However, in the mountainous areas, as well as in the near-coastal areas, where there were not many terrestrial data (around $\varphi = 45^\circ$ and $\lambda = 16^\circ$), differences have values larger than 15 cm.

8.3.1 Validation and fitting of geoid models using GNSS/levelling data

The final step in geoid modelling is fitting and validation of the gravimetric geoid model using GNSS/levelling data. In this step, different fitting parametric models can be used. No-fit parametric model corresponds to the gravimetric model, while all other fitting models are related to the hybrid model. Input data are differences between: 1. geoid undulations obtained from GNSS/levelling $N_{GNSS/levelling}$ and 2. geoid undulation interpolated from gravimetric geoid N_{geoid} . In ideal case, differences would have been randomly distributed and have mean near 0 cm. The procedure is described more thoroughly in section 4.8.

In validation step, new, non-standard fitting procedure has been implemented as it is believed it can give more realistic statistical results. The standard procedure is to start from a GNSS/levelling dataset, and split it on two datasets: parametric and control subsets. Points in both parametric and control subsets are randomly selected. Parametric subset is used for determination of parametric (fitting) coefficients, and control subset is used for independent validation of the goodness of fit of the hybrid geoid model. In a standard procedure, splitting of the dataset is usually repeated only once, so final statistics of the fitting procedure will largely depend on the randomly selected points in parametric and control subsets. The ratio parametric/control of selected points in each subset will also determine the final statistics. Especially if the number of points in GNSS/levelling dataset is less than (let's say) few hundreds points. To overcome this

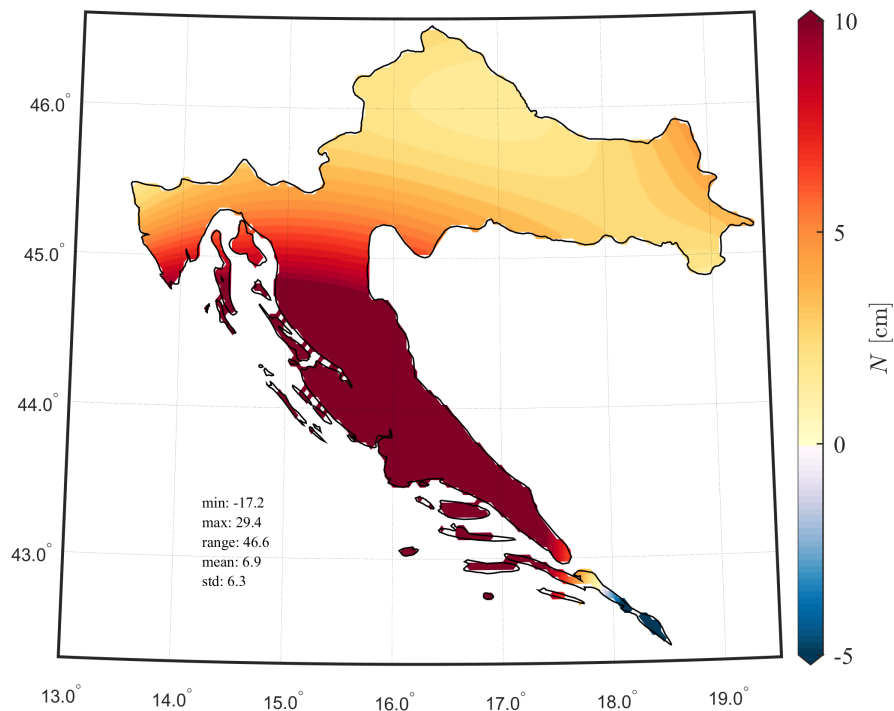


Figure 8.4: Transformation surface: difference between gravimetric and hybrid HRG2018-RCR models

drawback, fitting procedure in this study was modified and possibly improved in such way that fitting is repeated for n times, where n was provisionally taken as 20. So the aforementioned procedure of splitting the GNSS/levelling dataset on parametric and control datasets, then computing fitting parameters, and validation of geoid, was repeated 20 times. The advantage is that with repeating of the same procedure different points will be selected thus the importance points selection in parametric and control datasets will diminish and will not affect statistics. In few numerical experiments with various numbers of n , statistics of geoid accuracy after fitting may be different in some cases by more than 1 cm.

Table 8.22: Statistics of GEOFOUR geoid solution by different fitting parametric models. Units: [cm].

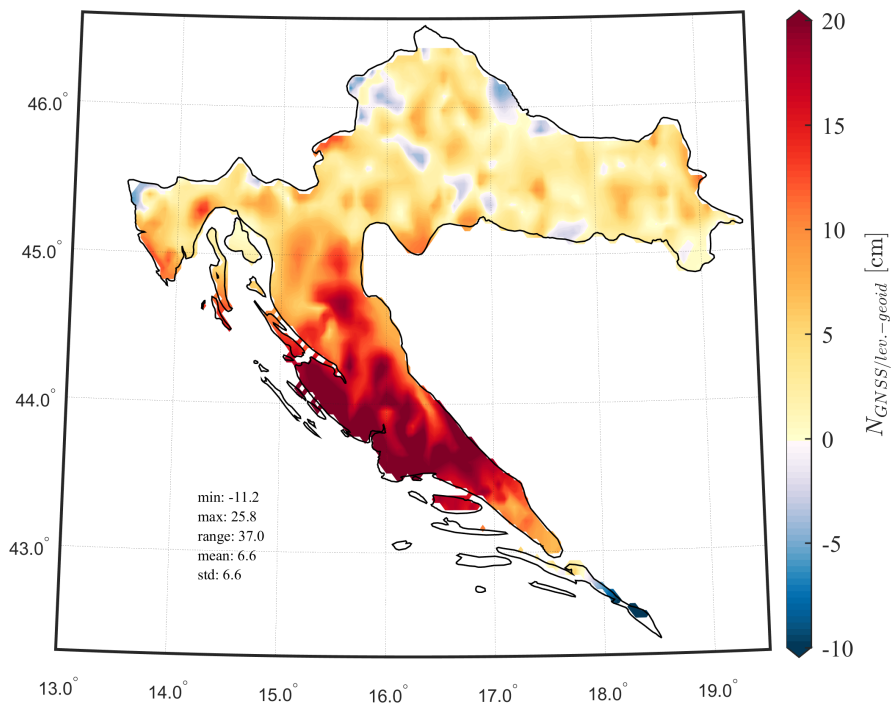
fit model	min	max	range	mean	st. dev.
nofit	-13.0	36.8	49.9	8.6	9.9
bias	-22.1	28.5	50.6	0.1	9.9
linear	-35.2	16.9	52.1	-0.2	6.8
2ndpoly	-10.6	11.9	22.6	-0.1	3.6
3rdpoly	-9.7	12.3	22.0	-0.0	3.1
3pfit	-34.9	16.7	51.7	-0.2	6.7
4pfit	-24.9	17.3	42.1	-0.2	5.8
5pfit	-21.2	16.6	37.8	-0.2	5.6
7pfit	-9.7	14.3	24.0	-0.1	3.3

Statistics of the gravimetric and fitted geoid models is given in table 8.22. Nine parametric models are tested, along with no-fit. 3rd polynomial parametric models gives the smallest standard deviation of 3.0 cm with mean value 0.0 cm. Other parametric models which give close results are 7p fit and 2nd polynomial. It is indicative that in all other solutions (except this final geoid solution) 3rd polynomial always gives the smallest standard deviation. More simpler parametric models, such as bias, also model systematic errors but not comparable to the 3rdpoly or 7p fit.

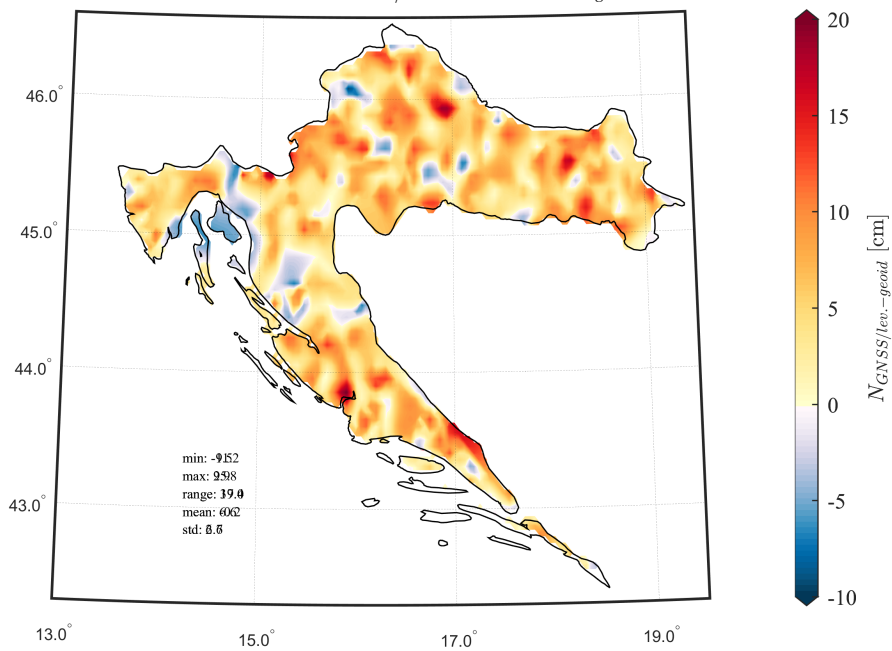
Geoid undulation differences $\delta N_{GNSS/lev.-geoid}$ of gravimetric and hybrid solutions are gridded over the study area of the Republic of Croatia to uncover areas in which differences between control and computed geoid have large and biased values. Gridding was done with 495 points corresponding to the number of available GNSS/levelling points. Gridded differences δN , where N_{geoid} are interpolated from gravimetric and hybrid geoids HRG2018-RCR-gra HRG2018-RCR-hyb, are shown in figures 8.5a and 8.5b.

According to figure 8.5a, over the continental area of Croatia the differences have values smaller than 5 cm. The problematic area is in southern part of the study area and over the Velebit mountains where differences δN have values larger than 30 cm. The reason is probably in the less quality data and computation method, as well as in the complex topography in this area.

On figure 8.5b fitted differences δN are gridded and visualized. 3rd polynomial is used as a fitting parametric model as it showed the best agreement with GNSS/levelling (table 8.22). According to the figure, large amount of the systematic error present in the gravimetric differences (shown in figure 8.5a) is eliminated in fitting procedure. Differences δN over the whole Croatian area seem to be randomly distributed without evident areas with extreme values. Fitted differences do not have higher values than the rest of the area low-land area. This suggests that 3rd polynomial is optimal choice for gravimetric geoid model fitting onto the GNSS/levelling points.



(a) $\delta N_{GNSS/lev.-HRG2018-RCR-gra}$



(b) $\delta N_{GNSS/lev.-HRG2018-RCR-hyb}$

Figure 8.5: Gridded geoid undulation differences $\delta N_{GNSS/lev.-geoid}$ for gravimetric and hybrid geoid models HRG2018-RCR

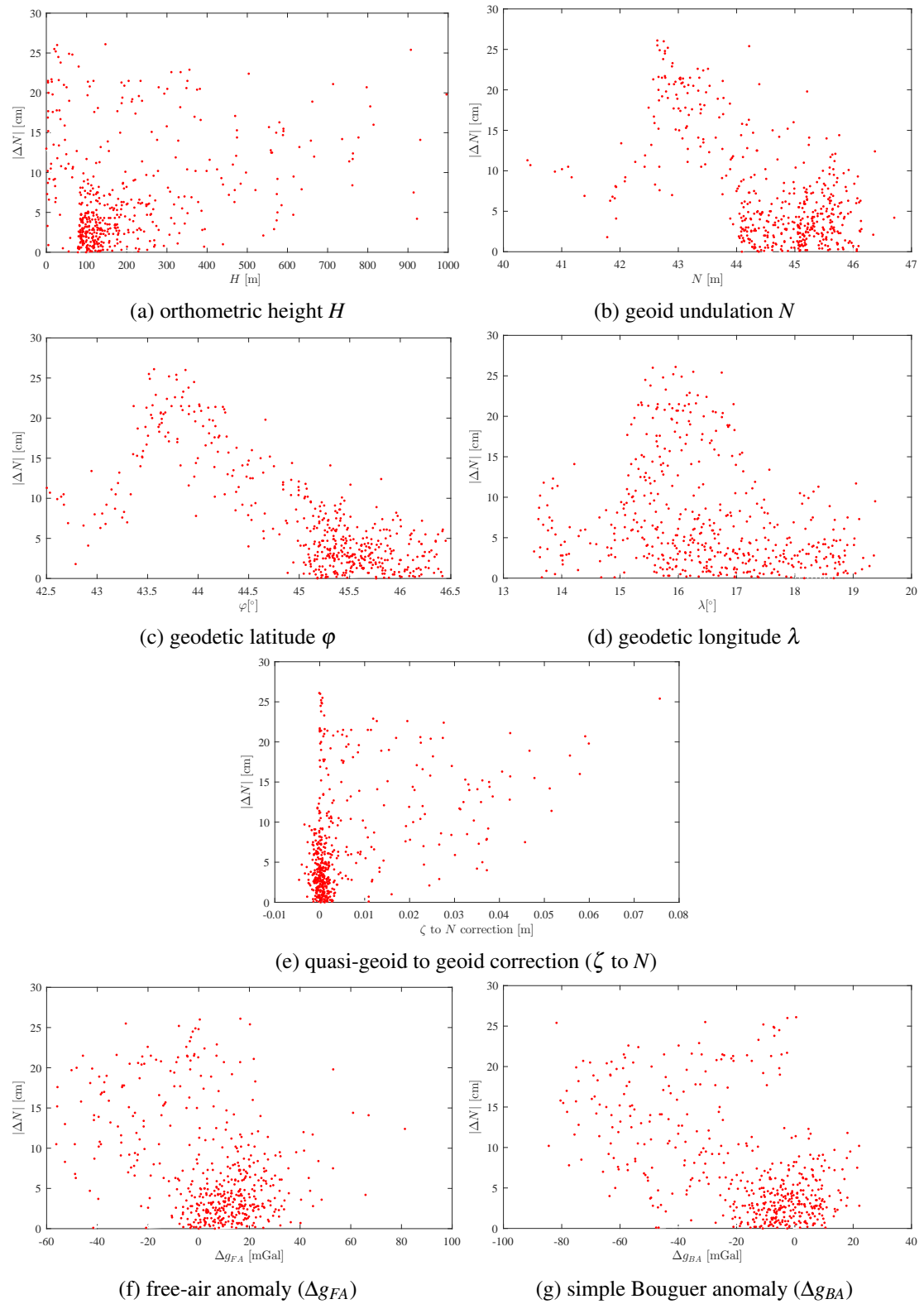


Figure 8.6: Absolute values of differences (residuals) between GNSS/levelling points and gravimetric geoid as a function of different variables

Geoid undulation differences as a function of different variables

On figure 8.6 geoid undulation differences $\delta N_{GNSS/lev.-geoid}$ for gravimetric geoid HRG2018-RCR-gra are analysed as a function of different variables.

It is seen from subfigure *a* that most of the GNSS/levelling points have orthometric heights between 100 and 200 m and have values of differences less than 10 cm. Furthermore, for GNSS/levelling points which have orthometric heights from 0 to 100 m all differences have values from 10 to 25 cm. These are points which are located near the coastline. This suggests that gravimetric geoid does not agree well with GNSS/levelling along the coastline (which is also observed in figure 8.5a). There are only very few points monumented on the larger orthometric heights ($H > 400$ m) making it harder to validate geoid models in mountainous areas. For $H > 400$ m differences δN increase as there are only very few points that have values less than 5 cm.

Differences δN have values larger than 15 cm for the geoid undulation N around 43 m (subfigure *b*). However, most of the GNSS/levelling points have geoid undulation between 44 and 46 m. When differences δN are compared to geodetic latitude and longitude (subfigures *c* and *d*) it can be seen that they values larger than 15 cm around $\varphi = 44^\circ$ and $\lambda = 16^\circ$. Analyzing the dependency of the differences as a function of the quasi-geoid to geoid correction it follows that with the increase of the difference between quasi-geoid and geoid differences δN are also increased. Quasi-geoid and geoid surfaces differ the most in mountainous areas where this correction also has higher values than in flat areas. Dependency of gravity differences about free-air and simple Bouguer anomaly (subfigures *f* and *g*) reveal that differences tend to increase for larger values of both types of anomalies.

8.3.2 Relative geoid accuracy validation

Besides for absolute positioning where height of the point is determined by GNSS positioning and then transformed to orthometric in the needed national MSL-based vertical datum by using hybrid geoid model, relative heightening using GNSS/levelling method shall also be assessed. The results of relative geoid accuracy validation are compared with 'classical' precise and technical levelling and their corresponding allowed misclosure limits by the distance in km. It is known that accuracy of levelling for heights transfer exponentially decreases with the distance and as such accumulates errors. The validation procedure is described in section 4.8.1.

The results of relative geoid accuracy validation are shown in figure 8.7. It follows from the figure that hybrid geoid models are of comparable accuracy with precise levelling for transfer of the heights over the distances larger than 250 km, and far better than technical levelling even after 40 km. KTH gravimetric geoid is for distances larger than 50 km better than technical levelling, while RCR gravimetric geoid indicates errors for the distances between 200 and 350 km. This means that time-consuming and expensive levelling can already be substituted for most of the engineering tasks. For hybrid geoid models relative accuracy is improved and is constant for all distances. As expected, for distances that are smaller than approximately 200 km, precise levelling is superior to GNSS/levelling. However, if geoid accuracy becomes 1 cm in absolute sense it can be expected that the relative accuracy will be comparable with precise levelling, except for very small distances.

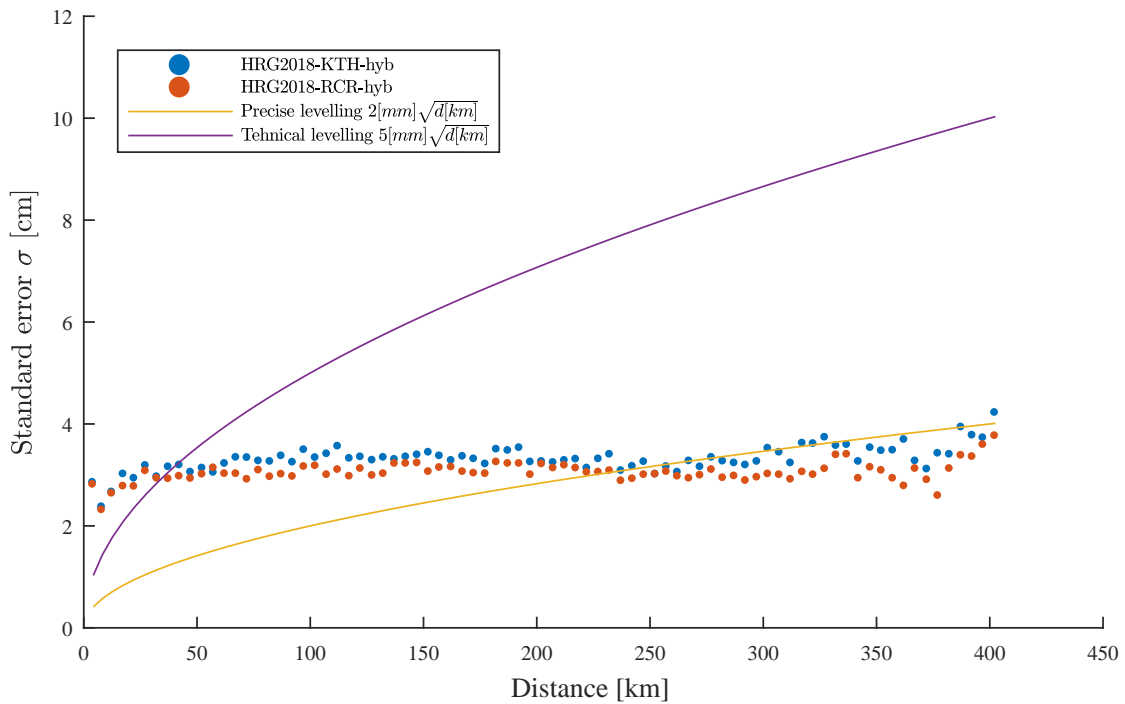


Figure 8.7: Relative geoid accuracy of gravimetric and hybrid models HRG2018-RCR and HRG2018-KTH

8.4 Review

Conclusions can be drawn from the results presented in the previous section as well as from the results of the analysis of other solutions that were computed with all kinds of combinations of input parameters and models.

Crustal models in geoid determination. Crustal density values and models can result in the differences between solutions of few centimeters in gravimetric geoid determination. Differences have systematic trend; increase mean value and not affecting standard deviation. In hybrid, fitted to GNSS/levelling in LVD, solutions these differences are modeled and filtered. Therefore, results of fitted geoid models are nearly similar and not depended on the used crustal values and models. Comparable result emerged in e.g. [Omang \(2000\)](#).

Constant crustal density value for Croatia. Optimal results are obtained when using the constant crustal density value $\rho_c = 2250 \text{ kgm}^{-3}$, instead of the global estimation of $\rho_c = 2670 \text{ kgm}^{-3}$. This value is confirmed in three independent computation tasks: 1) smallest standard deviation and mean values obtained when residual gravity anomalies $\Delta g_{FA-GGM-RTM}$ are calculated, 2) smallest standard deviations of geoid models computed using RCR and KTH approaches when compared to GNSS/levelling dataset, 3) obtained when eight layers from the global crustal model CRUST1.0 are averaged. Finally, these results agree with first attempts of mean crustal density values determination in one part of Croatia [Čolić et al. \(1992\)](#).

Selection of input gravity anomalies. One of the most important steps before geoid computation is selection of the input data (residual gravity anomalies $\Delta g_{FA-GGM-RTM}$). Solutions which agreed the best with GNSS/levelling in all geoid computation methods are derived with the same input data.

Selection of the GGM model: satellite-only vs. combined GGM. It is an open question whether to use satellite-only or combined GGM model in computation of GGM effects in remove and restore steps. Although data combining and spectral wavelengths mixing probably should be avoided the results on this study area show that solutions which give smallest standard deviation are obtained using combined-data EGM2008 model with maximal degree ($n_{max} = 2190$).

Geoid computation methods. Each geoid computation method has its own input parameters, advantages and drawbacks. It is impossible to make general conclusions, but most of our results confirm past research. Analytic Stokes integration is the most exact, but is time-consuming, whereas spectral methods are superb in terms of computational speed. In some cases FFT might produce outliers or void values. If spectral methods are compared, planar approximation (GEOFOUR) is simple and the most accurate. Lest Square Collocation is by far the most complex and time consuming method. In this case where around twenty thousand points are used, computation of geoid lasted more than few hours. The amount of point gravity data in this study showed to be manageable for LSC, but if more data are available, it would soon become impossible to use them for computations in one step. Another issue is the spatial extent of the available data. Generally, Stokes integration require knowledge of data of at least 1 to 2° (and normally 3 to 5°) from the borders of the computed geoid, which means that gravity data from surrounding countries or sea areas are needed. This makes data collection and creation of the gravity database more complex. The most important step in LSC is derivation and selection of covariance function, which depends on more than ten different input parameters. This implies that researcher has to select some input values without knowing exactly what impact does it have on the computed geoid solution. Simpler alternative is using flat-Earth covariances with block computations, which seem to give similar results as the 3D LSC. However, block computation may provide inconsistencies on the block boundaries as well as unknown errors because different covariance functions are used for each block. Such issue may also be resolved by using the same covariance function for the entire computation area. In any case, LSC method, along with GEOFOUR, resulted in the most precise geoid solution of all compared methods.

Gravimetric vs fitted geoid model. The results show a strong correlation between gravimetric (no fit) and hybrid (fitted) solutions. Gravimetric geoid solutions which have the smallest standard deviation compared to GNSS/levelling data, will also have smallest standard deviation in hybrid geoid models. This is important if some country decides to implement a new geoid-based vertical datum. In that case, from different gravimetric geoid solutions, one solution has to be selected. The question arises: by which criteria should gravimetric geoid model be selected and declared as a vertical datum. The most logical answer would be the solution which agrees the best with the real geoid surface, and this would probably be the geoid surface defined by the points in the GNSS/levelling dataset.

Selection of the fitting parametric model. Generally, from all tested parametric models, the 3rd polynomial model results in the best agreement of gravimetric geoid models with GNSS/levelling dataset. Seven parametric model (7-p) also produces well agreement while other parametric models still leave some systematic errors which propagate into the statistics. As a rule, the most important thing in fitting is that mean error, which indicates systematic bias between gravimetric geoid solution and local mean-sea-level vertical datum, is completely removed. In other words, after fitting mean error should be less than few millimeters. It is worth to mention here that completely another approach was implemented in the determination of the HRG2009 quasi-geoid model (see, [Bašić and Bjelotomić 2014](#)), when GNSS/levelling data were used as input data together with gravity anomalies in LSC method. Then, no fitting procedure was necessary as geoid was already fitted to the LVD HVRS71.

Chapter 9

Conclusions

“If we knew what it was we were doing, it would not be called research, would it?”

Albert Einstein, 1879-1955

Surface crustal density models were developed for the territory of Croatia. The most realistic model was computed with Parasnis-Nettleton’s method. Largest differences between models were those developed by Airy-Heiskanen’s and Parasnis-Nettleton’s methods, while smallest differences were between models developed by Pratt-Hayford’s and Parasnis-Nettleton’s methods.

A new methodology and software routines were developed and used for modelling of topographic effects in all steps of regional geoid determination allowing inclusion of surface crustal density models and 3D crustal models with up to eight layers. Developed routines may be used for seamless gravity field modelling, determination of gravimetric and hybrid geoid models, validation of global geopotential models, and gridding of gravity anomalies. Any number and combination of input parameters and models may be defined before starting computations. Compared to the past, unrelated programming routines required much manual work from the researcher which resulted in computational and efficiency problems when large number of different variants of models had to be computed and compared.

Geoid models were computed using different constant crustal density values, developed 2D crustal density models, and publicly available 3D crustal models. The results indicate that a mean value of $\rho_c = 2250 \text{ kgm}^{-3}$ is more appropriate for the territory of the Republic of Croatia compared to the globally estimated value $\rho_c = 2670 \text{ kgm}^{-3}$. Compared to the constant crustal density values, improvement of the accuracy of gravimetric geoid models by using surface crustal models is around 2 cm in mean value, while standard deviation is not affected. Using 3D crustal models, instead of surface density models, geoid models accuracy is changed by less than 1 cm in mean value, while standard deviation is not changed. Therefore, implementation of the reliable surface crustal density model into gravity field modelling and geoid determination for now seems to be optimal option, as 3D crustal density models still have coarse resolution and unknown reliability. Importance of implementation of the optimal and realistic crustal density information will increase in the foreseeing future when absolute geoid accuracy

reaches the ultimate goal 1 cm .

Different gridding (interpolation) methods with variable input parameters for several types of gravity anomalies were tested. The smallest errors in gridding were produced by using Kriging method for all types of gravity anomalies. Concerning Kriging method, it is crucial to find and apply optimal variogram model based on input data, otherwise gridding accuracy will suffer. Moving average and polynomial regression gridding methods showed errors of more than 20 mGal. Additionally, differences between gridding methods are smaller if input gridded data is smoother. For example, differences between first and second most accurate gridding method for *rough* free-air gravity anomalies are 2.2 mGal, while for *smooth* complete Bouguer anomalies 0.7 mGal. The best type of anomalies Δg for gridding are complete and simple Bouguer anomalies with standard deviation of 2.1 mGal. As expected, free-air gravity anomalies showed to be non-suitable for interpolation. Taking into account the simplicity of calculation and small differences in accuracy when gridding complete Bouguer anomalies, gridding may be sufficiently well done using simple Bouguer anomalies, although complete Bouguer anomalies will generally result in highest gridding accuracy.

In GGM validation, combined data models EGM2008 and EIGEN-6C4 showed best agreement with GNSS/levelling and gravity data. From satellite-only GGMs, ITU-GGC16 and GOCONS-GCF-2-TIM-R5 indicate best agreement of all validated models.

Detailed numerical investigation of the influence of all input parameters and models in residual gravity field modelling for RCR approach was done. The results allowed usage of the residual gravity anomalies $\Delta g_{FA-GGM-RTM}$ with smallest possible mean error and standard deviation as input data in geoid determination. Input parameters which have the strongest influence on residual gravity anomalies as they change mean and standard deviation by more than 3 mGal: maximum degree of expansion of GGM, resolution of the reference and fine DEM, and crustal density. Selection of the global geopotential model or digital elevation model and gridding method of digital elevation models have moderate influence changing mean or standard deviation between 1 and 3 mGal. More detailed conclusions are given in chapter 6, section 6.3.

The influence and sensitivity of input parameters and models in KTH approach was investigated. It is now much clearer how different parameters affect the accuracy of geoid models, and how to select optimal combination of input parameters to derive the best possible solution starting from the input data and models.

A new gravimetric and hybrid geoid models for the territory of Croatia were determined using KTH and RCR approaches. Standard deviation of the best hybrid geoid model HRG2018-RCR is 3.0 cm, and HRG2018-KTH is 3.5 cm.

In comparison of different spatial and spectral geoid computation methods planar FFT (GEFOUR) and LSC resulted in the smallest standard deviation of 3.0 cm and 3.1 cm with mean values of 0.0 cm after fitting to GNSS/levelling. When hybrid geoid models are compared, differences between accuracies of geoid computation methods compared to GNSS/levelling are generally less than 1 cm.

Comparison of the differences (grid - grid) between gravimetric geoid models computed with different methods of RCR approach and KTH approach reveal mean biases of more than 10 cm. The biggest differences are between best gravimetric models solutions of KTH and RCR approaches where mean difference is around 90 cm. After 1-parameteric fitting, mean difference

is reduced down to 0.0 cm.

Different parametric models are used for transformation of gravimetric to hybrid geoid model and for GGM validation. In all cases 3rd polynomial model resulted in the smallest standard deviation with almost complete elimination of mean. Seven-parametric model in some cases achieved comparable results, but was never better.

Future research

In this thesis several topics related to regional gravity field modelling and geoid determination were investigated. The results obtained throughout PhD research opened and generated new topics and ideas for conducting research in the future. Some of them are:

- Validation of the created surface crustal density models using independent geophysical data. Creation and publication of a unique and verified combined surface crustal density model which could be used in all geodetic and geophysical applications.
- Development of the 3D crustal density and Moho depths models for the territory of the Republic of Croatia using available data, e.g. from GOCE or GRACE-FO satellite gravity missions or other geophysical and geological data.
- Repeat computations on other areas worldwide and analyze the influence of different parameters and models in gravity field modelling and geoid determination using RCR and KTH approaches (chapters 6 and 7).
- Perform numerical investigations of the influence of all input parameters and models on the accuracy of computed geoid model in RCR approach.
- Compare RCR and KTH approaches on other areas worldwide. Compute geoid with the Stokes-Helmert (UNB) approach and compare it with the RCR and KTH approaches.
- Include other types of gravity-field data, such as deflections of vertical or gravity gradients, and investigate their's impact on the accuracy of geoid models.
- Validate, control and update gravity and GNSS/levelling databases. Special focus should be on densification of the databases in mountainous, coastal, and marine areas.
- Investigate requirements for replacement of the present MSL-based Height Reference System (HRS) HVRS71 with the geoid-based height reference system which would be consistent with the most recent recommendations of the IAG realization of International Height Reference System (IHRS) and World Height System (WHS) (see, [Ihde et al. 2017](#), [Sánchez and Sideris 2017](#)).

Bibliography

- Abbak, R. A., B. Erol, and A. Ustun (2012). Comparison of the KTH and remove–compute–restore techniques to geoid modelling in a mountainous area. *Computers & geosciences* 48, 31–40. DOI: [10.1016/j.cageo.2012.05.019](https://doi.org/10.1016/j.cageo.2012.05.019).
- Abbak, R. A. and A. Ustun (2015). A software package for computing a regional gravimetric geoid model by the KTH method. *Earth Science Informatics* 8(1), 255–265. DOI: [10.1007/s12145-014-0149-3](https://doi.org/10.1007/s12145-014-0149-3).
- Abd-Elmotaal, H. A. (2017). Gravimetric geoid for Egypt implementing Moho depths and optimal geoid fitting approach. *Studia Geophysica et Geodaetica*, 1–18. DOI: [10.1007/s00190-002-0300-7](https://doi.org/10.1007/s00190-002-0300-7).
- Abdalla, A. (2009). *Determination of a gravimetric geoid model of Sudan using the KTH method*. Msc, Royal Institute of Technology (KTH). URL: <http://urn.kb.se/resolve?urn=urn:nbn:se:kth:diva-199670>.
- Abdalla, A. and D. Fairhead (2011). A new gravimetric geoid model for Sudan using the KTH method. *Journal of African Earth Sciences* 60(4), 213–221. DOI: [10.1016/j.jafrearsci.2011.02.012](https://doi.org/10.1016/j.jafrearsci.2011.02.012).
- Abdalla, A. and S. Mogren (2015). Implementation of a rigorous least-squares modification of Stokes' formula to compute a gravimetric geoid model over Saudi Arabia (SAGEO13). *Canadian Journal of Earth Sciences* 52(10), 823–832. DOI: [10.1139/cjes-2014-0192](https://doi.org/10.1139/cjes-2014-0192).
- Abdalla, A. and R. Tenzer (2011). The evaluation of the New Zealand's geoid model using the KTH method. *Geodesy and Cartography* 37(1), 5–14. DOI: [10.3846/13921541.2011.558326](https://doi.org/10.3846/13921541.2011.558326).
- Abdollahzadeh, M. and M. Alamdari (2011). Application of Molodensky's Method for Precise Determination of Geoid in Iran. *Journal of Geodetic Science* 1(3), 259–270. DOI: [10.2478/v10156-011-0004-0](https://doi.org/10.2478/v10156-011-0004-0).
- Abrams, M., H. Tsu, G. Hulley, K. Iwao, D. Pieri, T. Cudahy, and J. Kargel (2015). The Advanced Spaceborne Thermal Emission and Reflection Radiometer (ASTER) after fifteen years: Review of global products. *International Journal of Applied Earth Observation and Geoinformation* 38, 292–301. DOI: [10.1016/j.jag.2015.01.013](https://doi.org/10.1016/j.jag.2015.01.013).
- Ågren, J. (2004). *Regional geoid determination methods for the era of satellite gravimetry: numerical investigations using synthetic Earth gravity models*. Ph. D. thesis, Royal Institute of Technology (KTH). URL: <http://urn.kb.se/resolve?urn=urn:nbn:se:kth:diva-55>.
- Ågren, J., L. E. Sjöberg, and R. Kiamehr (2009). The new gravimetric quasigeoid model KTH08 over Sweden. *Journal of Applied Geodesy* 3(3), 143–153. DOI: [10.1515/JAG.2009.015](https://doi.org/10.1515/JAG.2009.015).
- Ågren, J., G. Strykowski, M. Bilker-Koivula, O. Omang, S. Märdla, R. Forsberg, A. Ellmann, T. Oja, I. Liepinš, E. Paršeliūnas, et al. (2016). The NKG2015 gravimetric geoid model for the Nordic-Baltic region. In *Gravity, Geoid and Height Systems, IAG Symp GGHS2016*, pp. 19–23. DOI: [10.13140/RG.2.2.20765.20969](https://doi.org/10.13140/RG.2.2.20765.20969).
- Ågren, J., G. Strykowski, M. Bilker-Koivula, O. Omang, S. Märdla, T. Oja, I. Liepinš, E. Paršeliūnas, R. Forsberg, J. Kaminskis, et al. (2015). On the development of the new Nordic gravimetric geoid model NKG2015. *Presentation at 26th IUGG general assembly, Prague, Czech Republic*.
- Airy, G. B. (1855). On the computation of the effect of the attraction of mountain-masses, as disturbing the apparent astronomical latitude of stations in geodetic surveys. *Philosophical Transactions of the Royal Society of London* 145, 101–104. <http://www.jstor.org/stable/108511>.
- Akyilmaz, O., A. Ustun, C. Aydin, N. Arslan, S. Doganalp, C. Guney, H. Mercan, S. Uygur, M. Uz, and O. Yagci (2016a). ITUGGC16 The combined global gravity field model including GRACE & GOCE data up to degree and order 280. <http://pmd.gfz-potsdam.de/icgem/showshort.php?id=escidoc:1602889>.
- Akyilmaz, O., A. Ustun, C. Aydin, N. Arslan, S. Doganalp, C. Guney, H. Mercan, S. Uygur, M. Uz, and O. Yagci (2016b). ITUGRACE16 The global gravity field model including GRACE data up to degree and order 180 of ITU

- and other collaborating institutions. <http://pmd.gfz-potsdam.de/icgem/showshort.php?id=escidoc:1640888>.
- Amante, C. and B. W. Eakins (2009). *ETOPO1 1 arc-minute global relief model: procedures, data sources and analysis*. US Department of Commerce, National Oceanic and Atmospheric Administration, National Environmental Satellite, Data, and Information Service, National Geophysical Data Center, Marine Geology and Geophysics Division Colorado.
- Amos, M. J. (2007). *Quasigeoid modelling in New Zealand to unify multiple local vertical datums*. Ph. D. thesis, Curtin University of Technology. URL: <https://espace.curtin.edu.au/handle/20.500.11937/1949>.
- Andersen, O. B. (2013). Marine gravity and geoid from satellite altimetry. In *Geoid Determination*, pp. 401–451. Springer. DOI: [10.1007/978-3-540-74700-0-9](https://doi.org/10.1007/978-3-540-74700-0-9).
- Andersen, O. B. and P. Knudsen (2016). Deriving the DTU15 Global high resolution marine gravity field from satellite altimetry. In *ESA Living Planet Symposium 2016*.
- Arana, D., P. O. Camargo, and G. N. Guimaraes (2017). Hybrid geoid model: Theory and application in Brazil. *Anais da Academia Brasileira de Ciências* 89(3), 1943–1959. DOI: [10.1590/0001-3765201720160802](https://doi.org/10.1590/0001-3765201720160802).
- Asgharzadeh, M., R. Von Frese, H. Kim, T. Leftwich, and J. Kim (2007). Spherical prism gravity effects by Gauss-Legendre quadrature integration. *Geophysical Journal International* 169(1), 1–11. DOI: [10.1111/j.1365-246X.2007.03214.x](https://doi.org/10.1111/j.1365-246X.2007.03214.x).
- Ayhan, M. E. (1993). Geoid determination in Turkey (TG-91). *Bulletin géodésique* 67(1), 10. DOI: [10.1007/BF00807293](https://doi.org/10.1007/BF00807293).
- Bagherbandi, M. (2011). *An isostatic earth crustal model: And its applications*. Ph. D. thesis, Division of Geodesy and Geoinformatics, Royal Institute of Technology (KTH). URL: <http://urn.kb.se/resolve?urn=urn:nbn:se:kth:diva-31989>.
- Bagherbandi, M. and L. E. Sjöberg (2012). Non-isostatic effects on crustal thickness: a study using CRUST2.0 in Fennoscandia. *Physics of the Earth and Planetary Interiors* 200, 37–44. DOI: [10.1016/j.pepi.2012.04.001](https://doi.org/10.1016/j.pepi.2012.04.001).
- Bajracharya, S. (2004). *Terrain effects on geoid determination*. MSc thesis, Department of Geomatics Engineering, University of Calgary.
- Banks, E. R. (1968). *Isostatic and Bouguer gravity anomalies along the Inside Passage of Alaska and British Columbia*. Msc thesis.
- Barthelmes, F. (2009). Definition of functionals of the geopotential and their calculation from spherical harmonic models. *104132(3)*, 0902–2. DOI: [10.2312/GFZ.b103-0902-26](https://doi.org/10.2312/GFZ.b103-0902-26).
- Barthelmes, F. (2014). Global Models. *Encyclopedia of Geodesy*, Springer International Publishing, 1–9. DOI: [10.1007/978-3-319-02370-0-43-1](https://doi.org/10.1007/978-3-319-02370-0-43-1).
- Barzaghi, R., B. Betti, A. Borghi, G. Sona, and V. Tornatore (2002). The Italian quasi-geoid ITALGEO99. *Bollettino di geodesia e scienze affini* 61(1), 33–51.
- Barzaghi, R., A. Borghi, D. Carrion, and G. Sona (2007). Refining the estimate of the Italian quasi-geoid. *Bollettino di Geodesia e Scienze Affini* 3, 145–160.
- Barzaghi, R., G. S. Vergos, and A. Albertella (2017). The GEOMED2 project: Geoid and circulation in the Mediterranean Sea. In *IAG-IASPEI Joint Scientific Assemblies 2017*.
- Bašić, T. (2000). Detaljni model geoida Republike Hrvatske HRG2000. *Izvešća Državne geodetske uprave o znanstveno-stručnim projektima iz 2000. godine*, 11–22. in Croatian.
- Bašić, T. (2009). Unique transformation model and new geoid model of the Republic of Croatia. In *I. CROPOS konferencija*.
- Bašić, T. and O. Bjelotomić (2014). HRG2009: New High Resolution Geoid Model for Croatia. In *Gravity, Geoid and Height Systems*, pp. 187–191. Springer. DOI: [10.1007/978-3-319-10837-7-24](https://doi.org/10.1007/978-3-319-10837-7-24).
- Bašić, T. and M. Brkić (1999a). Novi hrvatski geoid i njegov značaj za GPS mjerenja. *Zbornik radova HGD simpozija Državne geodetske osnove i zemljišni informacijski sustavi, Opatija 12(14)*, 263–271.
- Bašić, T. and M. Brkić (1999b). The latest efforts in the geoid determination in Croatia. *B. Geofis. Teor. Appl* 40, 379–386.
- Bašić, T., M. Brkić, and H. Sünkel (1999). A new, more accurate geoid for Croatia. *Physics and Chemistry of the Earth, Part A: Solid Earth and Geodesy* 24(1), 67–72. DOI: [10.1016/S1464-1895\(98\)00012-X](https://doi.org/10.1016/S1464-1895(98)00012-X).

- Bašić, T. and G. Buble (2007). Usporedba globalnog modela visina SRTM3 s postojećim digitalnim modelima reljefa na području Hrvatske. *Geodetski list* 61(2), 93–111. URL: <http://hrcak.srce.hr/16782>.
- Bašić, T. and K. Čolić (1993). Gravity Field Determination for the Territory of Croatia. In *Geodesy and Physics of the Earth*, pp. 137–140. Springer. DOI: [10.1007/978-3-642-78149-0-34](https://doi.org/10.1007/978-3-642-78149-0-34).
- Bašić, T. and Ž. Hećimović (2006). Latest geoid determinations for the Republic of Croatia. In *IAG International Symposium Gravity, Geoid and Space Missions GGSM2004, Session*, Volume 3, pp. 83–92.
- Bašić, T., D. Medak, and B. Pribičević (2000). Technical report on the project: Establishment of new geoidal points in the Republic of Croatia in 2000.
- Bassin, C. (2000). The current limits of resolution for surface wave tomography in North America. *EOS Trans. AGU. 81: Fall Meet. Suppl., Abstract*.
- Becker, J., D. Sandwell, W. Smith, J. Braud, B. Binder, J. Depner, D. Fabre, J. Factor, S. Ingalls, S. Kim, et al. (2009). Global bathymetry and elevation data at 30 arc seconds resolution: SRTM30_PLUS. *Marine Geodesy* 32(4), 355–371. DOI: [10.1080/01490410903297766](https://doi.org/10.1080/01490410903297766).
- Benahmed Daho, S. and S. Kahlouche (2000). The new gravimetric geoid in Algeria. *IGeS Bulletin* (10), 85–90.
- Bezděk, A. and J. Sebera (2013). Matlab script for 3D visualizing geodata on a rotating globe. *Computers & geosciences* 56, 127–130. DOI: [10.1016/j.cageo.2013.03.007](https://doi.org/10.1016/j.cageo.2013.03.007).
- Biagi, L. and F. Sanso (2001). Tcight: a new technique for fast rtc computation. In *Gravity, Geoid and Geodynamics 2000*, pp. 61–66. Springer. DOI: [10.1007/978-3-662-04827-6-10](https://doi.org/10.1007/978-3-662-04827-6-10).
- Bilker-Koivula, M. (2010). Development of the Finnish height conversion surface FIN2005N00. *Nordic journal of surveying and real estate research* 7(1).
- Bjelotomić, O. (2015). *High Resolution Geoid Modelling of Croatia*. PhD thesis, Faculty of Geodesy, University of Zagreb.
- Bjelotomić, O., T. Bašić, and D. Markovinović (2015). Refinement of the geoid model on the islands with sparse terrestrial gravity data. In *26th IUGG General Assembly 2015*.
- Bjerhammar, A. (1962). A general method for an explicit determination of the shape of the earth from gravimetric data. *Bulletin Géodésique (1946-1975)* 65(1), 215–220. DOI: [10.1007/BF02529718](https://doi.org/10.1007/BF02529718).
- Bjerhammar, A. (1969). On the boundary value problem of physical geodesy. *Tellus* 21(4), 451–516. DOI: [10.1111/j.2153-3490.1969.tb00460.x](https://doi.org/10.1111/j.2153-3490.1969.tb00460.x).
- Blitzkow, D., A. C. Oliveira Cancoro de Matos, G. do Nascimento Guimarães, M. C. Pacino, E. Andrés Lauría, M. Nunes, F. Flores, N. Orihuela Guevara, R. Alvarez, J. Napoleon Hernandez, et al. (2016). Gravity and geoid model for South America. In *EGU General Assembly Conference Abstracts*, Volume 18, pp. 1626.
- Bottoni, G. P. and R. Barzaghi (1993). Fast collocation. *Journal of Geodesy* 67(2), 119–126. DOI: [10.1007/BF01371375](https://doi.org/10.1007/BF01371375).
- Bowie, W. (1927). *Isostasy-The Science of the Equilibrium of the Earth's Crust*. New York: EP Button and Company, 275.
- Brkić, M. (1994a). An improved method of Earth's Crust Masses Modelling. *Geodetski list* 48(3), 253–264.
- Brkić, M. (1994b). *An Improved Method of Earth's Crust Masses Modelling for Geodetic and Geophysical Purposes*. MSc thesis, Faculty of Science, Department of Geophysics, University of Zagreb.
- Brkić, M. (2001a). Terrain Correction by means of Spatial Density Model. *Geodetski list* 55(1), 3–18.
- Brkić, M. (2001b). *Three-dimensional modelling of Earth's Crust for purposes of Geodesy and Geophysics: Terrain Correction in Spatial and Spectral domain*. PhD thesis, Faculty of Science, Department of Geophysics, University of Zagreb.
- Brkić, M. (2016). Bošković and the Theory of Isostasy. In *Ruđer Bošković i geoznanosti= Ruđer Bošković and the Geosciences*. Geodetski fakultet Sveučilišta u Zagrebu, Državna geodetska uprava, Hrvatska komora ovlaštenih inženjera geodezije.
- Brkić, M. and T. Bašić (1997). Three Layer Earth's Crust Approximation in Topographic Reductions: A Theory and Practice. In *XXII EGS-General Assembly (Local, regional and global relations of gravity with other geological and geophysical fields)*.
- Brkić, M. and T. Bašić (2000). Računanje korekcije reljefa u prostornoj i spektralnoj domeni. *Geodetski list* 54(77),

- 4.
- Brkić, M. and T. Bašić (2001). Terrain correction by means of simple spatial density model. *XXVI EGS-General Assembly, Nice, March*, 25–30.
- Brockmann, J. M., N. Zehentner, E. Höck, R. Pail, I. Loth, T. Mayer-Gürr, and W.-D. Schuh (2014). EGM_TIM_RL05: An independent geoid with centimeter accuracy purely based on the GOCE mission. *Geophysical Research Letters* 41(22), 8089–8099. DOI: [10.1002/2014GL061904](https://doi.org/10.1002/2014GL061904).
- Brovelli, M. A. and F. Sansó (1993). The Geomed Project: the state of the art. *Annals of Geophysics* 36(5-6). DOI: [10.4401/ag-4247](https://doi.org/10.4401/ag-4247).
- Bucha, B. and J. Janák (2013). A MATLAB-based graphical user interface program for computing functionals of the geopotential up to ultra-high degrees and orders. *Computers & geosciences* 56, 186–196. DOI: [10.1016/j.cageo.2013.03.012](https://doi.org/10.1016/j.cageo.2013.03.012).
- Burkhard, R. K. (1985). *Geodesy for the Layman*. US Department of Commerce, National Oceanic and Atmospheric Administration.
- Capponi, M., A. H. Mansi, and D. Sampietro (2018). Improving the computation of the gravitational terrain effect close to ground stations in the GTE software. *Studia Geophysica et Geodaetica*, 1–17. DOI: [10.1007/s11200-017-0814-3](https://doi.org/10.1007/s11200-017-0814-3).
- Carlson, R. E. and T. A. Foley (1991). The parameter R2 in multiquadric interpolation. *Computers & Mathematics with Applications* 21(9), 29–42. DOI: [10.1016/0898-1221\(91\)90123-L](https://doi.org/10.1016/0898-1221(91)90123-L).
- Casenave, F., L. Métivier, G. Pajot-Métivier, and I. Panet (2016). Fast computation of general forward gravitation problems. *Journal of Geodesy* 90(7), 655–675. DOI: [10.1007/BF00053511](https://doi.org/10.1007/BF00053511).
- Cella, F. (2015). GTeC- A versatile MATLAB® tool for a detailed computation of the terrain correction and Bouguer gravity anomalies. *Computers & Geosciences* 84, 72–85. DOI: [10.1016/j.cageo.2015.07.015](https://doi.org/10.1016/j.cageo.2015.07.015).
- Chai, Y. and W. J. Hinze (1988). Gravity inversion of an interface above which the density contrast varies exponentially with depth. *Geophysics* 53(6), 837–845. DOI: [10.1190/1.1442518](https://doi.org/10.1190/1.1442518).
- Chen, Q., Y. Shen, W. Chen, X. Zhang, and H. Hsu (2016). An improved GRACE monthly gravity field solution by modeling the non-conservative acceleration and attitude observation errors. *Journal of geodesy* 90(6), 503–523. DOI: [10.1007/s00190-016-0889-6](https://doi.org/10.1007/s00190-016-0889-6).
- Claessens, S. J., C. Hirt, M. Amos, W. Featherstone, and J. Kirby (2011). The NZGEOID09 model of New Zealand. *Survey Review* 43(319), 2–15. DOI: [10.1179/003962610X12747001420780](https://doi.org/10.1179/003962610X12747001420780).
- Coggon, J. (1976). Magnetic and gravity anomalies of polyhedra. *Geoexploration* 14(2), 93–105. DOI: [10.1016/0016-7142\(76\)90003-X](https://doi.org/10.1016/0016-7142(76)90003-X).
- Čolić, K., T. Bašić, S. Petrović, B. Pribičević, and M. Ratkajec (1993). Improved geoid solution for Slovenia and a part of Croatia. In *Geodesy and Physics of the Earth*, pp. 141–144. Springer. DOI: [10.1007/978-3-642-78149-0-35](https://doi.org/10.1007/978-3-642-78149-0-35).
- Čolić, K., T. Bašić, S. Petrović, B. Pribičević, M. Ratkajec, H. Sünkel, and N. Kühtreiber (1992). New geoid solution for Slovenia and part of Croatia. In *Proceed. of the First Continental Workshop on the Geoid in Europe, P. Holota and M. Vermeer (eds.)*, pp. 158–165.
- Čolić, K., T. Bašić, B. Pribičević, and D. Medak (1996). A Geodetic-Gravimetric Method for Better Modelling of Geological Structures in the Test Area of Croatia. *Geologia Croatica* 49(2), 211–215. DOI: [10.4154/GC.1996.13](https://doi.org/10.4154/GC.1996.13).
- Čolić, K., B. Pribičević, M. Ratkajec, R. Stopar, F. Šumanovac, and J. Velić (1992). Initial digital density model of the surface Earth's core masses in the test area "Slovenia and surrounding part of Croatia" for the regional uses in physical geodesy. *Geodetski list* 3, 263–281.
- Čolić, K., B. Pribičević, and D. Švehla (1999). Astrogeodetic geoid of the Republic of Croatia. In *XXII General Assembly of the International Union of Geodesy and Geophysics (IUGG)*.
- Corchete, V. (2010). The high-resolution gravimetric geoid of Italy: ITG2009. *Journal of African Earth Sciences* 58(3), 580–584. DOI: [10.1016/j.jafrearsci.2010.05.010](https://doi.org/10.1016/j.jafrearsci.2010.05.010).
- Corchete, V., M. Chourak, and D. Khattach (2005). The high-resolution gravimetric geoid of Iberia: IGG2005. *Geophysical Journal International* 162(3), 676–684. DOI: [10.1111/j.1365-246X.2005.02690.x](https://doi.org/10.1111/j.1365-246X.2005.02690.x).
- Corchete, V., M. Chourak, D. Khattach, and E. Benaim (2007). The high-resolution gravimetric geoid of Morocco:

- MORGEO. *Journal of African Earth Sciences* 48(4), 267–272. DOI: 10.1016/j.jafrearsci.2007.04.002.
- Corchete, V., D. Flores, and F. Oviedo (2006). The first high-resolution gravimetric geoid for the Bolivian tableland: BOLGEO. *Physics of the Earth and Planetary Interiors* 157(3), 250–256. DOI: 10.1016/j.pepi.2006.04.004.
- Corchete, V. and M. Pacino (2007). The first high-resolution gravimetric geoid for Argentina: GAR. *Physics of the earth and planetary interiors* 161(3), 177–183. DOI: 10.1016/j.pepi.2007.01.012.
- Cressie, N. (1990). The origins of Kriging. *Mathematical geology* 22(3), 239–252. DOI: 10.1007/BF00889887.
- Daho, B. S. A., S. Kahlouche, and J. D. Fairhead (2006). A procedure for modelling the differences between the gravimetric geoid model and GPS/levelling data with an example in the north part of Algeria. *Computers & Geosciences* 32(10), 1733–1745. DOI: 10.1016/j.cageo.2006.04.003.
- Danila, U. (2012). *Mold2012: a new gravimetric quasigeoid model over Moldova*. Ph. D. thesis, Royal Institute of Technology (KTH). URL: <http://urn.kb.se/resolve?urn=urn:nbn:se:kth:diva-105755>.
- Daras, I. (2008). *Determination of a gravimetric geoid model of Greece using the method of KTH*. Ph. D. thesis, Royal Institute of Technology (KTH). URL: <http://urn.kb.se/resolve?urn=urn:nbn:se:kth:diva-199682>.
- de Matos, A., D. Blitzkow, G. Guimarães, and M. Lobianco (2014). GOCE and the Geoid in South America. In *Earth on the Edge: Science for a Sustainable Planet*, pp. 529–534. Springer.
- de Matos, A. C. O. C., D. Blitzkow, W. C. Machado, M. A. Nunes, N. V. Lengruher, E. M. L. Xavier, and L. P. S. Fortes (2016). MAPGEO2015: O NOVO MODELO DE ONDULAÇÃO GEOIDAL DO BRASIL. *Revista Brasileira de Cartografia* 68(10).
- Denker, H. (1988). *Hochauflösende regionale Schwerfeldbestimmung mit gravimetrischen und topographischen Daten*. Phd, Fachrichtung Vermessungswesen d. Univ. Nr. 156.
- Denker, H. (2013). Regional gravity field modeling: theory and practical results. In *Sciences of Geodesy-II*, pp. 185–291. Springer. DOI: 10.1007/978-3-642-28000-9-5.
- Denker, H. (2015). A new European gravimetric (quasi) geoid EGG2015. *26th IUGG General Assembly, June*.
- Denker, H., J.-P. Barriot, R. Barzaghi, D. Fairhead, R. Forsberg, J. Ihde, A. Kenyeres, U. Marti, M. Sarrailh, and I. Tziavos (2009). The development of the European gravimetric geoid model EGG07. In *Observing Our Changing Earth*, pp. 177–185. Springer. DOI: 10.1007/978-3-540-85426-5-21.
- Denker, H., D. Behrend, and W. Torge (1997). The European gravimetric quasigeoid EGG96. In *Gravity, Geoid and Marine Geodesy*, pp. 532–539. Springer. DOI: 10.1007/978-3-662-03482-8-71.
- Denker, H. and W. Torge (1992). Recent developments of the European geoid project. In *Proc. First Continental Workshop on the Geoid in Europe (ed. Holota, P.), Prague, May*, pp. 31–39.
- Denker, H. and W. Torge (1998). The European gravimetric quasigeoid EGG97-An IAG supported continental enterprise. In *Geodesy on the move*, pp. 249–254. Springer. DOI: 10.1007/978-3-642-72245-5-36.
- Dragčević, D., M. Pavasović, and T. Bašić (2016). Accuracy validation of official Croatian geoid solutions over the area of City of Zagreb. *Geofizika* 33(2), 183–206. DOI: 10.15233/gfz.2016.33.9.
- Draper, N. R. and H. Smith (2014). *Applied regression analysis*. John Wiley & Sons. DOI: 10.1002/9781118625590.
- D’Urso, M. (2013). On the evaluation of the gravity effects of polyhedral bodies and a consistent treatment of related singularities. *Journal of geodesy* 87(3), 239–252. DOI: 10.1007/s00190-012-0592-1.
- D’Urso, M. (2014). Gravity effects of polyhedral bodies with linearly varying density. *Celestial Mechanics and Dynamical Astronomy* 120(4), 349–372. DOI: 10.1007/s10569-014-9578-z.
- D’Urso, M. (2015). The gravity anomaly of a 2D polygonal body having density contrast given by polynomial functions. *Surveys in Geophysics* 36(3), 391–425. DOI: 10.1007/s10712-015-9317-3.
- Einstein, A. (1950). On the generalized theory of gravitation. *Scientific American* 182(4), 13–17.
- El-Ashquer, M., B. Elsaka, and G. El-Fiky (2017). EGY-HGM2016: an improved hybrid local geoid model for Egypt based on the combination of GOCE-based geopotential model with gravimetric and GNSS/levelling measurements. *Arabian Journal of Geosciences* 10(11), 251. DOI: 10.1007/s12517-017-3042-9.
- Ellmann, A. (2004). *The geoid for the Baltic countries determined by the least squares modification of Stokes formula*. Ph. D. thesis, Royal Institute of Technology (KTH).
- Ellmann, A. (2005a). Computation of three stochastic modifications of Stokes’ formula for regional geoid determination. *Computers & Geosciences* 31(6), 742–755. DOI: 10.1016/j.cageo.2005.01.008.

- Ellmann, A. (2005b). Two deterministic and three stochastic modifications of Stokes's formula: a case study for the Baltic countries. *Journal of Geodesy* 79(1), 11–23. DOI: [10.1007/s00190-005-0438-1](https://doi.org/10.1007/s00190-005-0438-1).
- Ellmann, A. and L. E. Sjöberg (2004). Ellipsoidal correction for the modified Stokes formula. *Bollettino di geodesia e scienze affini* 63(3), 153–172.
- Esan, O. (2000). *Spectral analysis of gravity field data and errors in view of sub-decimeter geoid determination in Canada*. Msc, Department of Geomatics, University of Calgary, Calgary, Canada. http://www.ucalgary.ca/engo_webdocs/MGS/00.20137.OEsan.pdf.
- Everest, G. (1830). *An Account of the Measurement of an Arc of the Meridian Between the Parallels of 180 3' and 240 7': Being a Continuation of the Grand Meridional Arc of India as Detailed by the Late Lieut.-Col. Lambton in the Volumes of the Asiatic Society of Calcutta*. J.L. Cox.
- Fan, H. (2002). *Development of the Mozambican geoid model MOZGEO 2002*. Ph. D. thesis, Royal Institute of Technology (KTH).
- Fan, J. and I. Gijbels (1996). *Local polynomial modelling and its applications: monographs on statistics and applied probability*, Volume 66. CRC Press.
- Farr, T. G., P. A. Rosen, E. Caro, R. Crippen, R. Duren, S. Hensley, M. Kobrick, M. Paller, E. Rodriguez, L. Roth, D. Seal, S. Shaffer, J. Shimada, J. Umland, M. Werner, M. Oskin, D. Burbank, and D. Alsdorf (2007). The Shuttle Radar Topography Mission. *Reviews of Geophysics* 45(2). DOI: [10.1029/2005RG000183](https://doi.org/10.1029/2005RG000183).
- Featherstone, W. (2001). Absolute and relative testing of gravimetric geoid models using Global Positioning System and orthometric height data. *Computers & Geosciences* 27(7), 807–814. DOI: [10.1016/S0098-3004\(00\)00169-2](https://doi.org/10.1016/S0098-3004(00)00169-2).
- Featherstone, W. (2003). Software for computing five existing types of deterministically modified integration kernel for gravimetric geoid determination. *Computers & Geosciences* 29(2), 183–193. DOI: [10.1016/S0098-3004\(02\)00074-2](https://doi.org/10.1016/S0098-3004(02)00074-2).
- Featherstone, W., J. Evans, and J. Olliver (1998). A Meissl-modified Vaníček and Kleusberg kernel to reduce the truncation error in gravimetric geoid computations. *Journal of Geodesy* 72(3), 154–160. DOI: [10.1007/s001900050157](https://doi.org/10.1007/s001900050157).
- Featherstone, W., J. Kirby, C. Hirt, M. Filmer, S. Claessens, N. Brown, G. Hu, and G. Johnston (2011). The augeoid09 model of the Australian height datum. *Journal of Geodesy* 85(3), 133–150. DOI: [10.1007/s00190-010-0422-2](https://doi.org/10.1007/s00190-010-0422-2).
- Featherstone, W., J. Kirby, A. Kearsley, J. Gilliland, G. Johnston, J. Steed, R. Forsberg, and M. Sideris (2001). The AUSGeoid98 geoid model of Australia: data treatment, computations and comparisons with GPS-levelling data. *Journal of Geodesy* 75(5), 313–330. DOI: [10.1007/s001900100177](https://doi.org/10.1007/s001900100177).
- Featherstone, W., J. McCubbine, N. Brown, S. Claessens, M. Filmer, and J. Kirby (2018). The first Australian gravimetric quasigeoid model with location-specific uncertainty estimates. *Journal of Geodesy* 92(2), 149–168. DOI: [10.1007/s00190-017-1053-7](https://doi.org/10.1007/s00190-017-1053-7).
- Fecher, T., R. Pail, and T. Gruber (2015). Global gravity field modeling based on GOCE and complementary gravity data. *International Journal of Applied Earth Observation and Geoinformation* 35, 120–127. DOI: [10.1016/j.jag.2013.10.005](https://doi.org/10.1016/j.jag.2013.10.005).
- Fei, Z. and M. G. Sideris (2000). A new method for computing the ellipsoidal correction for Stokes's formula. *Journal of Geodesy* 74(2), 223–231. DOI: [10.1007/s001900050280](https://doi.org/10.1007/s001900050280).
- Flury, J. (2006). Short-wavelength spectral properties of the gravity field from a range of regional data sets. *Journal of Geodesy* 79(10), 624–640. DOI: [10.1007/s00190-005-0011-y](https://doi.org/10.1007/s00190-005-0011-y).
- Forsberg, R. (1984). A study of terrain reductions, density anomalies and geophysical inversion methods in gravity field modelling. Technical report, Ohio State, Univ. Columbus Dept. of Geodetic Science. URL: www.dtic.mil/dtic/tr/fulltext/u2/a150788.pdf.
- Forsberg, R. (1985). Gravity field terrain effect computations by FFT. *Journal of Geodesy* 59(4), 342–360. DOI: [10.1007/BF02521068](https://doi.org/10.1007/BF02521068).
- Forsberg, R. (1987). A new covariance model for inertial gravimetry and gradiometry. *Journal of Geophysical Research: Solid Earth* 92(B2), 1305–1310. DOI: [10.1029/JB092iB02p01305](https://doi.org/10.1029/JB092iB02p01305).
- Forsberg, R. (1991). A new high-resolution geoid of the Nordic area. In *Determination of the Geoid*, pp. 241–250. Springer. DOI: [10.1007/978-1-4612-3104-2-29](https://doi.org/10.1007/978-1-4612-3104-2-29).

- Forsberg, R. (1993). Modelling the fine-structure of the geoid: methods, data requirements and some results. *Surveys in geophysics* 14(4), 403–418. DOI: [10.1007/BF00690568](https://doi.org/10.1007/BF00690568).
- Forsberg, R., J. Kaminskis, and D. Solheim (1997). Geoid of the Nordic and Baltic region from gravimetry and satellite altimetry. In *Gravity, Geoid and Marine Geodesy*, pp. 540–547. Springer. DOI: [10.1007/978-3-662-03482-8-72](https://doi.org/10.1007/978-3-662-03482-8-72).
- Forsberg, R. and M. Sideris (1993). Geoid computations by the multi-band spherical FFT approach. *Manuscripta Geodaetica* 18, 82–90.
- Forsberg, R. and G. Strykowski (2005). Geoid determination and fit to GPS/levelling. In *NGK Workshop – The Establishment of a New Vertical Reference for Iceland*.
- Forsberg, R. and C. C. Tscherning (1981). The use of height data in gravity field approximation by collocation. *Journal of Geophysical Research: Solid Earth* 86(B9), 7843–7854. DOI: [10.1029/JB086iB09p07843](https://doi.org/10.1029/JB086iB09p07843).
- Forsberg, R. and C. C. Tscherning (2008). An overview manual for the GRAVSOFTE geodetic gravity field modelling programs. *Contract report for JUPEM*. 2nd edition.
- Förste, C., S. Bruinsma, O. Abrikosov, F. Flechtner, J.-C. Marty, J.-M. Lemoine, C. Dahle, H. Neumayer, F. Barthelmes, R. König, et al. (2014). EIGEN-6C4-The latest combined global gravity field model including GOCE data up to degree and order 1949 of GFZ Potsdam and GRGS Toulouse. In *EGU General Assembly Conference Abstracts*, Volume 16.
- Förste, C., S. Bruinsma, S. Rudenko, O. Abrikosov, J.-M. Lemoine, J.-C. Marty, H. Neumayer, and R. Biancale (2015). EIGEN-6S4: A time-variable satellite-only gravity field model to d/o 300 based on LAGEOS, GRACE and GOCE data from the collaboration of GFZ Potsdam and GRGS Toulouse. In *EGU General Assembly Conference Abstracts*, Volume 17.
- Fotopoulos, G. (2005). Calibration of geoid error models via a combined adjustment of ellipsoidal, orthometric and gravimetric geoid height data. *Journal of Geodesy* 79(1), 111–123. DOI: [10.1007/s00190-005-0449-y](https://doi.org/10.1007/s00190-005-0449-y).
- Fotopoulos, G. (2013). Combination of heights. In *Geoid Determination*, pp. 517–544. Springer. DOI: [10.1007/978-3-540-74700-0-11](https://doi.org/10.1007/978-3-540-74700-0-11).
- Fotopoulos, G., C. Kotsakis, and M. G. Sideris (2003). How accurately can we determine orthometric height differences from GPS and geoid data? *Journal of Surveying Engineering* 129(1), 1–10. DOI: [10.1061/\(ASCE\)0733-9453\(2003\)129:1\(1\)](https://doi.org/10.1061/(ASCE)0733-9453(2003)129:1(1)).
- Franke, R. (1982). Scattered data interpolation: tests of some methods. *Mathematics of computation* 38(157), 181–200. DOI: [10.2307/2007474](https://doi.org/10.2307/2007474).
- Franke, R. and G. Nielson (1980). Smooth interpolation of large sets of scattered data. *International Journal for Numerical Methods in Engineering* 15(11), 1691–1704. DOI: [10.1002/nme.1620151110](https://doi.org/10.1002/nme.1620151110).
- Fullea, J., M. Fernandez, and H. Zeyen (2008). FA2BOUG-A FORTRAN 90 code to compute Bouguer gravity anomalies from gridded free-air anomalies: Application to the Atlantic-Mediterranean transition zone. *Computers & Geosciences* 34(12), 1665–1681. DOI: [10.1016/S0079-1946\(97\)00241-3](https://doi.org/10.1016/S0079-1946(97)00241-3).
- Gachari, M. (1998). A high resolution gravimetric geoid of the eastern Africa region. *Survey Review* 34(269), 421–436. DOI: [10.1179/sre.1998.34.269.421](https://doi.org/10.1179/sre.1998.34.269.421).
- Garcia-Abdeslem, J. (2005). The gravitational attraction of a right rectangular prism with density varying with depth following a cubic polynomial. *Geophysics* 70(6), J39–J42. DOI: [10.1190/1.2122413](https://doi.org/10.1190/1.2122413).
- Gatchalian, R., R. Forsberg, and A. Olesen. PGM2016: A new Geoid Model for the Philippines.
- Gauss, C. F. (1828). *Disquisitiones generales circa superficies curvas*. Typis Dieterichianis.
- Gerlach, C. (2003). *Zur Höhensystemumstellung und Geoidberechnung in Bayern*. Ph. D. thesis, Bayerischen Akademie der Wissenschaften.
- Gerlach, C. and V. Ophaug (2017). Accuracy of Regional Geoid Modelling with GOCE. DOI: [10.1007/1345-2017-6](https://doi.org/10.1007/1345-2017-6).
- GFZ (2017a). International Centre for Global Gravity Field Models (ICGEM). <http://icgem.gfz-potsdam.de/home>. International Centre for Global Earth Models.
- GFZ (2017b). Spherical harmonic coefficients of the topography. <http://icgem.gfz-potsdam.de/tom-rektopo>. International Centre for Global Earth Models.
- Gilardoni, M., M. Reguzzoni, and D. Sampietro (2016). GECON: a global gravity model by locally combining GOCE

- data and EGM2008. *Studia Geophysica et Geodaetica* 60(2), 228. DOI: 10.1007/s11200-015-1114-4.
- Godah, W. and J. Krynski (2015). A new gravimetric geoid model for the area of Sudan using the least squares collocation and a GOCE-based GGM. In *IGFS 2014*, pp. 123–129. Springer. DOI: 10.1007/1345-2015-196.
- Goli, M. and M. Najafi-Alamdari (2011). Planar, spherical and ellipsoidal approximations of Poisson's integral in near zone. *Journal of Geodetic Science* 1(1), 17–24. DOI: 10.2478/v10156-010-0003-6.
- Gomez, M., D. Del Cogliano, R. Perdomo, and J. L. Hormaechea (2014). A new combined quasigeoid model in Tierra del Fuego. *Geologica Acta* 12(3). DOI: 10.1344/GeologicaActa2014.12.3.4.
- Grad, M., T. Tiira, and E. W. Group (2009). The Moho depth map of the European Plate. *Geophysical Journal International* 176(1), 279–292. DOI: 10.1111/j.1365-246X.2008.03919.x.
- Grgić, I., T. Bašić, and M. Šljivarić (2014). Primjena modela geoida HRG2009 u tunelogradnji. *Geodetski list* 68(2), 89–104. URL: <http://hrcak.srce.hr/123584>.
- Grgić, I., M. Lučić, M. Repanić, O. Bjelotomić, M. Liker, D. Markovinović, and T. Bašić (2010). Preliminary works on creation of the new croatian geoid model HRG2009. *Bollettino di Geodesia e Scienze Affini* 69(2-3), 165–177.
- Grgić, I., M. Lučić, and M. Trifković (2015). Visinski sustavi u nekim europskim zemljama. *Geodetski list* 69(2), 79–96. URL: <http://hrcak.srce.hr/142565>.
- Grgić, M., M. Varga, and T. Bašić (2015). Empirical research of interpolation methods in distortion modeling for the coordinate transformation between local and global geodetic datums. *Journal of Surveying Engineering* 142(2), 05015004. DOI: 10.1061/(ASCE)SU.1943-5428.0000154.
- Grombein, T., K. Seitz, and B. Heck (2013). Optimized formulas for the gravitational field of a tesseroid. *Journal of Geodesy* 87(7), 645–660. DOI: 10.1007/s00190-016-0907-8.
- Grubbs, F. E. (1969). Procedures for detecting outlying observations in samples. *Technometrics* 11(1), 1–21. DOI: 10.1080/00401706.1969.10490657.
- Guo, D.-M., H.-Z. Xu, and M. Chen (2017). Precise Geoid Determination over Hong Kong from Heterogeneous Data Sets using a Hybrid Method. *Marine Geodesy*, 1–12. DOI: 10.1080/01490419.2017.1309330.
- Haagmans, R., E. De Min, and M. Van Gelderen (1993). Fast evaluation of convolution integrals on the sphere using 1D FFT, and a comparison with existing methods for Stokes' integral. *Manuscripta geodaetica* 18(5), 227–227.
- Harkness, W. (1891). *The Solar Parallax and Its Related Constants: Including the Figure and Density of the Earth*, Volume 3. US Government Printing Office.
- Hayford, J. F. (1909). *Geodesy: The Figure of the Earth and Isostasy from Measurements in the United States*. Number 82. US Government Printing Office.
- Hayford, J. F. and W. Bowie (1912). *Geodesy: The Effect of Topography and Isostatic Compensation Upon the Intensity of Gravity*. Number 10. US Govt. Print. Off.
- Hećimović, Ž. (2005). European Vertical Reference Network (EUVN) considering CHAMP and GRACE-gravity models. In *Symposium of the IAG Subcommission for Europe (EUREF)*.
- Hećimović, Ž. and T. Bašić (2002). Globalni geopotencijalni modeli na teritoriju Hrvatske. *Geodetski list* 57(80), 73–89.
- Hećimović, Željko. (2000). *Modeliranje referentne plohe visinskih sustava*. Phd thesis, Faculty of Geodesy, University of Zagreb. in Croatian.
- Heck, B. and W. Grüniger (1987). Modification of Stokes' integral formula by combining two classical approaches. *Proceedings of the XIX General Assembly of the International Union of Geodesy and Geophysics* 2, 309–337.
- Heck, B. and K. Seitz (2003). Solutions of the linearized geodetic boundary value problem for an ellipsoidal boundary to order e^3 . *Journal of Geodesy* 77(3), 182–192. DOI: 10.1007/s00190-002-0309-y.
- Heck, B. and K. Seitz (2007). A comparison of the tesseroid, prism and point-mass approaches for mass reductions in gravity field modelling. *Journal of Geodesy* 81(2), 121–136. DOI: 10.1007/s00190-006-0094-0.
- Heiskanen, A. W. and H. Moritz (1967). *Physical Geodesy*. San Francisco, USA: W.H. Freeman and Co Ltd. ISBN 0716702339.
- Heiskanen, W. (1931). Isostatic tables for the reduction of gravimetric observations calculated on the basis of Airy's hypothesis. *Bulletin Géodésique (1922-1941)* 30(1), 110–153. DOI: 10.1007/BF03029991.
- Heiskanen, W. A. and F. A. Vening Meinesz (1958). *The Earth and its gravity field*. McGraw-Hill Book Company,

- Inc; New York.
- Herceg, M., I. Artemieva, and H. Thybo (2015). Sensitivity analysis of crustal correction for calculation of lithospheric mantle density from gravity data. *Geophysical Journal International* 204(2), 687–696. DOI: [10.1093/gji/ggv431](https://doi.org/10.1093/gji/ggv431).
- Hinze, W. J. (2003). Bouguer reduction density, why 2.67? *Geophysics* 68(5), 1559–1560. DOI: [10.1190/1.1620629](https://doi.org/10.1190/1.1620629).
- Hirt, C. and M. Kuhn (2014). Band-limited topographic mass distribution generates full-spectrum gravity field: Gravity forward modeling in the spectral and spatial domains revisited. *Journal of Geophysical Research: Solid Earth* 119(4), 3646–3661. DOI: [10.1002/2013JB010900](https://doi.org/10.1002/2013JB010900).
- Hirvonen, R. (1961). The reformation of geodesy. *Journal of Geophysical Research* 66(5), 1471–1478. DOI: [10.1007/BF02529717](https://doi.org/10.1007/BF02529717).
- Hjelt, S.-E. (1974). The gravity anomaly of a dipping prism. *Geoexploration* 12(1), 29–39. DOI: [10.1016/0016-7142\(74\)90004-0](https://doi.org/10.1016/0016-7142(74)90004-0).
- Hofmann-Wellenhof, B. and H. Moritz (2005). *Physical Geodesy*. Springer Verlag.
- Holmes, S., N. Pavlis, P. Novák, et al. (2006). Harmsynth: A Fortran program for very-high-degree harmonic synthesis. Technical report, version 05/01.
- Huang, J. (2002). *Computational methods for the discrete downward continuation of the Earth gravity and effects of lateral topographical mass density variation on gravity and the geoid*. Phd, Department of Geodesy and Geomatics Engineering, Technical Report No. 216, University of New Brunswick, Fredericton, New Brunswick, Canada. <http://www2.unb.ca/gge/Pubs/TR216.pdf>.
- Huang, J., P. Vaníček, S. Pagiatakis, and W. Brink (2001). Effect of topographical density on geoid in the Canadian Rocky Mountains. *Journal of geodesy* 74(11-12), 805–815. DOI: [10.1007/s001900000145](https://doi.org/10.1007/s001900000145).
- Huang, J. and M. Véronneau (2013). Canadian gravimetric geoid model 2010. *Journal of geodesy* 87(8), 771–790. DOI: [10.1007/s00190-013-0645-0](https://doi.org/10.1007/s00190-013-0645-0).
- Hunegnaw, A. (2001). *Geoid determination over Ethiopia with emphasis on downward continuation of gravity anomalies*. Ph. D. thesis, Royal Institute of Technology (KTH). URL: <http://urn.kb.se/resolve?urn=urn:nbn:se:kth:diva-3255>.
- Hwang, C., C.-G. Wang, and Y.-S. Hsiao (2003). Terrain correction computation using Gaussian quadrature. *Computers & geosciences* 29(10), 1259–1268. DOI: [10.1016/j.cageo.2003.08.003](https://doi.org/10.1016/j.cageo.2003.08.003).
- IAG, I. (2017). ISG. <http://www.isgeoid.polimi.it/index.html>. International Service for the Geoid.
- Ihde, J., L. Sánchez, R. Barzaghi, H. Drewes, C. Foerste, T. Gruber, G. Liebsch, U. Marti, R. Pail, and M. Sideris (2017). Definition and proposed realization of the international height reference system (IHRs). *Surveys in Geophysics* 38(3), 549–570. DOI: [10.1007/s10712-017-9409-3](https://doi.org/10.1007/s10712-017-9409-3).
- Illiffe, J., M. Ziebart, P. Cross, R. Forsberg, G. Strykowski, and C. C. Tscherning (2003). OSGM02: A new model for converting GPS-derived heights to local height datums in Great Britain and Ireland. *Survey Review* 37(290), 276–293. DOI: [10.1179/sre.2003.37.290.276](https://doi.org/10.1179/sre.2003.37.290.276).
- Ince, E. S. (2011). *Geoid Investigation for the New Vertical Datum in Canada*. Msc, Department of Geomatics, University of Calgary, Calgary, Canada. www.ucalgary.ca/engo_webdocs/MGS/11.20344_ElmasInce.pdf.
- Inerbayeva, D. (2010). *Determination of a gravimetric geoid model of Kazakhstan using the KTH-method*. MSc thesis, Royal Institute of Technology (KTH). URL: <http://urn.kb.se/resolve?urn=urn:nbn:se:kth:diva-52284>.
- Ismail, Z. (2016). *Détermination de l'exactitude d'un géoïde gravimétrique*. Ph. D. thesis, PSL Research University. URL: <https://tel.archives-ouvertes.fr/tel-01431701>.
- Ismail, Z. and O. Jamet (2015). Accuracy of unmodified Stokes' integration in the RCR procedure for geoid computation. *Journal of Applied Geodesy* 9(2), 112–122. DOI: [10.1515/jag-2014-0026](https://doi.org/10.1515/jag-2014-0026).
- Jekeli, C. (1978). An investigation of two models for the degree variances of global covariance functions. Technical report, Ohio State, Univ. Columbus Dept. of Geodetic Science.
- Jekeli, C. (1981). Modifying Stokes' function to reduce the error of geoid undulation computations. *Journal of Geophysical Research: Solid Earth* 86(B8), 6985–6990. DOI: [10.1029/JB086iB08p06985](https://doi.org/10.1029/JB086iB08p06985).
- Jekeli, C. (2000). Heights, the Geopotential, and Vertical Datums. Technical report, Ohio State, Univ. Columbus

- Dept. of Geodetic Science. URL: <https://kb.osu.edu/dspace/handle/1811/78667>.
- Jensen, H. (1950). Formulas for the astronomical correction to the precise levelling. *Bulletin Géodésique (1946-1975)* 17(1), 267–277. DOI: [10.1007/BF0252592](https://doi.org/10.1007/BF0252592).
- Journel, A. G. and C. J. Huijbregts (1978). *Mining geostatistics*. Academic press.
- JPL, N. (2017). ASTER GDEM. DOI: [10.5067/aster/astgtm.002](https://doi.org/10.5067/aster/astgtm.002).
- Jung, K. (1961). Schwerkraftverfahren in der angewandten Geophysik. *Leipzig, Akademische Verlagsgesellschaft Geest & Portig*.
- Kamguia, J., C. Tabod, R. Nouayou, J. Tadjou, E. Manguelle-Dicoum, and H. Kande (2007). The Local Geoid Model of Cameroon: CGM05. *Nordic Journal of Surveying and Real Estate Research Volume 4*(2).
- Kasenda, A. (2009). *High precision geoid for modernization of height systems in Indonesia*. Ph. D. thesis, The University of New South Wales Sydney.
- Kaula, W. M. (1966). Tests and combination of satellite determinations of the gravity field with gravimetry. *Journal of Geophysical Research* 71(22), 5303–5314. DOI: [10.1029/JZ071i022p05303](https://doi.org/10.1029/JZ071i022p05303).
- Kaula, W. M. (2013). *Theory of satellite geodesy: applications of satellites to geodesy*. Courier Corporation.
- Kearsley, A. (1988). Tests on the recovery of precise geoid height differences from gravimetry. *Journal of Geophysical Research: Solid Earth* 93(B6), 6559–6570. DOI: [10.1029/JB093iB06p06559](https://doi.org/10.1029/JB093iB06p06559).
- Kearsley, A., M. Sideris, J. Krynski, R. Forsberg, and K. Schwarz (1985). White Sands revisited: A comparison of techniques to predict deflections of the vertical, Rep. 30007, Div. of Surv. Eng., Univ. of Calgary, Alberta.
- Kern, M. (2003). *An analysis of the combination and downward continuation of satellite, airborne and terrestrial gravity data*. Phd thesis, Department of Geomatics Engineering, University of Calgary.
- Ketelaar, A. (1976). A system for computer-calculation of the terrain correction in gravity surveying. *Geoexploration* 14(1), 57–65. DOI: [10.1016/0016-7142\(76\)90036-3](https://doi.org/10.1016/0016-7142(76)90036-3).
- Ketelaar, A. (1987). Terrain correction for gravity measurements, using a digital terrain model (DTM). *Geoexploration* 24(2), 109–124. DOI: [10.1016/0016-7142\(87\)90085-8](https://doi.org/10.1016/0016-7142(87)90085-8).
- Kiamehr, R. (2006a). *Precise Gravimetric Geoid Model for Iran Based on GRACE and SRTM Data and the Least-Squares Modification of Stokes' Formula: with Some Geodynamic Interpretations*. Ph. D. thesis, Royal Institute of Technology (KTH).
- Kiamehr, R. (2006b). The impact of lateral density variation model in the determination of precise gravimetric geoid in mountainous areas: a case study of Iran. *Geophysical Journal International* 167(2), 521–527. DOI: [10.1111/j.1365-246X.2006.03143.x](https://doi.org/10.1111/j.1365-246X.2006.03143.x).
- Kiamehr, R. and L. Sjöberg (2005). Comparison of the qualities of recent global and local gravimetric geoid models in Iran. *Studia Geophysica et Geodaetica* 49(3), 289–304. DOI: [10.1007/s11200-005-0011-7](https://doi.org/10.1007/s11200-005-0011-7).
- Kiliçoğlu, A., A. Direnç, H. Yıldız, M. Bölme, B. Aktuğ, M. Simav, and O. Lenk (2011). Regional gravimetric quasi-geoid model and transformation surface to national height system for Turkey (THG-09). *Studia Geophysica et Geodaetica* 55(4), 557. DOI: [10.1007/s11200-010-9023-z](https://doi.org/10.1007/s11200-010-9023-z).
- Klu, M. A. (2015). *Determination of a geoid model for Ghana using the Stokes-Helmert method*. Phd, University of New Brunswick, New Brunswick, Canada. URL: <https://unbscholar.lib.unb.ca/islandora/object/unbscholar%3A7108>.
- Kostecký, J., I. Pešek, J. Šimek, O. Švábenský, J. Weigel, and A. Zeman (2004). Quasigeoids for the territory of the Czech Republic. *Studia geophysica et geodaetica* 48(3), 503–518. DOI: [10.1023/B:SGEG.0000037469.70838.39](https://doi.org/10.1023/B:SGEG.0000037469.70838.39).
- Kotsakis, C. and M. G. Sideris (1999). On the adjustment of combined GPS/levelling/geoid networks. *Journal of Geodesy* 73(8), 412–421. DOI: [10.1007/s001900050261](https://doi.org/10.1007/s001900050261).
- Krarup, T. (1969). A contribution to the mathematical foundation of physical geodesy. *Geod. Inst. Copenhagen, Medd., No. 44, 80 p. 44*.
- Ku, C. C. (1977). A direct computation of gravity and magnetic anomalies caused by 2-and 3-dimensional bodies of arbitrary shape and arbitrary magnetic polarization by equivalent-point method and a simplified cubic spline. *Geophysics* 42(3), 610–622. DOI: [10.1190/1.1440732](https://doi.org/10.1190/1.1440732).
- Kuczynska-Siehien, J., A. Lyszkowicz, and M. Birylo (2016). Geoid determination for the area of Poland by the least squares modification of Stokes' formula. *Acta Geodyn. Geomater* 13(1), 181. DOI: [10.13168/AGG.2015.0041](https://doi.org/10.13168/AGG.2015.0041).

- Kuhar, M., S. Berk, B. Koler, K. Medved, O. Omang, and D. Solheim (2011). Vloga kakovostnega višinskega sistema in geoida za izvedbo GNSS-višinomerstva. *Geodetski vestnik* 55(2), 226–234. DOI: [10.15292/geodetski-vestnik.2011.02.226-234](https://doi.org/10.15292/geodetski-vestnik.2011.02.226-234).
- Kuhn, M. (2000). *Geoidbestimmung unter Verwendung verschiedener Dichtehypothesen*. Ph. D. thesis, Deutsche Geodaetische Kommission Bayer. Akad. Wiss.
- Kuhn, M. (2001). Density modelling for geoid determination. In *Gravity, Geoid and Geodynamics 2000*, pp. 271–276. Springer. DOI: [10.1007/978-3-662-04827-6-46](https://doi.org/10.1007/978-3-662-04827-6-46).
- Kuhn, M. (2003). Geoid determination with density hypotheses from isostatic models and geological information. *Journal of Geodesy* 77(1), 50–65. DOI: [10.1007/s00190-002-0297-y](https://doi.org/10.1007/s00190-002-0297-y).
- Kühtreiber, N. (1998a). Improved gravimetric geoid AGG97 of Austria. In *Geodesy on the Move*, pp. 306–311. Springer. DOI: [10.1007/978-3-642-72245-5-45](https://doi.org/10.1007/978-3-642-72245-5-45).
- Kühtreiber, N. (1998b). Precise geoid determination using a density variation model. *Physics and Chemistry of the Earth* 23(1), 59–63. DOI: [10.1016/S0079-1946\(97\)00242-5](https://doi.org/10.1016/S0079-1946(97)00242-5).
- Kühtreiber, N. (2002). High precision geoid determination of Austria using heterogeneous data. In *Gravity and Geoid 2002, Proceedings of 3rd meeting of the Int. Gravity and Geoid Commission, Thessaloniki, Greece*, pp. 144–149.
- Kuroishi, Y. (2009). Improved geoid model determination for Japan from GRACE and a regional gravity field model. *Earth, planets and space* 61(7), 807–813. DOI: [10.1186/BF03353191](https://doi.org/10.1186/BF03353191).
- Kuroishi, Y., H. Ando, and Y. Fukuda (2002). A new hybrid geoid model for Japan, GSIGEO2000. *Journal of Geodesy* 76(8), 428–436. DOI: [10.1007/s00190-002-0266-5](https://doi.org/10.1007/s00190-002-0266-5).
- Kuroishi, Y. and W. Keller (2005). Wavelet approach to improvement of gravity field–geoid modeling for Japan. *Journal of Geophysical Research: Solid Earth* 110(B3). DOI: [10.1029/2004JB003371](https://doi.org/10.1029/2004JB003371).
- Lasagna, P. A. L. (2017). *Geoid Modelling in the Sultanate of Oman*. MSc thesis, York University, Toronto Ontario. URL: <http://hdl.handle.net/10315/33619>.
- Laske, G., G. Masters, Z. Ma, and M. Pasyanos (2013a). CRUST 1.0 A New Global Crustal Model at 1°x1°. <https://igppweb.ucsd.edu/gabi/crust1.html>.
- Laske, G., G. Masters, Z. Ma, and M. Pasyanos (2013b). Update on CRUST1.0 - A 1° global model of Earth's crust. In *Geophys. Res. Abstracts*, Volume 15, pp. 2658.
- Lee, D.-T. and B. J. Schachter (1980). Two algorithms for constructing a Delaunay triangulation. *International Journal of Computer & Information Sciences* 9(3), 219–242. DOI: [10.1007/BF00977785](https://doi.org/10.1007/BF00977785).
- Lemoine, F. G., S. C. Kenyon, K. Factor, R. G. Trimmer, N. K. Pavlis, D. S. Chinn, C. M. Cox, S. M. Klosko, S. B. Luthcke, M. H. Torrence, Y. M. Wang, R. G. Williamson, E. C. Pavlis, R. H. Rapp, and T. R. Olson (1998). The development of the joint NASA GSFC and the National Imagery and Mapping Agency (NIMA) geopotential model EGM96. Technical report, NASA, USA.
- Li, X. and H.-J. Götze (2001). Ellipsoid, geoid, gravity, geodesy, and geophysics. *Geophysics* 66(6), 1660–1668. DOI: [10.1190/1.1487109](https://doi.org/10.1190/1.1487109).
- Li, Z., T. Hao, Y. Xu, and Y. Xu (2011). An efficient and adaptive approach for modeling gravity effects in spherical coordinates. *Journal of Applied Geophysics* 73(3), 221–231. DOI: [10.1016/j.jappgeo.2011.01.004](https://doi.org/10.1016/j.jappgeo.2011.01.004).
- Liebsch, G., U. Schirmer, J. Ihde, H. Denker, and J. Müller (2006). Quasigeoidbestimmung für Deutschland. *DVW Schriftenreihe* 49, 127–146.
- Liker, M., M. Lučić, B. Barišić, M. Repanić, I. Grgić, and T. Bašić (2010). Analysis of recent global geopotential models over the Croatian territory. In *Gravity, Geoid and Earth Observation*, pp. 283–288. Springer. DOI: [10.1007/978-3-642-10634-7-36](https://doi.org/10.1007/978-3-642-10634-7-36).
- Listing, J. B. (1873). *Über unsere jetzige Kenntniss der Gestalt und Grösse der Erde: Aus den Nachrichten der K. Ges. der Wiss.* Dieterich.
- Łyszkowicz, A. (2010). Quasigeoid for the area of Poland computed by least squares collocation. *Technical Sciences* 13. DOI: [10.2478/v10022-010-0014-7](https://doi.org/10.2478/v10022-010-0014-7).
- Ma, X. and D. Watts (1994). Terrain correction program for regional gravity surveys. *Computers & Geosciences* 20(6), 961–972. DOI: [10.1016/0098-3004\(94\)90037-X](https://doi.org/10.1016/0098-3004(94)90037-X).
- Mankhemthong, N., D. I. Doser, and M. R. Baker (2012). Practical Estimation of Near-surface Bulk Density Vari-

- ations Across the Border Ranges Fault System, Central Kenai Peninsula, Alaska. *Journal of Environmental and Engineering Geophysics* 17(3), 151–158.
- Marchenko, A. N., D. A. Marchenko, and A. N. Lopushansky (2017). Gravity field models derived from the second degree radial derivatives of the GOCE mission: a case study. *Annals of Geophysics* 59(6), 0649. DOI: [10.4401/ag-7049](https://doi.org/10.4401/ag-7049).
- Marti, U. (1997). Das Geoid in der Schweiz 1997. *Geodätisch-geophysikalische Arbeiten in der Schweiz* 56.
- Marti, U. (2004). High-precision combined geoid determination in Switzerland. In *Gravity, geoid and space missions (GGSM) 2004 Symposium, Porto*.
- Marti, U. (2007). Comparison of high precision geoid models in Switzerland. In *Dynamic planet*, pp. 377–382. Springer. DOI: [10.1007/978-3-540-49350-1-55](https://doi.org/10.1007/978-3-540-49350-1-55).
- Marti, U. and A. Schlatter (2002). The new height system in Switzerland. In *Vertical reference systems*, pp. 50–55. Springer. DOI: [10.1007/978-3-662-04683-8-11](https://doi.org/10.1007/978-3-662-04683-8-11).
- Martinec, Z. (1993). Effect of lateral density variations of topographical masses in view of improving geoid model accuracy over Canada. *Final report of contract DSS (23244-2)*, 4356.
- Martinec, Z. (1996). Stability investigations of a discrete downward continuation problem for geoid determination in the Canadian Rocky Mountains. *Journal of Geodesy* 70(11), 805–828. DOI: [10.1007/BF00867158](https://doi.org/10.1007/BF00867158).
- Martinec, Z. and E. Grafarend (1997). Solution to the Stokes boundary-value problem on an ellipsoid of revolution. *Studia geophysica et geodaetica* 41(2), 103–129. DOI: [10.1023/A:1023380427166](https://doi.org/10.1023/A:1023380427166).
- MATLAB, M. (2016). *version 8.6.0.267246 (R2015b)*. Natick, Massachusetts: The MathWorks Inc.
- Mayer-Guerr, T. (2015). The combined satellite gravity field model GOCO05s. In *EGU General Assembly Conference Abstracts*, Volume 17.
- Mayer-Gürr, T., N. Zehentner, B. Klinger, and A. Kvas (2014). ITSG-Grace2014: a new GRACE gravity field release computed in Graz. In *GRACE Science Team Meeting (GSTM), Potsdam*, Volume 29, pp. 2014.
- Meissl, P. (1971). Preparations for the Numerical Evaluation of Second Order Molodensky Type Formulas. Technical report, DTIC Document.
- Merry, C., D. Blitzkow, H. Abd-Elmotaal, H. Fashir, S. John, F. Podmore, and J. Fairhead (2005). A preliminary geoid model for Africa. In *A Window on the Future of Geodesy*, pp. 374–379. Springer. DOI: [10.1007/3-540-27432-4-64](https://doi.org/10.1007/3-540-27432-4-64).
- Meyer, T. H., D. R. Roman, and D. B. Zilkoski (2007). What Does Height Really Mean? Technical report, Department of Natural Resources and the Environment, University of Connecticut, USA.
- Milbert, D. (1991). GEOID90: A high-resolution geoid for the United States. *Eos, Transactions American Geophysical Union* 72(49), 545–554.
- Molinari, I. and A. Morelli (2011a). EPcrust: a reference crustal model for the European Plate. *Geophysical Journal International* 185(1), 352–364. DOI: [10.1111/j.1365-246X.2011.04940.x](https://doi.org/10.1111/j.1365-246X.2011.04940.x).
- Molinari, I. and A. Morelli (2011b). EPcrust model: crustal model for the European plate. <http://eurorem.bo.ingv.it/EPcrust-solar/>.
- Molodenskii, M. (1958). Grundbegriffe der geodatischen Gravimetrie. *Berlin, Verlag Technik*.
- Molodenskii, M. (1962). Methods for study of the external gravitational field and figure of the Earth. *Jerusalem, Israel Program for Scientific Translations, 1962*; [available from the Office of Technical Services, US Dept. of Commerce, Washington].
- Mooney, W., G. Laske, and G. Masters (1996). CRUST 5.1: A global crustal model at 5 degrees by 5 degrees. *J. Geophys. Res.*
- Moritz, H. (1968). On the use of the terrain correction in solving Molodensky's problem. Report, Ohio State, Univ. Columbus Dept. of Geodetic Science.
- Moritz, H. (1978). Least-squares collocation. *Reviews of geophysics* 16(3), 421–430. DOI: [10.1029/RG016i003p00421](https://doi.org/10.1029/RG016i003p00421).
- Moritz, H. (1980). Geodetic reference system 1980. *Bulletin géodésique* 54(3), 395–405.
- Moritz, H. (1989). *Advanced physical geodesy* (2nd ed.).
- Moritz, H. (2000). Geodetic reference system 1980. *Journal of Geodesy* 74(1), 128–133. DOI: [10.1007/978-3-662-04683-8-11](https://doi.org/10.1007/978-3-662-04683-8-11).

- 10.1007/S001900050278.
- Nagy, D. (1966a). The gravitational attraction of a right rectangular prism. *Geophysics* 31(2), 362–371. DOI: 10.1190/1.1439779.
- Nagy, D. (1966b). The prism method for terrain corrections using digital computers. *Pure and Applied Geophysics PAGEOPH* 63(1), 31–39. DOI: 10.1007/BF00875156.
- Nagy, D., G. Papp, and J. Benedek (2000). The gravitational potential and its derivatives for the prism. *Journal of Geodesy* 74(7-8), 552–560. DOI: 10.1007/s001900000116.
- Nahavandchi, H. (1998). *Precise gravimetric-GPS geoid determination with improved topographic corrections applied over Sweden*. Ph. D. thesis, Royal Institute of Technology (KTH). URL: <http://urn.kb.se/resolve?urn=urn:nbn:se:kth:diva-2726>.
- Nakiboglu, S. (1979). Hydrostatic figure and related properties of the Earth. *Geophysical Journal International* 57(3), 639–648. DOI: 10.1111/j.1365-246X.1979.tb06782.x.
- Naliboff, J., C. Lithgow-Bertelloni, L. Ruff, and N. de Koker (2012). The effects of lithospheric thickness and density structure on Earth's stress field. *Geophysical Journal International* 188(1), 1–17. DOI: 10.1111/j.1365-246X.2011.05248.x.
- Nettleton, L. (1939). Determination of density for reduction of gravimeter observations. *Geophysics* 4(3), 176–183.
- NOAA (2017). ETOPO1 Global Relief Model. <https://www.ngdc.noaa.gov/mgg/global/>.
- Nsombo, P. (1998). Preliminary geoid over Zambia. *Journal of Geodesy* 72(3), 144–153. DOI: 10.1007/s001900050156.
- Obenson, G. (1974). A 1973 gravimetric geoid of Africa. *Geophysical Journal International* 37(2), 271–283. DOI: 10.1111/j.1365-246X.1974.tb01238.x.
- Odera, P. A., Y. Fukuda, and Y. Kuroishi (2012). A high-resolution gravimetric geoid model for Japan from EGM2008 and local gravity data. *Earth, planets and space* 64(5), 361–368. DOI: 10.5047/eps.2011.11.004.
- Olliver, J. (2007). The gravimetric geoid of Tanzania. *Survey review* 39(305), 212–225. DOI: 10.1179/003962607X165186.
- Omang, O. and R. Forsberg (2000). How to handle topography in practical geoid determination: three examples. *Journal of Geodesy* 74(6), 458–466. DOI: 10.1007/s001900000107.
- Omang, O. and R. Forsberg (2002). The northern European geoid: a case study on long-wavelength geoid errors. *Journal of Geodesy* 76(6-7), 369–380. DOI: 10.1007/s00190-002-0261-x.
- Omang, O. C. D. (2000). *The Challenge of Precise Geoid Determination: Applied to Norwegian Extremities: Glaciers, Fjords and Mountains*. Ph. D. thesis, Agricultural University of Norway, Department of Mapping Sciences.
- Ophaug, V. and C. Gerlach (2017). On the equivalence of spherical splines with least-squares collocation and Stokes' formula for regional geoid computation. *Journal of Geodesy*, 1–16. DOI: 10.1007/s00190-017-1030-1.
- Pagiatakis, S. and C. Armenakis (1999). Gravimetric geoid modelling with GIS. *International Geoid Service Bulletin* 8, 105–112.
- Pagiatakis, S., D. Fraser, K. McEwen, A. Goodacre, and M. Véronneau (1999). Topographic mass density and gravimetric geoid modelling. *Boll. Geofis. Teor. Appl* 40, 189–194.
- Pail, R., T. Fecher, D. Barnes, J. Factor, S. Holmes, T. Gruber, and P. Zingerle (2016). The experimental gravity field model XGM2016. <http://pmd.gfz-potsdam.de/icgem/showshort.php?id=escidoc:2245911>.
- Paul, M. (1973). A method of evaluating the truncation error coefficients for geoidal height. *Bulletin Géodésique (1946-1975)* 110(1), 413–425. DOI: 10.1007/BF02521951.
- Pavasović, M. (2007). Analiza globalnih geopotencijalnih modela reda i stupnja do 360 na području Republike Hrvatske. *Ekscentar* (10), 70–78. URL: <http://hrcak.srce.hr/20682>.
- Pavasović, M. (2008). *Analiza mjesečnih rješenja kvazigeoida iz GRACE satelitske misije na teritoriju Republike Hrvatske*. MSc thesis, Faculty of Geodesy, University of Zagreb. in Croatian.
- Pavasović, M., M. Šljivarić, M. Rezo, M. Kranjec, D. Markovinović, and T. Bašić (2008). Quasigeoid solutions from satellite missions on the territory of the Republic of Croatia. In *Simpozij ovlaštenih inženjera geodezije (1; 2008)*.
- Pavlis, N. K., J. K. Factor, and S. A. Holmes (2007). Terrain-related gravimetric quantities computed for the next

- EGM. In *Proceedings of the 1st international symposium of the international gravity field service*, Volume 18, pp. 318–323.
- Pavlis, N. K., S. A. Holmes, S. C. Kenyon, and J. K. Factor (2008). An Earth gravitational model to degree 2160: EGM2008. *EGU General Assembly 2008*(4), 4–2.
- Pavlis, N. K., S. A. Holmes, S. C. Kenyon, and J. K. Factor (2012). The development and evaluation of the Earth Gravitational Model 2008 (EGM2008). *Journal of Geophysical Research: Solid Earth* 117(B4). DOI: [10.1029/2011JB008916](https://doi.org/10.1029/2011JB008916).
- Petit, G. and B. Luzum (2010). IERS conventions (2010). URL: <https://www.iers.org/IERS/EN/Publications/TechnicalNotes/tn36.html>.
- Petrović, S. and K. Čolić (1994). Estimating the density jump at the Mohorovičić discontinuity from the correlation with the geoid. *Manuscripta Geodaetica* 20(1), 46–51.
- Piñón, D., K. Zhang, S. Wu, and S. Cimbaro (2017). A New Argentinean Gravimetric Geoid Model: GEOIDEAR. DOI: [10.1007/1345-2017-267](https://doi.org/10.1007/1345-2017-267).
- Pizzetti, P. (1894). *Sulla espressione della gravità alla superficie del geoide supposto ellissoidico*. Tip. della R. Accademia dei Lincei.
- Pizzetti, P. (1911). Sopra il calcolo teorico delle deviazioni del geoide dall'ellissoide. *Atti della Reale Accademia della Scienze di Torino* 46, 331.
- Pohánka, V. (1988). Optimum expression for computation of the gravity field of a homogeneous polyhedral body. *Geophysical Prospecting* 36(7), 733–751. DOI: [10.1111/j.1365-2478.1988.tb02190.x](https://doi.org/10.1111/j.1365-2478.1988.tb02190.x).
- Powell, M. J. (1992). The theory of radial basis function approximation. *Advances in numerical analysis* 2, 105–210.
- Pratt, J. H. (1855). On the attraction of the Himalaya Mountains, and of the elevated regions beyond them, upon the plumb-line in India. *Philosophical Transactions of the Royal Society of London* 145, 53–100. <http://www.jstor.org/stable/108510>.
- Press, W., S. Teukolsky, W. Vetterling, and B. P. Flannery (1992). Numerical recipes in FORTRAN: The art of scientific computing. *Cambridge University Press*, 704–716.
- Rapp, R. H. (1972). Geopotential coefficient behavior to high degree and geoid information by wavelength. Technical report, Ohio State, Univ. Columbus Dept. of Geodetic Science.
- Rapp, R. H. (1973). Improved models for potential coefficients and anomaly degree variances. *Journal of Geophysical Research* 78(17), 3497–3500. DOI: [10.1029/JB078i017p03497](https://doi.org/10.1029/JB078i017p03497).
- Rapp, R. H. (1979). *Potential coefficient and anomaly degree variance modelling revisited*. URL: www.dtic.mil/get-tr-doc/pdf?AD=ADA082322.
- Rapp, R. H. (1982). Degree variances of the Earth's potential, topography and its isostatic compensation. *Journal of Geodesy* 56(2), 84–94. DOI: [10.1007/BF02525594](https://doi.org/10.1007/BF02525594).
- Reguzzoni, M., D. Sampietro, and F. Sansò (2013). Global Moho from the combination of the CRUST2.0 model and GOCE data. *Geophysical Journal International* 195(1), 222–237. DOI: [10.1093/gji/ggt247](https://doi.org/10.1093/gji/ggt247).
- Reguzzoni, M., G. Sona, R. Barzaghi, F. Sansò, A. Albertella, D. Carrion, C. Iapige De Gaetani, and L. Rossi (2017). The International Service for the Geoid and its products. In *EGU General Assembly Conference Abstracts*, Volume 19, pp. 9988.
- Repanić, M., M. Kuhar, and I. Malović (2015). High precision vertical gravity gradient determination in Croatia. *Acta Geodaetica et Geophysica* 50(2), 151–171. DOI: [10.1007/s40328-015-0102-z](https://doi.org/10.1007/s40328-015-0102-z).
- Rexer, M. and C. Hirt (2015). Spectral analysis of the Earth's topographic potential via 2D-DFT: a new data-based degree variance model to degree 90,000. *Journal of Geodesy* 89(9), 887–909. DOI: [10.1007/s00190-015-0822-4](https://doi.org/10.1007/s00190-015-0822-4).
- Rezo, M., D. Markovinović, and M. Šljivarčić (2014). Influence of the Earth's topographic masses on vertical deflection. *Tehnički vjesnik* 21(4), 697–705. URL: <https://hrcak.srce.hr/index.php?id-clanak-jezik=186233-show=clanak>.
- Ries, J., S. Bettadpur, R. Eanes, Z. Kang, U. Ko, C. McCullough, P. Nagel, N. Pie, S. Poole, T. Richter, et al. (2016). The Combination Global Gravity Model GGM05C. *Center for Space Research—The University of Texas at Austin, Texas, CSE-TM-16-01*.
- Ries, J., S. Bettadpur, S. Poole, and T. Richter (2011). Mean background gravity fields for GRACE processing. In

- GRACE science team meeting, Austin, TX*, pp. 8–10.
- Roussel, C., J. Verdun, J. Cali, and F. Masson (2015). Complete gravity field of an ellipsoidal prism by Gauss–Legendre quadrature. *Geophysical Supplements to the Monthly Notices of the Royal Astronomical Society* 203(3), 2220–2236. DOI: [10.1093/gji/ggv438](https://doi.org/10.1093/gji/ggv438).
- Rožić, N. and L. Feil (2001). Studija o obnovi i održavanju visinskog sustava Republike Hrvatske. Technical report, DGU. Izvješća o znanstveno-stručnim projektima.
- Rózsa, S. (2002a). Local geoid determination using variable surface densities. *Periodica Polytechnica. Civil Engineering* 46(2), 205.
- Rózsa, S. (2002b). The Estimation of Lateral Density Variations Using Gravity and Elevation Data: Its Application for Geoid Determination in Hungary. In *Gravity and Geoid 2002 - GG2002, 3rd Meeting of the International Gravity and Geoid Commission*, pp. 114–120.
- Sadiq, M., C. C. Tscherning, and Z. Ahmad (2010). Regional gravity field model in Pakistan area from the combination of CHAMP, GRACE and ground data using least squares collocation: A case study. *Advances in space research* 46(11), 1466–1476. DOI: [10.1016/j.asr.2010.07.004](https://doi.org/10.1016/j.asr.2010.07.004).
- Sampietro, D., M. Capponi, D. Triglione, A. Mansi, P. Marchetti, and F. Sansò (2016). GTE: a new software for gravitational terrain effect computation: theory and performances. *Pure and Applied Geophysics* 173(7), 2435–2453. DOI: [10.1007/s00024-016-1265-4](https://doi.org/10.1007/s00024-016-1265-4).
- Sánchez, L., R. Čunderlík, N. Dayoub, K. Mikula, Z. Minarechová, Z. Šíma, V. Vatrt, and M. Vojtíšková (2016). A conventional value for the geoid reference potential W_0 . *Journal of Geodesy* 90(9), 815–835. DOI: [10.1007/s00190-016-0913-x](https://doi.org/10.1007/s00190-016-0913-x).
- Sánchez, L. and M. G. Sideris (2017). Vertical datum unification for the International Height Reference System (IHRs). *Geophysical Journal International* 209(2), 570–586. DOI: [10.1093/gji/ggx025](https://doi.org/10.1093/gji/ggx025).
- Sandwell, D. T. (1987). Biharmonic spline interpolation of GEOS-3 and SEASAT altimeter data. *Geophysical research letters* 14(2), 139–142. DOI: [10.1029/GL014i002p00139](https://doi.org/10.1029/GL014i002p00139).
- Sansó, F. and M. G. Sideris (2013). *Geoid Determination*. Springer-Verlag Berlin Heidelberg. DOI: [10.1007/978-3-540-74700-0](https://doi.org/10.1007/978-3-540-74700-0).
- Sansò, F. and C. Tscherning (2003). Fast spherical collocation: theory and examples. *Journal of Geodesy* 77(1), 101–112. DOI: [10.1007/s00190-002-0310-5](https://doi.org/10.1007/s00190-002-0310-5).
- Scheinert, M., J. Müller, R. Dietrich, D. Damaske, and V. Damm (2008). Regional geoid determination in Antarctica utilizing airborne gravity and topography data. *Journal of Geodesy* 82(7), 403–414. DOI: [10.1007/s00190-007-0189-2](https://doi.org/10.1007/s00190-007-0189-2).
- Schmidt, M., M. Fengler, T. Mayer-Gürr, A. Eicker, J. Kusche, L. Sánchez, and S.-C. Han (2007). Regional gravity modeling in terms of spherical base functions. *Journal of Geodesy* 81(1), 17–38. DOI: [10.1007/s00190-006-0101-5](https://doi.org/10.1007/s00190-006-0101-5).
- Schwabe, J., M. Scheinert, R. Dietrich, F. Ferraccioli, and T. Jordan (2012). Regional geoid improvement over the Antarctic Peninsula utilizing airborne gravity data. In *Geodesy for Planet Earth*, pp. 457–464. Springer. DOI: [10.1007/978-3-642-20338-1-55](https://doi.org/10.1007/978-3-642-20338-1-55).
- Schwarz, K. (1984). Data types and their spectral properties. *Local gravity field approximation, Beijing International Summer School*.
- Schwarz, K., M. Sideris, and R. Forsberg (1987). Orthometric heights without leveling. *Journal of Surveying Engineering* 113(1), 28–40. DOI: [10.1061/\(ASCE\)0733-9453\(1987\)113:1\(28\)](https://doi.org/10.1061/(ASCE)0733-9453(1987)113:1(28)).
- Schwarz, K., M. Sideris, and R. Forsberg (1990). The use of FFT techniques in physical geodesy. *Geophysical Journal International* 100(3), 485–514. DOI: [10.1111/j.1365-246X.1990.tb00701.x](https://doi.org/10.1111/j.1365-246X.1990.tb00701.x).
- Shen, W. and J. Han (2013). Improved Geoid Determination Based on the Shallow-Layer Method: A Case Study Using EGM08 and CRUST2.0 in the Xinjiang and Tibetan Regions. *Terrestrial, Atmospheric & Oceanic Sciences* 24(4). DOI: [10.3319/TAO.2012.11.12.01\(TibXS\)](https://doi.org/10.3319/TAO.2012.11.12.01(TibXS)).
- Shepard, D. (1968). A two-dimensional interpolation function for irregularly-spaced data. In *Proceedings of the 1968 23rd ACM national conference*, pp. 517–524. ACM. DOI: [10.1145/800186.810616](https://doi.org/10.1145/800186.810616).
- Sibson, R. (1981). A brief description of natural neighbor interpolation. *Interpreting multivariate data*, 21–36.

- Sideris, M. G. (1995). Fourier geoid determination with irregular data. *Journal of Geodesy* 70(1), 2–12. DOI: [10.1007/BF00863415](https://doi.org/10.1007/BF00863415).
- Sideris, M. G. (2013). Geoid determination by FFT techniques. In *Geoid Determination*, pp. 453–516. Springer. DOI: [10.1007/978-3-540-74700-0-10](https://doi.org/10.1007/978-3-540-74700-0-10).
- Sideris, M. G. and B. B. She (1995). A new, high-resolution geoid for Canada and part of the US by the 1D-FFT method. *Journal of Geodesy* 69(2), 92–108. DOI: [10.1007/BF00819555](https://doi.org/10.1007/BF00819555).
- Sjöberg, L., A. Gidudu, and R. Ssengendo (2015). The Uganda Gravimetric Geoid Model 2014 Computed by The KTH Method. *Journal of Geodetic Science* 5(1). DOI: [10.1515/jogs-2015-0007](https://doi.org/10.1515/jogs-2015-0007).
- Sjöberg, L. E. (1977). On the Errors of spherical Harmonic Developments of Gravity at the Surface of the Earth. Technical report, Ohio State, Univ. Columbus Dept. of Geodetic Science.
- Sjöberg, L. E. (1986). Comparison of some methods of modifying Stokes' formula. *Bollettino di geodesia e scienze affini* 45(3), 229–248.
- Sjöberg, L. E. (1991). Refined least squares modification of Stokes' formula. *Manuscripta Geodaetica* 16, 367–375.
- Sjöberg, L. E. (2001). Topographic and atmospheric corrections of gravimetric geoid determination with special emphasis on the effects of harmonics of degrees zero and one. *Journal of Geodesy* 75(5), 283–290.
- Sjöberg, L. E. (2003a). A computational scheme to model the geoid by the modified Stokes formula without gravity reductions. *Journal of Geodesy* 77(7), 423–432. DOI: [10.1007/s00190-006-0112-2](https://doi.org/10.1007/s00190-006-0112-2).
- Sjöberg, L. E. (2003b). A general model for modifying Stokes' formula and its least-squares solution. *Journal of Geodesy* 77(7-8), 459–464. DOI: [10.1007/s00190-003-0346-1](https://doi.org/10.1007/s00190-003-0346-1).
- Sjöberg, L. E. (2003c). A solution to the downward continuation effect on the geoid determined by Stokes' formula. *Journal of Geodesy* 77(1), 94–100. DOI: [10.1007/s00190-002-0306-1](https://doi.org/10.1007/s00190-002-0306-1).
- Sjöberg, L. E. (2003d). Improving modified Stokes' formula by GOCE data. *Bollettino di geodesia e scienze affini* 62(3), 215–225.
- Sjöberg, L. E. (2004a). A spherical harmonic representation of the ellipsoidal correction to the modified Stokes formula. *Journal of Geodesy* 78(3), 180–186. DOI: [10.1007/s00190-004-0378-1](https://doi.org/10.1007/s00190-004-0378-1).
- Sjöberg, L. E. (2004b). The effect on the geoid of lateral topographic density variations. *Journal of Geodesy* 78(1), 34–39. DOI: [10.1007/s00190-003-0363-0](https://doi.org/10.1007/s00190-003-0363-0).
- Sjöberg, L. E. (2005). A discussion on the approximations made in the practical implementation of the remove-compute-restore technique in regional geoid modelling. *Journal of Geodesy* 78(11-12), 645–653. DOI: [10.1007/s00190-004-0430-1](https://doi.org/10.1007/s00190-004-0430-1).
- Sjöberg, L. E. (2007). The topographic bias by analytical continuation in physical geodesy. *Journal of Geodesy* 81(5), 345–350. DOI: [10.1007/s00190-006-0112-2](https://doi.org/10.1007/s00190-006-0112-2).
- Sjöberg, L. E. and M. Bagherbandi (2017a). Applications and Comparisons of LSMSA and RCR. In *Gravity Inversion and Integration*, pp. 181–202. Springer. DOI: [10.1007/978-3-319-50298-4-6](https://doi.org/10.1007/978-3-319-50298-4-6).
- Sjöberg, L. E. and M. Bagherbandi (2017b). *Gravity Inversion and Integration, Theory and Applications in Geodesy and Geophysics*. Springer. DOI: [10.1007/978-3-319-50298-4](https://doi.org/10.1007/978-3-319-50298-4).
- Sjöberg, L. E. and A. Hunegnaw (2000). Some modifications of Stokes' formula that account for truncation and potential coefficient errors. *Journal of Geodesy* 74(2), 232–238. DOI: [10.1007/s001900050281](https://doi.org/10.1007/s001900050281).
- Sjöberg, L. E. and M. S. S. Joud (2017). New Modifications of Stokes' Integral. pp. 1–8. Springer Berlin Heidelberg. DOI: [10.1007/1345-2017-17](https://doi.org/10.1007/1345-2017-17).
- Sjöberg, L. E. and H. Nahavandchi (2000). The atmospheric geoid effects in Stokes' formula. *Geophysical Journal International* 140(1), 95–100. DOI: [10.1046/j.1365-246x.2000.00995.x](https://doi.org/10.1046/j.1365-246x.2000.00995.x).
- Smith, D., D. Robertson, and D. Milbert (2001). Gravitational attraction of local crustal masses in spherical coordinates. *Journal of Geodesy* 74(11), 783–795. DOI: [10.1007/s001900000142](https://doi.org/10.1007/s001900000142).
- Smith, D. and D. Roman (2001). GEOID99 and G99SSS: 1-arc-minute geoid models for the United States. *Journal of Geodesy* 75(9), 469–490. DOI: [10.1007/s001900100200](https://doi.org/10.1007/s001900100200).
- Smith, D. A. (2000). The gravitational attraction of any polygonally shaped vertical prism with inclined top and bottom faces. *Journal of Geodesy* 74(5), 414–420. DOI: [10.1007/s001900000102](https://doi.org/10.1007/s001900000102).
- Smith, D. A. and D. G. Milbert (1999). The GEOID96 high-resolution geoid height model for the United States.

- Journal of Geodesy* 73(5), 219–236. DOI: 10.1007/s001900050239.
- Smith, D. A. and H. Small (1999). The CARIB97 high-resolution geoid height model for the Caribbean Sea. *Journal of Geodesy* 73(1), 1–9. DOI: 10.1007/s001900050212.
- Smith, W. and P. Wessel (1990). Gridding with continuous curvature splines in tension. *Geophysics* 55(3), 293–305. DOI: 10.1190/1.1442837.
- Smith, W. H. and D. T. Sandwell (1997). Global sea floor topography from satellite altimetry and ship depth soundings. *Science* 277(5334), 1956–1962. DOI: 10.1126/science.277.5334.1956.
- Sneeuw, N. (2006). *Physical geodesy*. Institute of Geodesy, Stuttgart Universität. www.gis.uni-stuttgart.de/res/study/LNErdm.pdf.
- Somigliana, C. (1929). Teoria generale del campo gravitazionale dell'ellissoide di rotazione. *Memorie della Società Astronomica Italiana* 4, 425.
- Ssengendo, R. (2015). *A height datum for Uganda based on a gravimetric quasigeoid model and GNSS/levelling*. Ph. D. thesis, Royal Institute of Technology (KTH). URL: <http://urn.kb.se/resolve?urn=urn:nbn:se:kth:diva-172547>.
- Stokes, G. G. (1849). On the variation of gravity on the surface of the Earth. *Trans. Camb. Phil. Soc.* 8, 672–695.
- Surfer, G. (2016). *version 13.3.493 (R2016)*. Golden, Colorado, USA: Golden Software, LLC.
- Švehla, D. (1998). Preliminarno odredjivanje astro-geodetskog geoida grada Zagreba. *Ekscentar* (2-3), 44–45.
- Tenzer, R., W. Chen, D. Tsoulis, M. Bagherbandi, L. E. Sjöberg, P. Novák, and S. Jin (2015). Analysis of the refined CRUST1.0 crustal model and its gravity field. *Surveys in geophysics* 36(1), 139–165. DOI: 10.1007/s10712-014-9299-6.
- Tesauro, M., M. K. Kaban, and S. A. Cloetingh (2008). EuCRUST-07: A new reference model for the European crust. *Geophysical Research Letters* 35(5). DOI: 10.1029/2007GL032244.
- Tir, M., N. Rožić, and I. Razumović (2013). The quality of the Croatian Height Reference System. *International Multidisciplinary Scientific GeoConference: SGEM: Surveying Geology & mining Ecology Management* 2, 487.
- Tocho, C., G. Font, and M. Sideris (2007). A new high-precision gravimetric geoid model for Argentina. In *Dynamic Planet*, pp. 416–423. Springer. DOI: 10.1007/978-3-540-49350-1-61.
- Torge, W. (1993). Development, state of the art and problems at large scale geoid determinations. IAG General Meeting, Beijing, 8-13 Aug. 1993.
- Torge, W., G. Weber, and H. Wenzel (1983). Computation of a high resolution European Gravimetric Geoid (EGG 1). In *Inst. fuer Angewandte Geodaesie A European Astro-Gravimetric Geoid p 7-30 (SEE N84-27355 17-46)*.
- Tóth, G. (2009). New combined geoid solution HGTUB2007 for Hungary. In *Observing our Changing Earth*, pp. 405–412. Springer. DOI: 10.1007/978-3-540-85426-5-48.
- Toth, G., S. Rozsa, V. Andritsanos, J. Ádám, and I. Tziavos (2000). Towards a cm-geoid for Hungary: recent efforts and results. *Physics and Chemistry of the Earth, Part A: Solid Earth and Geodesy* 25(1), 47–52. DOI: 10.1016/S1464-1895(00)00008-9.
- Toushmalani, R. and A. Rahmati (2014). A new inversion method of estimation of simultaneous near surface bulk density variations and terrain correction across the Bandar Charak (Hormozgan-Iran). *SpringerPlus* 3(1), 135. DOI: 10.1186/2193-1801-3-135.
- Tscherning, C. (1976a). Computation of the second-order derivatives of the normal potential based on the representation by a Legendre series. *Manuscripta geodaetica* 1(1), 71–92.
- Tscherning, C. (1976b). Covariance expressions for second and lower order derivatives of the anomalous potential. Technical report, Ohio State, Univ. Columbus Dept. of Geodetic Science.
- Tscherning, C. (1982). Geoid determination for the Nordic countries using collocation. In *Proc. General Meeting International Association of Geodesy, Tokyo*, pp. 472–483.
- Tscherning, C. (1985). GEOCOL-A FORTRAN-program for gravity field approximation by collocation. *Technical Note, Geophysical Institute, University of Copenhagen* 11.
- Tscherning, C. C. (1994). Geoid determination by least-squares collocation using GRAVSOFT. *International School for the Determination and Use of the Geoid*, 10–15.
- Tscherning, C. C. (2013). Geoid determination by 3D least-squares collocation. In *Geoid Determination*, pp. 311–336. Springer. DOI: 10.1007/978-3-540-74700-0-7.

- Tscherning, C. C., R. Forsberg, and M. Vermeer (1990). Methods for the regional gravity field modelling from SST and SGG data. Technical report, Finnish Geodetic Institute Helsinki.
- Tscherning, C. C. and R. H. Rapp (1974). Closed covariance expressions for gravity anomalies, geoid undulations, and deflections of the vertical implied by anomaly degree variance models. Report, Ohio State, Univ. Columbus Dept. of Geodetic Science.
- Tsouliis, D. (1998). A combination method for computing terrain corrections. *Physics and Chemistry of the Earth* 23(1), 53–58. DOI: 10.1016/S0079-1946(97)00241-3.
- Tsouliis, D. (1999). Analytical and numerical methods in gravity field modelling of ideal and real masses. DGK, Reihe C 3769695488, Verlag der Bayerischen Akademie der Wissenschaften.
- Tsouliis, D. (2001). Terrain correction computations for a densely sampled DTM in the Bavarian Alps. *Journal of Geodesy* 75(5-6), 291–307. DOI: 10.1007/s001900100176.
- Tsouliis, D. (2012). Analytical computation of the full gravity tensor of a homogeneous arbitrarily shaped polyhedral source using line integrals. *Geophysics* 77(2), F1–F11. DOI: 10.1190/geo2010-0334.1.
- Tsouliis, D. (2013). Geodetic use of global digital terrain and crustal databases in gravity field modeling and interpretation. *Journal of Geodetic Science* 3(1), 1–6. DOI: 10.2478/jogs-2013-0003.
- Tsouliis, D., P. Novák, and M. Kadlec (2009). Evaluation of precise terrain effects using high-resolution digital elevation models. *Journal of Geophysical Research: Solid Earth* 114(B2). DOI: 10.1029/2008JB005639.
- Tsouliis, D. and K. Patlakis (2013). A spectral assessment review of current satellite-only and combined Earth gravity models. *Reviews of Geophysics* 51(2), 186–243. DOI: 10.1002/rog.20012.
- Tsouliis, D., H. Wziontek, and S. Petrovic (2003). A bilinear approximation of the surface relief in terrain correction computations. *Journal of Geodesy* 77(5-6), 338–344. DOI: 10.1007/s00190-003-0332-7.
- Tziavos, I. and W. Featherstone (2001). First results of using digital density data in gravimetric geoid computation in Australia. In *Gravity, Geoid and Geodynamics 2000*, pp. 335–340. Springer. DOI: 10.1007/978-3-662-04827-6-56.
- Tziavos, I., M. Sideris, and H. Sünkel (1996). The Effect of Surface Density Variation on Terrain Modeling- A Case Study in Austria. Technical Report 2.
- Tziavos, I. N. and M. G. Sideris (2013). Topographic reductions in gravity and geoid modeling. In *Geoid Determination*, pp. 337–400. Springer. DOI: 10.1007/978-3-540-74700-0-8.
- Tziavos, I. N., G. Vergos, and V. Grigoriadis (2010). Investigation of topographic reductions and aliasing effects on gravity and the geoid over Greece based on various digital terrain models. *Surveys in geophysics* 31(1), 23. DOI: 10.1007/s10712-009-9085-z.
- UCSD (2017). SRTM30+. <http://topex.ucsd.edu/WWW-html/srtm30-plus.html>.
- Uieda, L., V. C. Barbosa, and C. Braitenberg (2016). Tesseroids: Forward-modeling gravitational fields in spherical coordinates. *Geophysics* 81(5), F41–F48. DOI: 10.1190/geo2015-0204.1.
- Uieda, L., N. Ussami, and C. Braitenberg (2010). Computation of the gravity gradient tensor due to topographic masses using tesseroids. *Eos Trans. AGU* 91(26).
- Ulotu, P. (2009). *Geoid model of Tanzania from sparse and varying gravity data density by the KTH method*. Ph. D. thesis, Royal Institute of Technology (KTH). URL: <http://urn.kb.se/resolve?urn=urn:nbn:se:kth:diva-10270>.
- USGS (2017a). Earth Explorer. <http://earthexplorer.usgs.gov/>.
- USGS (2017b). Global 30 Arc-Second Elevation (GTOPO30). <https://lta.cr.usgs.gov/GTOPO30>.
- USGS (2017c). Shuttle Radar Topography Mission (SRTM) 1 Arc-Second Global. <https://lta.cr.usgs.gov/SRTM1Arc>.
- USGS (2017d). Shuttle Radar Topography Mission (SRTM) Void Filled. <https://lta.cr.usgs.gov/SRTMVf>.
- USGS (2017e). SRTM15. <ftp://topex.ucsd.edu/pub/srtm15-plus/>.
- Van Hees, G. S. (1991). Stokes formula using fast Fourier techniques. In *Determination of the Geoid*, pp. 405–408. Springer. DOI: 10.1007/978-1-4612-3104-2-47.
- Vaniček, P. (1976). *Physical geodesy*. University of New Brunswick, Department of Geodesy and Geomatics Engineering. www2.unb.ca/gge/Pubs/LN43.pdf.
- Vaniček, P. and W. Featherstone (1998). Performance of three types of Stokes's kernel in the combined solution for

- the geoid. *Journal of Geodesy* 72(12), 684–697. DOI: [10.1007/s001900050209](https://doi.org/10.1007/s001900050209).
- Vaníček, P., R. Kingdon, and M. Santos (2012). Geoid versus quasigeoid: a case of physics versus geometry. *Contributions to Geophysics and Geodesy* 42(1), 101–118. DOI: [10.2478/v10126-012-0004-9](https://doi.org/10.2478/v10126-012-0004-9).
- Vaníček, P. and A. Kleusberg (1987). The Canadian geoid-stokesian approach. *Manuscripta Geodaetica* 12(2), 86–98.
- Vaníček, P., A. Kleusberg, Z. Martinec, W. Sun, P. Ong, M. Najafi, P. Vajda, L. Harrie, P. Tomášek, and B. Horst (1995). Compilation of a precise regional geoid. Technical report, Geodetic Survey Division, Fredericton. Final report on research.
- Vaníček, P. and E. J. Krakiwsky (2015). *Geodesy: The Concepts*. Elsevier.
- Vaníček, P. and Z. Martinec (1994). The Stokes-Helmert scheme for the evaluation of a precise geoid. *Manuscripta geodaetica* 3(19), 119–128.
- Vaníček, P. and L. E. Sjöberg (1991). Reformulation of Stokes's theory for higher than second-degree reference field and modification of integration kernels. *Journal of Geophysical Research: Solid Earth* 96(B4), 6529–6539. DOI: [10.1029/90JB02782](https://doi.org/10.1029/90JB02782).
- Varga, M. (2012a). Testiranje Airy-Heiskanen modela topo-izostatske kompenzacije na području Republike Hrvatske. *Ekscentar* 1(15), 104–108. URL: <http://hrcak.srce.hr/81663>.
- Varga, M. (2012b). *Topo-isostatic model of the territory of the Republic of Croatia*. MSc thesis, Faculty of Geodesy, University of Zagreb.
- Varga, M. and T. Bašić (2013). Quality Assessment and Comparison of Global Digital Elevation Models on the Territory of the Republic of Croatia. *Kartografija i geoinformacije (Cartography and Geoinformation)* 12(20), 4–17.
- Varga, M. and T. Bašić (2015). Accuracy validation and comparison of global digital elevation models over Croatia. *International Journal of Remote Sensing* 36(1), 170–189. DOI: [10.1080/01431161.2014.994720](https://doi.org/10.1080/01431161.2014.994720).
- Varga, M., O. Bjelotomić, and T. Bašić (2016). Initial Considerations on Modernization of the Croatian Height Reference System. In *International Symposium on Engineering Geodesy–SIG 2016*.
- Varga, M., D. Dragčević, D. Pinter, M. Ramić, and I. Topolovec (2012). Regional geoids in the world. *Ekscentar: časopis studenata Geodetskog fakulteta Sveučilišta u Zagrebu* 148(15), 82–88.
- Vella, M. (2003). A new precise co-geoid determined by spherical FFT for the Malaysian peninsula. *Earth, planets and space* 55(6), 291–299. DOI: [10.1186/BF03351763](https://doi.org/10.1186/BF03351763).
- Vergos, G. S., I. N. Tziavos, and M. G. Sideris (2006). On the validation of CHAMP-and GRACE-type EGMs and the construction of a combined model. *Geodezija I Kartografija, Geodesy and Cartography* 55(3), 115–131.
- Vermeer, M. (2018). *Physical geodesy*. Aalto University, Helsinki. <https://users.aalto.fi/~mvermeer/fys-en.pdf>.
- Véronneau, M., R. Duval, and J. Huang (2006). A gravimetric geoid model as a vertical datum in Canada. *Geomatica* 60(2), 165–172.
- Véronneau, M. and J. Huang (2002). The Canadian gravimetric geoid model of 2000 (CGG2000). Technical report, Geodetic Survey Division.
- Vincent, S. and J. G. Marsh (1974). Global detailed gravimetric geoid. In *The use of artificial satellites for geodesy and geodynamics*, pp. 825–855.
- Vincenty, T. (1975). Direct and inverse solutions of geodesics on the ellipsoid with application of nested equations. *Survey review* 23(176), 88–93. DOI: [10.1179/sre.1975.23.176.88](https://doi.org/10.1179/sre.1975.23.176.88).
- Wang, Y., J. Saleh, X. Li, and D. Roman (2012). The US Gravimetric Geoid of 2009 (USGG2009): model development and evaluation. *Journal of Geodesy* 86(3), 165–180. DOI: [10.1007/s00190-011-0506-7](https://doi.org/10.1007/s00190-011-0506-7).
- Wenzel, H. G. (1981). Zur Geoidbestimmung durch kombination von schwereanomalien und einem kugelfunctionsmodell mit hilfe von integralformeln. *ZfV* 106(3), 102–111.
- Wenzel, H. G. (1982). Geoid computation by least squares spectral combination using integral kernels. *Proceed. IAG General Meet.*, 438–453.
- Wenzel, H.-G. (1985). *Hochauflösende Kugelfunktionsmodelle für das Gravitationspotential der Erde*. Universität Hannover.

- Werner, R. A. (2017). The solid angle hidden in polyhedron gravitation formulations. *Journal of Geodesy* 91(3), 307–328. DOI: [10.1007/s00190-016-0964-z](https://doi.org/10.1007/s00190-016-0964-z).
- Werner, R. A. and D. J. Scheeres (1996). Exterior gravitation of a polyhedron derived and compared with harmonic and mascon gravitation representations of asteroid 4769 Castalia. *Celestial Mechanics and Dynamical Astronomy* 65(3), 313–344. DOI: [10.1007/BF00053511](https://doi.org/10.1007/BF00053511).
- Wichiencharoen, C. (1982). The indirect effects on the computation of geoid undulations. Technical report, Ohio State, Univ. Columbus Dept. of Geodetic Science. <https://ntrs.nasa.gov/search.jsp?R=19830016735>.
- Wild-Pfeiffer, F. (2008). A comparison of different mass elements for use in gravity gradiometry. *Journal of Geodesy* 82(10), 637–653. DOI: [10.1007/s00190-008-0219-8](https://doi.org/10.1007/s00190-008-0219-8).
- Wong, L. and R. Gore (1969). Accuracy of geoid heights from modified Stokes kernels. *Geophysical Journal International* 18(1), 81–91. DOI: [10.1111/j.1365-246X.1969.tb00264.x](https://doi.org/10.1111/j.1365-246X.1969.tb00264.x).
- Yakubu, C. I., V. G. Ferreira, and C. Y. Asante (2017). Towards the Selection of an Optimal Global Geopotential Model for the Computation of the Long-Wavelength Contribution: A Case Study of Ghana. *Geosciences* 7(4), 113. DOI: [10.3390/geosciences7040113](https://doi.org/10.3390/geosciences7040113).
- Yamaguchi, Y., A. B. Kahle, H. Tsu, T. Kawakami, and M. Pniel (1998). Overview of Advanced Spaceborne Thermal Emission and Reflection Radiometer (ASTER). *IEEE Transactions on Geoscience and Remote Sensing* 36(4), 1062–1071. DOI: [10.1109/36.700991](https://doi.org/10.1109/36.700991).
- Yildiz, H., R. Forsberg, J. Ågren, C. Tscherning, and L. Sjöberg (2012). Comparison of remove-compute-restore and least squares modification of Stokes' formula techniques to quasi-geoid determination over the Auvergne test area. *Journal of Geodetic Science* 2(1), 53–64. DOI: [10.2478/v10156-011-0024-9](https://doi.org/10.2478/v10156-011-0024-9).
- Yun, H.-S. (1999). Precision geoid determination by spherical FFT in and around the Korean peninsula. *Earth, planets and space* 51(1), 13–18. DOI: [10.1186/BF03352204](https://doi.org/10.1186/BF03352204).
- Zhou, H., Z. Luo, Z. Zhou, Q. Li, B. Zhong, and H. Hsu (2016). A new time series of GRACE monthly gravity field models: HUST-Grace2016. <http://dataservices.gfz-potsdam.de/icgem/showshort.php?id=escidoc:1815895>.
- Ziebart, M., J. Iliffe, R. Forsberg, and G. Strykowski (2008). Convergence of the UK OSGM05 GRACE-based geoid and the UK fundamental benchmark network. *Journal of Geophysical Research: Solid Earth* 113(B12), n/a–n/a. DOI: [10.1029/2007JB004959](https://doi.org/10.1029/2007JB004959).

Appendix A

Flowcharts of KTH and RCR geoid determination approaches

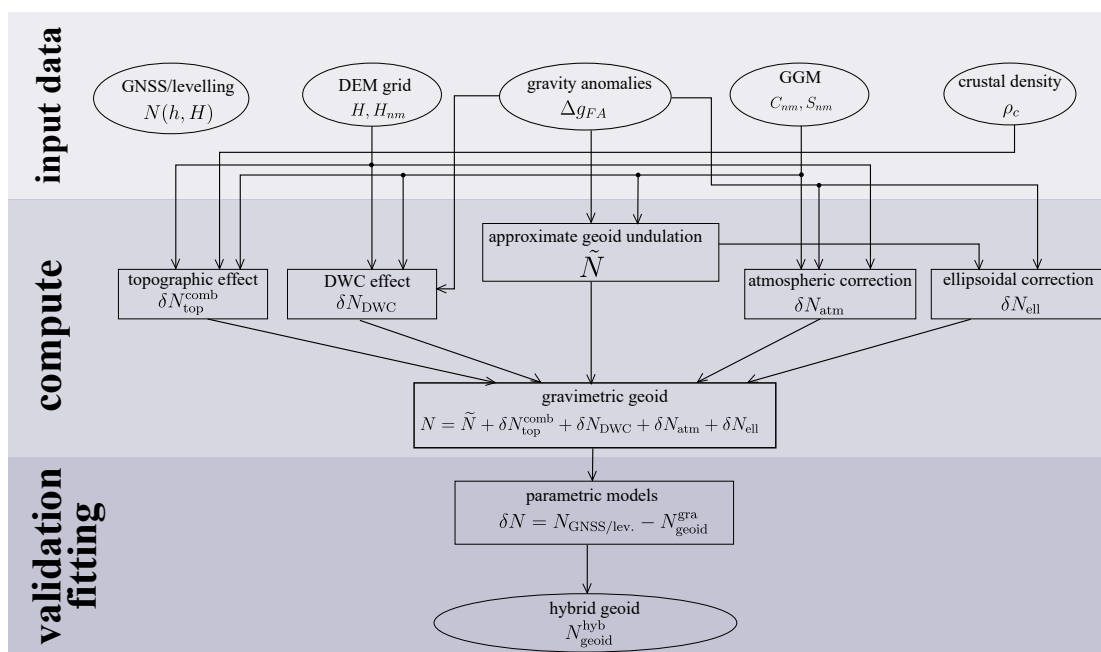


Figure A.1: Flowchart of geoid determination using KTH approach.

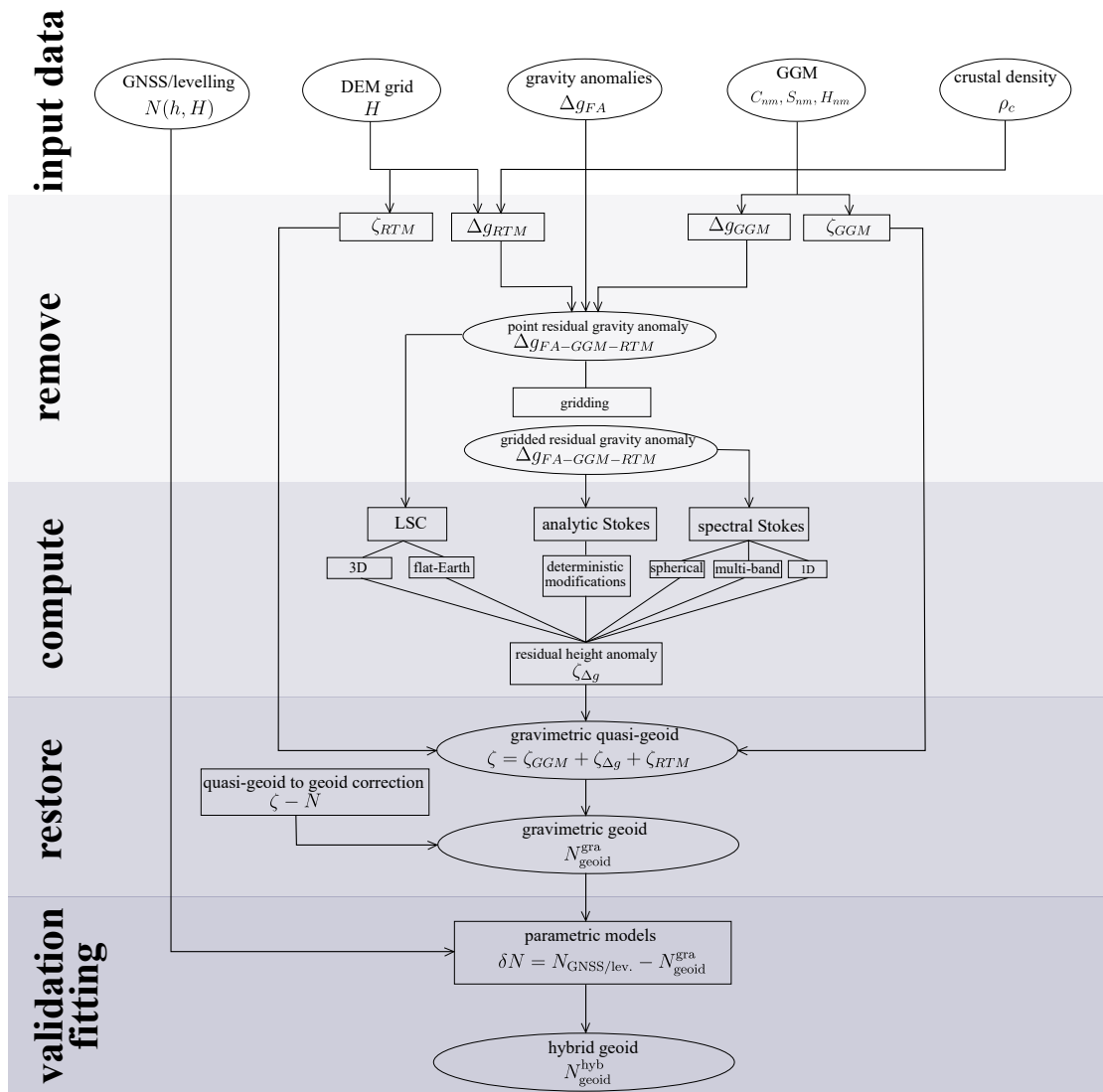


Figure A.2: Flowchart of geoid determination using RCR approach.

Appendix B

Gridded geoid undulation differences between KTH and RCR solutions

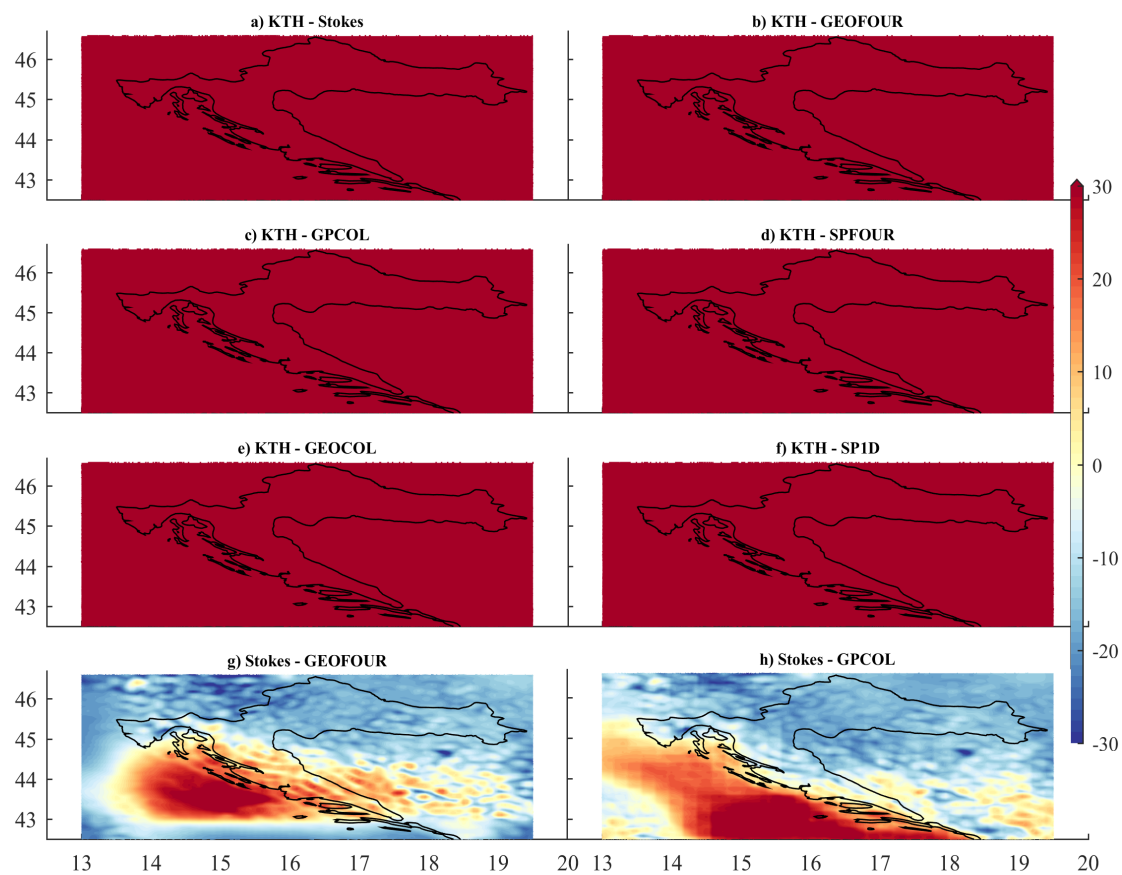


Figure B.1: Differences ($grid\ 1 - grid\ 2$) between gravimetric geoid models calculated by using different computation methods. Units: [cm]. Part 1/3.

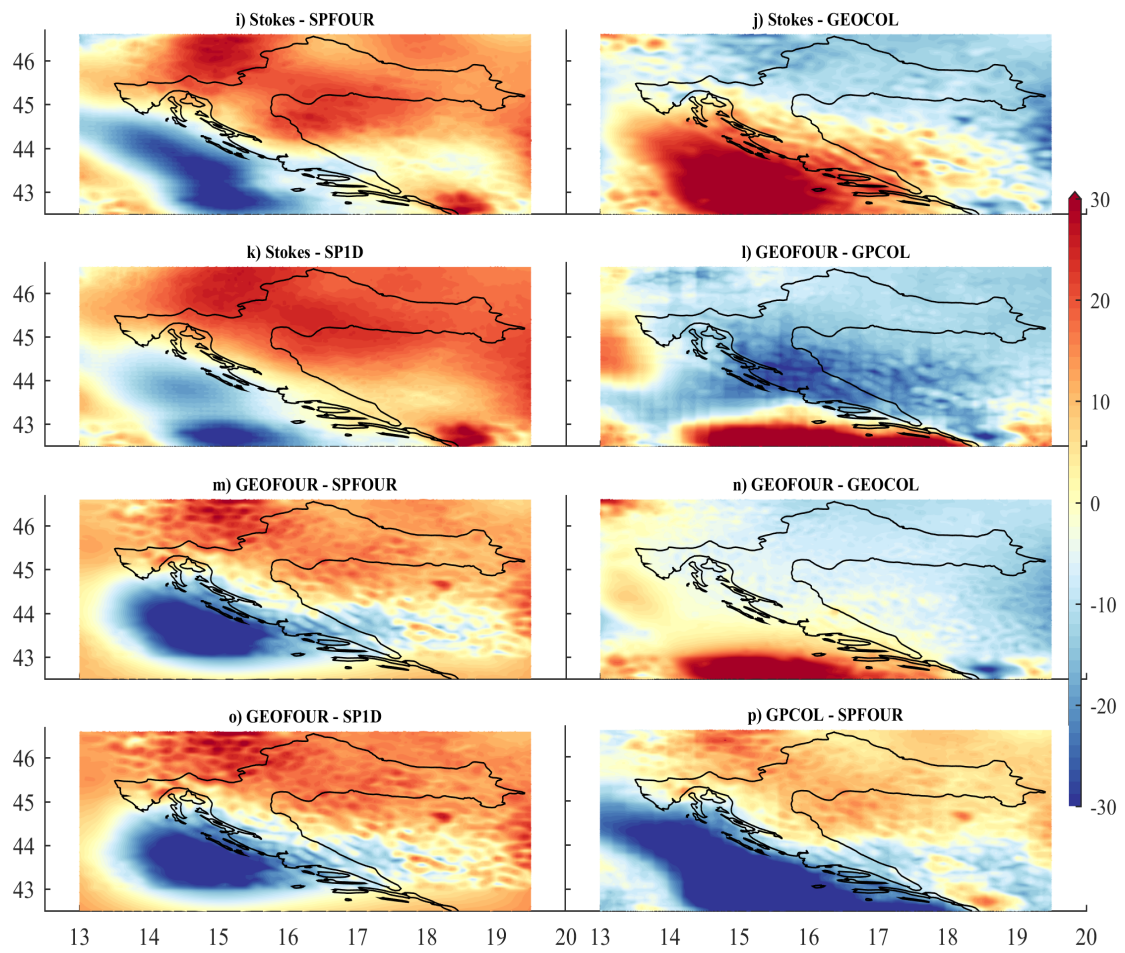


Figure B.2: Differences ($grid\ 1 - grid\ 2$) between gravimetric geoid models calculated by using different computation methods. Units: [cm]. Part 2/3.

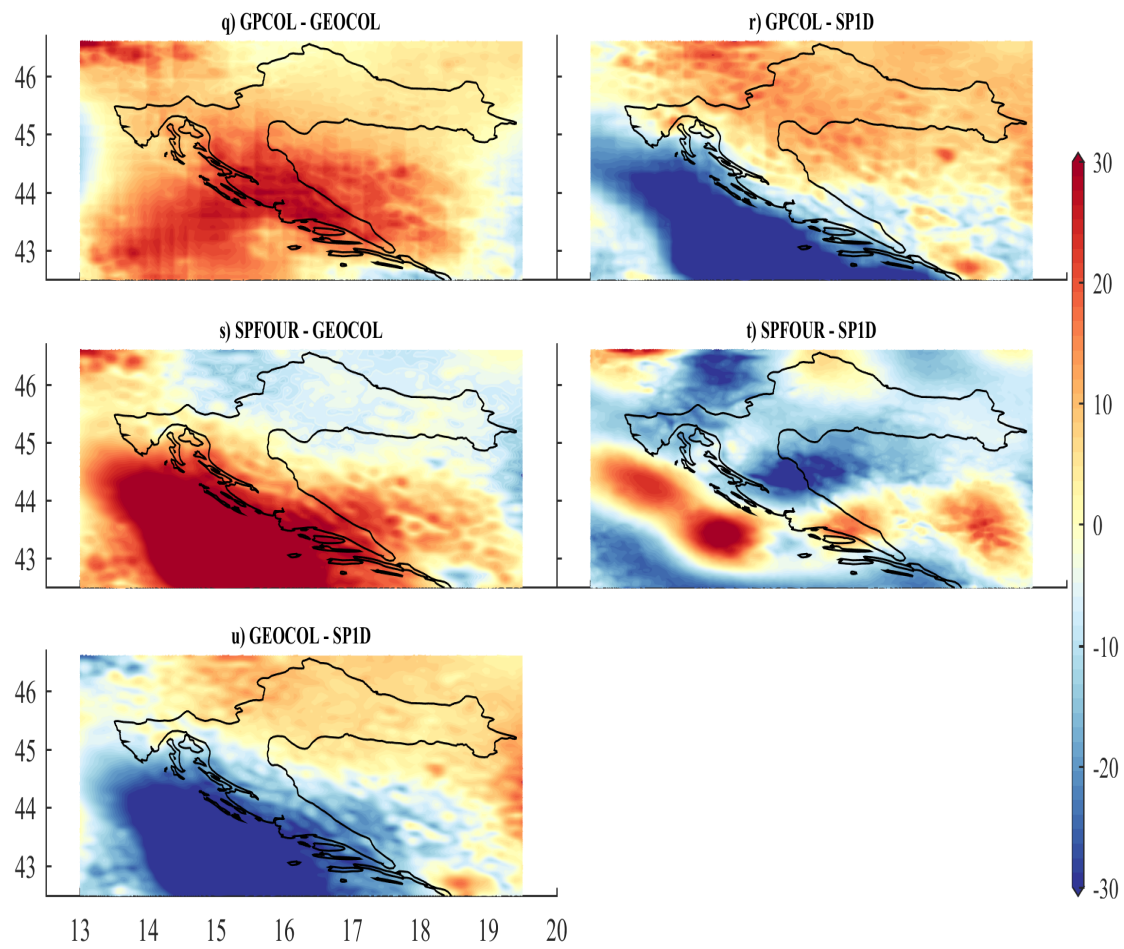


Figure B.3: Differences (*grid 1* – *grid 2*) between gravimetric geoid models calculated by using different computation methods. Units: [cm]. Part 3/3.

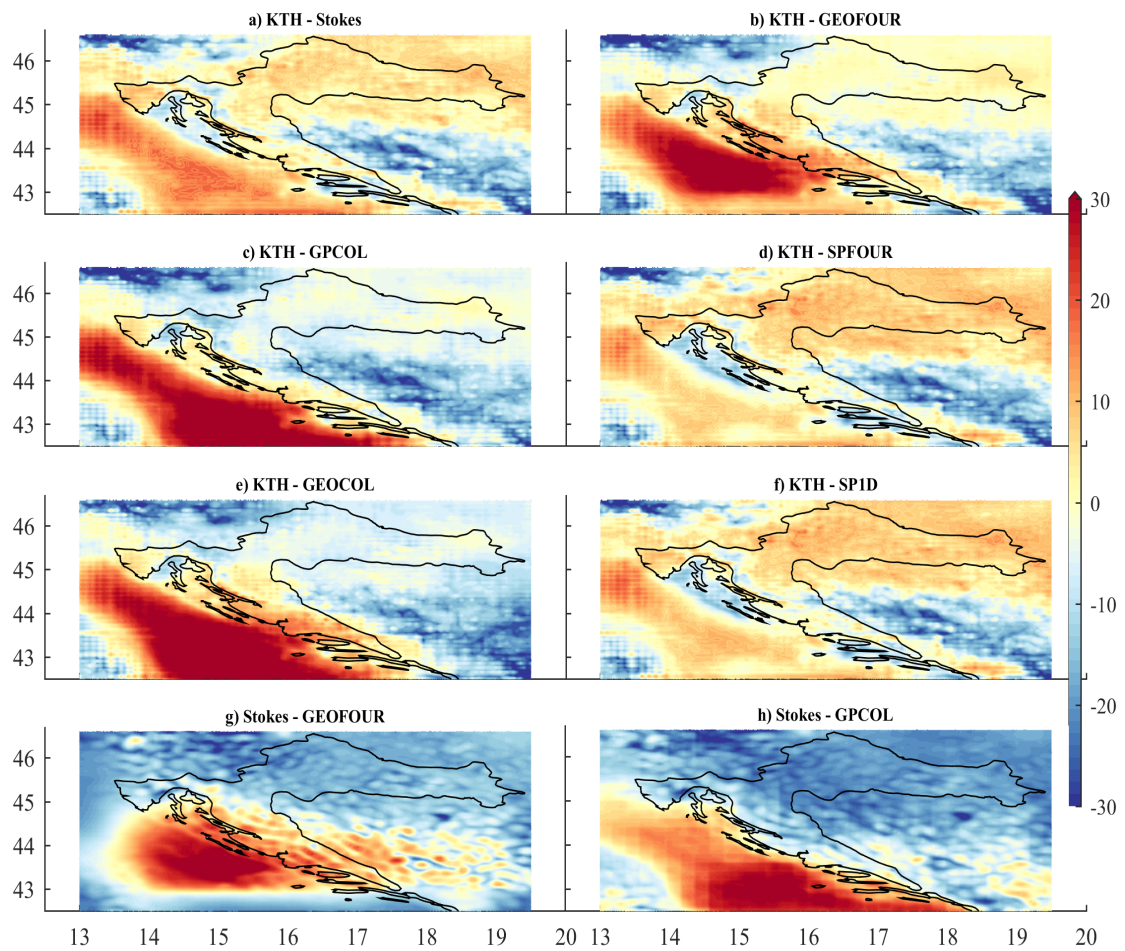


Figure B.4: Differences ($grid\ 1 - grid\ 2$) between gravimetric geoid models calculated by using different computation methods. Mean difference between models removed. Units: [cm]. Part 1/3.

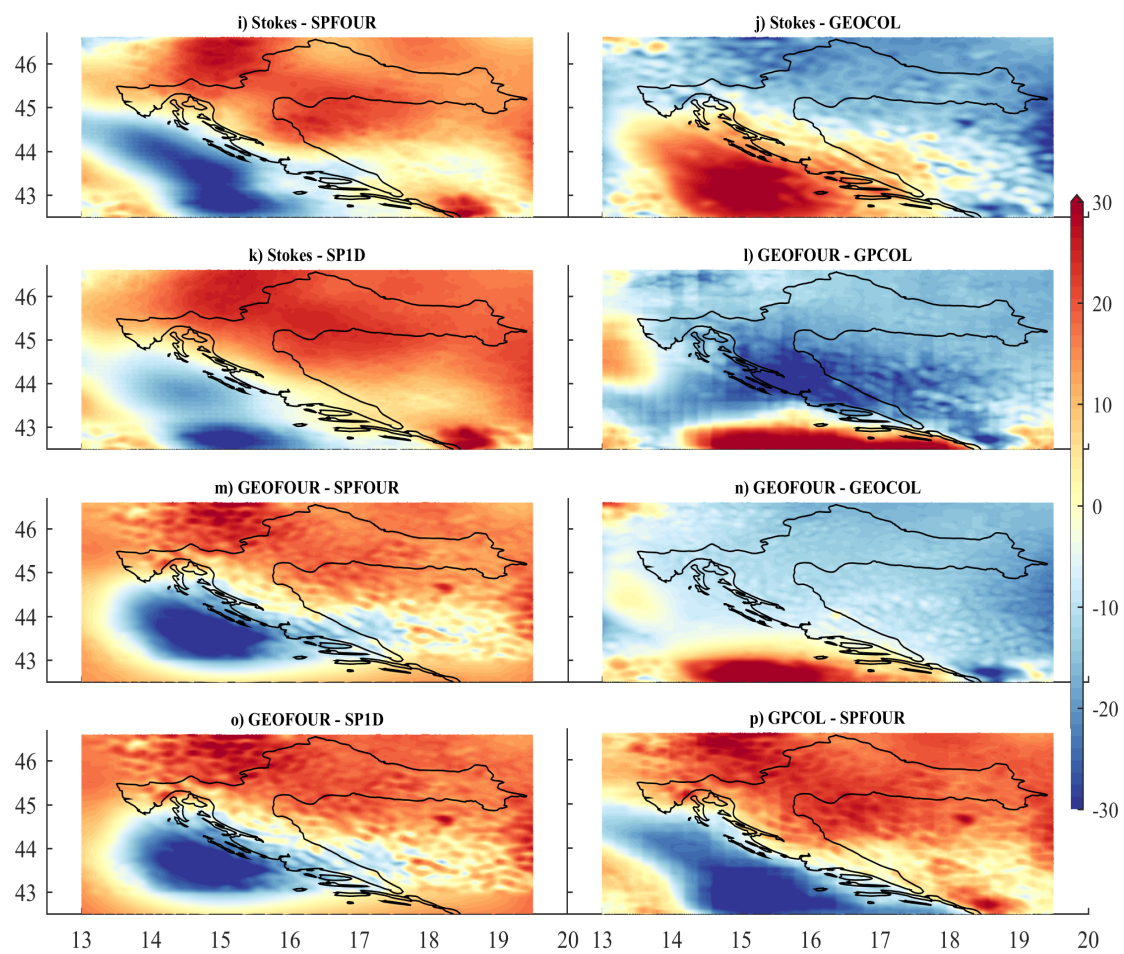


Figure B.5: Differences ($grid\ 1 - grid\ 2$) between gravimetric geoid models calculated by using different computation methods. Mean difference between models removed. Units: [cm]. Part 2/3.

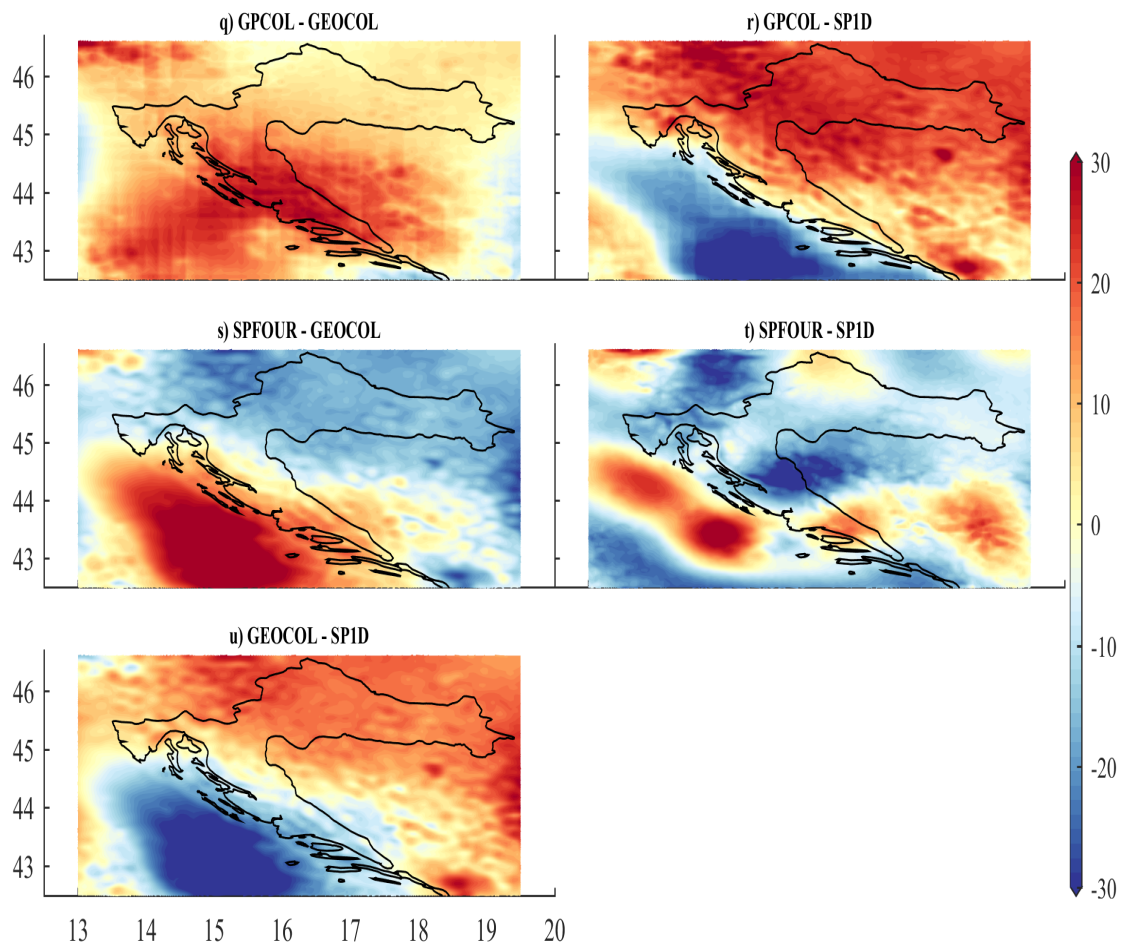


Figure B.6: Differences ($grid\ 1 - grid\ 2$) between gravimetric geoid models calculated by using different computation methods. Mean difference between models removed. Units: [cm]. Part 3/3.

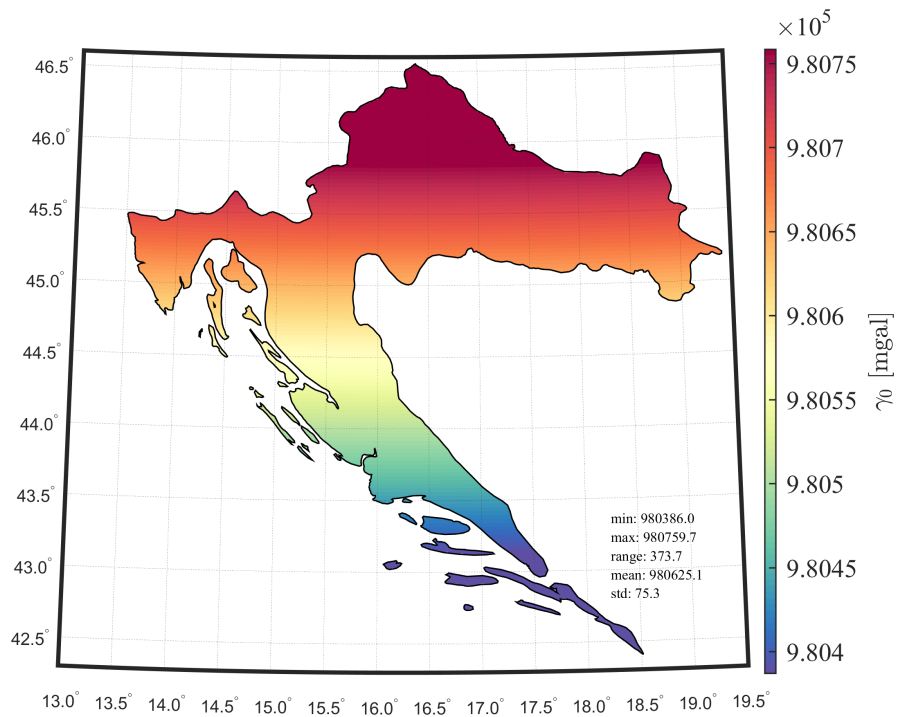
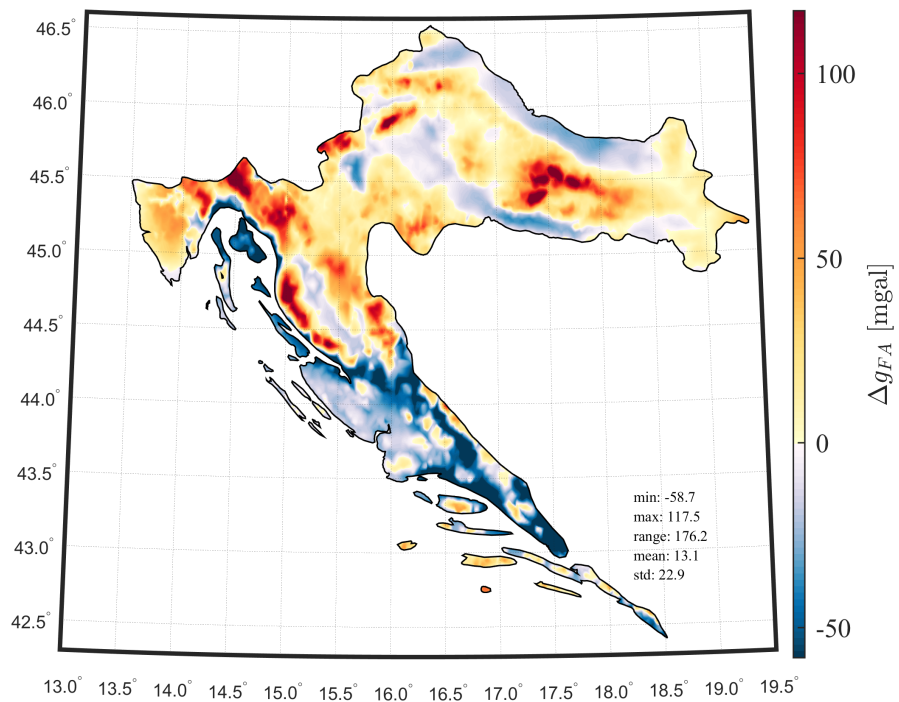
Appendix C

Models of topographic reductions and gravity anomalies

Developed models of gravity anomalies for the territory of the Republic of Croatia is given in this chapter. Initial data for development of models are free-air gravity anomalies Δg_{FA} from the database described in section 5.1, visualized in figure 5.1b.

Table C.1: Statistics of the gravity anomaly models. Units: [mgal].

Model of	min	max	range	mean	st. dev.
Δg_{FA}	-59	120	178	13	23
δg_{TC}	-0	21	21	2	3
Δg_{Faye}	-48	125	173	15	22
Δg_{sB}	-90	45	135	-18	26
Δg_{cB}	-84	47	131	-16	25
δg_{A-H}	-1	256	257	59	52
Δg_{A-H}	-187	39	226	-46	46

Figure C.1: Normal gravity γ_0 modelFigure C.2: Free-air gravity anomaly Δg_{FA} model

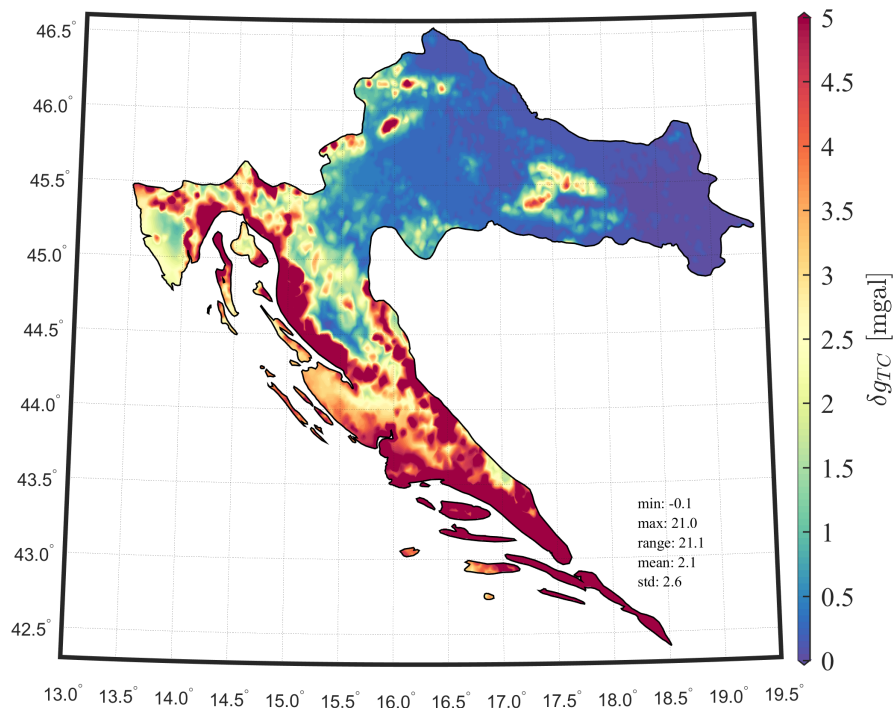


Figure C.3: Terrain correction δg_{TC} model

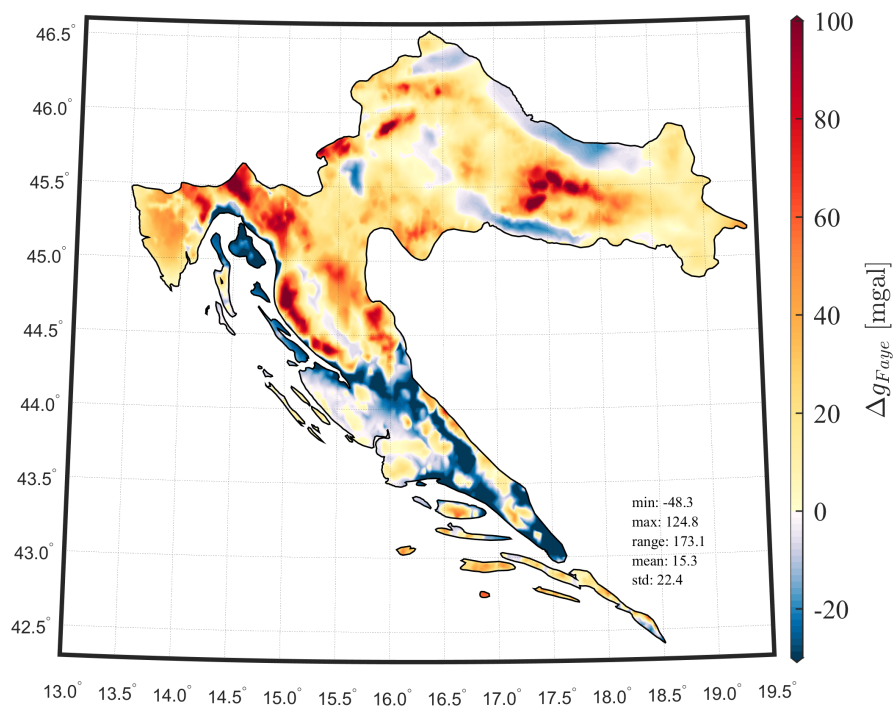
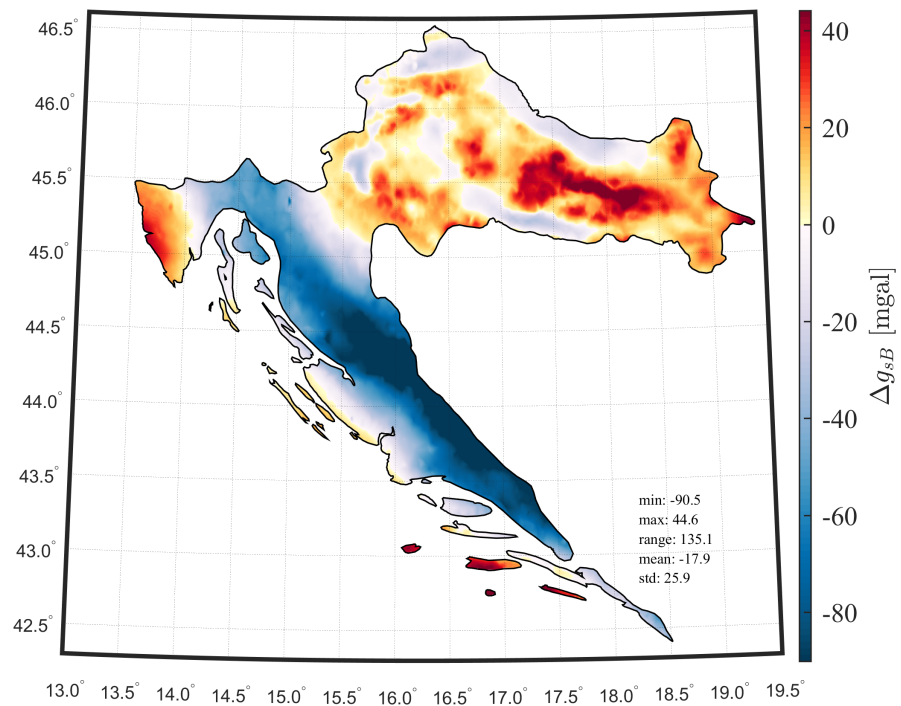
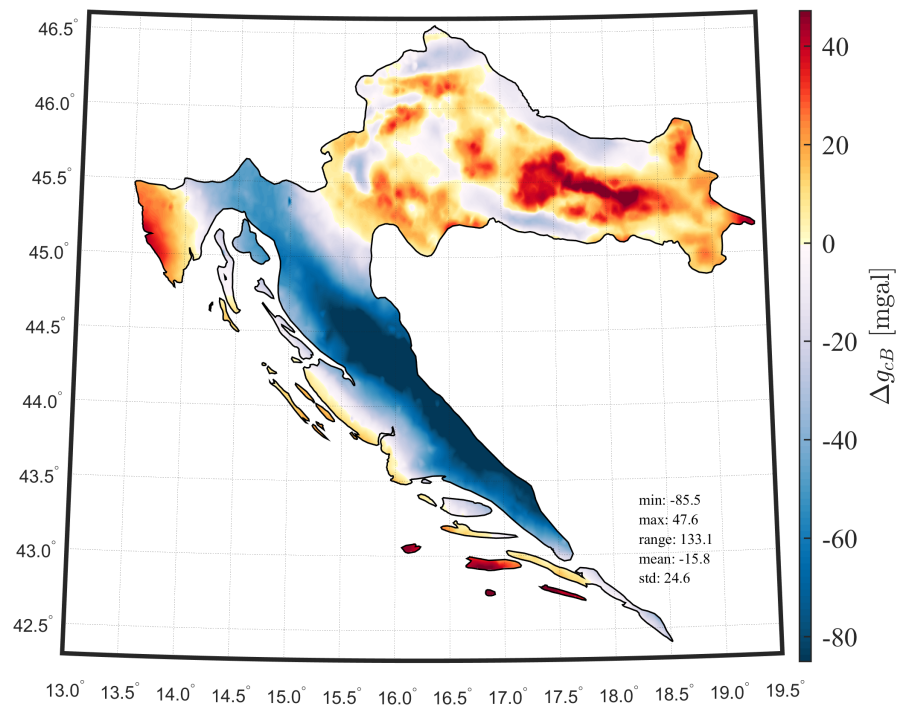


Figure C.4: Faye (Helmert) anomaly Δg_{Faye} model

Figure C.5: Simple Bouguer anomaly Δg_{sB} modelFigure C.6: Complete Bouguer anomaly Δg_{cB} model

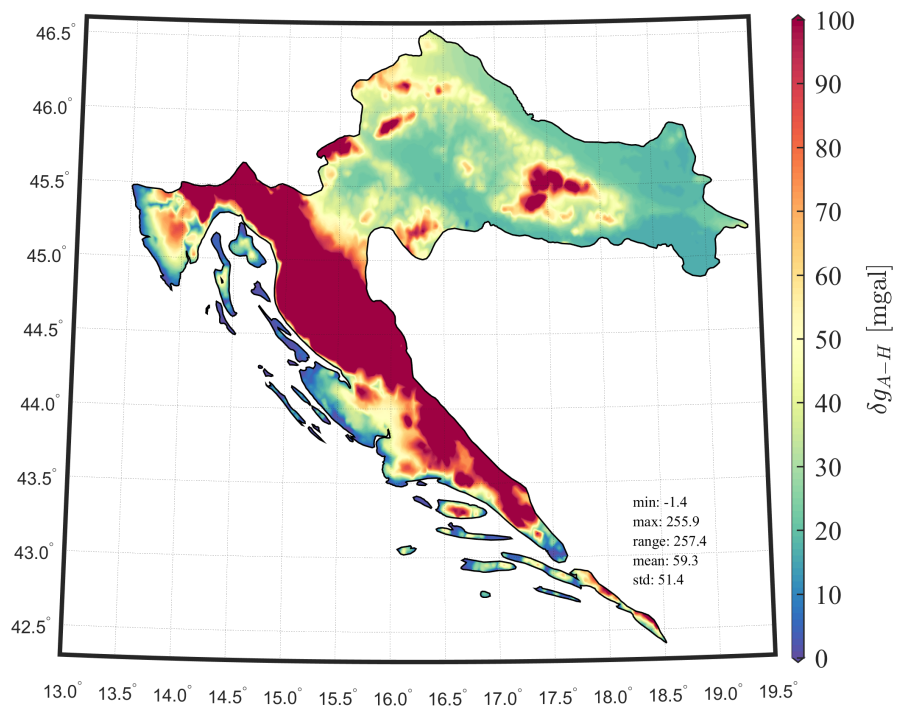


Figure C.7: Airy-Heiskanen topographic-isostatic reduction δg_{A-H} model

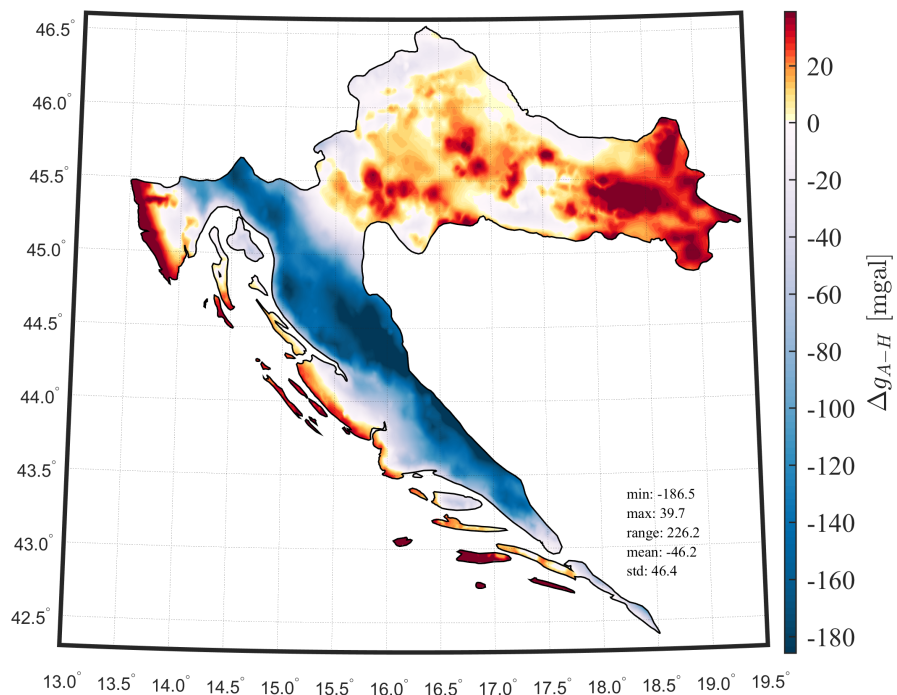


Figure C.8: Airy-Heiskanen topographic-isostatic anomaly Δg_{A-H} model

Appendix D

Developed software

Programming language: Matlab.

Total scripts: 160.

Total lines of code: 13260.

Listed routines enable automatized creation of gravimetric and hybrid geoid models and models of gravity anomalies with definition of input models and parameters. The routines are sorted in task-related sections and ordered in a structured and connected way. Short description of the most relevant routines:

- A00:
 - control script which runs all other routines,
 - definition of global input parameters, models, paths,
 - preparing, converting, structuring, filling gaps of the input models,
 - backup of the data that runs with each run of the main progra,
 - creation of folders
 - compilation of Fortran and C++ scripts.
- A1, A2, A3:
 - creation of the input gravity database,
 - automatizes fill of the gravity database,
 - creation of the anomaly and geoid grids,
- A5, A6: calculation of the global and terrain gravity effects,
- A7: cross-validation and gridding of gravity anomalies,
- A8: creation of crustal (2D) density grids,
- A9: vizualization of all gravity, GGM, DEM, density grids,
- B: calculation of GGM gravity effects using different input data and parameters (GGM models and maximum degree of SH),
- C1: creation of fine, coarse, reference DEMs,
- C2: calculation of terrain gravity effects using different input data parameters (DEM models, r_1 , r_2 , resolutions of DEMs),
- D:

- residual gravity field modeling using GGM and terrain gravity effects,
 - calculation of different types of gravity anomalies (Bouguer, topo-isostatic, Helmert, etc.),
 - visualization of gravity residuals,
 - selection of gravity residuals,
 - detection and filtering of outliers,
- E1 to E8: RCR geoid determination approach (Stokes, GEOFOUR, SPFOUR, GPCOL, LSC, and SP1D geoid determination methods) using various input data and parameters
 - F8: KTH geoid determination approach
 - G1: UNB geoid determination approach (results not presented in this thesis)
 - H1: GGM models validation on gravity and GNSS/levelling points
 - E23, E24, S_DR: all kinds of analysis', visualizations, statistics, etc.

Table D.1: A list of developed Matlab scripts

File name	Last modified	Lines of code
A00_ulazni_parametri	22-Aug-2017	145
A00a_supp_reset_all_computation_data_and_metadata	16-Aug-2017	343
A00aa_delete_bad_solutions_init	04-Aug-2017	33
A00ab_delete_bad_solutions	04-Aug-2017	244
A00b_create_unique_ids	08-Jun-2017	13
A00c_supp_delete_variables	04-Aug-2017	1
A00d_prepare_all_input_models	18-Sep-2017	89
A00db_fill_gaps_in_input_models	19-Sep-2017	31
A00f_backup	04-Aug-2017	35
A00g_consistency_solutions_check	08-Jun-2017	58
A00g_make_folders	09-Aug-2017	27
A00h_compile_software	02-Jun-2017	17
A1_A_stations_init	05-Sep-2017	87
A1_B_stations_fill	21-Jul-2017	60
A1_C_GGMplus_evaluation	03-Jun-2017	31
A2_geoid_grid	15-Jun-2017	42
A3_anomaly_grid	04-Oct-2017	26
A5_TC_efekti_svih_tocaka	22-Sep-2017	143
A6_GGM_efekti_svih_tocaka	24-Jun-2017	65
A7_A_cross_validation_best_gridding_method	23-Aug-2017	162
A7_B_grid_FA_anomaly	03-Jun-2017	30
A8_A_density_grid	25-Sep-2017	163
A8_B_density_grid_vizualization	06-Oct-2017	80
A9_vizualizacija_gridova	12-Oct-2017	174

Continued on next page

Table D.1 – continued from previous page

File name	Date modified	Lines of code
B0_graflab_init	18-Sep-2017	15
B1_A_graflab_metadata	02-Jun-2017	42
B1_B_graflab_remove_compute	02-Jun-2017	39
C0_A_TC_init	06-Oct-2017	109
C1_0_metadata_modeli	02-Jun-2017	191
C1_A_DMR_TCGRID	03-Apr-2017	18
C1_B_TC_DMR_fini	14-Apr-2017	18
C1_C_DMR_grubi	02-Jun-2017	26
C1_D_DMR_ref	02-Jun-2017	27
C1_E_rho	01-Aug-2017	58
C2_A_TC_remove_metadata	14-Jul-2017	92
C2_B_TC_remove_compute	02-Jun-2017	70
D1_AB_residuals_with_or_without_outliers	25-Jun-2017	48
D1_AC_recompute_residuals	21-Jul-2017	44
D1_AD_manually_create_residuals	10-Jul-2017	71
D1_A_gravity_residuals	21-Jul-2017	310
D1_B_vizualization_gravity_residuals	13-Sep-2017	183
D1_C_graph	19-Jul-2017	71
D1_C_graph_2	11-Sep-2017	168
D1_C_graph_3	11-Sep-2017	38
D2_A_select_gravity_residuals_for_4_RCR	04-Aug-2017	46
D2_B_outliers_gravity_GNSSlev	31-Jul-2017	31
D3_gridding_DWC_selected_gravity_residuals	25-Jul-2017	52
E1_A_Stokes_init	02-Aug-2017	20
E1_B_Stokes_metadata	02-Jun-2017	40
E1_C_Stokes_compute	15-Jun-2017	49
E20_restore_init	08-Jun-2017	32
E21_A_graflab_metadata	08-Jun-2017	31
E21_B_graflab_restore_compute	13-Jun-2017	43
E22_A_TC_metadata	08-Jun-2017	30
E22_B_TC_restore_compute	11-Jun-2017	71
E23_A_RCR_restore	10-Oct-2017	418
E23_A_RCR_restore_error	13-Jun-2017	29
E23_B_RCR_export_geoid_statistics	10-Oct-2017	171
E23_C_A_fit_gravimetric_geoid_and_independent_geoid_validation	21-Aug-2017	134
E23_C_B_vizualize_gravimetric_hybrid_residuals	11-Oct-2017	104
E23_C_C_differences_geoid_vs_GNSS_lev	10-Oct-2017	84
E23_C_D_statistics_of_all_geoid_compt_methods	10-Oct-2017	49
E23_C_E_relative_geoid_accuracy	10-Oct-2017	106

Continued on next page

Table D.1 – continued from previous page

File name	Date modified	Lines of code
E23_C_S_initialize_names_and_paths	17-Aug-2017	121
E24_A_A_RCR_mega_metadata	10-Aug-2017	43
E24_A_B_RCR_graph	18-Sep-2017	176
E24_B_RCR_geoid_vizualization	10-Aug-2017	201
E2_A_GEOFOUR_init	04-Aug-2017	15
E2_B_GEOFOUR_metadata	15-Jun-2017	33
E2_C_GEOFOUR_compute	04-Aug-2017	60
E3_A_GPCOL_init	04-Aug-2017	18
E3_B_GPCOL_metadata	08-Jun-2017	37
E3_C_GPCOL_compute	04-Aug-2017	94
E4_A_SPFOUR_init	03-Aug-2017	19
E4_B_SPFOUR_metadata	15-Jun-2017	41
E4_C_SPFOUR_compute	07-Aug-2017	65
E7_A_SP1D_init	03-Aug-2017	17
E7_B_SP1D_metadata	15-Jun-2017	39
E7_C_SP1D_compute	07-Aug-2017	60
E8_0_cov_init	04-Aug-2017	28
E8_1_A_empcov_metadata	08-Jun-2017	31
E8_1_B_empcov_compute	09-Jun-2017	45
E8_2_A_covfit_metadata	30-Jul-2017	59
E8_2_B_covfit_compute	30-Jul-2017	74
E8_3_0_statistics_of_covariances	30-Jul-2017	38
E8_3_1_vizualize_covariances	12-Oct-2017	79
E8_4_A_geocol_init	07-Aug-2017	16
E8_4_B_geocol_metadata	28-Jul-2017	41
E8_4_C_geocol_compute	04-Aug-2017	114
F1_A_KTH_init	07-Jul-2017	34
F1_B_KTH_metadata	02-Jun-2017	90
F1_C_KTH_compute	28-Jun-2017	179
F1_D_KTH_export_statistics	23-Jun-2017	35
F2_A_KTH_geoid_vizualization	05-Sep-2017	171
F2_B_KTH_graph	28-Jun-2017	137
F2_C_KTH_graph_3	28-Jun-2017	44
F2_S_KTH_recompute_statistics	07-Jun-2017	22
F2_S_KTH_remove_unnecesary_fields	07-Jun-2017	18
G1_A_UNB_init	08-Jun-2017	51
G1_B_A_UNB_effects_metadata	01-Jun-2017	55
G1_B_B_UNB_effects	01-Jun-2017	168
G1_C_A_UNB_graflab_init	27-Apr-2017	12

Continued on next page

Table D.1 – continued from previous page

File name	Date modified	Lines of code
G1_C_B_UNB_graflab_metadata	26-Apr-2017	31
G1_C_C_UNB_graflab_compute	26-Apr-2017	44
G1_D_A_UNB_Stokes_metadata	02-Jun-2017	43
G1_D_B_UNB_Stokes_compute	09-Jun-2017	90
G1_E_UNB_validation	02-Jun-2017	38
G1_F_A_UNB_effects_vizualization	19-Jun-2017	93
G1_F_B_UNB_graflab_vizualization	19-Jun-2017	78
G1_F_C_UNB_Stokes_vizualization	19-Jun-2017	101
G1_S_UNB_supp_vizualization	17-Feb-2017	21
G1_Z_UNB_DWC	03-Apr-2017	35
H1_A_GGM_validation	21-Aug-2017	170
H1_B_GGM_vizualization	14-Aug-2017	175
H1_C_A_GGM_graph	06-Oct-2017	107
H1_C_B_GGM_graph	10-Oct-2017	91
H1_C_C_GGM_residuals_map	06-Oct-2017	135
H1_C_D_GGM_all_parametric_models	06-Oct-2017	56
H1_C_E_GGM_statistics	22-Aug-2017	52
H1_D_A_GGM_spectral	19-Sep-2017	79
H1_D_B_GGM_spectral	20-Sep-2017	84
O1_A_input	11-Oct-2017	197
O2_A_graph_1_1	12-Oct-2017	100
O2_B_graph_2_vs_1	07-Oct-2017	116
O2_C_graph_correl	07-Jul-2017	36
S_DR_10_RCR_geoid_components_statistics	10-Oct-2017	190
S_DR_11_geoid_ili_razlike_geoida	10-Oct-2017	151
S_DR_12_A_geoid_statistics	13-Oct-2017	70
S_DR_12_S_A_geoid_statistics_metadata	13-Oct-2017	159
S_DR_12_S_B_add_space_between_rows	13-Oct-2017	35
S_DR_13_geoid_all_parametric_models	10-Oct-2017	64
S_DR_14_geoid_to_quasi_geoid_correction	10-Oct-2017	51
S_DR_15_FA_TC_Bouguer_TI_anomaly_map	13-Oct-2017	171
S_DR_16_unfiltered_filtered_residuals_map	06-Oct-2017	84
S_DR_16_unfiltered_filtered_residuals_map_animation	25-Sep-2017	85
S_DR_17_CRUST1	06-Oct-2017	99
S_DR_18_GGM_nmax	20-Sep-2017	29
S_DR_19_Stokes_kernel	13-Oct-2017	52
S_DR_1_statistika_anomaly_filter_non_filter	13-Sep-2017	21
S_DR_20_export_list_of_routines	16-Oct-2017	40
S_DR_21_leg_pol	13-Oct-2017	22

Continued on next page

Table D.1 – continued from previous page

File name	Date modified	Lines of code
S_DR_22_surface_spherical_harmonics	26-Sep-2017	20
S_DR_23_Schwarz1984	12-Oct-2017	15
S_DR_2_A_DEM_eksport	13-Oct-2017	27
S_DR_2_B	06-Oct-2017	26
S_DR_3_EGM2008	13-Oct-2017	48
S_DR_4_density_grid_publication_vizualize	13-Oct-2017	132
S_DR_5_CV	23-Aug-2017	159
S_DR_6_KTH_geoid	13-Oct-2017	118
S_DR_7_A_KTH_selected_solutions	11-Oct-2017	82
S_DR_7_B_KTH_best_solution	10-Oct-2017	39
S_DR_8_A_RCR_residuals_selected_solutions	10-Oct-2017	86
S_DR_O2_A_init	28-Jul-2017	56
S_DR_O2_B_D2_run	07-Jul-2017	34
S_func_R_2_text	16-Jun-2017	7
S_func_read_geoid_model	09-Aug-2017	32
S_rectangle_lines_from_points_lat_lon	22-Sep-2017	15
S_spoji_egm2008	21-Jun-2017	20
S_zero_padding	22-Jul-2017	0
N_or_g_fitting	11-Aug-2017	113
W0_LVD	07-Apr-2017	40
ertm2160_2013_v2	10-Oct-2014	219
expand_area_with_gravity	22-Feb-2017	36
ggmplus2013_v4	20-Jan-2017	221
h_H_N_fitting	11-May-2017	93
inv_chol	06-Sep-2016	11
legen_nm	25-Apr-2016	9
par_elips	10-May-2017	129
parametric_model_v2	29-May-2017	94
struct_unique_records	06-Feb-2017	43
test_access_ggmplus	20-Jan-2017	76
vincenty_distance	05-Apr-2017	108

Appendix E

Additional tables

Table E.1: Properties of height systems (after Meyer et al. 2007 and Ince 2011)

Type	Equation	Defines level surface	Misclosure	Physically meaningful	Rigorous implementation
Geopotential number	$C = \int_0^P g \delta n$	yes	no	yes	yes
Dynamic	$H^{dyn} = \frac{C}{\gamma_0}$	yes	no	yes	yes
Orthometric	$H = \frac{C}{\bar{g}}$	no	no	yes	no
Normal	$H^* = \frac{C}{\bar{\gamma}}$	no	no	no	yes
Normal-orthometric	$H^{NO} = \frac{C^*}{\bar{\gamma}}$	no	no	no	yes
Ellipsoidal	h	no	no	no	yes
Geoid undulation	$N = h - H$				
Height anomaly	$\zeta = h - H^*$				

Table E.2: A list of fitting parametric models (Daho et al. 2006, Fotopoulos 2013)

Name	\mathbf{A}_i^T
1-p	1
4-p	1, $\cos \varphi \cos \lambda$, $\cos \varphi \sin \lambda$, $\sin \varphi$
5-p	1, $\cos \varphi \cos \lambda$, $\cos \varphi \sin \lambda$, $\sin \varphi$, $\sin^2 \varphi$
7-p	1, $\cos \varphi \cos \lambda$, $\cos \varphi \sin \lambda$, $\sin \varphi$, $\sin^2 \varphi$, $\frac{\cos \varphi \sin \varphi \sin \lambda}{W}$, $\frac{\cos \varphi \sin \varphi \cos \lambda}{W}$; $W = \sqrt{1 - e^2 \sin^2 \varphi}$
differential similarity	$\cos \varphi \cos \lambda$, $\cos \varphi \sin \lambda$, $\sin \varphi$, $\frac{\sin \varphi \cos \varphi \sin \lambda}{W}$, $\frac{\sin \varphi \cos \varphi \cos \lambda}{W}$, $\frac{1 - f^2 \sin^2 \varphi}{W}$, $\frac{\sin^2 \varphi}{W}$
1 st poly.	1, $\Delta \varphi$, $\Delta \lambda$
2 nd poly.	1, $\Delta \varphi$, $\Delta \lambda$, $\Delta \varphi \Delta \lambda$, $\Delta \varphi^2$, $\Delta \lambda^2$
3 rd poly.	1, $\Delta \varphi$, $\Delta \lambda$, $\Delta \varphi \Delta \lambda$, $\Delta \varphi^2$, $\Delta \lambda^2$, $\Delta \varphi \Delta \lambda^2$, $\Delta \varphi^3$, $\Delta \lambda^3$
4 th poly.	1, $\Delta \varphi$, $\Delta \lambda$, $\Delta \varphi \Delta \lambda$, $\Delta \varphi^2$, $\Delta \lambda^2$, $\Delta \varphi^2 \Delta \lambda$, $\Delta \varphi \Delta \lambda^2$, $\Delta \varphi^3$, $\Delta \lambda^3$, $\Delta \varphi^2$, $\Delta \varphi^3 \Delta \lambda$, $\Delta \varphi \Delta \lambda^3$, $\Delta \varphi^4$, $\Delta \lambda^4$

Table E.3: Basic statistical measures used for analysis of results

name	acronym	equation
arithmetic mean	mean	$x_{\text{mean}} = \frac{1}{n} (\sum_{i=1}^n x_i)$
variance	σ	$x_{\sigma} = \frac{1}{n} (\sum_{i=1}^n x_i^2)$
root mean square	rms	$x_{\text{rms}} = \sqrt{\frac{1}{n} (\sum_{i=1}^n x_i^2)}$
standard deviation	st. dev.	$x_{\text{st.dev.}} = \sqrt{\frac{1}{n-1} \sum_{i=1}^n (x_i - \bar{x})^2}$

Table 9.4: Formulas for obtaining gravity values, topographic reductions and gravity anomalies

Functional	Type	Symbol	Formulas
gravity	Free-Air	g_{FA}	$= g + \delta g_{FA}$
	simple Bouguer	g_{sB}	$= g + \delta g_{FA} - \delta g_B$
	complete Bouguer	g_{cB}	$= g + \delta g_{FA} - \delta g_B + \delta g_{TC}$
	Faye (Helmert)	g_{Faye}	$= g + \delta g_{FA} - \delta g_{TC}$
	Airy-Heiskanen	g_{A-H}	$= g + \delta g_{FA} - \delta g_{A-H}$
	Pratt-Hayford	g_{P-H}	$= g + \delta g_{FA} - \delta g_{P-H}$
	Residual Terrain Model	g_{RTM}	$= g + \delta g_{FA} - \delta g_{RTM}$
reduction	Free-Air	δg_{FA}	$= -\frac{\partial g}{\partial H} H \approx -\frac{\partial \gamma}{\partial H} H$
	simple Bouguer	δg_B	$= 2\pi G \rho H_P$
	terrain correction	δg_{TC}	$= G \int \int \int_H^{H_P} \frac{\rho(x,y,z)(H_P-z)}{l^3} dx dy dz$
	Airy-Heiskanen	δg_{A-H}	$= \delta g_{A-H}^{\text{top}} - \delta g_{A-H}^{\text{comp}} = G \int \int \int_0^{H(x,y)} \frac{\rho(x,y,z)(H_P-z)}{l^3} dx dy dz - G \int \int_{-T_0-t-H_P}^{-T_0-H_P} \frac{\Delta \rho(x,y,z)(H_P-z)}{l^3} dx dy dz$
	Pratt-Hayford	δg_{P-H}	$= \delta g_{P-H}^{\text{top}} - \delta g_{P-H}^{\text{comp}} = G \int \int \int_0^{H(x,y)} \frac{\rho(x,y,z)(H_P-z)}{l^3} dx dy dz - G \int \int_{-D-H_P}^{-H_P} \frac{\Delta \rho(x,y,z)(H_P-z)}{l^3} dx dy dz$
	Residual Terrain Model	δg_{RTM}	$= 2\pi G \rho (H_P - H_{\text{ref}}) - G \int \int \int_{H_{\text{ref}}}^H \frac{\rho(x,y,z)(H_P-z)}{l^3} dx dy dz \approx 2\pi G \rho(x,y,z)(H - H_{\text{ref}}) - \delta g_{TC}$
anomaly	anomaly	Δg	$= g - \gamma_0$
	Free-Air	Δg_{FA}	$= g_{FA} - \gamma_0$
	simple Bouguer	Δg_{sB}	$= g_{sB} - \gamma_0$
	complete Bouguer	Δg_{cB}	$= g_{cB} - \gamma_0$
	Faye (Helmert)	Δg_{Faye}	$= g_{Faye} - \gamma_0$
	Airy-Heiskanen	Δg_{A-H}	$= g_{A-H} - \gamma_0$
	Pratt-Hayford	Δg_{P-H}	$= g_{P-H} - \gamma_0$
	Residual Terrain Model	Δg_{RTM}	$= g_{RTM} - \gamma_0$

List of Figures

2.1	Definition of spherical and rectangular coordinate systems (after Hofmann-Wellenhof and Moritz 2005)	13
2.2	The gravitational potential (after Hofmann-Wellenhof and Moritz 2005)	15
2.3	Geoid and ellipsoid (after Hofmann-Wellenhof and Moritz 2005)	18
2.4	3 rd Boundary Value Problem (after Hofmann-Wellenhof and Moritz 2005)	19
3.1	Reduction of gravity from Earth's topography surface S down to the geoid P	22
3.2	Bouguer plate: modelling the topography point-wise by an infinite plate of thickness H_p	24
3.3	Terrain correction, illustrating residual gravitational effect caused by surplus and deficiencies of the topographic masses (after Hofmann-Wellenhof and Moritz 2005, p. 136).	25
3.4	Rectangular prism (after Nagy 1966b).	27
3.5	Computation of terrain effects using fine and coarse resolution DEMs up to radiuses r_1 and r_2 , with spline densification around computation point P	28
3.6	Rectangular prisms for three cases: a) constant crustal density ρ_c , b) surface (2D) crustal density model, and c) 3D crustal density model.	29
3.7	Pratt-Hayford topographic-isostatic model: constant depth of compensation D and variable column density ρ_i (after Hofmann-Wellenhof and Moritz 2005).	31
3.8	Airy-Heiskanen topographic-isostatic model (after Hofmann-Wellenhof and Moritz 2005).	32
3.9	Geometry of the RTM reduction.	34
4.1	Determination of heights and height differences using two methods: classical levelling and GNSS/levelling (after Gerlach 2003)	40
4.2	Geoid undulation depending on the mass distributions of the Earth's crust (after Burkhard 1985)	40
4.3	Contribution of different data types in gravimetric geoid determination (after Schwarz et al. 1987).	42
4.4	Grid points of the developed lateral density models	45
4.5	Selected point gravity anomalies (blue dots) within the radius (black circle) of computing point (red dot) as input data for determination of ρ_c	46
4.6	The concept of the main surfaces in geodesy	48
4.7	The principle of gravimetric geoid determination (after Vermeer 2018)	48
4.8	Transformation of gravimetric to hybrid geoid model (after Arana et al. 2017)	49

4.9	Difference between geoid and co-geoid	51
4.10	Elements of the covariance function	55
4.11	Degree variances for EIGEN-6s4 and several analytic covariance models (Kaula, T-R, TM, Rapp)	62
4.12	Number of SH coefficients and spatial resolution of the GGMs as a function of the maximal SH degree of expansion n_{max}	63
4.13	Stokes integration using: a) geographic θ, λ (left) and, b) spherical ψ, α (right) coordinates (after Kuhn 2000).	68
4.14	Stokes' integration of point gravity data within spherical cap size ψ_0 around computation point P	69
4.15	Legendre polynomials for $n = 1, 2, 3, 5, 10, 20, 30$ as an argument of $t = \cos(\psi)$	69
4.16	Stokes' kernel $S(\psi)$ modifications as a function of the spherical distance ψ	71
4.17	Reference latitude bands for spherical multi-band kernel (after Forsberg and Sideris 1993)	74
4.18	Interpolation of N_{geoid}^i from the geoid model for each GNSS/levelling point.	75
4.19	Flowchart of geoid model accuracy validation.	77
4.20	The principle of relative geoid accuracy validation between two points A and B	78
5.2	The principle for filling gaps in the gravity database	88
5.3	Schematic diagram of the procedure for detection and filtering of outliers from the database	88
5.5	Map of residual anomalies $\Delta g_{FA-GGM-RTM}$ before and after filtering	90
5.6	Transformation of point gravity to the gravity grid	91
5.7	Schematic diagram of gridding methods validation	92
5.8	GNSS/levelling dataset	95
5.9	Gravity anomalies, geoid heights, and gravity gradients from EGM2008 for $n_{max} = 360$	97
5.10	Geoid undulation differences ($\delta N = N_{GNSS/lev.} - N_{GGM}$) as a function of different variables. EGM2008, $n_{max} = 2190$	101
5.11	Gridded geoid undulation differences $\delta N = N_{GNSS/lev.} - N_{GGM}$, EGM2008, no fit, $n_{max} = 2190$	102
5.14	Statistics of the differences between gravity and GNSS/levelling data, and GGM models as a function of maximal degree of expansion. For $30 < n_{max} < 300$. Fitting parametric model: nofit.	106
5.15	Statistics of the differences (residuals) between gravity and GNSS/levelling data, and GGM models as a function of maximal degree of expansion. For $200 < n_{max} < 2190$. Fitting parametric model: nofit.	107
5.12	Gravity anomaly differences ($\delta g = \Delta g_{grav.point} - \Delta g_{GGM}$) as a function of different variables. EGM2008, $n_{max} = 2190$	108
5.13	Gravity (free-air) anomaly differences $\delta g = \Delta g_{grav.point} - \Delta g_{GGM}$, EGM2008, no fit, $n_{max} = 2190$	109
5.16	Digital elevation model (DEM) can be either digital surface model (DSM) or digital terrain model (DTM) (after LINK)	110

5.17	DEM referenced to planar (left) and geographic coordinate (right) systems (after Kuhn 2000)	110
5.18	Earth's topography surface represented by two GDEMs	111
5.19	Geographic limits of the fine, coarse, and reference DEMs in the RCR approach geoid determination	113
5.20	Density and thickness models according to CRUST1	115
5.21	Crustal model CRUST1: Croatia	116
5.22	Schematic representation of the crustal density grid	117
5.23	Crustal density models for the Republic of Croatia	119
5.24	Differences between crustal density models ($\rho_c^{grid1} - \rho_c^{grid2}$)	120
5.25	Study area	121
6.2	Mean and st. dev. of $\Delta g_{FA-GGM-RTM}$ as a function of maximum degree n_{max} for EGM2008	127
6.1	Mean and st. dev. of $\Delta g_{FA-GGM-RTM}$ as a function of GGM up to $n_{max} = 250$	127
6.3	Mean and st. dev. of $\Delta g_{FA-GGM-RTM}$ as a function of digital elevation model (DEM)	128
6.4	Mean and st. dev. of $\Delta g_{FA-GGM-RTM}$ as a function of constant crustal density (ρ_c)	128
6.5	Mean and st. dev. of $\Delta g_{FA-GGM-RTM}$ as a function of resolution of the fine DEM (res fine DEM)	129
6.6	Mean and st. dev. of $\Delta g_{FA-GGM-RTM}$ as a function of resolution of the coarse DEM (res coarse DEM)	129
6.7	Mean and st. dev. of $\Delta g_{FA-GGM-RTM}$ as a function of resolution of the reference DEM (res ref DEM)	130
6.8	Mean and st. dev. of $\Delta g_{FA-GGM-RTM}$ as a function of low pass filter of the reference DEM (LPFref DEM)	130
6.9	Mean and st. dev. of $\Delta g_{FA-GGM-RTM}$ as a function of radius of inner zone r_1 (r_1)	131
6.10	Mean and st. dev. of $\Delta g_{FA-GGM-RTM}$ as a function of radius of outer zone r_2 (r_2)	131
6.11	Mean and st. dev. of $\Delta g_{FA-GGM-RTM}$ as a function of gridding method of the digital elevation model (DEM grid meth)	132
6.12	Mean and st. dev. of $\Delta g_{FA-GGM-RTM}$ as a function of reference DEM resolution (res ref DEM and reference DEM low pass filtering (LPF ref DEM). EGM2008, with $n_{max} = 2190$. Units: [mGal].	132
6.13	Mean and st. dev. of $\Delta g_{FA-GGM-RTM}$ as a function of maximum degree of GGM (n_{max}) and reference DEM resolution (res ref DEM). Units: [mGal].	133
6.14	Mean and st. dev. of $\Delta g_{FA-GGM-RTM}$ as a function of inner zone radius (r_1) and outer zone radius (r_2). Units: [mGal].	133
7.1	Gridded geoid undulation differences $\delta N_{GNSS/lev.-geoid}$ for gravimetric and hybrid KTH geoid models	140
7.2	Additive correction of on geoid undulation in KTH approach	141
7.3	Approximate geoid undulation (\tilde{N}), gravimetric and hybrid geoid models HRG2018-KTH-gra	142

7.4	Standard deviation of $\delta N_{GNSS/lev.-geoid}$ as a function of global geopotential model (GGM)	144
7.5	Standard deviation of $\delta N_{GNSS/lev.-geoid}$ as a function of maximum degree of GGM (n_{max})	144
7.6	Standard deviation of $\delta N_{GNSS/lev.-geoid}$ as a function of digital elevation model (DEM)	145
7.7	Standard deviation of $\delta N_{GNSS/lev.-geoid}$ as a function of gridding method of the digital elevation model (DEM grid meth)	145
7.8	Standard deviation of $\delta N_{GNSS/lev.-geoid}$ as a function of gridding method of the anomalies (anmly grid meth)	146
7.9	Standard deviation of $\delta N_{GNSS/lev.-geoid}$ as a function of density of the crust (ρ_c)	147
7.10	Standard deviation of $\delta N_{GNSS/lev.-geoid}$ as a function of resolution of the geoid (geoid res)	147
7.11	Standard deviation of $\delta N_{GNSS/lev.-geoid}$ as a function of spherical cap size (ψ_0)	148
7.12	Standard deviation of $\delta N_{GNSS/lev.-geoid}$ as a function of variance of terrestrial gravity data (C_0)	148
7.13	Standard deviation of $\delta N_{GNSS/lev.-geoid}$ as a function of Stokes integral stochastic solutions (v)	149
7.14	Standard deviation of $\delta N_{GNSS/lev.-geoid}$ as a function of input (gravity anomalies, DEMs) models resolution (inp mod res)	149
7.15	Standard deviation of $\delta N_{GNSS/lev.-geoid}$ as a function of Integration radius of anomalies in DWC (ψ_{DgR})	150
8.1	Empirical covariance function for the best solution	159
8.2	Quasi-geoid (ζ) to geoid (N) correction	166
8.3	Final gravimetric and hybrid geoid models HRG2018-RCR	168
8.4	Transformation surface: difference between gravimetric and hybrid HRG2018-RCR models	169
8.5	Gridded geoid undulation differences $\delta N_{GNSS/lev.-geoid}$ for gravimetric and hybrid geoid models HRG2018-RCR	171
8.6	Absolute values of differences (residuals) between GNSS/levelling points and gravimetric geoid as a function of different variables	172
8.7	Relative geoid accuracy of gravimetric and hybrid models HRG2018-RCR and HRG2018-KTH	174
A.1	Flowchart of geoid determination using KTH approach.	203
A.2	Flowchart of geoid determination using RCR approach.	204
B.1	Differences (<i>grid 1 – grid 2</i>) between gravimetric geoid models calculated by using different computation methods. Units: [cm]. Part 1/3.	205
B.2	Differences (<i>grid 1 – grid 2</i>) between gravimetric geoid models calculated by using different computation methods. Units: [cm]. Part 2/3.	206
B.3	Differences (<i>grid 1 – grid 2</i>) between gravimetric geoid models calculated by using different computation methods. Units: [cm]. Part 3/3.	207

B.4	Differences (<i>grid 1</i> – <i>grid 2</i>) between gravimetric geoid models calculated by using different computation methods. Mean difference between models removed. Units: [cm]. Part 1/3.	208
B.5	Differences (<i>grid 1</i> – <i>grid 2</i>) between gravimetric geoid models calculated by using different computation methods. Mean difference between models removed. Units: [cm]. Part 2/3.	209
B.6	Differences (<i>grid 1</i> – <i>grid 2</i>) between gravimetric geoid models calculated by using different computation methods. Mean difference between models removed. Units: [cm]. Part 3/3.	210
C.1	Normal gravity γ_0 model	212
C.2	Free-air gravity anomaly Δg_{FA} model	212
C.3	Terrain correction δg_{TC} model	213
C.4	Faye (Helmert) anomaly Δg_{Faye} model	213
C.5	Simple Bouguer anomaly Δg_{SB} model	214
C.6	Complete Bouguer anomaly Δg_{cB} model	214
C.7	Airy-Heiskanen topographic-isostatic reduction δg_{A-H} model	215
C.8	Airy-Heiskanen topographic-isostatic anomaly Δg_{A-H} model	215

List of Tables

1.1	A list of geoid models and corresponding references worldwide	8
1.2	Information and validation of previous geoid model solutions over Croatia . . .	9
2.1	Defining constants of GRS80 ellipsoid	16
2.2	Functionals of disturbing potential T in spherical approximation (e.g. Denker 1988)	17
3.1	Properties of gravity anomalies for different topographic reduction schemes (after Bajracharya 2004)	36
4.1	The relation between fundamental equation of physical geodesy (FEPR) and Stokes integral	41
4.2	Spectral sensitivity of the gravity field functionals (after Schwarz 1984 , Kuhn 2000 and Kern 2003)	43
4.3	Input parameters for development of surface crustal density models according to inversion by Airy-Heiskanen, Pratt-Hayford and Parasnis-Nettleton's topographic-isostatic models	44
4.4	The main characteristics of the orthometric and normal heights (after Marti and Schlatter 2002)	49
4.5	Parameters of the stochastic and deterministic modifications of the Stokes' kernel	55
4.6	Global analytic empirical degree-variance models for gravity anomalies (after Wenzel 1985 , p. 147 and Kern 2003)	61
4.7	Summary of least-squares collocation (after Moritz 1989 and Kern 2003)	64
4.8	Comparison of deterministic modifications of the Stokes' integral according to Kern (2003) (small ○; medium ◐; large ●)	72
5.1	Statistics of different types of gravity anomalies before and after filtering/outlier detection of the database. Units: [mgal].	86
5.2	List of input parameters for different gridding methods (GS Surfer software). .	93
5.3	Interpolation accuracy of different gridding methods for free-air Δg_{FA} (left) and residual gravity anomalies $\Delta g_{FA} - \Delta g_{GGM} - \Delta g_{RTM}$ (right). Sorted by RMS, units: [mGal].	93
5.4	Interpolation accuracy of different gridding methods for simple Δg_{sBoug} (left) and complete Bouguer anomalies Δg_{cBoug} (right). Sorted by RMS, units: [mGal].	94

5.5	Comparison of the best interpolation methods for different types of gravity anomalies. Sorted by RMS. Units: [mGal].	94
5.6	A list of the validated GGMs. Sorted descending by the publishing year (source: GFZ 2017a).	99
5.7	Statistics of geoid undulation differences $\delta N_{GNSS/lev.-GGM}$ for validated GGMs. Fitting parametric model: no fit (left) and 3rdpoly (right), sorted by RMS, units: [cm].	100
5.8	Statistics of differences $\delta N_{GNSS/lev.-GGM}$ using different fitting parametric models. Units: [cm].	103
5.9	Statistics of gravity anomaly differences $\delta g = \Delta g_{gravim.point} - \Delta g_{GGM}$ for validated GGMs. Fitting parametric model: nofit and 3rdpoly, sorted by RMS, units: [mGal].	103
5.10	Statistics of differences $\delta g_{grav.point-GGM}$ using different fitting parametric models. Model: GECO. Units: [mGal].	105
5.11	Basic characteristics of global digital elevation models selected for geoid modelling	112
5.12	Vertical accuracy of GDEMs across Croatia (Varga and Bašić 2015). Units: [m].	114
5.13	The main properties of used 3D crustal models	114
5.14	Input parameters for calculation of crustal density models using three inversion methods	116
5.15	Statistics and differences between developed crustal density models. Units: [kgm ⁻³].	118
5.16	A list of the existing software packages and routines used in computations . . .	123
6.1	Input data and parameters for computation of Δg_{GGM} contribution	126
6.2	Input data and parameters for computation of Δg_{RTM} contribution	126
7.1	Input data and parameters for geoid model determination using KTH approach .	137
7.2	Statistics of the geoid undulation differences $\delta N_{GNSS/lev.-geoid}$ for HRG2018-KTH geoid. Units: [cm].	138
7.3	Statistics of the gravimetric and hybrid geoid solutions giving smallest RMS compared to GNSS/levelling. Selected among more than 3000 different solutions. Units: [cm].	139
7.4	KTH approach additive corrections	142
8.1	Geoid computation methods in RCR approach	152
8.2	Statistics of residual gravity anomalies $\Delta g_{FA-GGM-RTM}$ selected for geoid computation	153
8.3	Statistics of the geoid undulation differences $\delta N_{GNSS/lev.-geoid}$ for gravimetric geoid models computed with constant values, 2D surface (lateral) and 3D crustal models. Units: ρ_c in [kgm ⁻³], statistics in [cm].	154
8.4	Statistics of the geoid undulation differences $\delta N_{GNSS/lev.-geoid}$ for hybrid (fitted) geoid models computed with constant values, 2D surface (lateral) and 3D crustal models. Units: ρ_c in [kgm ⁻³], statistics in [cm].	155

8.5	Input data and parameters for computation of geoid using Stokes method	155
8.6	Statistics of the differences between GNSS/levelling and selected geoid models computed using Stokes method. Fitting parametric model: 3rdpoly. Units: [cm].	156
8.7	Input data and parameters for computation of geoid using planar FFT method .	156
8.8	Statistics of the differences between GNSS/levelling and selected geoid models computed using planar FFT method. Fitting parametric model: 3rdpoly. Units: [cm].	157
8.9	Input data and parameters for computation of geoid using flat-Earth logarithmic LSC method	158
8.10	Statistics of the differences between GNSS/levelling and selected geoid models computed using flat-Earth logarithmic LSC method. Fitting parametric model: 3rdpoly. Units: [cm].	158
8.11	Input data and parameters for computation of geoid using LSC method	159
8.12	Statistics of the differences between GNSS/levelling and selected geoid models computed using least squares collocation method. Fitting parametric model: 3rdpoly. Units: [cm].	160
8.13	Input data and parameters for computation of geoid using spherical multi-band FFT method	161
8.14	Statistics of the differences between GNSS/levelling and selected geoid models computed using spherical multi-band FFT method. Fitting parametric model: 3rdpoly. Units: [cm].	161
8.15	Input data and parameters for computation of geoid using spherical 1D FFT method	162
8.16	Statistics of the differences between GNSS/levelling and selected geoid models computed using spherical 1D FFT method. Fitting parametric model: 3rdpoly. Units: [cm].	162
8.17	Comparison of the statistics of geoid undulation differences ($\delta N_{GNSS/lev.-geoid}$). Geoid models are computed using different RCR methods and KTH approach. Fit: 3rdpoly, units: [cm].	163
8.18	Statistics of gravimetric geoid models computed using different computation methods. Units: [cm].	164
8.19	Statistics of the differences ($\delta N = grid - grid$) between gravimetric geoid models computed using different computation methods. Units: [cm].	165
8.20	Statistics of the <i>remove</i> gravity anomaly contributions of the input residual gravity anomalies $\Delta g_{FA} - \Delta g_{GGM} - \Delta g_{RTM}$. Units: [mGal].	167
8.21	Statistics of the <i>compute</i> and <i>restore</i> geoid undulation contributions of the HRG2018-RCR geoid. Units: [m].	167
8.22	Statistics of GEOFOUR geoid solution by different fitting parametric models. Units: [cm].	170
C.1	Statistics of the gravity anomaly models. Units: [mgal].	211
D.1	A list of developed Matlab scripts	218
E.1	Properties of height systems (after Meyer et al. 2007 and Ince 2011)	223

E.2 A list of fitting parametric models (Daho et al. 2006, Fotopoulos 2013) 224

E.3 Basic statistical measures used for analysis of results 224

9.4 Formulas for obtaining gravity values, topographic reductions and gravity anomalies 225

Curriculum Vitae

Matej Varga was born in Zagreb on March 18th, 1989. He finished Third Mathematical Gymnasium in Zagreb in 2007. From 2007 to 2012 he studied undergraduate and graduate study programmes in geodesy and geoinformatics at the Faculty of Geodesy, University of Zagreb. His grades were among the 10% of the most successful students. During his studies he received two scholarships from the Ministry of Science, Education and Sports, and from Ministry of Defense. As a student he was editor-in-chief of the student magazine Ekscentar.



After graduation, he was employed at the Chair of State Survey (Department of Geomatics, Faculty of Geodesy, University of Zagreb) as a teaching fellow and research assistant. He has been involved in practical exercises and field survey within several subjects at the undergraduate and graduate study programmes including State Survey, Geodetic Reference Systems, Physical Geodesy, Geophysical Geodesy and Satellite Geodesy. He was a principal investigator in five Master Theses.

His main research interests are gravity and geomagnetic field modelling and surveying, geoid modelling, geodetic reference systems and transformations, and geometrical geodesy. He was co-researcher in five national and international scientific projects including Croatian Geomagnetic Repeat Stations Network, GEOMED-2 and Geopotential and Geodynamics of the Adriatic. As an author or coauthor he published more than 25 publications. In 2017, as an academic researcher he visited IfE at the LUH in Germany.

He is an associate editor in the Journal of Geodetic Science and regular reviewer of two international journals. He is a member of the Croatian Chamber of Chartered Geodetic Engineers, Croatian Geodetic Society and Croatian Cartographic Society. He is a corresponding member of the IAG Joint Working Group: Unified Height System, Strategy for the Realization of the IHRS.

He is proficient in English and German languages. His hobbies are guitar playing, football refereeing, fitness and chess.

More information: Personal page: [Homepage](#)
 Research profiles: [Research Gate](#), [CROSBI](#), [Google Scholar](#), [ORCID](#).
 Business e-mail: 1st: mvara@geof.hr.
 Personal e-mail (permanent): mvara1989@gmail.com.

List of publications

Book chapters

1. Brkić, M.; **Varga, Matej**; Poslončec-Petrić, V. *Geomagnetic field for the epoch 2009.5*. Osnovna geomagnetska mreža Republike Hrvatske 2004.-2012., s kartama geomagnetskog polja za epohu 2009.5. Brkić, M., editor(s). Zagreb: State Geodetic Administration, 2013. pp. 33-38.

Articles in international journals

1. **Varga, Matej**; Bašić, T. *Accuracy validation and comparison of global digital elevation models over Croatia*. International Journal of Remote Sensing. 36 (2015), 1; 170-189. DOI: [10.1080/01431161.2014.994720](https://doi.org/10.1080/01431161.2014.994720).
2. **Varga, Matej**; Grgić, M.; Bašić, T. *Empirical Comparison of the Geodetic Coordinate Transformation Models: a Case Study of Croatia*. Survey Review - Directorate of Overseas Surveys. 48 (2015); 1-13. DOI: [10.1080/00396265.2015.1104092](https://doi.org/10.1080/00396265.2015.1104092).
3. Grgić, M.; **Varga, Matej**; Bašić, T. *Empirical Research of Interpolation Methods in Distortion Modeling for the Coordinate Transformation between Local and Global Geodetic Datums*. Journal of Surveying Engineering. 142 (2015), 2; 5-15. DOI: [10.1061/\(asce\)su.1943-5428.0000154](https://doi.org/10.1061/(asce)su.1943-5428.0000154).

International and national conference papers and posters

1. Bašić, A.; **Varga, Matej**; Bašić, T. *Practical height issues in 3D cadastral*. Zbornik radova 10. simpozija ovlaštenih inženjera geodezije: Prostorni registri za budućnost / Paar, R. (ed.). Opatija, Hrvatska, 19-22.10.2017. 84-89 (in Croatian).
2. Lozo, M.; **Varga, Matej**; Bašić, T. *Modern Height Reference System as a Precondition of the implementation of the 3D Cadastre*. Prostorni registri za budućnost / Paar, R. (ed.). Opatija, Hrvatska, 19-22.10.2017. 26-31.
3. **Varga, Matej**; Skočić, Š.; Bašić, T. *Investigations of the effects of topographic/bathymetric masses and crustal parameters in gravity field modeling*. 17th International Multidisciplinary Scientific Geoconference SGEM 2017, Issue 22, Volume 17. Sofia : STEF92 Technology Ltd, 2017. 383-388.
4. **Varga, Matej**; Vidić, I.; Bašić, T. *Analysis of satellite based global gravity field models on GNSS/levelling and reference gravity stations worldwide*. 17th International Multidisciplinary Scientific Geoconference SGEM 2017, Issue 22, Volume 17. Sofia : STEF92 Technology Ltd., 2017. 99-106.
5. Barzaghi, R.; Vergos, G. S.; ... ; **Varga, Matej**. *Gravimetric geoid model development in the Mediterranean Sea within the Geomed2 project*. IAG Symposia Series. Springer.
6. Barzaghi, R.; Vergos, G. S.; ... **Varga, Matej**; ... *The GEOMED2 project: Multi-resolution aspects and aliasing in topographic effects for geoid and gravity determination*. IAG-IASPEI 2017 Online abstracts.
7. Barzaghi, R.; Vergos, G. S.; ... **Varga, Matej**; ... *The GEOMED2 project: Geoid and circulation in the Mediterranean Sea*. IAG-IASPEI 2017 Online abstracts.
8. **Varga, Matej**; Bjelotomić, O.; Bašić, T. *Initial Considerations on Modernization of the Croatian Height Reference System*. Proceedings of the International Symposium on Engineering Geodesy - SIG 2016. 2016. 225-233.
9. Barzaghi, R.; Vergos, G. S.; ...; **Varga, Matej**;... *Gravimetric geoid model development in the Mediterranean Sea within the Geomed2 project*. IAG Symposia Series. Springer.
10. Barzaghi, R.; Vergos, G. S.; ...; **Varga, Matej**; ... *Investigation of the contribution of topographic effects on regional geoid modeling within the Geomed2 project*. GGHS2016 abstracts.
11. **Varga, Matej**; Grgić, M.; Bjelotomić, O.; Bašić, T. *PGREP - towards a REpository of worldwide resources used in Physical Geodesy*. GGHS2016 abstracts.
12. Barzaghi, R.; Vergos, G. S.; ...; **Varga, Matej**; ... *Improved representations of the Mediterranean Geoid within the GE-OMED 2 project. Contributions of local gravity, GOCE and Cryosat2 data*. Proceedings of ESA LP 2016.
13. Barzaghi, R.; Vergos, G. S.; ...; **Varga, Matej**; ... *Theoretical and numerical investigations towards a new geoid model for the Mediterranean Sea - The GEOMED2 project*. EGU abstracts.
14. Barzaghi, R.; Albertella, A.; ...; **Varga, Matej**; ... *The GEOMED 2 project: A high resolution geoid of the Mediterranean Sea*. 26th International Union of Geodesy and Geophysics (IUGG) General Assembly 2015. 2015.
15. Grgić, M.; **Varga, Matej**; Bašić, T. *The Empirical Comparison of Coordinate Transformation Models and Distortion Modeling Methods Based on a Case Study of Croatia*. AGU meeting abstract database 2015. 2015.
16. Vujčić, Eugen; Kovács, P.; Brkić, M.; **Varga, Matej**. *Regional geomagnetic field model for Croatia*. IUGG Abstracts. 2015.

17. **Varga, Matej**; ...; Bašić, T.: *Accuracy validation of global digital elevation models SRTM and ASTER using GNSS stations of CROPOS permanent network*. Zbornik radova 4. CROPOS konferencije. 2015. 106-113.
18. Grgić, M.; ... **Varga, Matej**; ...: *Empirical comparison of different transformation models and T7D model over the area of the city of Zagreb*. Zbornik radova 4. CROPOS konferencije. 2015. 96-105.
19. Grgac, I.; ...; **Varga, Matej**; ...: *Comparison of heights determined with CROPOS VPPS service and geometric levelling in Earth gravity field*. Zbornik radova 3. CROPOS konferencije. 2013. 118-125.
20. Grgić, M.; ...; **Varga, Matej**; ...: *Application of the Trimble xFill system for Augmentation of Global Navigation Systems*. Zbornik radova 3. CROPOS konferencije. 2013. 126-132.

Articles in other journals

1. **Varga, Matej**. *Geomagnetic Anomalies over the Territory of the Republic of Croatia*. Geodetski list: glasilo Hrvatskoga geodetskog društva. 68 (2014), 3; 173-184.
2. Šugar, D.; **Varga, Matej**; Cindrić, M. *Night-time Geomagnetic Field Observations on the POKUpsko Repeat Station*. Geodetski list: glasilo Hrvatskoga geodetskog društva. 67 (90) (2013), 1; 13-27.
3. **Varga, Matej**; Bašić, T. *Quality Assessment and Comparison of Global Digital Elevation Models on the Territory of Republic of Croatia*. Kartografija i geoinformacije: časopis Hrvatskoga kartografskog društva. 12 (2013), 20; 4-17.
4. Grgić, M.; **Varga, Matej**. *The Establishment of the Natura 2000 Network and the Role of the INSPIRE Directive*. Ekscentar: časopis studenata Geodetskog fakulteta Sveučilišta u Zagrebu. 16 (2013); 54-57.
5. **Varga, Matej**; Dragčević, D.; Pinter, D.; Ramić, M.; Topolovec, I. *Review of the regional geoid models around the world*. Ekscentar: časopis studenata Geodetskog fakulteta Sveučilišta u Zagrebu. 148 (2012), 15; 82-88.
6. **Varga, Matej**. *Validation of the Airy-Heiskanen topo-isostatic compensation model over the territory of Republic Croatia*. Ekscentar: časopis studenata Geodetskog fakulteta Sveučilišta u Zagrebu. 148 (2012), 15; 104-108.
7. **Varga, Matej**. *Global Geodetic Observing System - GGOS*. Ekscentar: časopis studenata Geodetskog fakulteta Sveučilišta u Zagrebu. 124 (2011); 69-75.
8. **Varga, Matej**. *Ruder Bošković in geodesy*. Ekscentar: časopis studenata Geodetskog fakulteta Sveučilišta u Zagrebu. 124 (2011); 94-96.
9. Luketić, A.; **Varga, Matej**; Žižić I. *Analysis of the CROPOS on the calibration base of the Faculty of Geodesy, Zagreb*. Ekscentar: časopis studenata Geodetskog fakulteta Sveučilišta u Zagrebu. 112 (2010), 12; 48-51.

Mentoring

1. Bašić, A. (2017). *Unification of the local height reference systems by determination of vertical datum shifts and potential values W_0* . Zagreb: Faculty of Geodesy. MSc Thesis. Supervisor: Bašić, T. Principal investigator: **Matej Varga**.
2. Lozo, A. (2017). *Investigations of the accuracy of the regional gravimetric geoid models in Europe*. Zagreb: Faculty of Geodesy. MSc Thesis. Supervisor: Bašić, T. Principal investigator: **Matej Varga**.
3. Vidaković, M. *Reduction of the Earth's Magnetic Field's Historical Data*. MSc Thesis. Zagreb: Faculty of Geodesy, 29.09. 2016, 82 pages. Supervisor: Brkić, M., Principal investigator: **Matej Varga**.
4. Vidić, I. *Validation of Global Geopotential Models using GNSS/levelling and gravimetric data worldwide*. MSc Thesis. Zagreb: Faculty of Geodesy, 29.09. 2016, 67 pages. Supervisor: Bašić, T., Principal investigator: **Matej Varga**.
5. Skočić, Š. *Analysis of influence of the Digital Elevation Models and Physical Parameters in Modeling of the Earth's Gravity Field*. MSc Thesis. Zagreb: Faculty of Geodesy, 10.07. 2015, 65 pages. Supervisor: Bašić, T., Principal investigator: **Matej Varga**.
6. Grgac, I. *The Application of Gravity in Height Systems*. MSc Thesis. Zagreb: Faculty of Geodesy, 20.09. 2013., 66 pages. Supervisor: Bašić, T., Principal investigators: Marko Pavasović and **Matej Varga**.

